

# LIGHT-MATTER INTERACTION IN HYBRID QUANTUM PLASMONIC SYSTEMS

Zur Erlangung des akademischen Grades eines  
DOKTORS DER NATURWISSENSCHAFTEN (Dr. rer. nat.)

an der KIT-Fakultät für Physik des  
Karlsruher Instituts für Technologie (KIT)

angenommene

DISSERTATION

von

Dipl.-Phys. Jakob Straubel

Tag der mündlichen Prüfung      18.05.2018

1. Referent      Prof. Dr. Carsten Rockstuhl

2. Korreferent      Prof. Dr. David Hunger



Dieses Werk ist lizenziert unter einer Creative Commons Namensnennung -  
Weitergabe unter gleichen Bedingungen 4.0 International Lizenz (CC BY-SA 4.0):  
<https://creativecommons.org/licenses/by-sa/4.0/deed.de>

# Contents

<b>Abstract</b>	<b>v</b>
<b>Publication List</b>	<b>vii</b>
<b>1 Introduction</b>	<b>1</b>
<b>2 Theoretical Framework</b>	<b>5</b>
2.1 Elements of Solid-State Optics . . . . .	6
2.2 Elements of Surface Physics . . . . .	12
2.3 Scattering of Light . . . . .	22
2.4 Elements of Quantum Optics . . . . .	29
2.5 Cavity Quantum Electrodynamics . . . . .	36
<b>3 Semi-Classical Model and Parameters</b>	<b>45</b>
3.1 Cavity QED Interaction Model . . . . .	45
3.2 Model Parameter Genesis . . . . .	49
<b>4 Optical Nanoantenna Applications</b>	<b>65</b>
4.1 From Quenching to Emission Enhancement . . . . .	67
4.2 Mode Conversion within Bimodal Nanoantennas . . . . .	76
4.3 Bimodal Nanoantenna as Single Photon Source . . . . .	83
4.4 Bimodal Nanoantenna Emitting in Entangled Modes . . . . .	93
<b>5 Summary &amp; Outlook</b>	<b>103</b>
<b>Bibliography</b>	<b>I</b>



# LIGHT-MATTER INTERACTION IN HYBRID QUANTUM PLASMONIC SYSTEMS

by

JAKOB STRAUBEL

Dissertation accepted by the KIT Department of Physics

Attempting to implement quantum information related applications utilizing atoms and photons, as they naturally form quantum systems supporting superposition states, hybrid quantum plasmonic systems emerged in the past as a platform to study and engineer light-matter interaction. This platform combines the unrivaled electromagnetic field localization of surface plasmon polaritons, boosting the light-matter coupling rate, with the tremendous integration potential of truly nanoscale structures, and both the significant emission rates of nanoantennas and photonic transmission velocities.

In this work, a classical description of surface plasmon polaritons is combined with a light-matter interaction model based on a cavity quantum electrodynamical formalism. The resulting composite semi-classical method, introduced and described in this thesis, provides efficient and versatile means to simulate the dynamical behavior of radiative atomic transitions coupled to plasmonic cavity modes in the weak incoherent coupling regime. Both the emission into the far field and various dissipation mechanisms are included by expanding the model to an open quantum system.

The variety of light-matter interaction applications that can be modeled with the outlined method is indicated by the four different exemplary scenarios detailed in the application chapter of this thesis. The classical description of localized surface plasmon polaritons is benchmarked by reproducing the experimental measurements of the molecular fluorescence manipulation through optical nanoantennas in a collaborative effort with experimental partners. Furthermore, in the weak light-matter coupling regime, the potential of achieving a higher nanoantenna functionality and simultaneously realizing more elaborate quantum dynamics is revealed by the three remaining applications. Each pivotally involving a bimodal nanoantenna and demonstrating different quantum optical phenomena, the implementation of cavity radiation mode conversion, non-classical cavity emission statistics, and non-classical cavity emission properties is shown and described in the application chapter.



## PUBLICATION LIST

### PEER REVIEWED JOURNALS

The peer reviewed publications immediately relevant for this thesis are shown in **bold** font.

#### AS A PART OF THE DIPLOMA PROJECT:

- K. Słowik, R. Filter, J. Straubel, F. Lederer, and C. Rockstuhl, 'STRONG COUPLING OF OPTICAL NANOANTENNAS AND ATOMIC SYSTEMS', *Physical Review B* 88 (19), 195414 (2013)
- R. Filter, K. Słowik, J. Straubel, F. Lederer, and C. Rockstuhl, 'NANOANTENNAS FOR ULTRABRIGHT SINGLE PHOTON SOURCES', *Optics Letters* 39 (5), 1246 (2014)
- K. Słowik, R. Filter, J. Straubel, F. Lederer, and C. Rockstuhl, 'COUPLING OF QUANTUM EMITTERS AND METALLIC NANOANTENNAE FOR THE GENERATION OF NONCLASSICAL LIGHT AT HIGH RATES', *Physica Scripta* 2014 (T160), 014037 (2014)

#### AS A PART OF THE PHD PROJECT:

- G. Toscano, J. Straubel, A. Kwiatkowski, C. Rockstuhl, F. Evers, H. Xu, N. A. Mortensen, and M. Wubs, 'RESONANCE SHIFTS AND SPILL-OUT EFFECTS IN SELF-CONSISTENT HYDRODYNAMIC NANOPLASMONICS', *Nature Communications* Vol. 6, 7132 (2015)
- **H. Chen, J. Yang, E. Rusak, J. Straubel, R. Guo, Y. W. Myint, J. Pei, M. Decker, I. Staude, C. Rockstuhl, Y. Lu, Y. S. Kivshar, D. N. Neshev**, 'MANIPULATION OF PHOTOLUMINESCENCE OF TWO-DIMENSIONAL  $\text{MoSe}_2$  BY GOLD NANOANTENNAS', *Scientific Reports* 6, 22296 (2016)
- **J. Straubel, R. Filter, C. Rockstuhl, and K. Słowik**, 'PLASMONIC NANOANTENNA BASED TRIGGERED SINGLE-PHOTON SOURCE', *Physical Review B* 93 (19), 195412 (2016)
- **J. Straubel, R. Filter, C. Rockstuhl, and K. Słowik**, 'EFFICIENT MODE CONVERSION IN AN OPTICAL NANOANTENNA MEDIATED BY QUANTUM EMITTERS', *Optics Letters* 41 (10), 2294 (2016)
- **J. Straubel, R. Sarniak, C. Rockstuhl, and K. Słowik**, 'ENTANGLED LIGHT FROM BIMODAL OPTICAL NANOANTENNAS', *Physical Review B* 95 (8), 085421 (2017)
- M.-S. Kim, B. V. Lahijani, N. Deschermes, J. Straubel, F. Negredo, C. Rockstuhl, M. Hayrinen, M. Kuittinen, M. Roussey, H. P. Herzig, 'SUBWAVELENGTH FOCUSING OF BLOCH SURFACE WAVES', *ACS Photonics* 2017 4 (6), 1477 (2017)
- J. Oppermann, J. Straubel, K. Słowik, and C. Rockstuhl, 'QUANTUM DESCRIPTION OF RADIATIVE DECAY IN OPTICAL CAVITIES', *Physical Review A* 97 (1), 013809 (2018)
- J. Oppermann, J. Straubel, I. Fernandez-Corbaton, and C. Rockstuhl, 'A NORMALIZATION APPROACH FOR SCATTERING MODES TO BE OF USE IN CLASSICAL AND QUANTUM ELECTRODYNAMICS', submitted to *Physical Review A*, unpublished

---

## CONFERENCE CONTRIBUTIONS

- K. Słowik, R. Filter, J. Straubel, C. Rockstuhl, and F. Lederer, '*A fully quantum description of hybrid nanosystems: Coupling of atoms and metallic nanoantennas*', presented at CEWQO 2013, Stockholm, Sweden, 2013
- K. Słowik, R. Filter, J. Straubel, C. Rockstuhl, and F. Lederer, '*Optical properties of hybrid atomic and plasmonic systems in the weak and strong coupling regime*', presented at Metamaterials'2013, Bordeaux, France, 2013
- R. Filter, K. Słowik, J. Straubel, F. Lederer, and C. Rockstuhl, '*Nanoantennas for ultrabright single photon sources*', presented at Nanolight 2014, Benasque, Spain, 2014
- C. Rockstuhl, J. Straubel, J. Hou, C. Bösel, K. Słowik, and R. Filter, '*Weak and strong coupling of quantum emitters with optical nanoantennas*', presented at META'2014, Singapore, Singapore, 2014
- C. Rockstuhl, R. Filter, K. Słowik, J. Straubel, J. Hou, C. Bösel, and G. Toscano, '*Quantum optical properties of hybrid plasmonic nanostructures*', presented at Metamaterials'2014, Copenhagen, Denmark, 2014
- K. Słowik, J. Straubel, R. Filter, R. Sarniak, and C. Rockstuhl, '*Engineering quantum states of light with optical nanoantennas*', presented at CEWQO 2015, Warsaw, Poland, 2015
- G. Toscano, J. Straubel, and C. Rockstuhl, '*Hydrodynamic model for surface plasmon polaritons in metallic nanostructures*', presented at WAVES 2015, Karlsruhe, Germany, 2015
- G. Toscano, A. Kwiatkowski, J. Straubel, C. Rockstuhl, '*Electron Tunneling in Plasmonic Nanogaps Explored Using the Self-consistent Hydrodynamic Model*', presented at PIERS 2015, Prague, Czech Republic, 2015
- K. Słowik, E. Rusak, M. Göddel, J. Straubel, M. Kühn, F. Weigend, C. Rockstuhl, '*Nanoantennas for controlled enhancement and interference of higher-multipole molecular transitions*', presented at META'2016, Malaga, Spain, 2016
- H. Chen, J. Yang, E. Rusak, J. Straubel, R. Guo, Y. W. Myint, J. Pei, M. Decker, I. Staude, C. Rockstuhl, Y. Lu, Y. S. Kivshar, D. N. Neshev, '*Manipulation of photoluminescence of 2D MoSe<sub>2</sub> by gold nanoantennas*', presented at SPIE Optics + Photonics 2016, San Diego, United States, 2016
- J. Straubel, K. Słowik, R. Sarniak, R. Filter, and C. Rockstuhl, '*Use of plasmonic nanoantennas in non-classical light sources*', presented at NANOMETA 2017, Seefeld, Austria, 2017
- K. Słowik, J. Straubel, and C. Rockstuhl, '*Antennas for Photons: Light-Matter Coupling at Nanoscale*', presented at IEEE ICP2018, Langkawi Island, Malaysia, 2018

# 1 Introduction

Technological progress has been the driving force behind the exponential growth of global wealth since the Industrial Revolution<sup>[1]</sup>. While initially mechanization replaced manual labor, the Information Revolution is characterized by computer-based automatization of conceptual, managerial, and administrative functions and the coordination of the production flow<sup>[2]</sup>. Consequently, the Information Age has been accompanied by tremendous advancements in information and communication technology since its onset between 1945 and 1970.

The most prominent example and archetypal for such advancements is the development of means to store, transmit, and process information from the mid-1980s to the mid-2000s. In this period, characterized by the transition from predominantly analog to digital means, the development progressed at exponential growth rates<sup>[3]</sup>. This progression brings Moore's rule of thumb to mind, regarding the predicted biennial doubling of the number of transistors in solid-state integrated circuits, which held throughout various evolutionary stages of transistor technology<sup>[4]</sup>. But with single transistors approaching spatial dimensions of tens of nanometers, fundamental limits of this technological ansatz become evident. The line for further down scaling has to be drawn due parasitic resistance, parasitic capacitance, and thermal noise. Together they cancel out the benefits from further increasing the integration density<sup>[5]</sup>.

While reaching technological limits only affects the prospects of further developments in the same vein and not the prospects of an entire technological platform, it does certainly call for a reevaluation of the chosen ansatz for the technological implementation. Classical information science defines information itself, as reducing the possible answers to a specific problem and can deal with the various technical aspects of processing and transmitting information<sup>[6]</sup>. It also identifies information as negentropy, which in turn inherently introduces the classical limitations of the integration of information computation devices<sup>[7]</sup>.

In light of the rapid advancements in the past, unhindered by aspects of the technological implementation, the existence of fundamental classical limitations

---

renders reaching them only a question of time. Hence, the development of means beyond classical information has emerged as one of the most relevant tasks of the Information Age. This has motivated vast research activity in and around the topic of quantum information<sup>[8–10]</sup>, its processing<sup>[11,12]</sup>, transmission<sup>[13–15]</sup>, and storage<sup>[16–18]</sup>.

Switching from classical bits to qubits, as coherent superposition states of quantum two-level systems, the continuous quantum state amplitudes hugely surpass the classical single bit in terms of information content. To perform quantum information processing, the initial quantum state must be controlled and the superposition character must be preserved<sup>[19]</sup>. This is equivalent to the detachment of the qubits from environmental influence, which immediately counteracts any pronounced interaction with the environment to facilitate efficient external measurements. Consequently, meeting such difficult requirements severely limits the number of promising physical platforms to implement quantum information processing. With the spin of an electron and the polarization of a photon forming quantum two-level systems that are well-investigated, technologically accessible and not least fundamental in nature, atoms and photons arise as one such platform.

### **Light-Matter Interaction with Hybrid Quantum Plasmonic Systems**

This renders the implementation of quantum information processing a question of light-matter interaction and requires purposeful manipulation of individual atoms and photons, whose coupling is specifically engineered in a controlled environment. While different systems, such as laser-cooled ion traps<sup>[20,21]</sup>, have been proposed and demonstrated to provide the functionality needed, optical nanoantennas<sup>[22,23]</sup>, featuring localized surface plasmon polaritons, have the potential to contribute unique properties and elevate light-matter interaction towards the goal of quantum information processing.

Providing the characteristic localization<sup>[24,25]</sup> of electromagnetic field energy that has emerged as the trademark of plasmonic resonances, it is evident that metallic nanoantennas are predestinated to be involved in the interaction of single photons with single quantum systems. Furthermore, obviously advantageous with respect to the suitability as a light-matter interaction platform, optical nanoantennas can couple electromagnetic field energy to a variety of different individual quantum systems, such as atoms, molecules, quantum dots, or nitrogen-vacancy centers in diamond. Hence, any unique property any of these systems exhibit can be exploited utilizing plasmonic nanoantennas. Additionally, the field localization and other properties of the nanoantenna can be directly controlled through its geo-

metrical shaping<sup>[26,27]</sup> in the fabrication process. Finally, since various classical application scenarios<sup>[28–33]</sup> can benefit from the electromagnetic field energy localization and other properties of nanoantennas, there is already a long-standing research activity, bringing forth a wide range of antenna geometries, immediately available from experimental fabrication.

The quantized energy exchange involving single photons and single transitions in quantum systems can be modeled employing a cavity quantum electrodynamics formalism, with the cavity representing the plasmonic nanoantenna. Directly including a quantum system featuring radiative transitions forms a hybrid quantum-plasmonic system, the central subject of this thesis. Doing justice to the highly radiative nature of the localized plasmon polaritons, resulting in significant emission emanating from the nanoantenna, the hybrid quantum-plasmonic system needs to be modeled as an open quantum system coupled to far-field radiation.

The central drawback, in light of all these benefits, are the Ohmic losses inherently linked to the metallic media and optical frequencies involved in surface plasmon polaritons<sup>[34]</sup>. While the loss mechanism itself has found its own field of biological applications<sup>[35]</sup>, the Ohmic losses currently still remain energy dissipated or information lost for any information or communication applications proposed so far. Consequently, the losses form a hurdle that must enter the considerations and ultimately must be overcome by any proposed scheme of photonic functionality involving nanoantennas.

### **Aim and Structure of the Thesis**

To characterize the nanoantenna properly, aiming to produce representative calculations of the quantum dynamics with the interaction model, two fundamentally different approaches are established at the inception of the work documented in this thesis. On the one hand, Green's function based methods that allow for a coherent modeling of classical and quantum aspects with the Green's function, hence exploiting the classical character of plasmonic resonances<sup>[36]</sup>. But the expenses of this approach amount to abundant numerical calculations necessary to obtain the Green's function for nanoantennas of arbitrary geometrical shape. On the other hand, density functional theory allows for an entirely quantum physical modeling of the hybrid quantum-plasmonic system and its dynamics. This is achieved by decomposing the nanoantenna into individual atoms and calculating the electron density states of the composite structure. While state-of-the-art computation facilities manage to handle this numerical challenge, the extent of the numerical effort involved can be indicated by the myriad of individual atoms that is necessary to

---

represent a metal structure of the dimensions of at least a few nanometers.

The fact that both established approaches require tremendous numerical work and capabilities has contributed to the disparity between experimental and theoretical activity involving optical nanoantennas for quantum information purposes. The aim of the work documented in this thesis is the development of a semi-classical model to describe the light-matter interaction mediated by a plasmonic cavity. This model shall both exploit the classical character of plasmonic resonances and efficiently handle arbitrary geometrical shapes of the nanoantenna. To facilitate the merger of classical and quantum physical modeling, the classical foundations of the surface plasmon resonance are outlined as well as the approximations and assumptions of both quantum optical and cavity quantum electrodynamical elements involved. The second chapter contains this theoretical framework of the classical and quantum physical part of the model.

These requirements lead to a numerical light scattering method that can describe the weak light-matter coupling regime. This final model calculates quantum dynamics while determining the parameters involving the plasmonic cavity through classical simulations. Chapter three details the model as well as the classical simulations.

The qualitatively predictive means of the classical modeling are demonstrated by reproducing experimentally measured molecular fluorescence manipulations due to nanoantennas, ranging from quenching to emission enhancement. Finally, the proposed implementation of three different quantum optical applications is documented. These utilize not just the full semi-classical model but indicate the potential of the weak coupling regime for quantum optical and ultimately quantum information purposes. Chapter four details the dynamics and phenomena involved in a total of four different exemplary applications, each published in a peer-reviewed journal.

Chapter five as the final chapter contains a brief summary of the main elements and results of the work documented in this thesis, as well as comments regarding possible further developments.

## 2 Theoretical Framework

At first it is crucial to outline the theoretical framework, within which classical numerical calculations are used to generate parameters for the cavity quantum electrodynamic light-matter interaction model. This is the core of the semi-classical model that is developed in the context of this work and that is employed to study quantum optical phenomena utilizing optical nanoantennas featuring localized plasmon polaritons.

Firstly, the classical foundations of the numerical simulations are summarized. Then the plasmon resonance is introduced and its suitability for light-matter interaction is illuminated, which leads to the study of localized surface plasmon polaritons. These collective excitations yield a light-matter interaction scenario of light being resonantly scattered by sub-wavelength metal structures.

By quantizing the electromagnetic field, photons as quantized field energy naturally emerge. Quantized radiation fields in form of number states are introduced and specific properties, such as entanglement in number states, is described.

Finally, utilizing the means of cavity quantum electrodynamics, the actual quantized light-matter interaction is described on the basis of the Jaynes-Cummings model. This initially closed interaction system is opened up to radiation fields and various loss channels through incorporation of a master equation formulation. Employing such open interaction systems allows for the description of light-matter interaction influencing the radiation emitted into the far field.

With the theoretical framework delineated, the ensuing chapter is devoted to the specific technical calculation of the cavity parameters by classical means. This allows for the quantum physical dynamics to represent actual quantized light-matter interaction systems involving optical nanoantennas.

Ultimately, the subsequent chapter outlines the engineering of the emission for four applications, in form of radiation rate, radiation mode, non-classical radiation statistics, and non-classical radiation properties, of light-matter interaction systems, each containing a specially designed optical nanoantenna.

---

## 2.1 Elements of Solid-State Optics

### Optical Field Equations

A theoretical description of the influencing of light-matter interaction through controlling the photonic environment<sup>[37]</sup>, naturally originates from Maxwell's equations. The most general form of the differential electromagnetic field equations is<sup>[38]</sup>:

$$\nabla \cdot \tilde{\mathbf{D}}(\mathbf{r}, t) = \tilde{\rho}_{\text{ext}}(\mathbf{r}, t) \quad , \quad \nabla \cdot \tilde{\mathbf{B}}(\mathbf{r}, t) = 0 \quad , \quad (2.1)$$

$$\nabla \times \tilde{\mathbf{E}}(\mathbf{r}, t) = -\partial_t \tilde{\mathbf{B}}(\mathbf{r}, t) \quad , \quad \nabla \times \tilde{\mathbf{H}}(\mathbf{r}, t) = \tilde{\mathbf{j}}_{\text{mac}}(\mathbf{r}, t) + \partial_t \tilde{\mathbf{D}}(\mathbf{r}, t) \quad . \quad (2.2)$$

Here, the electric field  $\tilde{\mathbf{E}}$ , electric flux density  $\tilde{\mathbf{D}}$ , magnetic field  $\tilde{\mathbf{H}}$ , and magnetic flux density  $\tilde{\mathbf{B}}$  appear as three-dimensional vector fields, which are coupled to one another. Furthermore, Maxwell's equations identify external charge densities  $\tilde{\rho}_{\text{ext}}(\mathbf{r}, t)$  as the source of the fields in Eqns. (2.1), while the electromagnetic fields themselves circulate variations in time of the respective other field in Eqns. (2.2). Additionally, the magnetic field circulates macroscopic electric current densities  $\tilde{\mathbf{j}}_{\text{mac}}(\mathbf{r}, t)$  as well. In this general form, the dynamics in media as a consequence on an incident electromagnetic field are included with further material specific equations being given:

$$\tilde{\mathbf{D}}(\mathbf{r}, t) = \varepsilon_0 \tilde{\mathbf{E}}(\mathbf{r}, t) + \tilde{\mathbf{P}}(\mathbf{r}, t) \quad \& \quad \tilde{\mathbf{H}}(\mathbf{r}, t) = \frac{1}{\mu_0} \tilde{\mathbf{B}}(\mathbf{r}, t) - \tilde{\mathbf{M}}(\mathbf{r}, t) \quad , \quad (2.3)$$

with the electric polarization  $\tilde{\mathbf{P}}(\mathbf{r}, t)$  and magnetization  $\tilde{\mathbf{M}}(\mathbf{r}, t)$  as auxiliary response fields specific to a medium<sup>[39]</sup>.

As the introduction of auxiliary response fields already indicates, the general relation between them and the electromagnetic fields is very intricate. Here, effects such as linearity, homogeneity, isotropy, and locality have to be taken into consideration. Dispersion is probably the most prominent among those effects and while it leads to memory effects in the time domain, the Fourier transform to frequency space according to  $\mathcal{F}(\omega) = \frac{1}{2\pi} \int_{-\infty}^{\infty} dt \tilde{\mathcal{F}}(t) e^{i\omega t}$  introduces a frequency dependent susceptibility  $\chi(\omega)$ . At this point, it is important to point out, that a generally complex susceptibility can be implemented for both electric and magnetic responses. However, at optical frequencies it is reasonable to only consider electrical susceptibility, as magnetic susceptibility in natural materials vanishes above microwave frequencies<sup>[40]</sup>:

$$\mathbf{D}(\mathbf{r}, \omega) = \varepsilon_0 \mathbf{E}(\mathbf{r}, \omega) + \varepsilon_0 \chi_{\text{ele}}(\omega) \mathbf{E}(\mathbf{r}, \omega) \quad \& \quad \mathbf{H}(\mathbf{r}, \omega) = \frac{1}{\mu_0} \mathbf{B}(\mathbf{r}, \omega) \quad . \quad (2.4)$$

Here, this complex-valued electric susceptibility inherently assumes a linear medium, as the the vector fields of  $\mathbf{E}(\mathbf{r}, \omega)$  and  $\mathbf{D}(\mathbf{r}, \omega)$  are linearly connected, a homogeneous medium, as no spatial dependence is included in  $\chi_{\text{ele}}(\omega)$ , and an isotropic medium, as there is rather a scalar than a tensorial connection between the vector fields of  $\mathbf{E}(\mathbf{r}, \omega)$  and  $\mathbf{D}(\mathbf{r}, \omega)$ .

### Free Electron Gas Model

In order to describe surface plasmon polaritons, the material response considered in the following can be limited to metallic media. While phonons and electronic transitions have to be incorporated to describe dielectric materials at optical frequencies, metallic media responses are dominated by free electrons. Continuing the purely classical description so far, the classical Drude model<sup>[41]</sup> of a free electron gas on top of an ionic background employs the classical analogy of a generally damped movement due to an external force<sup>[42]</sup>:

$$\partial_t^2 \tilde{\mathbf{s}}(\mathbf{r}, t) + \kappa \partial_t \tilde{\mathbf{s}}(\mathbf{r}, t) = -\frac{e}{m} \tilde{\mathbf{E}}(\mathbf{r}, t) \quad , \quad (2.5)$$

with the electron's displacement  $\tilde{\mathbf{s}}(\mathbf{r}, t)$ , the electron's charge  $e$ , the electron's mass  $m$ , and a damping constant due to collisions  $\kappa$ . Next, it is reasonable to introduce an electric current density of the form  $\tilde{\mathbf{j}}(\mathbf{r}, t) = -Ne\partial_t \tilde{\mathbf{s}}(\mathbf{r}, t)$  due to the moving electrons. Applying the Fourier transform to frequency space and using the transition of time derivatives  $\partial_t$  to factors  $-i\omega$  yields

$$-i\omega \mathbf{j}(\mathbf{r}, \omega) + \kappa \mathbf{j}(\mathbf{r}, \omega) = \frac{e^2 N}{m} \mathbf{E}(\mathbf{r}, \omega) = \varepsilon_0 \omega_{\text{pla}}^2 \mathbf{E}(\mathbf{r}, \omega) \quad ,$$

with the plasma frequency  $\omega_{\text{pla}}^2 = \frac{e^2 N}{\varepsilon_0 m}$ . The solution establishes a complex conductivity  $\sigma(\omega)$  connecting the electric current density  $\mathbf{j}(\mathbf{r}, \omega)$  to the electric field  $\mathbf{E}(\mathbf{r}, \omega)$

$$\mathbf{j}(\mathbf{r}, \omega) = \frac{\varepsilon_0 \omega_{\text{pla}}^2}{\kappa - i\omega} \mathbf{E}(\mathbf{r}, \omega) = \sigma(\omega) \mathbf{E}(\mathbf{r}, \omega) \quad . \quad (2.6)$$

Please note that the effects of an external field incident on a dielectric media, which are omitted here due to brevity of the description, can be purely classically modeled as well. The analogy of a driven, damped harmonic oscillator for the electronic displacement away from the remaining ions<sup>[43]</sup> leads to an induced polarization  $\mathbf{P}(\mathbf{r}, \omega)$  rather than an induced current density  $\mathbf{j}(\mathbf{r}, \omega)$ . Hence, the same response model and the following classical formulation can be straight forward expanded to include dielectric media as well.

With the metallic material response at hand, the field equations (2.1) and (2.2)

request to be revisited. While these equations allow for an intuitive discussion of the relations and dynamics of observable physical quantities, the coupling of the electromagnetic field dynamics is an immediately evident obstacle that needs to be overcome in an attempt to solve Maxwell's equations. With the Fourier transform available as a versatile tool helping to solve differential equations by transforming derivatives to algebraic factors and the immensely important material response convenient as a complex-valued function of the frequency, the transformation to frequency space is inevitable. Now, Maxwell's equations take a form especially useful in optical applications:

$$\varepsilon_0 \nabla \cdot \mathbf{E}(\mathbf{r}, \omega) = \rho_{\text{ext}}(\mathbf{r}, \omega) - \nabla \cdot \mathbf{P}(\mathbf{r}, \omega) \quad , \quad (2.7)$$

$$\nabla \cdot \mathbf{H}(\mathbf{r}, \omega) = 0 \quad , \quad (2.8)$$

$$\nabla \times \mathbf{E}(\mathbf{r}, \omega) = i\omega\mu_0\mathbf{H}(\mathbf{r}, \omega) \quad , \quad (2.9)$$

$$\nabla \times \mathbf{H}(\mathbf{r}, \omega) = \mathbf{j}_{\text{mac}}(\mathbf{r}, \omega) - i\omega\mathbf{P}(\mathbf{r}, \omega) - i\omega\varepsilon_0\mathbf{E}(\mathbf{r}, \omega) \quad . \quad (2.10)$$

Here, the negligible magnetization  $\mathbf{M}(\mathbf{r}, \omega)$  at optical frequencies has already been discarded. Applying the curl to the curl equation of the electric field in Eqn. (2.9) and then replacing the arising curl of the magnetic field with the corresponding Maxwell's equation (2.10) yields

$$\nabla \times \nabla \times \mathbf{E}(\mathbf{r}, \omega) = i\omega\mu_0\mathbf{j}_{\text{mac}}(\mathbf{r}, \omega) + \omega^2\mu_0\mathbf{P}(\mathbf{r}, \omega) + \frac{\omega^2}{c^2}\mathbf{E}(\mathbf{r}, \omega) \quad ,$$

with the phase velocity in vacuum  $\varepsilon_0\mu_0 = c^{-2}$ . Now, both the induced polarization  $\mathbf{P}(\mathbf{r}, \omega)$  and the current density  $\mathbf{j}_{\text{mac}}(\mathbf{r}, \omega)$  can be replaced with expressions for the electric field  $\mathbf{E}(\mathbf{r}, \omega)$  according to Eqn. (2.3) and Eqn. (2.6) respectively. This leads to the general complex-valued dielectric function  $\varepsilon(\omega)$ , or relative permittivity, the canonical way of describing the linear material response in solid-state optics. Further specifying the relative permittivity to metallic media with a dominating induced current density  $\mathbf{j}(\mathbf{r}, \omega)$ , results in

$$\varepsilon(\omega) = 1 + \frac{i\sigma}{\varepsilon_0\omega} = 1 - \frac{\omega_{\text{pla}}^2}{\omega^2 + \kappa^2} + i\frac{\kappa\omega_{\text{pla}}}{\omega(\kappa^2 + \omega^2)} = \varepsilon'(\omega) + i\varepsilon''(\omega) \quad . \quad (2.11)$$

With this approach, on the one hand, it is possible to model the optical properties through plasma frequency  $\omega_{\text{pla}}$  and damping constant  $\kappa$ . On the other hand, this expression gives the permittivity of metals, based on experimental measurements<sup>[44]</sup>. Including the metallic relative permittivity rooted in experimental measurements, as it is carried out throughout this work, allows for the straight forward classic modeling of an extended catalog of metals<sup>[45]</sup>.

## Numerical Solution

With the electromagnetic field equations in a form that can be combined with the material response of metals, and extended to cover dielectrics as well, the next step is to face the actual solution of these equations. While analytical solutions provide absolute control and fundamental understanding of a mathematical problem, their rareness renders the symbolic manipulations of mathematical analysis a solution strategy very unlikely to succeed. Consequently, numerical approximations of discrete mathematics have enjoyed ever-rising interest in the advent of scientific calculations using computer software. To initially formulate the equation that shall be solved numerically, the curl is again applied to Eqn. (2.9) and Eqn. (2.10) is subsequently inserted, but now a potential material response is implemented through the relative permittivity and an additional external current source is included:

$$\nabla \times \nabla \times \mathbf{E}(\mathbf{r}, \omega) - \frac{\omega^2}{c^2} \varepsilon(\omega) \mathbf{E}(\mathbf{r}, \omega) = i\mu_0 \omega \mathbf{j}(\mathbf{r}, \omega) \quad . \quad (2.12)$$

The satisfaction of this vector wave equation throughout a designated domain  $\Omega$  with a given set of boundary conditions on  $\partial\Omega$  constitutes a boundary-value problem<sup>[46]</sup> as shown in Fig. 2.1. It is the central element of the numerical solution of the field dynamics. In this general form it allows for arbitrarily shaped metallic structures to be included and hence scenarios involving spheres, spheroids, rods, bars, discs, bow-ties, or other geometries can be described. Such a general approach calls for an extremely versatile numerical solver among the multitude of tools and techniques available to handle differential equations. The finite difference method (FDM) and the finite element method (FEM) are two very common examples of such numerical techniques.

Both FDM and FEM discretize the domain of the differential equation and give results on nodes. The FDM approximates with a discrete differential operator based on the difference quotient, which usually relies on environmental points in a structured grid to calculate a derivative. Consequently, its strong suit are rather simple geometries. FEM however, at the core discretizes space itself, but does not

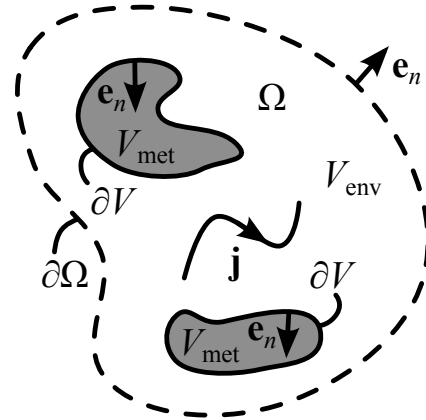


Figure 2.1: Boundary-value problem for selected metallic domains ( $V_{\text{met}}$ ) surrounded by a linear, dispersion-less, isotropic, local, homogeneous media ( $V_{\text{env}}$ ).

rely on a coherent or regular structure of the spatial discretization. Hence the FEM is most powerful in three-dimensional scenarios involving different materials and intricate geometries.

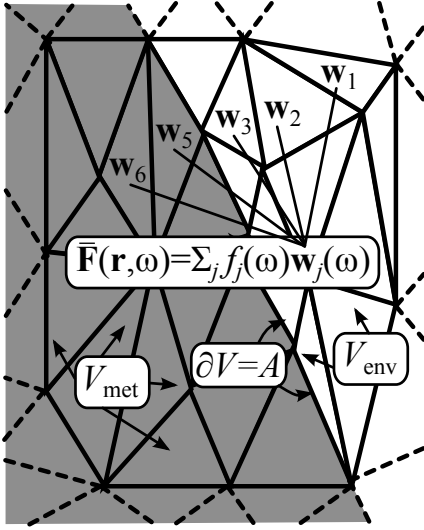


Figure 2.2: Combining coefficients  $f_m$  and base functions  $w_m$  to the approximative solution field  $\bar{\mathbf{F}}(\mathbf{r}, \omega)$ .

As all the classical simulations in this thesis have been done with FEM based methods, in the following their main ideas will be shortly described. Starting with a differential equation  $\mathcal{P}\mathbf{F} - Q = 0$ , with a general differential operator  $\mathcal{P}$ , acting on an unknown field  $\mathbf{F}$ , a forcing function  $Q$ , and boundary conditions  $\mathcal{B}(\mathbf{F})|_{\partial\Omega} = 0$ <sup>[47]</sup>, different solution strategies can be implemented within the FEM. Composing an approximative solution field  $\bar{\mathbf{F}}$ , as a linear combination of unknown coefficients  $f_m$  and base functions  $w_m$ , comes at a price of a residual  $\mathcal{R} = \mathcal{P}\bar{\mathbf{F}} - Q$ . The method of weighted residuals aims to minimize, ideally expunge, the residual in the considered domain  $\Omega$ , hence providing the best approxima-

tive, ideally exact, solution. With the inner product  $\langle w_j, \mathcal{R} \rangle$  in the function space of the base functions, the residual  $\mathcal{R}$  vanishes for an exact solution for vanishing  $\langle w_j, \mathcal{R} \rangle$  with any test function  $w_j$ . In case of an approximative solution, hence remaining residual, the inner product only vanishes for selected linear independent weighting functions  $u_j$ . With the inner product in form of an integral, the weighted residual equation takes the form<sup>[47]</sup>

$$\left( \int_{\Omega} d\Omega w_j \mathcal{P} w_m \right) \{f_m\} = \int_{\Omega} d\Omega w_j Q$$

in the so called Galerkin procedure to determine the unknown coefficients  $f_m$ . Here, the residual is locally weighted through the weighting functions and integrated over the entire domain. Unique to the Galerkin procedure, the base functions  $w_j$  are used as the weighting functions  $u_j$ , with  $\bar{\mathbf{F}} = \sum_m f_m w_m$ . The Galerkin procedure is for example employed by the commercial software package COMSOL Multiphysics<sup>[48]</sup>, which in turn is used to calculate all electromagnetic fields for the plasmonic applications presented in this work. Please note, that unlike the FDM, the FEM, or more specific the assembly of local solutions, does not require a structured or regular spatial grid, as indicated in Fig. 2.2. Hence, the spatial

discretization can rather take physical considerations into account, benefiting both precision and efficiency. Following this general algorithm of FEM, the vector wave equation (2.12) can be reformulated to<sup>[47]</sup>

$$0 = \int_{\Omega} d\Omega \left[ (\nabla \times \mathbf{E}(\mathbf{r}, \omega)) \cdot (\nabla \times \mathbf{V}(\mathbf{r}, \omega)) - \frac{\omega^2}{c^2} \varepsilon(\omega) \mathbf{E}(\mathbf{r}, \omega) \cdot \mathbf{V}(\mathbf{r}, \omega) \right] + \int_{\partial V + \partial \Omega} dA [\mathbf{V}(\mathbf{r}, \omega) \cdot (\mathbf{e}_n \times \nabla \times \mathbf{E}(\mathbf{r}, \omega))] + i\mu_0 \omega \int_{\Omega} d\Omega \mathbf{V}(\mathbf{r}, \omega) \cdot \mathbf{j}(\mathbf{r}, \omega) \quad , \quad (2.13)$$

with the approximative vector field  $\mathbf{V}(\mathbf{r}, \omega)$  locally assembled from the sub domains:  $\mathbf{V}(\mathbf{r}, \omega) = \sum_j v_j \mathbf{w}_j$ . Here the vector identity  $\mathbf{E} \cdot \nabla \times \mathbf{V} = \mathbf{V} \cdot \nabla \times \mathbf{E} - \nabla \cdot (\mathbf{E} \times \mathbf{V})$ , and the divergence theorem have been used.

By employing these numerical means of solid states optics, the electromagnetic dynamics in arbitrary geometrical setups involving metallic media of finite size can be simulated. Consequently, any field distribution or dynamic can be incorporated that results from light interacting with bulk metallic material.

### Concluding Remarks

To summarize, by employing classical solid-state optics and incorporating metallic material characteristics through linear response theory, the electromagnetic field can be described in presence of metallic structures at optical frequencies. Implementing a numerical solution algorithm of differential equations based on the FEM, enables the calculation of the electromagnetic field with arbitrary geometries involved. This allows for engineering of the photonic environment via the presence of metallic media, where the geometry of the metal structure can be completely devoted to the desired environmental effect.

## 2.2 Elements of Surface Physics

### Plasmon Resonance

Given the capability to determine the electromagnetic field distribution in metallic structures, revisiting the metallic material characteristics is worth the effort. The classical assumption of a free electron gas led to the relative permittivity as given in Eqn. (2.11). Plasma optics<sup>[49]</sup> further explores the consequences of this premise. Neglecting possible collisions in the free electron gas for the moment and consequently setting  $\kappa = 0$ , the simplified relative permittivity

$$\varepsilon(\omega) = 1 - \frac{\omega_{\text{pla}}^2}{\omega^2} \quad (2.14)$$

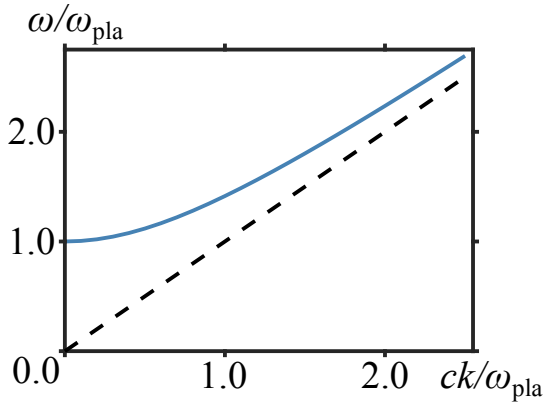


Figure 2.3: Dispersion relation that follows for plane waves in metallic media (solid blue line) in units of  $\omega_{\text{pla}}$  (black dashes = light line).

follows. This suggests the conduction electrons to move freely and without damping over a rigid positive ionic crystal. A contribution of the ionic background to the relative permittivity can easily be included by adding a constant background permittivity. But this does not essentially change what shall be discussed in the following and hence is omitted for the sake of simplicity. Furthermore, considering a scenario without external charge densities  $\rho_{\text{ext}}$  and macroscopic current densities  $\mathbf{j}_{\text{mac}}$ , the general wave equation (2.12) reduces to the well-known Helmholtz equation  $\Delta \mathbf{E}(\mathbf{r}, \omega) - \frac{\omega^2}{c^2} \varepsilon(\omega) \mathbf{E}(\mathbf{r}, \omega) = 0$ . Subsequently, the canonical harmonic plane wave ansatz with  $\mathbf{E}(\mathbf{r}, \omega) = \mathbf{E}_0 e^{i(\mathbf{k} \cdot \mathbf{r} - \omega t)}$  and the wave vector  $\mathbf{k}$  leads to the dispersion relation for electromagnetic waves

$$\varepsilon(\omega) \varepsilon_0 \mu_0 \omega^2 = |\mathbf{k}|^2 \quad (2.15)$$

Without sources of the electric field in form of external charge densities  $\rho_{\text{ext}}$ , the corresponding Maxwell equation takes the form  $\varepsilon_0 \varepsilon(\omega) \nabla \cdot \mathbf{E}(\mathbf{r}, \omega) = 0$ . Hence, transverse electromagnetic waves ( $\mathbf{k} \cdot \mathbf{E}(\mathbf{r}, \omega) = 0$ ) obey the dispersion relation for positive, arbitrary frequencies  $\omega$  as described in Eqn. (2.15) and depicted in Fig. 2.3. The specific form of the simplified relative permittivity in Eqn. (2.14) indicates two different dispersion regimes separated by the plasma frequency  $\omega_{\text{pla}}$ : For frequencies above  $\omega_{\text{pla}}$ , the simplified relative permittivity is positive and  $|\mathbf{k}|$  takes

a real value, following Eqn. (2.15). Hence, for this frequency range, transverse electromagnetic waves propagate in the medium with a transparent electron gas. However, for frequencies below the plasma frequency, Eqn. (2.14) gives a negative  $\varepsilon(\omega)$  and a purely imaginary wave vector follows from the dispersion relation. This results in evanescent waves that are exponentially damped in the medium on a characteristic length scale of  $\frac{1}{|\mathbf{k}|}$ . Please note, a complex-valued relative permittivity, as follows from the initial free electron gas model in Eqn. (2.11), entails a generally damped wave propagation in the medium.

While this treatment covers both attenuated and propagating transverse electromagnetic waves in metallic media, the transition between these two regimes deserves special attention. Following the treatment above, these transitions coincide with the roots of the relative permittivity:  $\varepsilon(\omega_{\text{lon}}) = 0$ , for the frequency  $\omega_{\text{lon}}$ , in the simplified case  $\omega_{\text{lon}} = \omega_{\text{pla}}$ . Here, both the wave vector  $\mathbf{k}$  and the field  $\mathbf{D}(\mathbf{r}, \omega)$  in the medium vanish through the dispersion relation in Eqn. (2.15) and the optical constitutive relation in Eqn. (2.4) respectively. With the continuing condition of sourcelessness of the electric field in the scenario under consideration being satisfied in this manner, reviewing the vector wave equation (2.12) at the frequency  $\omega_{\text{lon}}$  without additional currents yields

$$\nabla \times \nabla \times \mathbf{E}(\mathbf{r}, \omega_{\text{lon}}) = 0 \quad .$$

Here, implementing the harmonic plane wave ansatz again, this requirement transforms to  $\mathbf{k} \times \mathbf{k} \times \mathbf{E}(\mathbf{r}, \omega_{\text{lon}}) = 0$ . This results in longitudinally polarized waves with  $\mathbf{k} \parallel \mathbf{E}(\mathbf{r}, \omega_{\text{lon}})$  as solutions. Returning to the free electron gas model can further illuminate the response of metallic media, as they have been completely classically modeled so far. In the simplified case, without electronic collisions in the gas, i.e. with  $\kappa = 0$ , the displacement of the conduction electrons  $\tilde{\mathbf{s}}(\mathbf{r}, t)$  due to an incident electric field obeys

$$\partial_t^2 \tilde{\mathbf{s}}(\mathbf{r}, t) = -\frac{e}{m} \tilde{\mathbf{E}}(\mathbf{r}, t) \quad .$$

Apparently, the individual electrons behave as simple harmonic oscillators regarding their displacement due to the prevalent electric field. As a result of the longitudinal electromagnetic wave within the medium, the electron gas as a whole experiences a harmonic oscillation of the electron density along the wave vector  $\mathbf{k}$ .

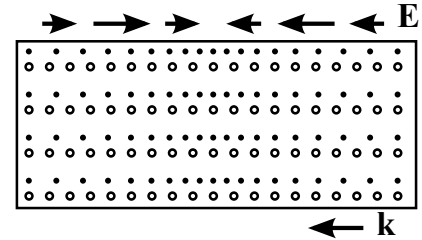


Figure 2.4: A longitudinal plane wave affects metallic media, with the field amplitude  $\mathbf{E}$  indicated at the top and the wave vector  $\mathbf{k}$  at the bottom.

---

Figure 2.4 symbolically depicts this behavior. With a rigid crystalline structure of ions, represented by the black circles in Fig. 2.4, each electron, represented by the black dots, is displaced according to the local field, whose amplitude is indicated by the arrows on top of the figure. This displacement, just like the local field, is homogeneous perpendicular to the wave vector orientation, indicated by the arrow at the bottom of the figure.

### Metallic Surface Effect

Since the metallic material response in form of an electron gas is essentially modeled as a plasma, a quantum of such a collective longitudinal excitation is called a plasmon. Accounting for the fact, that the metallic medium has so far been assumed to be an infinitely extended region, these collective excitations are called volume plasmons<sup>[50]</sup>, as they propagate through the volume of the crystal. They were first observed in form of discrete energy losses of electrons transmitted by thin metal films<sup>[51]</sup>. Other than in electron loss spectroscopy, volume plasmons can also be excited through the inelastic scattering of X-ray photons<sup>[52]</sup>. The probability to excite volume plasmons with photons drops proportional to the wave vector squared, hence, photons of visible light, with an orders of magnitude smaller wave vector, are far less likely to succeed. Consequently, volume plasmons with the energy of  $\hbar\omega_{\text{pla}}$  can not be considered a suitable candidate to be involved in controlling light-matter interaction.

However, attempts to describe such plasma losses by fast electrons in thin films in more detail<sup>[53]</sup> revealed energy losses at sub plasma energies, just as they have been measured in experiment. Consequently, the surface charges at the interface between the metal domain and the surroundings require further treatment. As the focus is again on the most characteristic features, it is reasonable to continue with the model of a free or nearly free electron gas and a rigid ionic crystal to determine the influence of an interface between two media, or more specifically the surface of a metal domain abutting an insulator. But now a microscopic ansatz shall be initially employed to discuss the situation. With moving electrons, that are attracted to the fixed nodes of an ionic crystal, and repel each other, the following Hamiltonian describes the electronic structure<sup>[54]</sup>:

$$\mathcal{H} = \sum_{j=1}^N \frac{p_j^2}{2m} - \sum_{\mathbf{R}} \sum_{j=1}^N \frac{Ze^2}{|\mathbf{r}_j - \mathbf{R}|} + \frac{1}{2} \sum_{u,v=1}^N \frac{e^2}{|\mathbf{r}_u - \mathbf{r}_v|} \quad . \quad (2.16)$$

Here, the individual electronic momenta  $p_j$  are used in the first term to describe the kinetic energy of the individual electrons. With the fixed positions of the ions in the

crystal contained in the set of vectors  $\mathbf{R}$  and the proton number  $Z$  of the specific metallic material, the second term represents the attraction between the fixed ions and each electron. Lastly, the inter-electron repulsion between each electron pair with positions  $\mathbf{r}_u$  and  $\mathbf{r}_v$  respectively is covered by the third term. Obviously, such a microscopic model results in a many-body problem. This can be solved directly by taking single electrons and a one-electron Schrödinger equation and including the influence of both the remaining electrons as well as the ions in a mean-field term in the potential<sup>[55]</sup>. But as the character of the volume plasmon resonance in form of a collective electron density oscillation already indicates, the treatment of the electron, or more general charge, density seems rather preferable in comparison to that of individual electrons. Consequently, following the density functional theory<sup>[56]</sup>, the many-body problem can be reformulated as a functional of the ground state charge density  $\zeta(\mathbf{r})$ . The density, that in turn minimizes the aforementioned functional, can be retrieved by solving coupled, ordinary differential equations<sup>[54]</sup>:

$$-\frac{1}{2}\Delta\psi_j(\mathbf{r}) + V_{\text{eff}}(\mathbf{r})\psi_j(\mathbf{r}) = \mathcal{E}_i\psi_j(\mathbf{r}) \quad . \quad (2.17)$$

These equations, very similar to the Schrödinger equation, describe single-electron state excitation eigenfunctions  $\psi_j$  and energies  $\mathcal{E}_i$ <sup>[57]</sup>. While the electronic states satisfy the Bloch condition  $\psi_j(\mathbf{r} + \mathbf{T}) = e^{i\mathbf{k}\cdot\mathbf{T}}\psi_j(\mathbf{r})$  with the primitive translation vector  $\mathbf{T}$  in the ionic crystal lattice, the electron density is calculated through  $\zeta(\mathbf{r}) = \sum_j |\psi_j(\mathbf{r})|^2$ . Both the electron-electron interaction and the electron-ion interaction appear in the effective potential:

$$V_{\text{eff}}(\mathbf{r}) = -\sum_{\mathbf{R}} \frac{Ze^2}{|\mathbf{r} - \mathbf{R}|} + \int d\mathbf{r}' \frac{\zeta(\mathbf{r}')}{|\mathbf{r} - \mathbf{r}'|} + V_{\text{exc}}(\mathbf{r}) \quad , \quad (2.18)$$

with a separate exchange-correlation potential  $V_{\text{exc}}(\mathbf{r})$ , whose implementation determines the quality of such a formulation. Approximating the exchange-correlation potential with the available one of a homogeneous electron gas<sup>[58]</sup> in the local density approximation is a very powerful, yet reliable, simplification.

The so called jellium model replaces a discrete ionic lattice with a uniformly charged background. It correctly predicts the spill-out of electrons into the outside domain<sup>[59]</sup> as well as electronic oscillations due to the screening of the charged background. But continuing with a rather simplistic modeling, as only the most fundamental features shall be described, a one-dimensional band model is employed to investigate the surface influence. Now, Eqn. (2.17) takes the form:

$$\left[-\partial_z^2 + V_{\text{mod}}(z)\right]\psi(z) = \mathcal{E}\psi(z) \quad . \quad (2.19)$$

The assumed semi-infinite ionic crystal lattice on the one side and semi-infinite vacuum on the other side are included via the model potential<sup>[54]</sup>:

$$V_{\text{mod}}(z) = \begin{cases} 2V_{\text{gap}} \cos(Tz) - V_0 & , \text{ for } z \leq \frac{\Xi}{2} \\ V_0 & , \text{ for } z \geq \frac{\Xi}{2} \end{cases} \quad (2.20)$$

Here, the one-dimensional crystal lattice consists of ions placed at  $z_{\text{ion}} = -m\Xi$  with  $m \in \mathbb{N}_0$  and the distance between the ions  $\Xi$ .  $V_{\text{gap}}$  is half of the energy gap at the Brillouin zone boundary and  $T = 2\pi\Xi^{-1}$  is the wavenumber of the shortest reciprocal lattice vector. While the screened ions are modeled with a periodic potential, the surface itself is included in form of a simple potential wall  $V_0$ . Inserting a plane wave ansatz  $\psi(z) = C_1 \exp\{ikz\} + C_2 \exp\{-i(k-T)z\}$  in Eqn. (2.19) yields states  $\psi(z) = \exp\{i\delta z\} \cos\left(\frac{T}{2}z + \phi\right)$ . Here, the wavenumber has been decomposed into the Brillouin zone boundary and its deviation from it:  $k = \frac{T}{2} + \delta$ , with an additional phase  $\phi$ . The corresponding energies as a function of the deviation  $\delta$  from the Brillouin zone boundary are

$$\mathcal{E}(\delta) = \frac{T^2}{4} + \delta^2 \pm \sqrt{T^2\delta^2 + V_{\text{gap}}^2} - V_0 \quad .$$

Imaginary  $\delta$  lead to valid solutions if  $\delta < \frac{V_{\text{gap}}}{T}$ . These solutions that diverge in the bulk can be matched with the exponential decay in vacuum, yielding a surface state

$$\psi_{\text{sur}}(z) = \begin{cases} e^{\delta z} \cos\left(\frac{T}{2}z + \phi\right) & , \text{ for } z \leq \frac{\Xi}{2} \\ e^{-qz} & , \text{ for } z > \frac{\Xi}{2} \end{cases} \quad (2.21)$$

This matching of the solutions in both half-spaces can be achieved through variation of the phase  $\phi$ <sup>[60]</sup>. The wavenumber outside the solid state surface obeys  $q = \sqrt{V_0 - \mathcal{E}}$ .

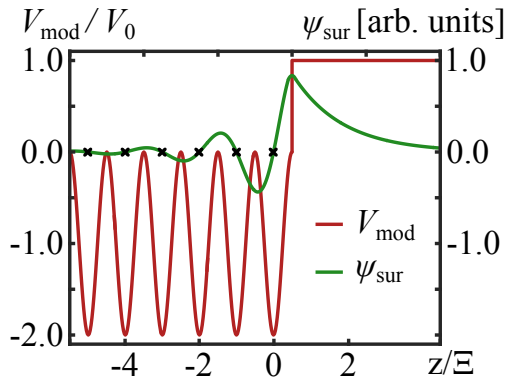


Figure 2.5: The model potential (red) yields a surface state (green) for a 1D interface between a lattice and vacuum.

Briefly recapitulating, while the behavior of a nearly free electron gas over an ionic crystal is a many body problem, the reformulation in terms of a charge density and the approximation of local homogeneity allow for a reduction to a one dimensional problem. Already the one dimensional combination of a periodic potential of the crystal with vacuum leads to a surface state<sup>[61]</sup> as it is shown in Fig 2.5. Here, the black crosses indi-

cate the positions of the ions, and both the resulting model potential (red) with a semi-infinite periodicity and the resulting surface state (green), matched at the boundary, are shown. Consequently, remaining within the free electron gas model, surface states must be taken into consideration and in the following light incident on a metallic surface shall be further examined.

### Surface Plasmon Resonance

Assuming the most fundamental scenario of an interface between a metallic material and vacuum, an infinitely extended two dimensional plane is considered. With the surface normal of the plane parallel to the  $z$  axis, just as it has been chosen before, and invariance assumed in the  $y$  direction, the situation, relevant to a surface state of the charge density, can be chosen to be located in the  $xz$ -plane. This very configuration is shown in Fig. 2.6.

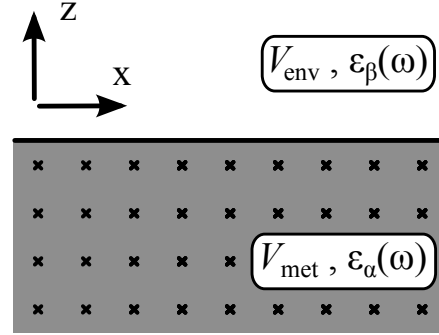


Figure 2.6: Scenario under consideration: The metal-insulator interface is normal to the  $z$  axis.

With the aim to characterize the field dynamics, the description of the discrete ionic crystal, indicated by black crosses in Fig. 2.6, returns again to a homogeneous metallic medium, where the behavior of the free electron gas is modeled by a relative permittivity  $\varepsilon(\omega)$ . Consequently, the optical field equations (2.7) - (2.10) in combination with the material permittivity are applied. In case of the specific scenario depicted in Fig. 2.6, the homogeneity in  $y$  direction results in the vanishing of the corresponding derivatives, while derivatives in  $x$  give  $ik$  for surface propagation with the plane wave ansatz<sup>[62]</sup>. Utilizing this, the curl equations (2.9) and (2.10) for the individual components of the vector field obey:

$$\begin{aligned}
 \partial_z H_x - ikH_z &= -i\omega\varepsilon_0\varepsilon(\omega) E_y & , & & \partial_z E_x - ikE_z &= i\omega\mu_0 H_y & , \\
 \partial_z E_y &= -i\omega\mu_0 H_x & , & & \partial_z H_y &= i\omega\varepsilon_0\varepsilon(\omega) E_x & , \\
 ikE_y &= i\omega\mu_0 H_z & , & & ikH_y &= -i\omega\varepsilon_0\varepsilon(\omega) E_z & .
 \end{aligned}$$

As the grouping of the component equations in two columns indicates, there are electromagnetic plane waves with two different polarizations, that satisfy these conditions. Transverse electric waves with nonzero components  $E_y$ ,  $H_x$ , and  $H_z$  yield an electric wave equation from combining the equations in the left column:

$$\partial_z^2 E_y + \left[ \frac{\omega^2}{c^2} \varepsilon(\omega) - k^2 \right] E_y = 0 \quad .$$

---

In the metallic domain  $V_{\text{met}}$  for  $z < 0$  with the permittivity  $\varepsilon_\alpha(\omega)$  and the wavenumber  $\alpha = \frac{\omega}{c} \sqrt{\varepsilon_\alpha(\omega)}$  the solutions for the non-vanishing components are:

$$E_y(z) = E_\alpha e^\mu \quad , \quad H_x(z) = -iE_\alpha \sqrt{\frac{\varepsilon_0 \varepsilon_\alpha(\omega)}{\mu_0}} e^\mu \quad , \quad H_z(z) = E_\alpha \sqrt{\frac{\varepsilon_0}{\mu_0}} e^\mu \quad ,$$

with  $\mu = ikx + \alpha z$ . In the surrounding domain  $V_{\text{sur}}$  for  $z > 0$  with the permittivity  $\varepsilon_\beta(\omega)$  and the wavenumber  $\beta = \frac{\omega}{c} \sqrt{\varepsilon_\beta(\omega)}$  the solutions for the same non-vanishing components are:

$$E_y(z) = E_\beta e^\nu \quad , \quad H_x(z) = iE_\beta \sqrt{\frac{\varepsilon_0 \varepsilon_\beta(\omega)}{\mu_0}} e^\nu \quad , \quad H_z(z) = E_\beta \sqrt{\frac{\varepsilon_0}{\mu_0}} e^\nu \quad ,$$

with  $\nu = ikx - \beta z$ . Implementing the compulsory continuity of the field components  $E_y$  and  $H_x$  leads to the condition  $E_\beta(\alpha + \beta) = 0$ . A surface propagation additionally requires both  $\Re\{\alpha\} > 0$  and  $\Re\{\beta\} > 0$ . Consequently, the condition is only met for  $E_\beta = 0$  and  $E_\alpha = 0$ . Therefore, a transverse electric wave cannot propagate according to the desired surface confinement.

The combination of the right column of equations yields transverse magnetic waves with nonzero components  $E_x$ ,  $E_z$ , and  $H_y$  and a magnetic wave equation:

$$\partial_z^2 H_y + \left[ \frac{\omega^2}{c^2} \varepsilon(\omega) - k^2 \right] H_y = 0 \quad .$$

The permittivity  $\varepsilon_\alpha(\omega)$  and the wavenumber  $\alpha$  are again valid in the metal  $V_{\text{met}}$ , and the solutions of the wave equation are:

$$H_y(z) = H_\alpha e^\mu \quad , \quad E_x(z) = iH_\alpha \sqrt{\frac{\mu_0}{\varepsilon_0 \varepsilon_\alpha(\omega)}} e^\mu \quad , \quad E_z(z) = -H_\alpha \sqrt{\frac{\mu_0}{\varepsilon_0 \varepsilon_\alpha^2(\omega)}} e^\mu \quad (2,22)$$

with  $\mu = ikx + \alpha z$ . The permittivity  $\varepsilon_\beta(\omega)$  and the wavenumber  $\beta$  are valid in the surroundings  $V_{\text{sur}}$ , and here the wave equation is solved by:

$$H_y(z) = H_\beta e^\nu \quad , \quad E_x(z) = -iH_\beta \sqrt{\frac{\mu_0}{\varepsilon_0 \varepsilon_\beta(\omega)}} e^\nu \quad , \quad E_z(z) = -H_\beta \sqrt{\frac{\mu_0}{\varepsilon_0 \varepsilon_\beta^2(\omega)}} e^\nu \quad ,$$

with  $\nu = ikx - \beta z$ . From the continuity of  $H_y$  and  $\varepsilon(\omega) E_z$  follow both  $H_\alpha = H_\beta$  and  $\frac{\alpha}{\beta} = -\frac{\varepsilon_\alpha(\omega)}{\varepsilon_\beta(\omega)}$ . Hence, a different sign in the real parts of the relative permittivities of the involved media is required to realize surface propagation. This is given in the chosen scenario of a metal-vacuum boundary, or in general the combination of a metal with an insulating material. The wave equation for the magnetic field further yields  $\alpha^2 = k^2 - \frac{\omega^2}{c^2} \varepsilon_\alpha(\omega)$  and  $\beta^2 = k^2 - \frac{\omega^2}{c^2} \varepsilon_\beta(\omega)$ . Finally, these relations between wavenumbers both parallel and perpendicular to the interface and relative

permittivities in the different media can be combined to a dispersion relation for the wave propagation along the interface itself:

$$k = \frac{\omega}{c} \sqrt{\frac{\varepsilon_\alpha(\omega) \varepsilon_\beta(\omega)}{\varepsilon_\alpha(\omega) + \varepsilon_\beta(\omega)}} . \quad (2.23)$$

Therefore, transverse magnetic waves can propagate along the interface between metal and vacuum and the corresponding wavenumber obeys Eqn. (2.23). At this point it is relevant to note again that the specific choice of vacuum for the surrounding medium is motivated purely by simplicity and this treatment holds for non-conducting media in general as well.

To illuminate the dispersive behavior of the surface propagation in more detail, the free electron gas model for the metallic material shall be revisited. For this purpose it is convenient to rewrite the metallic permittivity (2.11) according to

$$\varepsilon_\alpha(\omega) = \varepsilon'_\alpha(\omega) + i\varepsilon''_\alpha(\omega) = 1 - \frac{\omega_{\text{pla}}^2}{\omega^2 + i\kappa\omega} .$$

With both  $\omega \in \mathbb{R}$  and  $\varepsilon_\beta(\omega) \in \mathbb{R}$  and assuming  $|\Re\{\varepsilon_\alpha(\omega)\}| > |\Im\{\varepsilon_\alpha(\omega)\}|$ , the complex wavenumber  $k = k' + ik''$  resulting from Eqn. (2.23) takes the form:

$$k' = \frac{\omega}{c} \sqrt{\frac{\varepsilon'_\alpha(\omega) \varepsilon_\beta(\omega)}{\varepsilon'_\alpha(\omega) + \varepsilon_\beta(\omega)}} \quad \text{and} \quad k'' = \frac{\omega}{c} \sqrt{\left(\frac{\varepsilon'_\alpha(\omega) \varepsilon_\beta(\omega)}{\varepsilon'_\alpha(\omega) + \varepsilon_\beta(\omega)}\right)^3 \frac{\varepsilon''_\alpha}{2\varepsilon_\alpha'^2}} .$$

While  $k''$  describes absorption,  $k'$  can be discussed in terms of the real part of the metallic permittivity. Both  $\Re\{k\}$  and  $\Im\{k\}$  are plotted in Fig. 2.7 for the specific scenario of a metal with negligible collisions as in Eqn. (2.14) and vacuum with  $\varepsilon_\beta(\omega) = 1$ . Here, for small  $k'$  and with smaller values, the dispersion relation approaches the light line (black dashed line) from below, but  $k'$  always remains larger than  $\frac{\omega}{c}$ . The wavenumber of the surface propagation grows for  $\varepsilon'_\alpha \rightarrow -\varepsilon_\beta$ , or in this specific case  $\varepsilon'_\alpha \rightarrow -1$ , until the frequency reaches the so called surface plasmon frequency  $\omega_{\text{sur}} = \omega_{\text{pla}}(1 + \varepsilon_\beta)^{-1/2}$ , or in this specific case  $\omega_{\text{sur}} = \frac{\omega_{\text{pla}}}{\sqrt{2}}$ . In the idealized situation of a collision-free electron gas, there is a region of purely imaginary

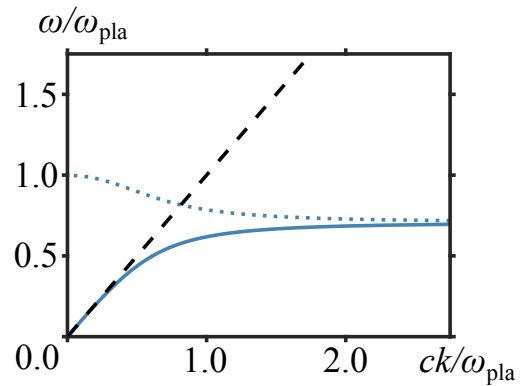


Figure 2.7: For transverse magnetic waves at a metal-vacuum interface, the dispersion relation features  $\Re\{k\}$  (blue solid line),  $\Im\{k\}$  (blue dotted line), and a light line (black dashes) in units of  $\omega_{\text{pla}}$ .

frequency  $\omega_{\text{sur}} = \omega_{\text{pla}}(1 + \varepsilon_\beta)^{-1/2}$ , or in this specific case  $\omega_{\text{sur}} = \frac{\omega_{\text{pla}}}{\sqrt{2}}$ . In the idealized situation of a collision-free electron gas, there is a region of purely imaginary

wavenumber, hence precluded propagation for surface waves. This ends at the plasma frequency and is followed by the transparency for higher frequencies, as already observed for volume plasmons. At this point it is important to note that when considering a more realistic material response model, with a complex relative permittivity, the wavenumber generally remains complex and the surface propagation is connected to damping as well. Consequently, there is a maximum, finite wavenumber at  $\omega_{\text{sur}}$  until which surface plasmons are supported, but the fundamental characteristics, as they are discussed in the idealized case, still hold.

Further important properties immediately follow from the considerations regarding transverse magnetic surface waves so far: With the exponential decay of the fields with increasing distance  $|z|$  normal to the interface,  $\sim e^{\alpha z}$  for  $z < 0$  and  $\sim e^{-\beta z}$  for  $z > 0$ , the spatial extension of the field follows from  $\alpha$  and  $\beta$ . The amplitude has dropped to  $\frac{1}{e}$  of the surface value at the characteristic distances  $z_\alpha = \frac{1}{|\alpha|}$  and  $z_\beta = \frac{1}{|\beta|}$  respectively. In case of the metal-vacuum interface under consideration<sup>[63]</sup>

$$z_\alpha = \frac{c}{\omega} \sqrt{\frac{\varepsilon'_\alpha + \varepsilon_\beta}{\varepsilon_\alpha'^2}} \quad \& \quad z_\beta = \frac{c}{\omega} \sqrt{\frac{\varepsilon'_\alpha + \varepsilon_\beta}{\varepsilon_\beta^2}}$$

follow. On the one hand, for small  $k$  close to the light line, the field expands significantly into the outside domain from the solid state surface, resembling the guided photon field of a Sommerfeld-Zenneck wave<sup>[64]</sup>. For larger  $k$ , on the other hand, the spatial extensions become more similar and well below the vacuum wavelength. This field localization at the surface is the most relevant aspect of surface plasmons for light-matter interaction purposes, as it allows to address individual quantum systems, such as atoms or quantum dots, directly in a controlled manner.

While these propagating surface plasmons provide the field localization desired, one fundamental problem remains with respect to light-matter interaction purposes: As already mentioned,  $k'$  always remains larger than  $\frac{\omega}{c}$ , which is below the light line. Hence, at a given photon energy  $\hbar\omega$ , any projection  $\hbar\frac{\omega}{c} \sin \theta$  impinging under the angle  $\theta$  of the corresponding momentum lacks a fraction  $\hbar\Delta k'$ . There are ways to realize this phase-matching, e.g. with a grating coupler, where the wavenumber parallel to the surface can gain integer multiples of the wavenumber of the grating constant  $\frac{2\pi}{x_{\text{gra}}}$ . Another possibility is the usage of an additional dielectric medium with  $\varepsilon_\gamma > 1$ . The reflection at the interface of the dielectric results in a wavenumber parallel to the surface of  $\sqrt{\varepsilon_\gamma} \frac{\omega}{c} \sin \theta$  and through tunneling of the excitation fields a surface plasmon at the metal-vacuum interface can propagate. Two techniques involving dielectric prisms are customary: the Kretschmann method<sup>[65]</sup> and the Otto configuration<sup>[66]</sup>.

This enables the surface plasmon excitation with visible light and consequently the introduction of surface plasmon polaritons as quasi particles characterized by combined excitations of light quanta and quanta of collective surface electron charge density oscillations. Hence, incident light from the far field can be transformed to electromagnetic fields bound to a solid state surface. This is the exact reason why surface plasmon polaritons are a very promising candidate for directly influencing light-matter interaction. But one significant problem remains: To ensure the direct transformation of photonic energy into collective surface oscillation, the aforementioned additional measures in form of either precise structuring of the surface or preparation of multiple layers must be taken. But these measures inhibit the means available to engineer the local field, hence undermining the intention to utilize plasmon polaritons to influence light-matter interaction. Furthermore, both the required surface grating or the layered media hinder a true miniaturization to create compact on-chip devices, utilizing the atomic or molecular dimensions of the interaction partner. Therefore, a further step to so called localized surface plasmon polaritons must be taken. This will be discussed in the following chapter.

### **Concluding Remarks**

To summarize, continuing the description by classical means, the free electron gas model for the metallic material response results in longitudinal propagation of the electromagnetic fields associated with charge density oscillations. These charge density waves can not be excited by visible light in the bulk. But the free electron gas model enables a surface state of the charge density, which in turn can be excited either through structuring of the surface or layered preparation. However, these limitations narrow the range of available geometrical modifications. Hence, further optimization is desirable.

---

## 2.3 Scattering of Light

### Localized Surface Plasmon Polaritons

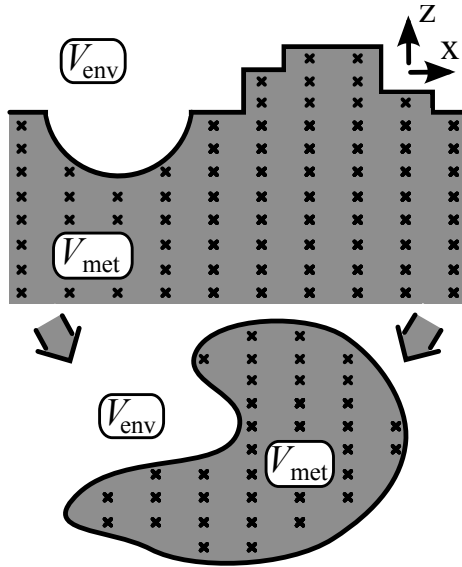


Figure 2.8: Regarding geometrical features constraining the wave vector, a rough surface and closed surface are analogous.

The transition from propagating to localized surface plasmon polaritons most naturally ensues from considering more realistic circumstances than before. Namely, including the aspect of surface roughness instead of the assumption of an atomically smooth interface. With the surface roughness rather small in comparison to the incident wavelength, but big in comparison to the atomic length scale, the geometric shapes, deviating from the smooth surface, can then support localized resonances. But instead of a collective charge oscillation propagating along the surface, the ancillary geometrical boundary conditions, that arise from the protrusions and depressions in the interface constituting the roughness, result in standing waves of sur-

face charge density, whose frequency follows from the permittivity of the bulk material. This situation of the geometry of the surface additionally constraining the wavenumber can be applied straightforward to metallic structures of the dimensions mentioned (see Fig. 2.8). Accordingly, such metallic structures are responsive to incident light at optical frequencies as well and support localized surface plasmon polaritons. Furthermore, as the standing waves of the free surface electron gas are obviously accompanied by similarly localized agglomerations of field intensity in form of hot spots, sub-wavelength metallic structures expand the field localization to spot sizes on the nanometer scale. With respect to light-matter interaction, this finally enables the truly local addressing and interacting with individual atoms, molecules, or more generally quantum systems.

In the general case of arbitrary geometries involved, as they can be numerically handled using Eqn. (2.13), naturally further analytical expressions for the electromagnetic fields surrounding a metallic structure are precluded. But with the intention to illuminate the most fundamental aspects involved in localized plasmons, spherical symmetry shall be assumed for the moment. Furthermore, the extent of the structure in question shall not exceed 1% of the wavelength of the incident elec-

tromagnetic field. This is the regime of the quasi-static approximation<sup>[67]</sup>, and even though this treatment can be expanded to handle structures up to 10% of the irradiating wavelength<sup>[68]</sup> through including perturbative corrections for dynamic effects, for the moment, a metallic sphere with a diameter  $2R$  in the single-digit nanometer range, in accordance with the quasi-static requirements, shall be considered. As the name of the approximation already indicates, due to the vast discrepancy in dimension of the wavelength and the structure, the problem can be reduced to a quasi-static one. Hence, spatially applying electrostatics, the Laplace equation for the scalar potential can be solved. Utilizing the azimuthal symmetry of the problem, the general solution can be written in terms of Legendre Polynomials  $P_l$ <sup>[38]</sup>:

$$\Delta\Phi(r, \theta) = 0 \quad \Rightarrow \quad \Phi(r, \theta) = \sum_{l=0}^{\infty} [X_l r^l + Y_l r^{-(l+1)}] P_l(\cos(\theta)) \quad ,$$

with the order of the polynomials  $l$ , and the polar angle  $\theta$ . Assuming a finite potential at the origin of the coordinate system in the center of the sphere, and matching the tangential electric field and normal flux density at the surface of the sphere, the potential in the two domains involved,  $V_{\text{env}}$  and  $V_{\text{met}}$  respectively, take the form:

$$\begin{aligned} \Phi_{\text{met}}(r, \theta) &= -\frac{3\varepsilon_{\beta}}{\varepsilon_{\alpha}(\omega) + 2\varepsilon_{\beta}} E_0 r \cos \theta \\ \Phi_{\text{env}}(r, \theta) &= -E_0 r \cos \theta + \frac{\varepsilon_{\alpha}(\omega) - \varepsilon_{\beta}}{\varepsilon_{\alpha}(\omega) + 2\varepsilon_{\beta}} E_0 R^3 \frac{\cos \theta}{r^2}. \end{aligned}$$

Here,  $E_0$  is the amplitude of the incident field:  $\mathbf{E}_0 = E_0 \mathbf{e}_z$ . The frequency-dependent permittivity  $\varepsilon_{\alpha}$  is used to represent the metallic material response. It is apparent from the scalar potential in the environment that the incident field is superimposed by the field of an electric dipole that originates from the center of the dipole. Consequently, the corresponding electric field, relevant for the light-matter interaction, reads:

$$\begin{aligned} \mathbf{E}_{\text{env}}(\mathbf{r}, \omega) &= \mathbf{E}_0 + \frac{3\mathbf{n}(\mathbf{r}) [\mathbf{n}(\mathbf{r}) \cdot \mathbf{p}(\omega)] - \mathbf{p}(\omega)}{4\pi\varepsilon_0\varepsilon_{\beta}r^3} \quad , \quad \text{with} \quad (2.24) \\ \mathbf{p}(\omega) &= 4\pi\varepsilon_0\varepsilon_{\beta}R^3 \frac{\varepsilon_{\alpha}(\omega) - \varepsilon_{\beta}}{\varepsilon_{\alpha}(\omega) + 2\varepsilon_{\beta}} \mathbf{E}_0 \quad . \end{aligned}$$

In this formulation it is obvious, that the dipole, induced in the metallic sphere, experiences a resonance for  $\varepsilon_{\alpha}(\omega) = -2\varepsilon_{\beta}$ , the so-called Fröhlich condition. The losses in form of  $\Im\{\varepsilon_{\alpha}(\omega)\}$  prevent a diverging behavior.

A similar treatment, resulting in analytic expressions of induced fields, can be performed for ellipsoids<sup>[69]</sup>. In case of metallic structures larger than the size re-

quirement of the quasi-static approximation, a rigorous electrodynamic treatment of the retardation effects is still possible assuming spherical symmetry. Here, again the symmetry of the problem is used and the fields involved are expanded in terms of vector spherical harmonics<sup>[70]</sup> in the so called Mie theory<sup>[71]</sup>. But with a numerical solver at hand that can deal with arbitrary geometrical scenarios and with the intention to influence the light matter interaction through geometrical structuring of the environment, the limitation to a specific type of geometry is not reasonable. But this brief foray into spherical geometries already shows that the next step for a comprehensive theoretical description is the investigation of the scattering and absorption of light by metallic structures.

### Scattering and Absorption by Metal

The investigation of the light scattering shall begin with fundamental energetic considerations. The work being done in media due to an electric field results in a change of the charge  $\delta e$  in the presence of a potential  $\Phi$ . This change in charge can be connected to a change in electric flux density  $\tilde{\mathbf{D}}(\mathbf{r}, t)$  over a surface via Gauß's law. Furthermore applying the divergence theorem yields<sup>[40]</sup>:

$$\delta W = \Phi \delta e = - \int d\mathbf{A} \delta \tilde{\mathbf{D}}(\mathbf{r}, t) \cdot \Phi = - \int dV \nabla \cdot (\delta \tilde{\mathbf{D}}(\mathbf{r}, t) \Phi) \quad .$$

As no further sources in form of external charge density distributions shall be included and the potential can be replaced by the electric field, the work done can be reformulated to:

$$\delta W = - \int dV (\Phi \nabla \cdot \delta \tilde{\mathbf{D}}(\mathbf{r}, t) + \delta \tilde{\mathbf{D}}(\mathbf{r}, t) \cdot \nabla \Phi) = \int dV \tilde{\mathbf{E}}(\mathbf{r}, t) \cdot \delta \tilde{\mathbf{D}}(\mathbf{r}, t) \quad . \quad (2.25)$$

A similar inquiry regarding the magnetic field can be performed. But the magnetic field does no work on moving charges due to  $\tilde{\mathbf{F}}(\mathbf{r}, t) \perp \mathbf{v}$ , following from the Lorentz force  $\tilde{\mathbf{F}}(\mathbf{r}, t) = e (\tilde{\mathbf{E}}(\mathbf{r}, t) + \mathbf{v} \times \tilde{\mathbf{B}}(\mathbf{r}, t))$ . Consequently, the work done due to an applied magnetic field results in induced electric fields, which in turn act on the current sources of the magnetic field. The Lorentz force acting for  $\delta t$  on a charge moving with  $\mathbf{v}$  can be superimposed for accumulations of point charges, since the term for the magnetic flux density vanishes. Including the charge density  $\rho$  per volume  $dV$  instead of the charge and substituting the moving charge density with the current  $\mathbf{j}$ , leads to<sup>[72]</sup>:

$$\delta W = \int dV \rho \delta t \mathbf{v} \cdot (\tilde{\mathbf{E}}(\mathbf{r}, t) + \mathbf{v} \times \tilde{\mathbf{B}}(\mathbf{r}, t)) = \delta t \int dV \tilde{\mathbf{j}}(\mathbf{r}, t) \cdot \tilde{\mathbf{E}}(\mathbf{r}, t) dV \quad .$$

The current  $\tilde{\mathbf{j}}(\mathbf{r}, t)$  can be replaced with the curl of the magnetic field, as no additional changes of the electric field are considered. In the next step, the vector product rule for the divergence of an outer product is applied. As the resulting volume integral over the divergence of  $\tilde{\mathbf{E}}(\mathbf{r}, t) \times \tilde{\mathbf{H}}(\mathbf{r}, t)$  can be transformed using the divergence theorem and the surface infinitely expanded, it ultimately vanishes. To reach the desired formulation, the curl of the electric field is substituted, according to the corresponding Maxwell equation:

$$\begin{aligned} \delta W &= -\delta t \int dV \tilde{\mathbf{E}}(\mathbf{r}, t) \cdot (\nabla \times \tilde{\mathbf{H}}(\mathbf{r}, t)) = -\delta t \int dV \tilde{\mathbf{H}}(\mathbf{r}, t) \cdot (\nabla \times \tilde{\mathbf{E}}(\mathbf{r}, t)) \\ &= \int dV \tilde{\mathbf{H}}(\mathbf{r}, t) \cdot (\delta t \partial_t \tilde{\mathbf{B}}(\mathbf{r}, t)) = \int dV \tilde{\mathbf{H}}(\mathbf{r}, t) \cdot \delta \tilde{\mathbf{B}}(\mathbf{r}, t) \quad . \end{aligned} \quad (2.26)$$

The change in energy due to both applied electric and magnetic fields accounted for in this manner, a general electromagnetic energy density can be defined by combining Eqn. (2.25) and Eqn. (2.26). The time derivative of this electromagnetic field energy density, relevant for interaction dynamics involving the electromagnetic field, yields:

$$\partial_t w_{\text{eme}} = \tilde{\mathbf{E}}(\mathbf{r}, t) \cdot \partial_t \tilde{\mathbf{D}}(\mathbf{r}, t) + \tilde{\mathbf{H}}(\mathbf{r}, t) \cdot \partial_t \tilde{\mathbf{B}}(\mathbf{r}, t) \quad . \quad (2.27)$$

With the time derivative of the energy density at hand, it is natural to introduce the electromagnetic energy flux density in form of the Poynting vector  $\tilde{\mathbf{S}}(\mathbf{r}, t) = \tilde{\mathbf{E}}(\mathbf{r}, t) \times \tilde{\mathbf{H}}(\mathbf{r}, t)$ . It stands to reason, that an inspection of the sources and sinks of the energy flux is of greater interest. From the divergence of the Poynting vector follows:

$$\begin{aligned} \nabla \cdot \tilde{\mathbf{S}}(\mathbf{r}, t) &= \tilde{\mathbf{H}}(\mathbf{r}, t) \cdot (\nabla \times \tilde{\mathbf{E}}(\mathbf{r}, t)) - \tilde{\mathbf{E}}(\mathbf{r}, t) \cdot (\nabla \times \tilde{\mathbf{H}}(\mathbf{r}, t)) \\ &= -\left( \tilde{\mathbf{H}}(\mathbf{r}, t) \cdot \partial_t \tilde{\mathbf{B}}(\mathbf{r}, t) + \tilde{\mathbf{E}}(\mathbf{r}, t) \cdot \partial_t \tilde{\mathbf{D}}(\mathbf{r}, t) \right) - \tilde{\mathbf{E}}(\mathbf{r}, t) \cdot \tilde{\mathbf{j}}(\mathbf{r}, t) \quad . \end{aligned} \quad (2.28)$$

Here, the vector identity for the divergence of an outer product of vectors  $\nabla \cdot (\mathbf{E} \times \mathbf{H})$  is combined with the curl Maxwell equations (2.2). Equation (2.28) is called Poynting theorem and describes the energy dynamics regarding electromagnetic fields. This becomes clearer once an integration over a finite domain  $\Omega$  is applied. From the divergence theorem follows the surface integral of the energy flow  $\int_{\partial\Omega} d\mathbf{A} \cdot \tilde{\mathbf{S}}(\mathbf{r}, t)$ , the volume integral of the energy density time derivative  $\int_{\Omega} dV \partial_t w_{\text{eme}}$ , and the volume integral of the work done on induced currents  $\int_{\Omega} dV \tilde{\mathbf{E}}(\mathbf{r}, t) \cdot \tilde{\mathbf{j}}(\mathbf{r}, t)$ . This situation is schematically depicted in Fig. 2.9: The energy flow  $\mathbf{S}$  normal to a closed surface  $\partial\Omega$  accounts for both the change in electro-

magnetic field energy  $\partial_t w_{\text{eme}}$  and Ohmic losses in media in form of  $\mathbf{E} \cdot \mathbf{j}$ .

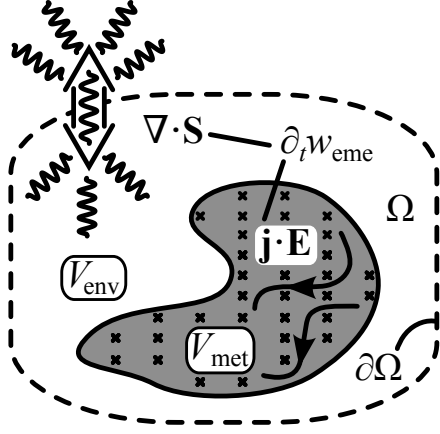


Figure 2.9: Setting that is considered in the Poynting theorem: two mechanisms effectuating change in electromagnetic field energy within finite domain  $\Omega$ .

This energy conservation in a limited spatial domain  $\Omega$  can be immediately transferred to the light-matter interaction scenario of interest. With electromagnetic energy in form of radiation from the far field entering the light-matter interaction domain, localized surface plasmon polaritons supported by the purposefully tailored metallic structure can be excited. Hence, electromagnetic energy is localized in form of concentrated hot spots resulting from the geometry of the metallic structure. As control of the location of the hot spots can be exerted by controlling the geometry of the metallic media structure, and with

quantum systems as interaction partners either placed according to the hot spots or the structure geometrically adapted to the fixed positions of the quantum systems, this is the mechanism that allows control of light-matter interaction in these hot spots unrivaled by other means and inherently nanoscopic in nature. Within the free-electron gas model not just the localized resonances, but also the absorption of energy is accounted for by Ohmic losses. And finally, the emission of electromagnetic fields into the far field either by the quantum system or by the metallic structure is monitored by the power flux out of the light-matter interaction domain.

The characteristic electromagnetic power outflow from the finite light-matter interaction domain into the far field, after an initial excitation of localized surface plasmon polaritons, can be detected in experimental setups. But as such detectors can generally not follow the fast oscillations associated with optical frequencies, to predict measurable emission from the metallic structure, the description has to switch from an instantaneous to a time-averaged Poynting vector. Additionally, a limitation of the generally complex-valued electromagnetic fields to real-valued, measurable quantities is necessary as well. Therefore,

$$\begin{aligned}
 \langle \tilde{\mathbf{S}}(\mathbf{r}, t) \rangle &= \frac{1}{t_{\text{osc}}} \int_0^{t_{\text{osc}}} dt \tilde{\mathbf{S}}(\mathbf{r}, t) = \frac{1}{4t_{\text{osc}}} \int_0^{t_{\text{osc}}} dt \left[ \tilde{\mathbf{E}}(\mathbf{r}, t) + \tilde{\mathbf{E}}^*(\mathbf{r}, t) \right] \times \left[ \tilde{\mathbf{H}}(\mathbf{r}, t) + \tilde{\mathbf{H}}^*(\mathbf{r}, t) \right] \\
 &= \frac{1}{2t_{\text{osc}}} \int_0^{t_{\text{osc}}} dt \left[ \Re \{ \tilde{\mathbf{E}}_{\text{slo}}(\mathbf{r}, t) \times \tilde{\mathbf{H}}_{\text{slo}}^*(\mathbf{r}, t) \} + \mathcal{C}_1 \cos(2\omega_{\text{opt}}t) + \mathcal{C}_2 \sin(2\omega_{\text{opt}}t) \right] \\
 &= \frac{1}{2} \Re \{ \mathbf{E}(\mathbf{r}, \omega) \times \mathbf{H}^*(\mathbf{r}, \omega) \} \quad , \quad (2.29)
 \end{aligned}$$

follows, with the ansatz of slowly varying amplitudes multiplied with fast optical oscillations for the electromagnetic fields  $\tilde{\mathbf{E}}(\mathbf{r}, t) = \tilde{\mathbf{E}}_{\text{slo}}(\mathbf{r}, t) e^{-i\omega_{\text{opt}} t}$ . The fast oscillating terms vanish due to the time average and in the frequency domain the averaged Poynting vector gives the simple form of the last line in Eqn. (2.29). As the description of the energy dynamics already indicates, the characteristic localized surface plasmon polariton resonance can be probed by scattering or extinction measurements. Such a scattering scenario is depicted in Fig. 2.10. With a well-defined field with controllable properties incident on the structure, the measurement of the scattered power outflow in relation to the incident irradiance  $I_{\text{inc}}$ , in case of plane waves  $I_{\text{inc}} = \sqrt{\frac{\epsilon_0}{4\mu_0}} E_{\text{inc},0}^2$  with the field amplitude  $E_{\text{inc},0}$ , gives the scattering cross section

$$C_{\text{sca}} = I_{\text{inc}}^{-1} \int_{\partial\Omega} d\mathbf{A} \cdot \langle \tilde{\mathbf{S}}(\mathbf{r}, t) \rangle = \frac{1}{2I_{\text{inc}}} \int_{\partial\Omega} d\mathbf{A} \cdot [\Re\{\mathbf{E}_{\text{sca}}(\mathbf{r}, \omega) \times \mathbf{H}_{\text{sca}}^*(\mathbf{r}, \omega)\}]$$

of the metallic structure. The comparison of the scattering cross section with the geometrical cross section of the structure exposed to the incident radiation gives a very reliable measure for the ability of the geometry to scatter light. Hence, geometrical optimization both through numerical simulations and in experimental measurement is possible. Similar to the scattering cross section, an absorption cross section can be defined:  $C_{\text{abs}} = I_{\text{inc}}^{-1} \int_{\Omega} dV \mathbf{E}_{\text{inc}}(\mathbf{r}, \omega) \cdot \mathbf{j}(\mathbf{r}, \omega)$ . Finally, through the definition of an extinction cross section as  $C_{\text{ext}} = C_{\text{sca}} + C_{\text{abs}}$ , which can be measured, the absorption cross section is also indirectly available.

At this point, having identified the processes participating in the local change in electromagnetic field energy as scattering and absorption, and, provided that the metallic structure is illuminated with a plane wave, having the corresponding cross sections available through experimental measurements, the classical description of the engineering of the photonic environment, or in other words the local electromagnetic field is complete and verifiable through measurement. The next step consists of incorporating the light-matter interaction itself and, with its inherently quantum physical nature due to individual transitions between electronic states being involved, requires quantum optical means.

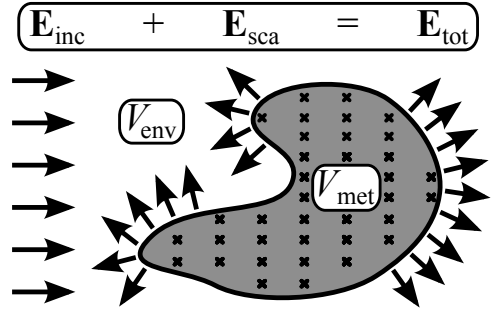


Figure 2.10: Incident field is scattered by a structure and superimposing incident and scattered gives total field.

---

## Concluding Remarks

To summarize, in the last stage of the classical description, the field localization accompanying the surface charge oscillation can be extended to hot spots of the field by using metallic sub-wavelength structures, whose closed surface results in standing surface charge waves. Now, the situation corresponds to a canonical scattering scenario. Consequently, the characterization of the localized surface plasmon polaritons can be performed by scattering means. This additionally enables experimental verification of theoretical considerations by measurement, as radiation into the far field is emitted.

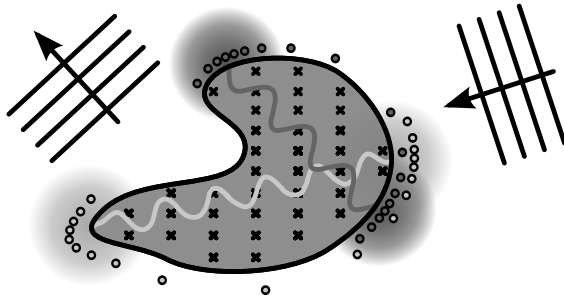


Figure 2.11: The classical considerations so far result in an extraordinary localization of electromagnetic energy.

Hence, on a completely classical basis, the control of the local field distribution can be used to influence light-matter interaction without describing the light-matter interaction directly. This reversible conversion of freely propagating to precisely localized electromagnetic fields has inspired the appellation of 'nanoantenna' to be bestowed upon the structures that support localized surface plasmon resonances.

The applications, whose description only requires classical means, range from imaging<sup>[73–75]</sup>, substance sensing<sup>[76–78]</sup>, down to single molecules<sup>[79,80]</sup>, proposed molecular interaction detection<sup>[81]</sup>, direct tumor<sup>[29,82]</sup> and related forms of therapy<sup>[83,84]</sup>, to antennas for energy harvesting<sup>[85,86]</sup>, optomechanical nanoswitches<sup>[87]</sup>, nanoelectrometers<sup>[88]</sup>, and nanometric hypersound generators<sup>[89]</sup>. Furthermore, highly efficient light sources<sup>[90,91]</sup>, telecommunication spectral demultiplexers<sup>[92,93]</sup>, photodetectors<sup>[94,95]</sup>, wireless nanonetworks<sup>[96,97]</sup>, electrooptic modulators<sup>[98,99]</sup> and directional couplers<sup>[100,101]</sup> can be described in this manner.

But the classical description so far cannot capture all phenomena and features involved in quantum information related purposes. Even though the direct coupling of the collective standing surface charge waves to incoming and outgoing photons follows a classical description, to include electronic transitions of quantum systems, non-classical statistics, or non-classical properties of the radiation involved, it is necessary to expand the modeling by incorporating elements of cavity quantum electrodynamics and quantum optics, respectively. This is what the second part of this chapter shall describe.

## 2.4 Elements of Quantum Optics

### Quantized Electromagnetic Fields

With the local electromagnetic field controlled by a nanoantenna, the light-matter interaction itself shall be incorporated into the theoretical model. The interaction between atoms, or more general, quantum systems and photons is inherently a single or few photon process, and consequently a description by quantized means is inevitable. Hence, the quantization of the electromagnetic field is the first essential step to take. An analogy to the classical Hamiltonian formulation<sup>[102]</sup>, where classical position  $q_j^{\text{cla}}$  and conjugate momentum  $p_j^{\text{cla}}$  of particle  $j$  provide the Hamiltonian expression for the energy of the system  $\mathcal{E} = \mathcal{H}(q_j^{\text{cla}}, p_j^{\text{cla}})$ . If the dynamics of the system follow the differential equations:  $\partial_t q_j^{\text{cla}} = \partial_{p_j^{\text{cla}}} \mathcal{H}$  and  $\partial_t p_j^{\text{cla}} = -\partial_{q_j^{\text{cla}}} \mathcal{H}$ , the system is expressed in canonical form and  $(q_j^{\text{cla}}, p_j^{\text{cla}})$  are pairs of canonical variables<sup>[103]</sup>. Therefore, performing a canonical quantization consists of associating available observables  $q_j$  and  $p_j$  with conjugate canonical variables and imposing the commutation relations  $[q_u, p_v] = i\hbar\delta_{uv}$  with the Hamiltonian  $\mathcal{H}(q_j, p_j)$ . Similar to the classical scenario of solving Maxwell's equation, the decoupling, or in other words identifying decoupled pairs of conjugate variables, is the first essential step in attempting to quantize the electromagnetic field.

According to the conventional procedure for the field quantization, where a finite cube with side length  $l$  is considered first. Inside the cube, the field is expanded into spatial Fourier components according to<sup>[103]</sup>

$$\tilde{\mathbf{E}}_{\mathbf{v}}(t) = \frac{1}{l^3} \int_V d^3r \tilde{\mathbf{E}}(\mathbf{r}, t) e^{-i\mathbf{k}_{\mathbf{v}} \cdot \mathbf{r}} \quad \text{are} \quad \tilde{\mathbf{E}}(\mathbf{r}, t) = \sum_{\mathbf{v}} \tilde{\mathbf{E}}_{\mathbf{v}}(t) e^{i\mathbf{k}_{\mathbf{v}} \cdot \mathbf{r}} \quad . \quad (2.30)$$

Here,  $\mathbf{v}$  is the integer component vector  $\mathbf{v} = (v_x, v_y, v_z)$  and each component accounts for the  $\frac{2\pi}{l}$  periodicity of the  $\mathbf{k}_{\mathbf{v}}$  vector. According to Eqn. (2.30), any field within the cube in  $\mathbf{k}$  space can be expanded in functions  $e^{i\mathbf{k}_{\mathbf{v}} \cdot \mathbf{r}}$ . Again using the transformation of derivatives after Fourier transform, Maxwell's equations containing divergences (2.1) give  $\mathbf{k}_{\mathbf{v}} \cdot \tilde{\mathbf{E}}_{\mathbf{v}}(t) = 0$  and  $\mathbf{k}_{\mathbf{v}} \cdot \tilde{\mathbf{B}}_{\mathbf{v}}(t) = 0$  for no additional sources. Consequently, transversality of the electromagnetic fields is obvious within the cube and the polarization, as the spatial orientation of the amplitude  $\tilde{\mathbf{E}}_{\mathbf{v}}(t)$ , can be defined in the plane normal to  $\mathbf{k}$ :  $\tilde{\mathbf{E}}_{\mathbf{v}}(t) = \sum_{p=1,2} \tilde{E}_{\mathbf{v}p}(t) \mathbf{e}_{\mathbf{v},p}$ . Now, an additional polarization index  $p$  is combined with the three spatial indices contained in  $\mathbf{v}$  to yield the full quantization index  $\xi = (v_x, v_y, v_z, p)$ . Due to the corresponding curl equation (2.2), each component  $\tilde{E}_{\xi}(t)$  can be associated with  $\tilde{B}_{\xi}(t)$ , using  $\mathbf{e}'_{\xi} = \mathbf{k}_{\xi} \times \mathbf{e}_{\xi}$ .

It is customary to introduce a vector potential  $\mathbf{A}(\mathbf{r}, t)$  with

$$\tilde{\mathbf{E}}(\mathbf{r}, t) = -\partial_t \tilde{\mathbf{A}}(\mathbf{r}, t) \quad \text{and} \quad \tilde{\mathbf{B}}(\mathbf{r}, t) = \nabla \times \tilde{\mathbf{A}}(\mathbf{r}, t)$$

in radiation gauge with  $\nabla \cdot \tilde{\mathbf{A}}(\mathbf{r}, t) = 0$  and  $\tilde{\Phi}(\mathbf{r}, t) = 0$ . Hence, the fields in  $\mathbf{k}$  space can be expressed through  $\tilde{E}_\xi = -\partial_t \tilde{A}_\xi$  and  $\tilde{B}_\xi = ik_\xi \tilde{A}_\xi$ . Implementing these substitutions in Maxwell's equations leads to

$$\partial_t \tilde{E}_\xi(t) = \omega_\xi^2 \tilde{A}_\xi(t) \quad \text{and} \quad \partial_t \tilde{A}_\xi(t) = -\tilde{E}_\xi(t) \quad .$$

These equations for the dynamics of the electromagnetic field can be decoupled by choosing  $Z_\xi^\pm(t) = \frac{1}{2} \mathcal{C}_{\text{qua}}^{-1} [\omega_\xi \tilde{A}_\xi(t) \pm i \tilde{E}_\xi(t)]$ , yielding  $\partial_t Z_\xi^\pm(t) \mp i \omega_\xi Z_\xi^\pm(t) = 0$  with the solution  $Z_\xi^\pm(t) = Z_\xi^\pm(0) e^{\pm i \omega_\xi t}$ . Returning to the fields by inverting the definitions of the complex variables  $Z_\xi^\pm(t)$ , gives  $\tilde{A}_\xi(t) = \mathcal{C}_{\text{qua}} \omega_\xi^{-1} [Z_\xi^-(t) + Z_\xi^+(t)]$  and  $\tilde{E}_\xi(t) = \mathcal{C}_{\text{qua}} [i Z_\xi^-(t) - i Z_\xi^+(t)]$ . While these expressions for the field can be inserted into the field expansions inside the cube, from  $(Z_\xi^+(t))^* = Z_\xi^-(t)$  follows  $\tilde{E}_{-\xi}(t) = \tilde{E}_\xi^*(t)$  and  $\tilde{A}_{-\xi}(t) = \tilde{A}_\xi^*(t)$  and finally

$$\begin{aligned} \tilde{\mathbf{A}}(\mathbf{r}, t) &= \sum_\xi \frac{\mathcal{C}_{\text{qua}}}{\omega_\xi} [Z_\xi^-(t) e^{i \mathbf{k}_\xi \cdot \mathbf{r}} + (Z_\xi^-(t))^* e^{-i \mathbf{k}_\xi \cdot \mathbf{r}}] \mathbf{e}_\xi \quad , \\ \tilde{\mathbf{E}}(\mathbf{r}, t) &= \sum_\xi \mathcal{C}_{\text{qua}} [i Z_\xi^-(t) e^{i \mathbf{k}_\xi \cdot \mathbf{r}} - i (Z_\xi^-(t))^* e^{-i \mathbf{k}_\xi \cdot \mathbf{r}}] \mathbf{e}_\xi \quad . \end{aligned} \quad (2.31)$$

With the electromagnetic field expanded in transverse polarized monochromatic plane waves, it is apparent that a set of normal modes in free space in form of the plane waves has risen naturally. At this point it is important to note, that the plane waves are not the only available set, as the field within a fixed volume  $l^3$  can be expanded in an arbitrary orthonormal complex vector function basis. The plane waves have emerged due to the choice of a cube and consequently periodic boundary conditions on its sides.

With the ansatz of integrating over the electromagnetic field energy density, according to Eqn. (2.27), in free space within the volume of interest  $l^3$ , the radiation energy is  $\mathcal{E}_{\text{rad}} = \frac{\varepsilon_0}{2} \int_{l^3} dV [\tilde{\mathbf{E}}^2(\mathbf{r}, t) + c^2 \tilde{\mathbf{B}}^2(\mathbf{r}, t)]$ . Using the expansion of the fields within the cube and due to the periodicity of the wave vector and the transversal polarization, the energy is given by a sum over the energies of each normal mode  $\mathcal{E}_{\text{rad}} = 2\varepsilon_0 l^3 \sum_\xi \mathcal{C}_{\text{qua}}^2 |Z_\xi^-(t)|^2$ . Reformulating the evolution equations of the complex variables  $\partial_t \Re\{Z_\xi^-(t)\} = \omega_\xi \Im\{Z_\xi^-(t)\}$  and  $\partial_t \Im\{Z_\xi^-(t)\} = -\omega_\xi \Re\{Z_\xi^-(t)\}$ , the

equations

$$\begin{aligned}\partial_t q_\xi &= \partial_{p_\xi} \mathcal{H} \quad \text{with} \quad q_\xi = \sqrt{4\varepsilon_0 l^3 \omega_\xi^{-1}} \mathcal{C}_{\text{qua}} \Re\{Z_\xi^-(t)\} \quad , \\ \partial_t p_\xi &= -\partial_{q_\xi} \mathcal{H} \quad \text{with} \quad p_\xi = \sqrt{4\varepsilon_0 l^3 \omega_\xi^{-1}} \mathcal{C}_{\text{qua}} \Im\{Z_\xi^-(t)\} \quad .\end{aligned}$$

can be identified. From these equations, conjugate variables are identified as the real and imaginary part of the complex mode amplitude variables. Next, associating the conjugate variables with operators that meet the required commutation relations, the operator for the complex mode field amplitude is  $a_\xi = \frac{1}{\sqrt{2\hbar}} (q_\xi + ip_\xi)$ , where the constant  $\mathcal{C}_{\text{qua}}$  has been chosen for a convenient expression. Now, from the Hamilton equations for the conjugate variables, the Hamiltonian of quantized radiation follows

$$\mathcal{H} = \sum_{\xi} \frac{\omega_\xi}{2} (q_\xi^2 + p_\xi^2) = \sum_{\xi} \hbar\omega_\xi \left( a_\xi^\dagger a_\xi + \frac{1}{2} \right) \quad . \quad (2.32)$$

At this point, with the electromagnetic field decomposition in normal modes and the quantized field dynamics in form of the Hamiltonian formulation at hand, the foundation of the quantum description of a variety of effects involving light is possible. While all these phenomena graspable by quantum optical means are fascinating, the following shall be limited to what is relevant for the formulation of the interaction of quantized light with quantized matter or for the selected applications that follow.

### Number States and Selected Properties

The quantized radiation dynamics in Eq. (2.32) take a form analogous to an ensemble of quantized harmonic oscillators. Introducing the number operator  $n_\xi = a_\xi^\dagger a_\xi$  with non-negative integer eigenvalues<sup>[104]</sup> yields the eigenstates  $|n_\xi\rangle$  that are called number states and form a basis of the radiation states in each electromagnetic field mode. With the mode amplitude operators  $a_\xi |n_\xi\rangle = \sqrt{n} |n_\xi - 1\rangle$  and  $a_\xi^\dagger |n_\xi\rangle = \sqrt{n+1} |n_\xi + 1\rangle$  acting as annihilation and creation operators for the harmonic oscillator, each number state can be connected to the vacuum state  $|n_\xi\rangle = \frac{(a_\xi^\dagger)^n}{\sqrt{n!}} |0\rangle$ . Furthermore, while omitting the zero-point energy for the moment, the energy of the electromagnetic field in a number state amounts to  $\langle n_\xi | \mathcal{H} | n_\xi \rangle = \sum_{\xi'} \hbar\omega_{\xi'} \langle n_\xi | a_{\xi'}^\dagger a_{\xi'} | n_\xi \rangle = n\hbar\omega_\xi$ .

Contemplating these properties of the harmonic oscillator applied to the quantized radiation field, it is evident that each state  $|n_\xi\rangle$  contains  $n$  quanta of energy  $\hbar\omega_\xi$ , while the vacuum state  $|0\rangle$  contains none of these quanta. Obviously, these quantized excitations of the electromagnetic field can be identified as photons.

In this context, the creation and annihilation operator,  $a_\xi^\dagger$  respectively  $a_\xi$ , add or remove single photons from each electromagnetic field mode  $\xi$  and the number operator  $n_\xi$  gives the number of photons in each mode. At this point it is obvious that number states are the desirable formalism to describe quantized light-matter interaction. As Fig. 2.12 shows, from the decomposition of the radiation field into normal modes immediately follows the energetic dynamics of a harmonic oscillator for each mode. This, however, enables the formalistic adding, removing, and counting of photons in each mode and consequently the description of photons originating from the quantized light-matter interaction.

This concept of a radiation mode populated by photons can be generalized to multi-mode number states  $|n_1\rangle \otimes |n_2\rangle \otimes \dots \otimes |n_\xi\rangle \otimes \dots \equiv |n_1, n_2, \dots, n_\xi, \dots\rangle$ , where any multi-mode radiation state can be expanded according to

$$|\Psi_{\text{rad}}\rangle = \sum_{n_1=0}^{\infty} \sum_{n_2=0}^{\infty} \dots \sum_{n_\xi=0}^{\infty} \dots \mathcal{C}_{n_1, n_2, \dots, n_\xi, \dots} |n_1, n_2, \dots, n_\xi, \dots\rangle \quad .$$

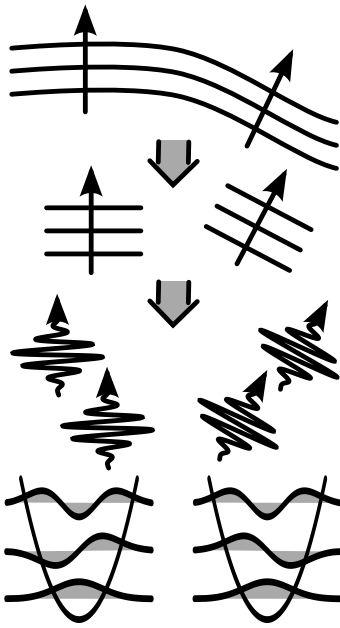


Figure 2.12: Normal modes emerge from the quantization itself, subsequently the Hamiltonian formulation spawns harmonic oscillator properties.

This is the most general expression of a pure state of individual quantized radiation modes and, assuming that these radiation modes can be distinguished by polarization or radiation pattern in an experimental scenario, any measurement or manipulation in general of one mode does not affect the other modes. While this can be a desirable circumstance for different applications, such as encoding different information in each radiation mode, it immediately leads to the probably most prominent non-classical property: entanglement<sup>[105]</sup>. The pure state consists of product states and their superpositions. In contrast to such a product state, by using joint observables, a state can be prepared so that it is not factorizable. But due to the superposition principle, it can be expressed as a sum of product states<sup>[106]</sup>  $|\Psi_{\text{ent}}\rangle = \sum_{\mu, \nu} \alpha_{\mu, \nu} |\mu_A\rangle \otimes |\nu_B\rangle$  with complex amplitudes  $\alpha_{\mu, \nu}$ . In addition to information about the separate measurements on arbitrary subsystems  $A$  and  $B$ , the entangled state also contains

information about the correlations between the measurements. And these correlations can exceed any classical counterpart. The example of an entangled physical system most relevant for light-matter interaction is probably a pair of po-

larization entangled photons emitted by a quantum dot<sup>[107–109]</sup>. But without further discussing this example and remaining with number states, a two-mode state shall be considered briefly. A state of the form<sup>[103]</sup>  $|\Psi_{\text{rad}}\rangle = \sum_{n=0}^{\infty} \mathcal{C}_n |n_{\mu}, n_{\nu}\rangle$ , with the coefficients  $\mathcal{C}_n$  and an equal number of photons in each mode, reveals perfect correlation, and therefore entanglement, in the measurement of the photon number, if more than one of the coefficients  $\mathcal{C}_n$  is non-zero. Including the photon number operators for each mode involved,  $n_{\mu}$  and  $n_{\nu}$  respectively, yields

$$(n_{\mu} - n_{\nu}) |\Psi_{\text{rad}}\rangle = \sum_{n=0}^{\infty} \mathcal{C}_n (n - n) |n_{\mu}, n_{\nu}\rangle = 0 \quad .$$

Hence,  $|\Psi_{\text{rad}}\rangle$  is an eigenstate of the difference of photon numbers in each mode and the corresponding eigenvalue is 0. Thusly, the perfect correlation between the photon number measurements leads to vanishing fluctuations  $\Delta(n_{\mu} - n_{\nu}) = 0$  in the difference of the instantaneous photon detection, whereas fluctuations remain for individual measurements of each mode. Such a fluctuation suppression can benefit various applications. Returning to more general considerations, if two physical objects are entangled in a measurable property and since their state can not be factorized, they are described as a single entity. As this circumstance holds even if the two objects are spatially separated, entanglement is also referred to as quantum non-locality. Entanglement in itself is a vast and fascinating topic of research, not least because of its exclusive quantum physical nature. But in the context of light-matter interaction with respect to quantum information purposes two prominent applications can be named that indicate its importance: the implementation of teleportation of information and the detecting eavesdropping in quantum cryptography to secure quantum communication

Through the introduction of entanglement the notion of mixed states in contrast to pure states has become evident. While one can define a state vector  $|\Psi_{\text{pur}}\rangle$  for a pure state, the ideal way to deal with mixed states is through the density operator  $\rho_{\text{mix}} = \sum_{\xi} w_{\xi} |\Psi_{\xi}\rangle \langle \Psi_{\xi}|$ , with  $\sum_{\xi} w_{\xi} = 1$  and  $w_{\xi} > 0$ . The density operator provides the same information as the state vector for a pure state and takes the form  $\rho_{\text{pur}} = |\Psi_{\text{pur}}\rangle \langle \Psi_{\text{pur}}|$ , hence projecting on the state vector. The expectation value of an observable  $\mathcal{O}_{\text{pur}}$  for a pure state consequently yields  $\langle \Psi_{\text{pur}} | \mathcal{O}_{\text{pur}} | \Psi_{\text{pur}} \rangle = \text{Tr}(\mathcal{O}_{\text{pur}} \rho_{\text{pur}})$ . This is most useful for mixed states, as  $\text{Tr}(\mathcal{O}_{\text{mix}} \rho_{\text{mix}})$  also holds for mixed states and the expectation value of an observable. In the context of light-matter interaction, this formalism becomes especially advantageous when examining subsystems that may not be possible to describe in terms of state vectors, but by a partial density operator that is found by tracing  $\rho_{\text{tot}}$  over the subspace that is complemen-

tary to the subspace of interest  $\rho_A = \text{Tr}_B(\rho_{\text{tot}})$ . With the partial density operator the probability of an arbitrary state in the Hilbert space of subsystem  $A$  is given by  $P_{|\Psi_A\rangle} = \text{Tr}(\rho_A |\Psi_A\rangle \langle \Psi_A|)$ . The benefits of reducing the complexity of a larger system to a subsystem of interest by such a procedure is evident and shall be of use in the specific entanglement application to come.

The final aspect of the general quantum optical framework deals with the detection of a quantized radiation mode as it is introduced in Eqn. (2.31). It is common practice to split the field into a positive and a negative frequency part<sup>[110]</sup>

$$\tilde{\mathbf{E}}(\mathbf{r}, t) = \tilde{\mathbf{E}}^+(\mathbf{r}, t) + \tilde{\mathbf{E}}^-(\mathbf{r}, t) = \sum_{\xi} \tilde{C} a_{\xi} e^{i(\mathbf{k}_{\xi} \cdot \mathbf{r} - \omega t)} \mathbf{e}_{\xi} + \sum_{\xi} \tilde{C}^* a_{\xi}^{\dagger} e^{-i(\mathbf{k}_{\xi} \cdot \mathbf{r} - \omega t)} \mathbf{e}_{\xi}^* \quad . \quad (2.33)$$

From this form it is apparent that  $\tilde{\mathbf{E}}^+(\mathbf{r}, t)$  corresponds to the absorption of a photon around the space time point  $(\mathbf{r}, t)$ . With the quantized electromagnetic field initially in state  $|\Psi_1\rangle$ , the photon absorption that is associated with the detection of a photon by some device, represents the transition to the state  $|\Psi_2\rangle$  of the field. The probability of this transition is then given by<sup>[111]</sup>  $\left| \langle \Psi_2 | \tilde{\mathbf{E}}^+(\mathbf{r}, t) | \Psi_1 \rangle \right|^2$ . Since the specific final state  $|\Psi_2\rangle$  is not relevant for a general detection event, it is reasonable to sum over all possible final states. Additionally, in the general case, the initial state may be a mixture of states rather than a pure state and consequently the corresponding density operator as a sum over initial states shall be used

$$I(\mathbf{r}, t) = \sum_{\Psi_1, \Psi_2} h_{\Psi_1} \langle \Psi_1 | \tilde{\mathbf{E}}^-(\mathbf{r}, t) | \Psi_2 \rangle \langle \Psi_2 | \tilde{\mathbf{E}}^+(\mathbf{r}, t) | \Psi_1 \rangle = \text{Tr} \left( \rho_{\Psi_1} \tilde{\mathbf{E}}^-(\mathbf{r}, t) \tilde{\mathbf{E}}^+(\mathbf{r}, t) \right) \quad , \quad (2.34)$$

with the intensity  $I(\mathbf{r}, t)$  of the electromagnetic field and the probabilities of the initial mixture of states  $h_{\Psi_1}$ . The final expression in Eqn. (2.34) can be identified as a first order correlation function  $G^{(1)}(\mathbf{r}_1, t_1; \mathbf{r}_2, t_2) = \text{Tr} \left( \rho \tilde{\mathbf{E}}^-(\mathbf{r}_1, t_1) \tilde{\mathbf{E}}^+(\mathbf{r}_2, t_2) \right)$  that deals with the amplitude correlation. In its normalized form it can be used to determine the fringe contrast of two interfering fields<sup>[110]</sup>. While a general, normally ordered  $n$ -th order correlation function can be defined, the second order correlation function is of higher interest in the context of light-matter interaction. The intensity correlations between two space time points separated by the time difference  $\tau$  are described by  $G^{(2)}(\tau) = \text{Tr} \left( \rho \tilde{\mathbf{E}}^-(\mathbf{r}, t) \tilde{\mathbf{E}}^-(\mathbf{r}, t + \tau) \tilde{\mathbf{E}}^+(\mathbf{r}, t + \tau) \tilde{\mathbf{E}}^+(\mathbf{r}, t) \right)$ . Now, the normalized form for a single mode quantized field can be expressed through the harmonic oscillator operators and finally for a number state  $|n\rangle$  follows<sup>[112]</sup>:

$$g^{(2)}(\tau) = \frac{G^{(2)}(\tau)}{|G^{(1)}(0)|^2} = \frac{\langle a^{\dagger} a^{\dagger} a a \rangle}{\langle a^{\dagger} a \rangle^2} = \frac{\langle n^2 \rangle - \langle n \rangle}{\langle n \rangle^2} = 1 + \frac{(\Delta n)^2 - \langle n \rangle}{\langle n \rangle^2} \quad , \quad (2.35)$$

with the photon number variance  $(\Delta n)^2$ . In case of a number state  $|n\rangle$  the photon number variance vanishes and Eqn. (2.35) simplifies to  $g^{(2)}(\tau) = 1 - \frac{1}{n}$ . With the maximum of 1 of the normalized second order correlation for number states, the simplified form of Eqn. (2.35) elucidates that intensity correlation measurements of a radiation mode populated by a single photon yield 0. In this for quantum information purposes desirable situation, the photons can be assumed as separated or anti-bunched<sup>[113]</sup>. The value for the correlation increases with the number of photons in the measured mode and finally tends towards one for large numbers of photons. As quantum optics tends towards classical optics in the limit of many photons, a measurement of intensity fluctuation can determine in this way the potential quantum nature of the radiation field.

### **Concluding Remarks**

To summarize, in the first quantum physical part of the theoretical framework the quantum optical means necessary for quantized light-matter interaction are identified: With the electromagnetic field itself quantized the creation and annihilation of photons due to transitions between electronic states in the quantum systems can be described in so-called number states. Additionally, entanglement in number states and a method to measure the quantum nature of a number state via correlation functions are introduced.

---

## 2.5 Cavity Quantum Electrodynamics

### Electric Dipole Approximation

At this point, with quantized electromagnetic modes at hand, the quantized matter and the energy exchange between the two finally enter the considerations. The treatment shall begin with the interaction of an atom, or more general a quantum system, with a classical field. The quantum system shall be characterized by a single electronic transition between two states to determine the most fundamental aspects of this interaction. Here, it is common practice to invoke the principle of minimum coupling where the canonical momentum takes the form  $\mathbf{p} = m\dot{\mathbf{r}} + e\tilde{\mathbf{A}}(\mathbf{r}, t)$ . The corresponding Hamiltonian of semi-classical light-matter interaction takes the form<sup>[114]</sup>

$$\mathcal{H}_{\min} = \frac{1}{2m} \left[ \mathbf{p} - e\tilde{\mathbf{A}}(\mathbf{r}, t) \right]^2 + e\tilde{\Phi}(\mathbf{r}, t) + V(\mathbf{r}) \quad .$$

Besides the electromagnetic potentials  $\tilde{\mathbf{A}}(\mathbf{r}, t)$  and  $\tilde{\Phi}(\mathbf{r}, t)$ ,  $V(\mathbf{r})$  is supposed to model the binding of the electron to some central point. Imposing local gauge invariance, the physical predictions can not be affected by a gauge transformation, hence a modification of the Schrödinger equation is in order<sup>[115]</sup>

$$i\hbar\partial_t\Psi(\mathbf{r}, t) = \left( -\frac{\hbar^2}{2m} \left[ \nabla - i\frac{e}{\hbar}\tilde{\mathbf{A}}(\mathbf{r}_0, t) \right]^2 + V(\Delta\mathbf{r}) \right) \Psi(\mathbf{r}, t) \quad . \quad (2.36)$$

Here, radiation gauge with  $\nabla \cdot \tilde{\mathbf{A}}(\mathbf{r}, t) = 0$  and  $\tilde{\Phi}(\mathbf{r}, t) = 0$  has been applied again. Additionally, for an incident plane wave on the quantum system, the corresponding potential can be approximated by

$$\tilde{\mathbf{A}}(\mathbf{r}_0 + \Delta\mathbf{r}, t) = \tilde{\mathbf{A}}(t) e^{i\mathbf{k}\cdot\mathbf{r}_0} (1 + i\mathbf{k} \cdot \Delta\mathbf{r} + \dots) \approx \tilde{\mathbf{A}}(t) e^{i\mathbf{k}\cdot\mathbf{r}_0} = \tilde{\mathbf{A}}(\mathbf{r}_0, t) \quad .$$

Where the spatial coordinate is replaced by the location of the central point and the displacement from the central point  $\mathbf{r} = \mathbf{r}_0 + \Delta\mathbf{r}$ . This is naturally a valid approximation for  $\mathbf{k} \cdot \Delta\mathbf{r} \ll 1$ , which is, assuming displacement in atomic dimensions, well met for optical frequencies and equivalent to a quasi-static field experienced by the quantum system. But unlike for the quasi-static treatment of the optical nanoantenna, this does not constitute a limitation for the desired applications in light-matter interaction. Applying the gauge transformation  $\bar{\Psi}(\mathbf{r}, t) = \exp\{i\frac{e}{\hbar}\mathbf{r} \cdot \tilde{\mathbf{A}}(\mathbf{r}_0, t)\} \Psi(\mathbf{r}, t)$

and inserting  $\bar{\Psi}(\mathbf{r}, t)$  into the Schrödinger equation (2.36) yields

$$i\hbar\partial_t\bar{\Psi}(\mathbf{r}, t) = \left[ \frac{p^2}{2m} + V(\Delta\mathbf{r}) + e\mathbf{r} \cdot \partial_t\tilde{\mathbf{A}}(\mathbf{r}_0, t) \right] \bar{\Psi}(\mathbf{r}, t) = \left[ \mathcal{H}_{\text{elc}} + e\mathbf{r} \cdot \partial_t\tilde{\mathbf{A}}(\mathbf{r}_0, t) \right] \bar{\Psi}(\mathbf{r}, t) .$$

In this formulation, the unperturbed dynamics of the electron in the central potential  $V(\Delta\mathbf{r})$  can be identified, governed by  $\mathcal{H}_{\text{elc}}$ . Replacing the vector potential by the electric field, the term responsible for the interaction between the quantum system and the field takes the form:  $\mathcal{H}_{\text{int}} = e\mathbf{r} \cdot \partial_t\tilde{\mathbf{A}}(\mathbf{r}_0, t) = -e\mathbf{r} \cdot \tilde{\mathbf{E}}(\mathbf{r}_0, t)$ . Now,  $\mathbf{d} = e\mathbf{r}$  can be identified as a dipole moment characteristic for the quantum system under investigation, hence the name dipole approximation for this simplification of the interaction between field and quantum system. Consequently, electronic transitions in a quantum system can be approximated by an electric dipole when interacting with the free radiation field (see Fig. 2.13). Including higher orders in  $\mathbf{k} \cdot \Delta\mathbf{r}$  would lead to the emergence of magnetic dipole and electric quadrupole interactions<sup>[116]</sup>, and consequently the restriction to an electric dipole is not a fundamental limitation of the general formalism.

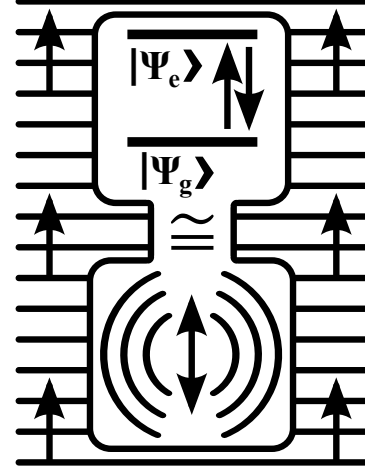


Figure 2.13: A two-level system in an external field is equivalent to an electric point dipole in lowest order approximation.

### Jaynes-Cummings Model and Master Equation

This treatment of the interaction between quantized matter and a classical field is the first connection between the two main constituents of the theoretical framework: the classical and the quantum physical description. From the form of the final interaction Hamiltonian follows that the quantum systems can be classically modeled as electric point dipoles in this lowest order approximation.

Advancing from the semi-classical light-matter interaction, finally the interaction between quantized matter and quantized electromagnetic radiation shall be modeled. Compartmentalizing the problem in three parts:  $\mathcal{H} = \mathcal{H}_{\text{qus}} + \mathcal{H}_{\text{fld}} + \mathcal{H}_{\text{int}}$ , namely the bare quantum system given by  $\mathcal{H}_{\text{qus}}$ , the radiation field by  $\mathcal{H}_{\text{fld}}$ , and the interaction between the two by  $\mathcal{H}_{\text{int}}$ , the bare quantum system shall be treated first. Considering photonic emission and absorption events involving photons that constitute different transitions between eigenstates  $|\Psi_n\rangle$  of the quantum system, the characteristic eigenvalue equation of the quantum system reads  $\mathcal{H}_{\text{qus}}|\Psi_n\rangle = \mathcal{E}_n|\Psi_n\rangle$ .

Using the orthonormality of the eigenstates  $\langle \Psi_u | \mathcal{H}_{\text{qus}} | \Psi_v \rangle = \delta_{uv} \mathcal{E}_u$ , the corresponding Hamiltonian can be reformulated

$$\mathcal{H}_{\text{qus}} = \sum_{u,v} |\Psi_u\rangle \langle \Psi_u| \mathcal{H}_{\text{qus}} |\Psi_v\rangle \langle \Psi_v| = \sum_u \mathcal{E}_u |\Psi_u\rangle \langle \Psi_u| \quad .$$

Furthermore, to initially grasp the fundamental aspects of quantized light-matter interaction, the quantum system shall be reduced to a two-level system with the ground state  $|\Psi_g\rangle$  and the excited state  $|\Psi_e\rangle$ . Neglecting constant energy terms in the Hamiltonian formulation and according to the closure theorem follows<sup>[112]</sup>

$$\mathcal{H}_{\text{qus}} = \frac{1}{2} (\mathcal{E}_e - \mathcal{E}_g) (|\Psi_e\rangle \langle \Psi_e| - |\Psi_g\rangle \langle \Psi_g|) = \frac{1}{2} \hbar \omega_{\text{eg}} (|\Psi_e\rangle \langle \Psi_e| - |\Psi_g\rangle \langle \Psi_g|) \quad .$$

Here, the transition energy  $\hbar \omega_{\text{eg}}$  necessary to facilitate the transition between  $|\Psi_g\rangle$  and  $|\Psi_e\rangle$  has been introduced. In the next step, the quantized field involved in the light-matter interaction shall be considered. For this purpose it is expedient to recapitulate the preceding parts of the quantum physical framework. With the quantized free field radiation in Eqn. (2.32) and following the notion of initially modeling only the essentials, the discrete set of available field modes shall be reduced to solely one mode providing photons of the required transition energy  $\hbar \omega_{\text{eg}}$  with the Hamiltonian  $\mathcal{H}_{\text{fld}} = \hbar \omega_{\text{eg}} a^\dagger a$ . The last part remaining is the actual energy exchange of the interaction itself between photons and the two-level system  $\mathcal{H}_{\text{int}}$ . The electric dipole approximation that emerged from the semi-classical treatment  $\mathcal{H}_{\text{int}} = -e \mathbf{r} \cdot \tilde{\mathbf{E}}(\mathbf{r}_0, t)$  shall be the starting point of the fully quantized treatment<sup>[115]</sup>. In the context of a two-level system transition, the corresponding transition dipole moment  $\mathbf{d}_{uv} = e \langle \Psi_u | \mathbf{r} | \Psi_v \rangle$  can be introduced via  $e \mathbf{r} = \sum_{u,v} e |\Psi_u\rangle \langle \Psi_u| \mathbf{r} | \Psi_v\rangle \langle \Psi_v| = \sum_{u,v} \mathbf{d}_{uv} |\Psi_u\rangle \langle \Psi_v|$ . Since the interaction involves photonic creation or annihilation, the field description according to Eqn. (2.33) is beneficial and the local single mode electric field for a quantum system at the origin amounts to  $\mathbf{E}_{\text{pho}}(\mathbf{r}_0) (a + a^\dagger)$ , with the single excitation field amplitude  $\mathbf{E}_{\text{pho}}(\mathbf{r}_0)$ . Combining the local field with the dipole transition, using  $\mathbf{d}_{\text{ge}} = \mathbf{d}_{\text{eg}}$ , and neglecting vanishing  $\mathbf{d}_{\text{gg}}$  and  $\mathbf{d}_{\text{ee}}$  due to assumed centrosymmetry yields

$$\begin{aligned} \mathcal{H}_{\text{int}} &= -e \mathbf{r} \cdot \tilde{\mathbf{E}}(\mathbf{r}_0, t) = -\mathbf{d}_{\text{ge}} \cdot \mathbf{E}_{\text{pho}}(\mathbf{r}_0) (|\Psi_e\rangle \langle \Psi_g| + |\Psi_g\rangle \langle \Psi_e|) (a + a^\dagger) \\ &= \hbar g (|\Psi_e\rangle \langle \Psi_g| a + a^\dagger |\Psi_g\rangle \langle \Psi_e|) \quad . \end{aligned}$$

Here, the light-matter coupling rate  $g = -\hbar^{-1} \mathbf{d}_{\text{ge}} \cdot \mathbf{E}_{\text{pho}}(\mathbf{r}_0)$  has been introduced. Upon inspection of the terms emerging from  $(|\Psi_e\rangle \langle \Psi_g| + |\Psi_g\rangle \langle \Psi_e|) (a + a^\dagger)$ , those involving the transition from  $|\Psi_g\rangle$  to  $|\Psi_e\rangle$  and the simultaneous creation of a field

mode photon, as well as the transition from  $|\Psi_e\rangle$  to  $|\Psi_g\rangle$  combined with the annihilation of a photon have been neglected, as they violate energy conservation in the restricted model of a single field mode interacting with a single two-level system. The energy balance features either a surplus or a shortage of  $2\hbar\omega_{eg}$  in the case of the energy conservation violation and the resulting omission of the corresponding terms is called rotating-wave approximation. Implementing the atomic state transition operators associated with the Pauli matrices  $\sigma_{ge} = |\Psi_g\rangle\langle\Psi_e|$ ,  $\sigma_{eg} = |\Psi_e\rangle\langle\Psi_g|$ , and  $\sigma_z = |\Psi_e\rangle\langle\Psi_e| - |\Psi_g\rangle\langle\Psi_g|$ , the total Hamiltonian for the interaction of a single two-level system with a single electromagnetic field mode reads

$$\mathcal{H} = \mathcal{H}_{\text{qus}} + \mathcal{H}_{\text{fld}} + \mathcal{H}_{\text{int}} = \frac{1}{2}\hbar\omega_{eg}\sigma_z + \hbar\omega_{eg}a^\dagger a + \hbar g (\sigma_{eg}a + a^\dagger\sigma_{ge}) \quad , \quad (2.37)$$

and the corresponding interaction is depicted in Fig. 2.14. This description of fundamental quantized-light matter interaction is known as the Jaynes-Cummings model<sup>[117]</sup>. It is an essential part of cavity quantum electrodynamics (cavity QED)<sup>[118]</sup> and shall be the foundation for the quantized light-matter interaction as it will be theoretically described in the following. Recapitulating,

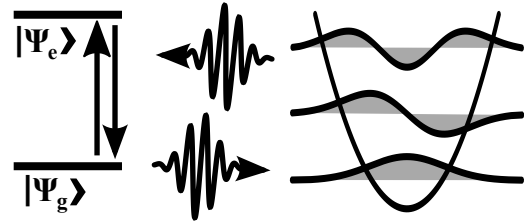


Figure 2.14: Constituting components of the Jaynes-Cummings model: A two-level system photonicly couples to a single cavity mode field in form of a harmonic oscillator.

the two constituting ingredients for the optical Jaynes-Cummings model are a quantum system that can be approximated by a two-level system in an optical frequency range and a single electromagnetic field mode in the same optical frequency range. There are plenty of suitable approximate two-level systems available in form of Rydberg atoms<sup>[119,120]</sup>, quantum dots<sup>[121,122]</sup>, or nitrogen-vacancy centers in diamond<sup>[123,124]</sup>, and since the transition is the only property relevant for the model itself, the broad variety of candidates can be fully exploited. The control over the electromagnetic field modes on the other hand is realized through a cavity. The functionality of a cavity in selecting field modes can be illuminated most plausibly by briefly referring to a Fabry-Perot resonator<sup>[125]</sup>. Assuming an evacuated chamber enclosed by perfect mirrors, the mode selection ability follows immediately: With the mirrors setting boundary conditions that any mode inside must meet, only modes with a wavelength equal to twice the distance between the mirrors or smaller by integer multiples of half of the wavelength can satisfy such a condition. Hence, the lowest frequency mode inside the cavity is the half-wavelength mode and often referred to as the fundamental mode. With increasing frequency the

---

mode density per spectral unit range rises as well. Consequently, such a simple cavity provides a single mode electromagnetic field for a sizable frequency range if the fundamental mode is used.

At this point, optical nanoantennas enter the treatment of quantized light-matter interaction, as they can be considered as optical cavities as well. The actual resonance mechanism might be more elaborate, involving surface waves confined by the geometry of the nanoantenna, but mode selection can also be realized with optical nanoantennas. One additional aspect constitutes them the prime candidate to facilitate quantized light-matter interaction: the proportionalities of the actual light-matter coupling rate:  $g = -\hbar^{-1} \mathbf{d}_{ge} \cdot \mathbf{E}_{\text{pho}}(\mathbf{r}_0)$ . With the transition dipole moment  $\mathbf{d}_{ge}$  being both characteristic and fixed for the quantum system, the direct proportionality of the coupling rate to the local electromagnetic field amplitude is the aspect that can be exploited to manipulate the light-matter interaction. This is also the mechanism due to whom quantized light-matter interaction benefits most from the unprecedented field localization of surface plasmon resonances in general and localized surface plasmon resonances in particular.

Closer inspection of the Jaynes-Cummings model reveals on the one hand the desired quantized light-matter interaction, but on the other hand completely reversible dynamics between the field mode and the two-level system. In other words, with such a closed system there is no way to observe any effects resulting from the manipulation of the light-matter interaction, because the photons within the cavity are only coupled to the two-level system and not to the far field. But with the observable far field incorporated into the model, the density matrix operator  $\rho(t) = \sum_j w_j |\Psi_j\rangle \langle \Psi_j|$  with the individual weights  $w_j$  has to be employed to handle the dynamics. Using the Schrödinger equation to determine the evolution of the single states  $\partial_t |\Psi_j\rangle = -\frac{i}{\hbar} \mathcal{H} |\Psi_j\rangle$ , the evolution of the density matrix yields

$$\partial_t \rho(t) = \sum_j w_j [(\partial_t |\Psi_j\rangle) \langle \Psi_j| + |\Psi_j\rangle (\partial_t \langle \Psi_j|)] = -\frac{i}{\hbar} [\mathcal{H}, \rho(t)] \quad . \quad (2.38)$$

To generate an open quantum system, the closed system of the Jaynes-Cummings model as a subsystem is combined with another subsystem representing the environment. In this context, the Hamiltonian dynamics describe the so-called reduced system while the environment is referred to as the reservoir. The theory of open quantum systems itself is again an extensive but fascinating topic, where, for the quantized light-matter interaction, only selected aspects are relevant. The coupled dynamics of reduced system and reservoir are again modeled by a composite Hamiltonian consisting of parts governing the pure components and one part

modeling the interaction. By assuming no influence of the reduced system on the reservoir, due to weak interaction in form of the Born approximation, the evolution can be limited to that of the reduced system. Furthermore, only considering short-lived memory effects is called Markov approximation and can be well justified at optical frequencies due to the orders of magnitude difference of optical frequencies and the inverse of optical excitation lifetimes. Finally, in a last approximation, the so called secular approximation, fast oscillating terms are averaged out and the Liouville equation (2.38) can be transformed into a master equation in Lindblad form<sup>[126]</sup>

$$\begin{aligned}\partial_t \rho(t) &= -\frac{i}{\hbar} [\mathcal{H}, \rho(t)] + \sum_j \Gamma_j \mathcal{L}_j(\rho(t), \mathcal{O}_j) \\ &= -\frac{i}{\hbar} [\mathcal{H}, \rho(t)] + \sum_j \Gamma_j \left[ \mathcal{O}_j \rho(t) \mathcal{O}_j^\dagger - \frac{1}{2} \left( \mathcal{O}_j^\dagger \mathcal{O}_j \rho(t) + \rho(t) \mathcal{O}_j^\dagger \mathcal{O}_j \right) \right].\end{aligned}\quad (2.39)$$

Here, the sum of Lindblad superoperators  $\mathcal{L}_j(\rho(t), \mathcal{O}_j)$  with the corresponding rates  $\Gamma_j$  can be considered a dissipator. While the Hamiltonian still models reversible interaction within the reduced system, consisting of cavity and two-level system in the basic scenario of quantized light-matter interaction, the superoperators acting on general operators  $\mathcal{O}_j$  now model the irreversible interaction between the reduced system and the reservoir, which in case of the light-matter interaction scenario are the quantized electromagnetic radiation modes of free space. In this formalism, the results of the reduced system emitting into free space radiation can be modeled as an irreversible process and hence the complete dynamical description of the infinitely many free space modes can be avoided. Such a master equation in Lindblad form can be numerically represented and solved<sup>[127]</sup> with non-commercial software<sup>[128]</sup>.

### Spontaneous Emission As Per Weisskopf-Wigner

Even though the quantized light-matter interaction has been modeled with a Jaynes-Cummings model and it has been coupled to free space radiation through a master equation formulation, one crucial element is still missing. While for significant coupling between the two-level system and the cavity, the cavity already emits into the far field, the emission of the two-level system itself is a process that needs to be incorporated. Analogous to the previous treatment of the coupling between a two-level system and a single cavity mode, now the coupling of the same two-level system to many modes of free space radiation leads in the rotating-wave approxi-

mation to

$$\mathcal{H} = \frac{1}{2}\hbar\omega_{eg}\sigma_z + \sum_j \hbar\omega_j a_j^\dagger a_j + \sum_j \hbar g_j \left( \sigma_{eg} a_j + a_j^\dagger \sigma_{ge} \right) .$$

Limiting the consideration to a single photonic excitation, and introducing the product state basis with one state  $|\Psi_e\rangle \otimes |0\rangle = |\Psi_e, 0\rangle$  for the excited two-level system and all radiation modes in the vacuum state, and many states  $|\Psi_g\rangle \otimes |1_j\rangle = |\Psi_g, 1_j\rangle$  for the two-level system in the ground state with one radiation mode containing the single excitation. Assuming harmonic time dependency of the product states, the Schrödinger equation gives<sup>[129]</sup>

$$\partial_t \mathcal{C}_j^g(t) = -i g_j e^{i(\omega_j - \omega_{eg})t} \mathcal{C}^e(t) \quad \text{and} \quad \partial_t \mathcal{C}^e(t) = -i \sum_j g_j e^{-i(\omega_j - \omega_{eg})t} \mathcal{C}_j^g(t)$$

for the expansion coefficients of the product state basis. A formal integration yields  $\partial_t \mathcal{C}^e(t) = -\sum_j |g_j| \int_0^t dt' e^{-i(\omega_j - \omega_{eg})(t-t')} \mathcal{C}^e(t')$ . Transitioning from discrete modes to a mode continuum and considering different angles between the local mode field and the transition dipole moment that determine the coupling rate  $g_j$ , the amplitude of the excited state obeys

$$\partial_t \mathcal{C}^e(t) = -\frac{\gamma}{2} \mathcal{C}^e(t) \quad \text{equivalent to} \quad \mathcal{C}^e(t) = e^{-0.5\gamma t} \mathcal{C}^e(0) ,$$

utilizing a Laplace transform. The excited two-level system evidently decays with a rate

$$\gamma_{ge}^{\text{spo}} = \frac{\omega_{ge}^3 |\mathbf{d}_{ge}|^2}{3\pi\epsilon_0 \hbar c^3} \quad (2.40)$$

when coupled to radiation. This is the Weisskopf-Wigner theory of spontaneous emission. Thusly, the excited two-level system irreversibly decays when coupled to the mode continuum of free space. While in the Jaynes-Cummings model, with one mode coupled to the two-level system, a revival of the excited state of the two-level system occurs. This revival is still possible with a finite probability for each individual mode of the free-space field, but destructive interference between different modes causes the irreversible decay when summing over all modes.

## Concluding Remarks

To summarize, the second half of the quantum physical part of the theoretical framework initially introduced the semi-classical coupling between radiation and a two-level system. Here, the dipole approximation embodies the first connection between classical and quantized description. The actual quantized light-matter in-

interaction is described in form of a Jaynes-Cummings model, coupling a single field mode to a two-level system. To combine the Jaynes-Cummings model and the radiation field, a master equation formulation in Lindblad form is employed. In the last part, the Weisskopf-Wigner theory of spontaneous emission gives the rate for the emission of a pure two-level system in dipole approximation.

Together with the elements of quantum optics, the influence of incident radiation, classical or not, on the light-matter interaction between cavity mode and electronic transition, in an open quantum system, can be described. Including all necessary dissipation mechanisms, the subsequent interaction dynamics as well as the state of radiation emitted back into the far field follow also from the model.

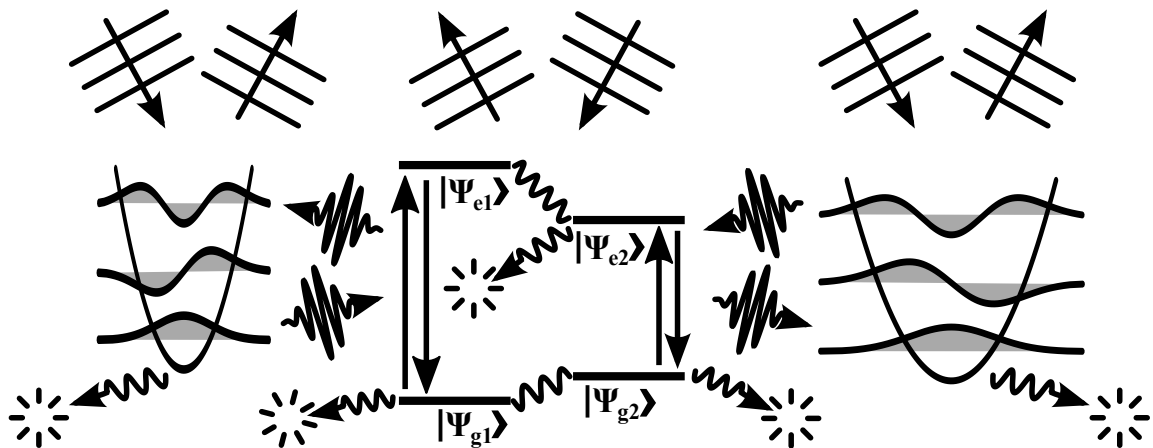


Figure 2.15: The quantum physical considerations enable the coupling of transitions in a quantum system to individual cavity modes and to both far-field radiation and dissipation channels.

So far, the description of the cavity in the light-matter interaction model has not been very specific. Limited to one cavity mode of photons that provide the transition energy of the quantum system, this is the way any optical cavity is modeled. Recalling the direct proportionality of the light-matter coupling rate  $g$  to the local field, it becomes evident that cavities featuring surface plasmon polaritons promise particularly high coupling rates.

But these nanoscale metal structures are also characterized by a rather low Q factor<sup>[130]</sup>, when compared to other optical cavities. Distinguishing between radiative and non-radiative losses, a low Q factor, i.e. high losses, results in bright radiation emitted from the cavity modes. Even though this emission rate rivals the light-matter coupling rate in the interaction dynamics, effectively reducing the benefits of plasmonic cavities, fast quantum information applications require significant emission rates, providing the desired information in form of photonic properties

---

or statistics. Consequently, the interaction dynamics of specifically low-Q cavities have been investigated<sup>[131–133]</sup>, aiming to optimize the trade-off between the brightness of the emission and the rate of the light-matter coupling.

But inextricably linked with these high radiative losses are also high non-radiative losses due to the inevitable Ohmic losses of metal at optical frequencies<sup>[34]</sup>. These absorption losses have to enter any general light-matter interaction consideration involving plasmonic cavities<sup>[134]</sup> and any proposed functionality must overcome this dissipation. This will also be a relevant aspect for the devices and configurations discussed in the application chapter. Since the absorption losses are inherently connected with plasmonic resonances, the topic of dielectric nanoantennas<sup>[135]</sup> has emerged, promoting the benefits of low losses<sup>[136]</sup> over the surface plasmonic field localization. However, facilitating and manipulating the interaction of single photons with single atoms, surface plasmon polaritons remain the most promising candidate. Besides attempts to optimize the fabrication and reduce the losses<sup>[137]</sup>, ideally, the absorption losses can constructively contribute to applications like photodetection<sup>[138]</sup> and solar photocatalysis<sup>[139]</sup>.

In the completed theoretical framework, the two chief constituents as classical and quantum physical modeling have taken shape. Before any specific application can be described or benchmarked, these two parts must be combined consistently, which shall be detailed in the following chapter.

## 3 Semi-Classical Model and Parameters

With the theoretical framework established, the two disjunct parts, the classical and the quantum physical description, need to be combined to provide a coherent modeling. The starting point for this merger is the cavity QED model, as it describes the desired quantized light-matter interaction.

### 3.1 Cavity QED Interaction Model

The Jaynes-Cummings model is at the core of cavity QED and likewise the essential element of the quantized light-matter interaction as it is modeled usually and in the following<sup>[119]</sup>. In this context, various aspects of the Jaynes-Cummings model have been investigated with respect to their influence on the light-matter interaction dynamics. Firstly, recapitulating two central approximations are applied to eventually yield the interaction of a single electronic transition and a single cavity mode: the electric dipole and the rotating-wave approximation.

*i.1* While the electric dipole approximation rather limits the transitions that can be incorporated, as the corresponding dipole moment determines the coupling rate between light and matter, transitions with vanishing dipole moments, such as magnetic dipole<sup>[140–142]</sup> or electric quadrupole transitions<sup>[143,144]</sup>, can be included by expanding the treatment to higher order terms<sup>[116]</sup>.

*i.2* The rotating-wave approximation on the other hand neglects counter-rotating contributions, whose interference with the present terms affects phase dependencies<sup>[145]</sup>.

With the approximations roughly classified in their impact on the dynamics of the model, the fundamental single mode-single transition interaction can be expanded or augmented in different ways. This widening of the basic Jaynes-Cummings model is especially interesting from an application point of view, as more complex behavior can be included and hence potentially more functionality implemented. The first set of mentioned expansions focusses of the transitions or quantum systems involved:

---

**ii.1** The inclusion of many identical electronic transitions in form of many quantum systems leads to interesting behavior. The corresponding Tavis-Cummings model<sup>[146]</sup> couples a single field mode to an ensemble of two-level quantum systems. In the most prominent application, the so-called Dicke model<sup>[147]</sup>, the collective of spin  $1/2$  quantum systems form a coupled state with a collective spin  $S$  and hence a collective quantum system with  $2S + 1$  equidistant energy levels can be described<sup>[148,149]</sup>.

**ii.2** Another relevant topic are three-level quantum systems<sup>[150,151]</sup>. They are categorized in ladder (three states with increasing energy),  $V$  (two higher energy states connected by negligible transition and shared lower energy state), or  $\Lambda$  (two lower energy states connected by negligible transition and shared higher energy state) configurations. They are particularly interesting, as they behave like a two-photon process in a two-level system for strong detuning between the single mode field and the intermediate state<sup>[152]</sup>.

The other set of expansions focuses on the photonic part of the interaction, meaning either the photons themselves or the photonic modes involved:

**iii.1** Firstly, the interaction between an electronic transition and a single field mode can be generalized such that general multi-photon interactions are considered<sup>[153,154]</sup>. Two-photon transitions constitute the simplest of these general multi-photon processes<sup>[155,156]</sup>. While such multi-photon transitions enjoy fundamental theoretical interest, the stark shifts of energy levels proportional to the photon number involved<sup>[157]</sup> need to be taken into account.

**iii.2** Lastly, the expansion of the Jaynes-Cummings model to include multiple cavity modes follows naturally, especially if the full potential of involved three- or generally many-level quantum systems<sup>[158]</sup> shall be explored. Obviously, including multiple field modes also holds potential when considering many quantum systems in a cavity<sup>[159]</sup> or just a single two-level system<sup>[160,161]</sup>. For two field modes interacting with a two-level system fluorescence quenching can be predicted<sup>[162]</sup>, while two modes coupled to a three-level system can yield correlations between the initially uncorrelated modes<sup>[163]</sup>.

From this plethora of expansions of the initial Jaynes-Cummings model, in the following the interaction between two distinct cavity modes and either a single two-level system or a single three-level system in  $\Lambda$  configuration with the states  $|\Psi_e\rangle$ ,  $|\Psi_1\rangle$ , and  $|\Psi_2\rangle$  shall be considered. This constitutes no limitation of the general theoretical model, as all of the above mentioned expansions can be implemented

in the Hamiltonian formulation, but is rather a conscious decision to realize very specific applications that will be described in the later part of the thesis. Consequently, expanding the Jaynes-Cummings Hamiltonian for light-matter interaction in Eq. (2.37) for the applications in the following yields:

$$\mathcal{H}_{\text{lmi}} = \sum_{\xi=1,2} \frac{1}{2} \hbar v_{e\xi} \sigma_{\xi,z} + \sum_{\xi=1,2} \hbar \omega_{\xi} a_{\xi}^{\dagger} a_{\xi} + \sum_{\xi=1,2} \hbar g_{\xi} \left( \sigma_{e\xi} a_{\xi} + a_{\xi}^{\dagger} \sigma_{\xi e} \right) , \quad (3.1)$$

with the operators  $\sigma_{\xi e} = |\Psi_{\xi}\rangle \langle \Psi_e|$  and  $\sigma_{\xi,z} = \sigma_{ee} - \sigma_{\xi\xi}$  with  $\xi = 1, 2$ . To accurately model the reversible energy exchange between the cavity field modes and electronic transitions involved the transition frequencies  $v_{e\xi}$ , the cavity mode frequencies  $\omega_{\xi}$  and the light-matter coupling rate  $g_{\xi}$  need to be determined and inserted into the model. But before addressing each of these parameters individually, the cavity QED model must be completed by considering an open system with the density matrix  $\rho_{\text{lmi}}(t)$  coupled to different decay channels. The steady state of the evolution is found by solving the stationary corresponding master equation in Lindblad form:

$$0 = \partial_t \rho_{\text{lmi}}(t) = -\frac{i}{\hbar} [\mathcal{H}_{\text{lmi}}, \rho_{\text{lmi}}(t)] + \sum_j \Gamma_j \mathcal{L}_j(\rho_{\text{lmi}}(t), \mathcal{O}_j) . \quad (3.2)$$

The different irreversible decay processes are represented by different superoperators  $\mathcal{L}_j(\rho_{\text{lmi}}(t), \mathcal{O}_j) = \mathcal{O}_j \rho_{\text{lmi}}(t) \mathcal{O}_j^{\dagger} - \frac{1}{2} \left( \mathcal{O}_j^{\dagger} \mathcal{O}_j \rho_{\text{lmi}}(t) + \rho_{\text{lmi}}(t) \mathcal{O}_j^{\dagger} \mathcal{O}_j \right)$ , and their associated decay rates  $\Gamma_j$ . The principal examples for such a process are obviously the losses of the cavity itself. Briefly returning to the picture of a Fabry-Perot resonator enclosed by two mirrors, the imperfect reflectivity of one of these mirrors results in emission into free space, at a rate  $\Gamma^{\text{rad}}$ , that can be measured in the far field and hence motivated the introduction of the open quantum system ansatz. Additionally, this radiative decay of the cavity can be extended to include a non-radiative cavity decay at a rate  $\Gamma^{\text{non}}$  as well. This does not require the introduction of a new dissipator, but rather a general cavity decay channel at a rate  $\Gamma^{\text{tot}} = \Gamma^{\text{rad}} + \Gamma^{\text{non}}$  combined with a radiative efficiency  $\eta = \Gamma^{\text{rad}}/\Gamma^{\text{tot}}$  of the cavity. Here, the Lindblad operator takes the form<sup>[164]</sup>

$$\mathcal{L}_{\xi}^{\text{cav}}(\rho_{\text{lmi}}(t), a_{\xi}) = a_{\xi} \rho_{\text{lmi}}(t) a_{\xi}^{\dagger} - \frac{1}{2} \left( a_{\xi}^{\dagger} a_{\xi} \rho_{\text{lmi}}(t) + \rho_{\text{lmi}}(t) a_{\xi}^{\dagger} a_{\xi} \right) , \quad (3.3)$$

as every mode supported by the cavity is modeled with its own decay channel. Another obvious decay mechanism worth incorporating is the emission of the quantum system into modes not supported by the cavity. This interaction with the infinite set of free field modes is treated in the epitome of the Weisskopf-Wigner theory in

---

the theoretical framework yielding the decay rate  $\gamma_{ge}^{\text{spo}}$  (see Eqn. (2.40)) for a two-level system or each transition in a general quantum system respectively. The associated Lindblad operator reads<sup>[164]</sup>

$$\mathcal{L}_{\xi e}^{\text{spo}}(\rho_{\text{lmi}}(t), \sigma_{\xi e}) = \sigma_{\xi e} \rho_{\text{lmi}}(t) \sigma_{e\xi} - \frac{1}{2} (\sigma_{\xi e} \sigma_{e\xi} \rho_{\text{lmi}}(t) + \rho_{\text{lmi}}(t) \sigma_{\xi e} \sigma_{e\xi}) \quad . \quad (3.4)$$

For the sake of completeness, a direct incoherent pumping of an electronic transition in the quantum system can be realized by interchanging  $\sigma_{\xi e}$  and  $\sigma_{e\xi}$  in Eqn. (3.4). With these two prevalent decay mechanisms incorporated, it is important to mention that the cavity decay has the more pronounced impact on the energy exchange and associated phenomena such as collapse and revival<sup>[165]</sup>. This highlights once again why optical nanoantennas, whose decay properties can be influenced through their geometrical shape, are the favorable candidate to implement any purposeful manipulation of quantized light-matter interaction.

Inserting Eqns. (3.1), (3.3), and (3.4) in Eqn. (3.2) gives the complete quantum physical dynamics that can be solved numerically, e.g. with the Python toolbox QuTiP2<sup>[128]</sup>. But for these calculated quantum dynamics to represent a specific quantized light-matter interaction scenario, with a specific quantum system and a specific optical nanoantenna as a cavity, a characteristic set of parameters, associated with the very scenario, has to be used in the calculation. The origin and numerical value of these parameters is the next step to provide a coherent description.

## 3.2 Model Parameter Genesis

With the goal to use optical nanoantennas for the quantized light-matter interaction, to benefit from their unique advantages, the cavity in the quantum model shall be realized by the metallic structure. Hence, the cavity modes, easiest to imagine as standing waves between the mirrors of a Fabry-Perot resonator<sup>[125]</sup>, are now the longitudinal standing surface charge waves associated with localized surface plasmon polaritons. How the parameters, required for the model of the quantum dynamics can be extracted from classical simulations shall be illuminated in the following.

### Quantum System Parameters

But firstly, these parameters can be grouped into parameters characteristic for the quantum system and its transitions and parameters resulting from the cavity involved. The quantum system parameters can be gathered either from experimental measurements and the corresponding literature or calculated by means such as density functional theory. The following can be identified as quantum system parameters:

- A.1** The transition frequency  $\nu_{eg}$ , which is determined by the difference in energy between the two states involved  $\mathcal{E}_e - \mathcal{E}_g = \hbar\nu_{eg}$ . Measurements<sup>[166,167]</sup> and calculations<sup>[168,169]</sup> can give the desired value. Please note that in the light-matter interaction model  $\nu$  will denote transition frequencies to clearly distinguish them from cavity mode frequencies denoted by  $\omega$ . This is motivated by a deliberate detuning between cavity modes and transition frequencies that will play an important role in two of the four applications discussed in this thesis.
- A.2** The spontaneous emission rate of the quantum system transitions into modes that are not supported by the cavity. As these emission processes can be considered as emission into free radiation modes, the Weisskopf-Wigner theory can be applied, yielding the rate  $\gamma_{ge}^{spo} = \frac{\nu_{ge}^3 |\mathbf{d}_{ge}|^2}{3\pi\epsilon_0\hbar c^3}$  from Eqn. (2.40). Consequently, to determine the spontaneous emission rate, the transition dipole moment  $\mathbf{d}_{ge}$  is required additional to the transition frequency  $\nu_{ge}$ . Similarly to  $\nu_{ge}$ ,  $\mathbf{d}_{ge}$  can be either measured<sup>[170,171]</sup> or calculated<sup>[172,173]</sup>.
- A.3** Rates of additional decay processes such as dephasing can be taken from literature as well, if the decay process needs to be included.

---

## Cavity Parameters

This leaves parameters characteristic to the cavity, in form of an optical nanoantenna, involved. These shall be calculated with the help of the classical considerations outlined at the beginning of theoretical framework. The parameters in question are:

**B.1** The resonance frequencies  $\omega_\xi$  of the modes that are supported by the cavity and that shall be utilized in the light-matter interaction.

**B.2** The coupling rate  $g_\xi$  between each cavity mode and the transitions in the quantum system.

**B.3** The cavity decay rate  $\Gamma^{\text{tot}}$  that in the following shall be considered to consist of both a radiative decay  $\Gamma^{\text{rad}}$  and a non-radiative decay  $\Gamma^{\text{non}}$  with  $\Gamma^{\text{tot}} = \Gamma^{\text{rad}} + \Gamma^{\text{non}}$ .

At this point it is important to mention that in the dipole approximation for the coupling rate the following expression can be found  $g = -\hbar^{-1} \mathbf{d}_{ge} \cdot \mathbf{E}_{\text{pho}}(\mathbf{r}_0)$ . Besides the transition dipole moment  $\mathbf{d}_{ge}$ , characteristic for the quantum system, this expression requires the local cavity mode electric field  $\mathbf{E}_{\text{pho}}(\mathbf{r}_0)$  that is equivalent to a single photonic excitation contained in this very cavity mode.

## Circumventing Mode Normalization

This single photon cavity field can be extracted from classical calculations by normalizing the electromagnetic energy contained in the field mode to the energy of a photon of the corresponding cavity resonance frequency. The electromagnetic field energy per mode can be calculated according to<sup>[40]</sup>

$$W(\omega_\xi) = \frac{1}{2} \int dV \epsilon_0 \partial_{\omega_\xi} [\omega_\xi \Re\{\epsilon(\omega_\xi)\}] |\mathbf{E}_{\text{pho}}(\mathbf{r}, \omega_\xi)|^2 + \frac{1}{2} \int dV \mu_0 |\mathbf{H}_{\text{pho}}(\mathbf{r}, \omega_\xi)|^2, \quad ,$$

following from Eqns. (2.25) and (2.26). While the aspect of cavity mode volume and the field energy contained within can be immediately addressed for dielectric cavities or optical microcavities<sup>[174–176]</sup>, the same concept of mode volume fails for optical nanoantennas, as they naturally emit radiation into the infinitely expanded far field. At the time of the work documented here, the issue of plasmonic mode volumes in terms of scattering modes of the far field, as they are used for all mentioned quantum optical purposes, has not been resolved. Consequently, an alternative way of determining the coupling rate needs to be employed.

As already mentioned in the classical part of the theoretical framework, the excitation and resonance of optical nanoantennas can be characterized by considering

the scattering of light by the metallic structure. The incident radiation can either originate from laser far field illumination in form of plane waves or from a localized source, such as an electric point dipole that represents a single quantum system transition in the dipole approximation. Since the excitation and decay of a localized plasmon resonance via incident photons or emitted photons respectively, can be treated as a plasmon polariton, the resonant behavior can be observed by monitoring the scattered energy. Using the electromagnetic field flux density in form of the time averaged Poynting vector from Eqn. (2.29), the scattered energy from within the light-matter interaction domain  $\Omega$  is accounted for by

$$W_{\text{sca}}(\omega) = \frac{1}{2} \int_{\partial\Omega} d\mathbf{A} \cdot [\Re\{\mathbf{E}_{\text{sca}}(\mathbf{r}, \omega) \times \mathbf{H}_{\text{sca}}^*(\mathbf{r}, \omega)\}] \quad . \quad (3.5)$$

Incorporating the energy conservation in the light-matter interaction domain  $\Omega$ , Ohmic losses can be identified as another channel to change the electromagnetic field energy inside. Because the currents involved can not be induced at optical frequencies, the time averaged Ohmic losses in metal can be determined by

$$W_{\text{abs}}(\omega) = \frac{1}{2} \int_{\Omega} dV [\Re\{\mathbf{E}_{\text{inc}}(\mathbf{r}, \omega) \cdot \mathbf{j}(\mathbf{r}, \omega)\}] \quad . \quad (3.6)$$

At this point the two decay channels, one radiative and the other non-radiative, of the cavity QED interaction model have been identified as the light scattering of the metallic nanoantenna and the Ohmic losses in the metal respectively. All the fields required to calculate both  $W_{\text{sca}}(\omega)$  and  $W_{\text{abs}}(\omega)$  can be extracted from a numerical simulation of the scattering of light by the optical nanoantenna. Additionally, by recording a spectrum over optical frequencies of the scattered energy  $W_{\text{sca}}(\omega)$ , the resonance frequency of the localized plasmons may already be identifiable by the scattering maximum. But to actually calculate the desired decay rates  $\Gamma^{\text{rad}}$  and  $\Gamma^{\text{non}}$  more information about the scattering of a single photon or the absorption of a single photon due to Ohmic losses are required.

### Alternative Modeling of Surface Plasmon Polaritons

Hence, to obtain both the light-matter coupling rate  $g_{\xi}$  and the decay rates  $\Gamma_{\xi}^{\text{rad}}$  and  $\Gamma_{\xi}^{\text{non}}$  for each mode  $\xi$  an alternative model is required, as the direct calculation via the single photon fields is fails. A brief investigation of the nature of the surface plasmon resonance shall resolve this problem.

Firstly, the electromagnetic fields associated with a surface plasmon deserve to be revisited. From Eqns. (2.22) and the required continuity at the interface

follows<sup>[177]</sup>

$$\mathbf{E}(\mathbf{r}, \omega) = -A_{\text{spw}} \sqrt{\frac{\mu_0}{\varepsilon_0 \varepsilon_{\alpha, \beta}}} \left( i \mathbf{e}_x + \frac{1}{\sqrt{\varepsilon_{\alpha, \beta}}} \mathbf{e}_z \right) e^{ikx} e^{-|z| \sqrt{k^2 - \frac{\omega^2}{c^2} \varepsilon_{\alpha, \beta}}}$$

for an interface normal to  $\mathbf{e}_z$  and a propagation assumed to be parallel to  $\mathbf{e}_x$ . Formally, the exponential decay proportional to the distance  $|z|$  away from the interface itself can be incorporated by only considering the field at the interface. Now, a square of side length  $l$  of the interface shall be considered with discrete,  $\frac{2\pi}{l}$ -periodic wavenumbers. In other words, with the field at the surface at hand, a canonical quantization procedure can be applied, involving the two-dimensional interface supporting the surface plasmon wave<sup>[177]</sup>. This results in discrete surface modes and ultimately complex surface mode field amplitudes revealing harmonic oscillatory behavior. Even though this result would allow for an alternative modeling of the surface plasmon polaritons, this quantization cannot be used, because these are not the surface fields relevant for the optical nanoantenna. These fields originate from the assumption of a smooth, infinite interface. These are also not the surface plasmon polaritons of interest, as these plasmon surface waves do not directly couple to propagating light below the plasma frequency (see Fig. 2.7).

An analogous quantization procedure can be performed for spherical nanoantennas<sup>[178]</sup>, since the analytical expressions for the local fields are available. But to meet the classical description and incorporate arbitrary cavity geometries, an approximative ansatz contained entirely within the established theoretical framework shall be employed.

To describe arbitrary geometrical structures, it is reasonable to return to the general considerations of phenomena involved with the surface of a metallic medium. Recalling, the one-dimensional modeling of the interface between an ionic crystal lattice with an electron gas and a potential wall, representing a passive dielectric, yields a surface state (2.21) that decays on atomic length scales. Thusly, the field localization already follows from the one-dimensional interface, independent of its form or roughness. Hence, any rough or closed surface can be decomposed into locally flat compartments. These local compartments can be considered as quasi-one-dimensional with respect to the surface state, when the standing surface charge wave is approximately constant across their spatial extent. Since the desired surface state also exists for the one-dimensional interface, the corresponding fields can be derived under the same approximation.

In the general Coulomb gauge without additional sources, the scalar potential  $\Phi(\mathbf{r})$  obeys the Laplace equation  $\Delta\Phi(\mathbf{r})$ . Accounting for the exponential decay of

the surface state with distance  $|z|$  to the interface, the corresponding scalar surface potential reads<sup>[54]</sup>

$$\Phi(\mathbf{r}) = \Phi_0 e^{i\mathbf{k}_{\text{sur}} \cdot \mathbf{r}_{\text{sur}}} e^{-\varsigma|z|} .$$

Here, the surface is oriented normal to the  $z$  axis, just as in every treatment in the theoretical framework and consequently, both  $\mathbf{k}_{\text{sur}}$  and  $\mathbf{r}_{\text{sur}}$  are locally in the  $xy$  plane. From plasma optics<sup>[49]</sup> in Eqn. (2.5) without collisions follows  $m\partial_t^2 \tilde{\mathbf{s}}(\mathbf{r}, t) = -e\tilde{\mathbf{E}}(\mathbf{r}, t)$  for the displacement  $\tilde{\mathbf{s}}(\mathbf{r}, t)$  of a free electron due to a field  $\tilde{\mathbf{E}}(\mathbf{r}, t)$ . Including a harmonic time dependence  $e^{-i\omega t}$  leads to  $e\tilde{E}(s_0) = m\omega^2 s_0$ . The field in the surface plane is proportional to the electronic displacement. Consequently, from these quasi-static considerations follows an electric field due to the displacement of the electron gas that reads as<sup>[54]</sup>

$$\tilde{\mathbf{E}}(\mathbf{r}, t) = \tilde{E}_0(\mathbf{k}_{\text{sur}}, t) \left( \frac{\mathbf{k}_{\text{sur}}}{|\mathbf{k}_{\text{sur}}|} + f(\varsigma) \right) e^{i\mathbf{k}_{\text{sur}} \cdot \mathbf{r}_{\text{sur}}} e^{-\varsigma|z|} e^{-i\omega t} .$$

Here,  $\varsigma$  is the projection of the wave vector along the  $z$  axis. Consequently, even the local fields for an one-dimensional interface generate a surface field of the general surface plasmon form<sup>[179]</sup>. With such a surface field approximated for rough and closed surfaces, the composition as a sum of local fields for discrete wave vectors follows. But focusing on energetic dynamics, including additional  $2T$ -periodic dynamics in form of  $f(t) = \sum_n f_n e^{i\frac{m\pi}{T}t}$  gives the vector potential<sup>[180]</sup>

$$\tilde{\mathbf{A}}(\mathbf{r}, t) = \sum_{\mathbf{k}_{\text{sur}}} \mathbf{A}_{\mathbf{k}_{\text{sur}}} e^{i\mathbf{k}_{\text{sur}} \cdot \mathbf{r}} e^{-\varsigma|z|} \sum_n e^{i\left(\frac{m\pi}{T} - \omega\right)t} .$$

Inspecting the change in electromagnetic field energy, according to Eqn. (2.27), the change of surface fields within a time window  $[0, T]$  can be determined via

$$W_{\text{eme}} = \int_0^T \int_{\text{sur}} dA dt \left[ \tilde{\mathbf{E}}(\mathbf{r}, t) \cdot \partial_t \tilde{\mathbf{D}}(\mathbf{r}, t) + \tilde{\mathbf{H}}(\mathbf{r}, t) \cdot \partial_t \tilde{\mathbf{B}}(\mathbf{r}, t) \right] .$$

Using the relations between the vector potential and the required fields:  $\tilde{\mathbf{E}}(\mathbf{r}, t) = -\partial_t \tilde{\mathbf{A}}(\mathbf{r}, t)$  with  $\tilde{\mathbf{D}}(\mathbf{r}, t) = \varepsilon_0 \varepsilon \left( \omega - \frac{m\pi}{T} \right) \tilde{\mathbf{E}}(\mathbf{r}, t)$ , and  $\tilde{\mathbf{H}}(\mathbf{r}, t) = \mu_0^{-1} \nabla \times \tilde{\mathbf{A}}(\mathbf{r}, t)$  with  $\tilde{\mathbf{B}}(\mathbf{r}, t) = \mu_0 \tilde{\mathbf{H}}(\mathbf{r}, t)$ , for processes that occur at frequencies much lower than optical frequencies  $1/T \ll \omega$ <sup>[180]</sup>, the total energy of the surface plasmons follows from<sup>[181]</sup>

$$W_{\text{eme}} = \sum_{\text{sur}} dA \varepsilon_0 \omega^2 f(\mathcal{S}) \left[ \mathbf{A}_{\mathbf{k}_{\text{sur}}} \mathbf{A}_{\mathbf{k}_{\text{sur}}}^* + \mathbf{A}_{\mathbf{k}_{\text{sur}}}^* \mathbf{A}_{\mathbf{k}_{\text{sur}}} \right] ,$$

with the surface  $\mathcal{S}$  involved. The behavior analogue to a harmonic oscillator immediately follows from this energy expression for the surface plasmons. Corre-

sponding operators in Eqn. (2.32) are introduced, but due to  $e^{i\mathbf{k}_{\text{sur}} \cdot \mathbf{r}}$ , these are still propagating surface modes. Standing wave modes can be constructed according to  $1/\sqrt{2} (e^{i\mathbf{k}_{\text{sur}} \cdot \mathbf{r}} + e^{-i\mathbf{k}_{\text{sur}} \cdot \mathbf{r}}) = \sqrt{2} \cos(\mathbf{k}_{\text{sur}} \cdot \mathbf{r})$  and  $1/\sqrt{2} (e^{i\mathbf{k}_{\text{sur}} \cdot \mathbf{r}} - e^{-i\mathbf{k}_{\text{sur}} \cdot \mathbf{r}}) = i\sqrt{2} \sin(\mathbf{k}_{\text{sur}} \cdot \mathbf{r})$ . Associating the complex mode amplitudes with operators according to  $A_{\mathbf{k}_{\text{sur}}} \rightarrow \bar{f}(\mathcal{S}) a_{\xi}$  and  $A_{\mathbf{k}_{\text{sur}}}^* \rightarrow \bar{f}(\mathcal{S}) a_{\xi}^{\dagger}$ , the construction of such standing wave modes is equivalent to the unitary transformation<sup>[103]</sup>

$$b_{+\varkappa}^{\dagger} = \frac{1}{\sqrt{2}} (a_{+\xi}^{\dagger} + a_{-\xi}^{\dagger}) \quad , \quad b_{-\varkappa}^{\dagger} = \frac{1}{\sqrt{2}} (a_{+\xi}^{\dagger} - a_{-\xi}^{\dagger}) \quad .$$

Recalling the central role of photon numbers and the vacuum state for the number states, it is important to note that a unitary transformation, like the one that yields standing wave modes, does not alter the vacuum state. Similarly, the observable total photon number, neglecting the zero-point energy, remains conserved under the standing wave transformation with

$$\mathcal{H} = \sum_{\xi=1,2} \hbar\omega_{\xi} a_{\xi}^{\dagger} a_{\xi} = \sum_{\varkappa=1,2} \hbar\omega_{\varkappa} b_{\varkappa}^{\dagger} b_{\varkappa} \quad .$$

In summary, decomposing any closed or rough surface in approximative locally flat, one-dimensional interfaces, the corresponding local surface fields take the form of surface plasmon fields. The canonical quantization involving the interface and these surface fields leads to harmonically oscillating surface plasmon polariton energy dynamics that hold also for standing surface waves instead of propagating ones.

### Lorentzian Resonance Lineshape

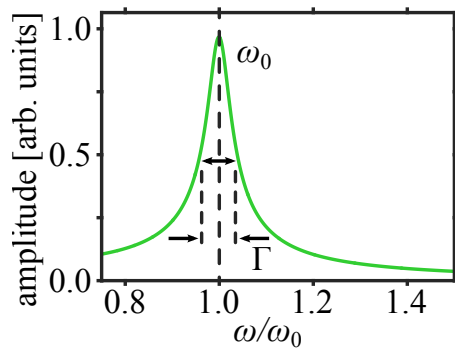


Figure 3.1: Lorentzian line shape results from harmonically oscillating mode fields.

The quantization shall not be used directly, but the harmonic oscillator behavior is the central point of the alternative route to determine the cavity parameters necessary for the quantized light-matter interaction. Hence, a driven, damped harmonic oscillator shall be used as the alternative model of the fields involved either in the scattering of light to determine the radiative decay rate  $\Gamma^{\text{rad}}$  or in the absorption of light in form of Ohmic loss to determine the non-radiative decay rate  $\Gamma^{\text{non}}$ :

$$\partial_t^2 o(t) + \Gamma^j \partial_t o(t) + \omega_0^2 o(t) = Q e^{-i\omega t} \quad , \quad (3.7)$$

with  $j = \text{rad}$  or  $j = \text{non}$  respectively, for both mechanisms. With an ansatz  $o(t) = \mathcal{P}(\omega) e^{-i\omega t}$  follows the amplitude

$$\mathcal{P}(\omega) = \frac{Q}{\omega_0^2 - \omega^2 - i\omega\Gamma^j} \quad ,$$

taking the form of a spectral Lorentzian line. Hence, the mode fields involved in the energy exchange harmonically oscillate and produce Lorentzian lines spectrally, as Fig. 3.1 shows. The central frequency of the line shape then corresponds to the resonance frequency  $\omega_0$  of the harmonic oscillation and the full width at half maximum of the line shape  $\Gamma^j$  corresponds to the damping rate of the oscillation. But modeling both the scattering and the absorption associated with a localized surface plasmon mode of the optical nanoantenna as driven, damped harmonic oscillations, the power spectra resulting from either the integration of the electromagnetic field energy flux density or the integration of the Ohmic losses require a line fit in form of

$$|\mathcal{P}(\omega)|^2 = \frac{Q^2}{(\omega_0^2 - \omega^2)^2 + \omega^2 (\Gamma^j)^2} \quad . \quad (3.8)$$

Fitting the simulated scattering and absorption spectra with the expression in Eqn. (3.8) yields both the cavity parameters  $\omega_\xi$  and  $\Gamma_\xi^{\text{tot}}$ . While the considerations above, revealing the harmonic oscillations of the mode fields, are chosen to justify the assumption of a Lorentzian line shape and the corresponding fit to determine the cavity parameters, there are more indicators that are worth mentioning to strengthen this crucial assumption:

- > The actual quantized light-matter interaction is modeled by means of cavity QED and the role of the cavity is primarily the selectivity regarding the supported modes. Investigating the mode density of a generally damped cavity via the calculations of multi-time correlation functions and the corresponding power spectrum reveals a spectral Lorentzian distribution<sup>[115]</sup>. This feature can be traced back to be a result of the Markov approximation, which omits any memory effects on the evolution of a system<sup>[182]</sup>. Since optical nanoantennas feature resonant behavior in scattering, see Eqn. (2.24), they can be considered as cavities, independent of the underlying physical mechanism. Consequently, the Lorentzian line shape is in agreement with the light-matter interaction model and would exclude scattering phenomena that do not match the cavity mode characteristic required.
- > In both the theoretical framework and the semi-classical model, the description of the plasmonic resonance itself relies on the very simple model of a

---

free electron gas over a rigid ionic crystal. This implicitly follows the notion of elementary excitations<sup>[183]</sup>, where weakly excited states of macroscopic structures are modeled as noninteracting elementary excitations. These elementary excitations can take the form of quasi particles or collective excitations and can represent fundamental physical properties of the macroscopic structure. This can be immediately transferred to the relatively low excited states corresponding to a few moving charge carriers in metal<sup>[184]</sup>. Already early solid-state optical investigations of plasmonic resonances found harmonic oscillatory behavior for the excitation and deexcitation of plasmons from purely classical considerations, deemed to hold for quantum physical treatment as well<sup>[185]</sup>. Furthermore, initial disagreements between experiment and theory could be resolved by expanding the idealized treatment based on a simple material response model in form of Eqn. (2.14) rather than introducing anomalous bulk properties of the metal<sup>[186]</sup>. Similarly, recent comparative studies of plasmonic resonances of nanometer scale structures in experiment and numerical simulation reveal accurate classical numerical predictions<sup>[36,187,188]</sup> based on purely classical material response models<sup>[189–191]</sup>. Hence, the idealized modeling of the metallic media still holds for numerical modeling of truly nanometer structures, indicating the validity of subsequent plasmonic excitation properties following from the same metallic modeling.

- > Finally, the free electron gas can be treated by means of plasma physics. Applying a collective-variable ansatz<sup>[192]</sup> to describe the plasma, density fluctuations are separated into collective plasma and individual particle components. An oscillatory equation can be found for the collective component<sup>[193]</sup>. Similarly, implementing a Hamiltonian formalism, harmonic oscillatory behavior is retrieved for the excitation of plasmons<sup>[194]</sup>. The approximations involved in such a treatment are the dispensation of collisions in the plasma, linear system equations due to only small deviations from equilibrium distribution of the plasma, the absence of coupling between different Fourier components in the Coulomb interaction of the electrons, and lastly only minor influence of the interaction on the systems properties. Additionally, the free electron gas as a quantum plasma, with a comparably low electron density, can only be treated as idealized with the weak coupling of classical plasmas<sup>[193]</sup>.

### **Incoherent Weak Coupling Regime**

Assuming harmonic oscillatory behavior and consequently a Lorentzian line shape for the excitation dynamics of localized surface plasmon polaritons, enables the as-

certainment of both the resonance frequencies  $\omega_\xi$  and decay rates  $\Gamma_\xi^j$  of the cavity modes of the optical nanoantenna. This leaves only the coupling rate  $g_\xi$  to be determined. Revisiting the evolution of an open cavity, featuring one resonant mode, that contains a quantum system characterized by one electronic transition, decay mechanisms and corresponding rates can be phenomenologically introduced in the Langevin theory<sup>[182]</sup>. For a master equation (2.39) with a Jaynes-Cummings Hamiltonian (2.37) and both dissipation through spontaneous emission (3.4) and cavity decay (3.3), the evolution of the population is governed by<sup>[195]</sup>

$$\partial_t \langle a^\dagger a \rangle = -\Gamma^{\text{tot}} \langle a^\dagger a \rangle + g \langle \sigma_{\text{eg}} a \rangle + g \langle a^\dagger \sigma_{\text{ge}} \rangle, \quad (3.9)$$

$$\partial_t \langle \sigma_{\text{eg}} \sigma_{\text{ge}} \rangle = -\gamma \langle \sigma_{\text{eg}} \sigma_{\text{ge}} \rangle - g \langle \sigma_{\text{eg}} a \rangle - g \langle a^\dagger \sigma_{\text{ge}} \rangle, \quad (3.10)$$

$$\partial_t \langle \sigma_{\text{eg}} a \rangle = -\frac{\gamma + \Gamma^{\text{tot}}}{2} \langle \sigma_{\text{eg}} a \rangle + g [\langle \sigma_{\text{eg}} \sigma_{\text{ge}} \rangle - \langle a^\dagger a \rangle]. \quad (3.11)$$

This evolution exhibits two distinct regimes: weak and strong coupling. In the strong coupling regime<sup>[196]</sup> the coupling between the cavity mode and the electronic transition at a rate  $g$  is the fastest process<sup>[197]</sup>, i.e. dominating. Strong coupling is also a prerequisite for the coherent, reversible exchange of energy quanta between the quantum system and the cavity mode<sup>[198]</sup>. Due to the importance of coherence for any elaborate quantum information application, the strong coupling regime has been the focus of many theoretical<sup>[199–202]</sup> and experimental studies<sup>[199,203–206]</sup>. In the weak coupling regime, which is equipollent to the incoherent energy exchange between quantum system and cavity mode, the coherences in the evolution equation set (3.9) - (3.11) can be adiabatically eliminated, yielding<sup>[207]</sup>

$$\partial_t \langle a^\dagger a \rangle = -(\Gamma^{\text{tot}} + R) \langle a^\dagger a \rangle + R \langle \sigma_{\text{eg}} \sigma_{\text{ge}} \rangle, \quad (3.12)$$

$$\partial_t \langle \sigma_{\text{eg}} \sigma_{\text{ge}} \rangle = -(\gamma + R) \langle \sigma_{\text{eg}} \sigma_{\text{ge}} \rangle + R \langle a^\dagger a \rangle. \quad (3.13)$$

Here,  $R$  takes the role of the effective coupling rate between the quantum system and the cavity mode. The quantum system can either decay via spontaneous emission at rate  $\gamma$  or exchange energy with the cavity mode at rate  $R$ , while the cavity mode can, additional to the energy exchange, decay at rate  $\Gamma^{\text{tot}}$ .  $R$  is given by  $R = \frac{4g^2}{\Gamma^{\text{tot}}}$ . In the weak coupling regime with  $R \ll \Gamma^{\text{tot}}$ , the quantum system relaxes at a rate of  $\gamma + R$  in Eqn. (3.13). Hence, the coupling to the cavity opened up another relaxation channel via the cavity mode at rate  $R$ . Consequently, defining an emission enhancement due to the coupling to the cavity of the quantum system,

---

using the cavity efficiency  $\eta = \Gamma^{\text{rad}}/\Gamma^{\text{tot}}$  yields<sup>[178,208]</sup>

$$F_{\text{qed}} = \frac{\gamma + R}{\gamma} = 1 + \frac{4g^2\eta}{\gamma\Gamma^{\text{tot}}} \quad , \quad (3.14)$$

as the ratio of the quantum system's relaxation rate with and without the coupling to the optical cavity in form of the nanoantenna. The enhancement of spontaneous emission can also be calculated classically<sup>[209,210]</sup> through the ratio of emitted power with and without the presence of the nanoantenna. For nanoantennas of arbitrary geometry, this can be numerically calculated via Eqn. (3.5). Consequently, equating<sup>[211]</sup> the classical emission enhancement due to the nanoantenna with the enhancement in the cavity QED model with the cavity mode coupling yields

$$\begin{aligned} F_{\text{cla}}(\omega_0) &= \frac{W_{\text{rad}}^{\text{na}}(\omega_0)}{W_{\text{rad}}^{\text{fs}}(\omega_0)} = \frac{\int_{\partial\Omega} d\mathbf{A} \cdot [\Re\{\mathbf{E}_{\text{tot}}^{\text{na}}(\omega_0) \times \mathbf{H}_{\text{tot}}^{\text{na}*}(\omega_0)\}]}{\int_{\partial\Omega} d\mathbf{A} \cdot [\Re\{\mathbf{E}_{\text{tot}}^{\text{fs}}(\omega_0) \times \mathbf{H}_{\text{tot}}^{\text{fs}*}(\omega_0)\}]} \\ &= F_{\text{qed}} = 1 + \frac{4g^2\eta}{\gamma\Gamma^{\text{tot}}} \quad , \end{aligned} \quad (3.15)$$

where the superscript 'na' indicates the presence of the nanoantenna and 'fs' its absence. Additionally, integrating over the total fields includes the spontaneous emission of the bare quantum system as an oscillating dipole as well. With the knowledge of the total cavity decay rate  $\Gamma^{\text{tot}}$  this enables the calculation of the coupling rate  $g$ , but this is only valid in the weak coupling regime of incoherent energy exchange. After the classical simulations are successfully performed, both  $\Gamma^{\text{tot}}$  and  $g$  are available, characterizing a resonant cavity mode and its light-matter coupling. Hence, for every application that shall be further discussed in this thesis, the cavity mode can and will be examined regarding the coupling regime to any transition, i.e. the ratio between  $\Gamma^{\text{tot}}$  and  $g$ . Once the weak coupling is ensured, which is the case for all quantum optical applications discussed, the cavity QED modeling can commence.

### Summary of the Model Parameter Genesis

At this point, all parameters necessary for the cavity QED light-matter interaction model shown in Fig. 3.2 are determined. The quantum system parameters, such as the transition dipole moment  $\mathbf{d}_{\text{ge}}$  and the transition frequency  $\nu_{\text{ge}}$ , are tabulated from external sources. The spontaneous emission rate  $\gamma_{\text{ge}}^{\text{spo}}$  of the bare quantum system is calculated according to Eqn. (2.40). The cavity parameters, such as the cavity mode resonance frequency  $\omega_0$  and the cavity decay rates  $\Gamma^{\text{j}}$ , are determined through a spectral Lorentzian line fit of the scattered and absorbed power, Eqn.

(3.5) and (3.6) respectively. Finally, the light-matter coupling rate  $g$  is calculated by equating the classical emission enhancement with the enhancement from the cavity QED model. This procedure can be carried out separately for each mode  $\xi$  that is supposed to enter the cavity QED model considerations.

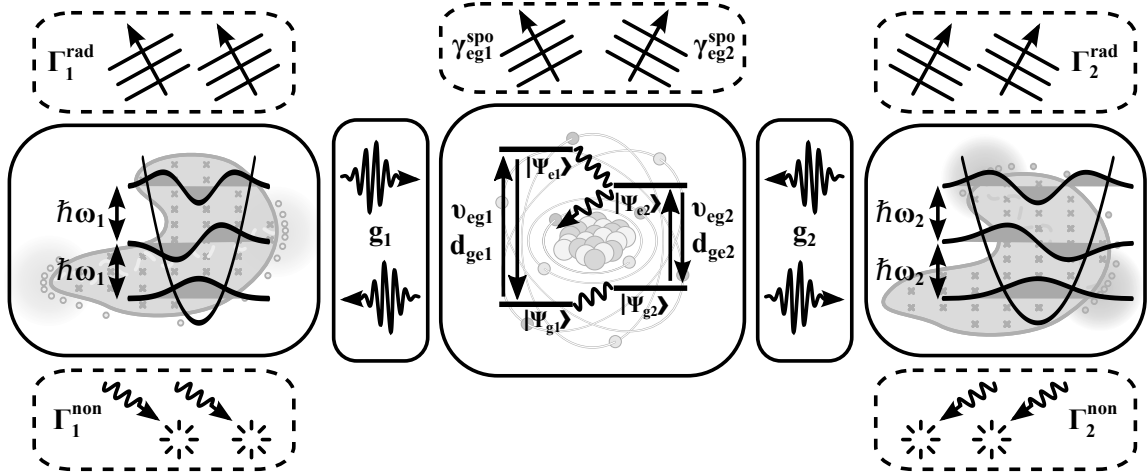


Figure 3.2: Open cavity QED model used in this work. The necessary parameters  $\omega_\xi$ ,  $\Gamma_\xi^j$ , and  $g_\xi$  are derived based on a semiclassical model.

### Beyond Single Lorentzian Line Shapes

With the assumption of a Lorentzian line shape being a crucial part of the alternative route to determine the parameters necessary for the quantized light-matter interaction model, it is reasonable to elaborate a little further on this point, as countless spectra of optical nanoantennas have been experimentally recorded and many spectral features were noted. While the resonance frequency  $\omega_0$  and the decay rate  $\Gamma^j$  for one cavity mode and the decay mechanism, either radiative or non-radiative, are determined through the line fit of the one corresponding Lorentzian, the entire method is by no means limited to only a single Lorentzian. Without further knowledge of the mode structure of any nanoantenna, its excitation through an incident illumination will assumingly excite multiple nanoantenna modes. Hence, accounting for the presence and excitability of multiple modes, in an initial attempt to reconstruct a spectrum, either experimentally recorded or numerically simulated, an incoherent sum of Lorentzians, according to

$$|\mathcal{P}^{\text{tot}}(\omega)|^2 = \left[ \sum_{\xi} |\mathcal{P}_{\xi}(\omega)| \right]^2 = \left[ \sum_{\xi} \frac{Q_{\xi}}{\sqrt{(\omega_{\xi}^2 - \omega^2)^2 + \omega^2 (\Gamma_{\xi}^j)^2}} \right]^2, \quad (3.16)$$

shall be employed to reproduce all notable spectral features. The correspond-

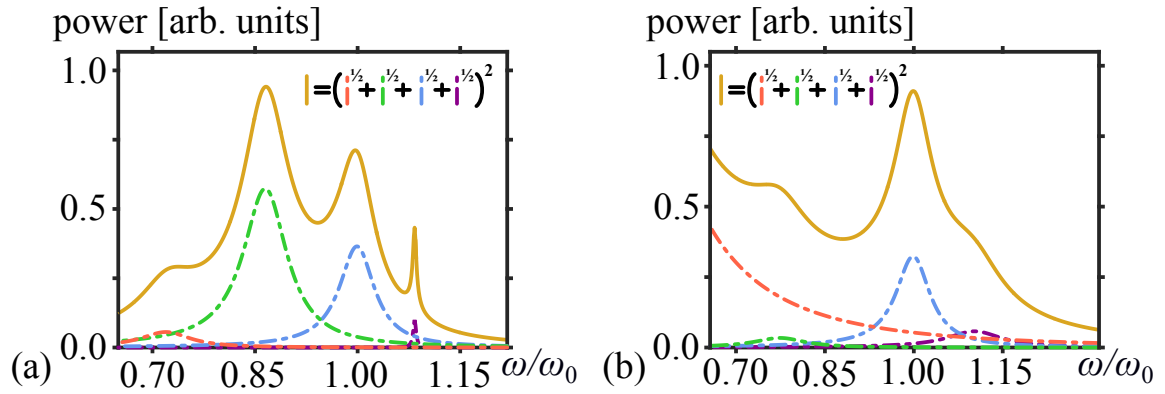


Figure 3.3: (a) Spectrum exhibiting four distinct local maxima, corresponding to four underlying Lorentzian lines. (b) Less obviously, again four Lorentzian lines are combined to form a spectral profile.

ing spectra may very clearly indicate that Lorentzian lines with different central frequencies, different line widths, and different amplitudes are the underlying features, as shown in Fig. 3.3(a) and in experimental measurements<sup>[212–220]</sup>. But judging only from the spectral profile, which is rather symptomatic for an experimental characterization of nanoantennas, the situation may not be such obvious<sup>[216,221–230]</sup>. Figure 3.3(b) depicts a spectral profile that is composed of four Lorentzian lines as well, but here the association of underlying Lorentzian lines is certainly not as apparent. However, by employing a number of Lorentzian lines to reconstruct spectral features, the characteristic parameters, such as the central frequency and the line width, of each individual mode involved can be straight forward determined.

At this point it is important to recall the direct method of calculating the decay rate by integrating the scattered power of the single photon field. The problem of multiple nanoantenna modes contributing to the scattering complicates the direct calculation significantly, because the relative excitation strength of each mode involved is required to unequivocally determine the decay rate corresponding to each mode. This information automatically follows from such a line fit procedure as it is outlined here, since the fit also produces a mode amplitude for each Lorentzian line.

### Fano Resonance Features

But another phenomenon demands consideration when discussing the assessment of modal features in the spectral response to excitation of nanoantennas or optical cavities in general: distinctly asymmetric line shapes, often associated

with the Fano effect<sup>[231,232]</sup> and quite extensively observed and discussed<sup>[233–235]</sup>. Without any further elaboration on the origin of the mechanism behind it, the asymmetry of the line shape can be attributed to interference of multiple resonances<sup>[236]</sup>. Please note that the line shape typically attributed to the Fano effect, as shown in Fig. 3.4(a), emerges from coupled resonances that differ significantly in line width. But the following shall demonstrate that a general asymmetry follows for all Fano-related line shapes with different sets of parameters. Consequently, expanding the simple harmonic oscillator model for a single plasmonic resonance to two coupled, damped oscillators, while only one of them is driven, to represent two interacting electromagnetic cavity modes<sup>[237]</sup> yields<sup>[238]</sup>

$$\partial_t^2 o_{\text{dri}} + \Gamma_{\text{dri}}^j \partial_t o_{\text{dri}} + \omega_{\text{dri}}^2 o_{\text{dri}} + \Theta o_{\text{cou}} = \mathcal{Q} e^{-i\omega t} \quad , \quad (3.17)$$

$$\partial_t^2 o_{\text{cou}} + \Gamma_{\text{cou}}^j \partial_t o_{\text{cou}} + \omega_{\text{cou}}^2 o_{\text{cou}} + \Theta o_{\text{dri}} = 0 \quad . \quad (3.18)$$

Here,  $o_{\text{dri}}$  denotes the driven harmonic oscillator, while  $o_{\text{cou}}$  denotes the second oscillator that is coupled to the first, but not driven itself. The ansatz  $o_{\text{dri/cou}}(t) = \mathcal{D}_{\text{dri/cou}}(\omega) e^{-i\omega t}$ , identical to the one used for the single oscillator, gives the amplitudes

$$\mathcal{D}_{\text{dri}}(\omega) = \frac{\omega_{\text{cou}}^2 - \omega^2 - i\omega\Gamma_{\text{cou}}^j}{\left(\omega_{\text{dri}}^2 - \omega^2 - i\omega\Gamma_{\text{dri}}^j\right) \left(\omega_{\text{cou}}^2 - \omega^2 - i\omega\Gamma_{\text{cou}}^j\right) + \Theta^2} \mathcal{Q} \quad , \quad (3.19)$$

$$\mathcal{D}_{\text{cou}}(\omega) = -\frac{\Theta}{\left(\omega_{\text{dri}}^2 - \omega^2 - i\omega\Gamma_{\text{dri}}^j\right) \left(\omega_{\text{cou}}^2 - \omega^2 - i\omega\Gamma_{\text{cou}}^j\right) + \Theta^2} \mathcal{Q} \quad , \quad (3.20)$$

for the driven and the coupled oscillator respectively. Consequently, for the purpose of fitting a spectral profile, either generated through scattering or absorption, the corresponding squared absolute values of the amplitudes read

$$|\mathcal{D}_{\text{dri}}(\omega)|^2 = \frac{\mu_{\text{cou}}}{\Theta^4 - 2\Theta^2 \left[ \omega^2 \Gamma_{\text{dri}}^j \Gamma_{\text{cou}}^j - \nu_{\text{dri}} \nu_{\text{cou}} \right] + \mu_{\text{dri}} \mu_{\text{cou}}} \mathcal{Q}^2 \quad , \quad (3.21)$$

$$|\mathcal{D}_{\text{cou}}(\omega)|^2 = \frac{\Theta^2}{\Theta^4 - 2\Theta^2 \left[ \omega^2 \Gamma_{\text{dri}}^j \Gamma_{\text{cou}}^j - \nu_{\text{dri}} \nu_{\text{cou}} \right] + \mu_{\text{dri}} \mu_{\text{cou}}} \mathcal{Q}^2 \quad . \quad (3.22)$$

Here, two variables were introduced to ensure rather compact expressions,  $\mu_{\text{dri/cou}} = \left(\omega_{\text{dri/cou}}^2 - \omega^2\right)^2 + \omega^2 \left(\Gamma_{\text{dri/cou}}^j\right)^2$  and  $\nu_{\text{dri/cou}} = \left(\omega - \omega_{\text{dri/cou}}\right) \left(\omega + \omega_{\text{dri/cou}}\right)$ . Monitoring the spectra of the two squared absolute values of the amplitudes, the coupled oscillator exhibits two separate maxima, roughly located at the resonance frequencies of the individual oscillators. The different widths of the resonances - the cou-

pled resonance is narrower - is also reflected in the amplitude spectrum shown in Fig. 3.4(b). These observations still hold for the amplitude spectrum of the driven oscillator: two distinct maxima emerge at the corresponding oscillator frequencies, while the coupled resonance is narrower than the driven one. But the relevant aspect of the spectrum of the driven oscillator is the visible asymmetry of the coupled oscillator line shape shown in Fig. 3.4(a). The asymmetry manifests in visibly

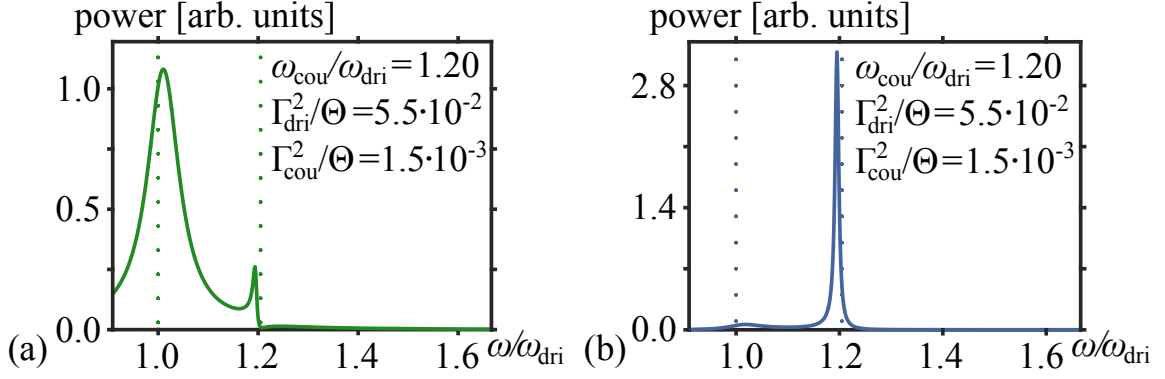


Figure 3.4: (a) Power spectrum shown for the driven oscillator. (b) Power spectrum shown for the coupled oscillator. The insets display the ratios of the characteristic parameters and the vertical dotted lines indicate the locations of  $\omega_{\text{dri}}$  and  $\omega_{\text{cou}}$ .

different slopes on either side of the resonance line as well as in destructive interference on the side of the steeper slope that significantly diminishes the total scattered or absorbed power. This combination of narrow peak and destructive interference is the most recognizable feature of a Fano resonance<sup>[233,239]</sup> and has been frequently observed in experiments<sup>[240–242]</sup>.

But Fano resonance lines can also take quite different shapes. The following is meant to concisely show how the choice of the characteristic parameter set  $\omega_{\text{dri}}$ ,  $\Gamma_{\text{dri}}$ ,  $\omega_{\text{cou}}$ ,  $\Gamma_{\text{cou}}$ , and  $\Theta$  influences the spectral profile of the Fano resonance. For this reason the characteristic parameters of the canonical Fano resonance with narrow peak and destructive interference as used in Fig. 3.4 shall be considered as the default ratios.

As an initial modification, reducing the spectral separation of the driven and the coupled resonance results in a cancellation in the power spectrum at the resonance frequency of the coupled oscillator<sup>[243]</sup>, while the driven resonance remains generally unaltered<sup>[239]</sup>. This behavior is shown in Fig. 3.5(a) and even though there are still two maxima visible, the significant difference in width of the two resonances can not be concluded from the spectral profile anymore. Similar profiles have been experimentally measured<sup>[244–251]</sup>.

The next modification of the default parameters in form of a narrower coupled

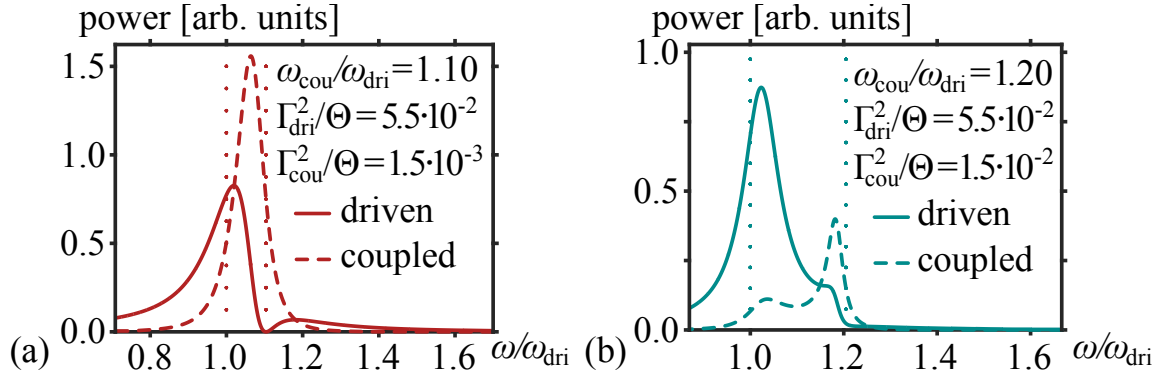


Figure 3.5: (a) Fano resonance with cancellation feature shown for parameter ratios inset. (b) Fano resonance with spectral step feature shown for parameter ratios inset. The vertical dotted lines indicate the spectral locations of  $\omega_{\text{dri}}$  and  $\omega_{\text{cou}}$ .

resonance results in a step-like feature signified by an inflection from concave to convex functional dependency as shown in Fig. 3.5(b). This is remarkable, since it can be accompanied by the presence of a saddle point, which culminates in the disappearance of any local extremum of the coupled resonance<sup>[239]</sup>. Consequently, only the asymmetry on the tail of the driven resonance line indicates the existence of another mode that should be taken into consideration. This has been experimentally observed as well<sup>[252–254]</sup>. Another parameter modification that tremendously

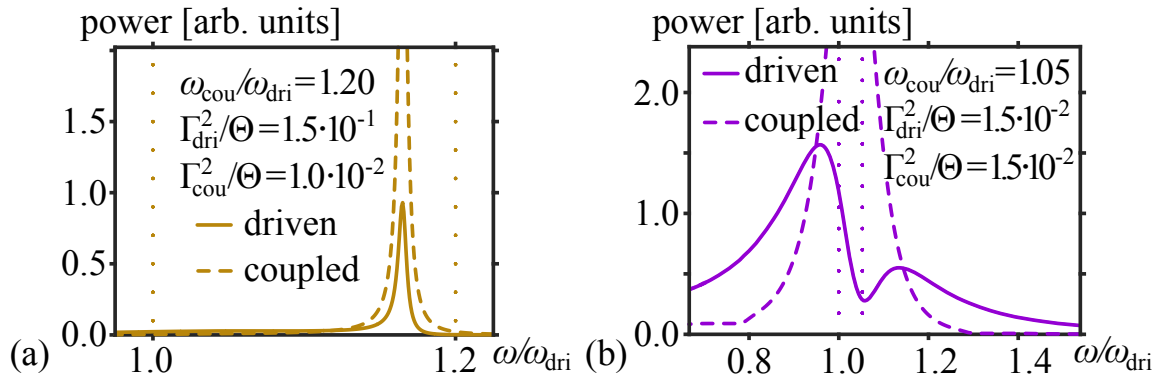


Figure 3.6: (a) Fano resonance displaying an isolated maximum shown for parameter ratios indicated in the inset. (b) Fano resonance featuring two shifted maxima shown for parameter ratios indicated in the inset. The vertical dotted lines indicate the spectral locations of  $\omega_{\text{dri}}$  and  $\omega_{\text{cou}}$ .

changes the appearance of the spectral profile of the Fano resonance is shown in Fig. 3.6(a). Here, the two resonances, both narrower than in the default set, but still widely separated, form a single sharp resonance line spectrally between each's resonance frequency. The sole indicator that this is not a single Lorentzian

---

resonance is the asymmetry between the slopes of the two tails<sup>[255]</sup>, similar to the canonical Fano resonance. Such Fano resonance spectra have been measured in experiments<sup>[256–259]</sup>.

The repercussions of the last parameter modification on the line shape resemble the first ones, depicted in Fig. 3.5(a): Figure 3.6(b) features two visible local maxima that enclose a local minimum. This characteristic spectral profile<sup>[260,261]</sup> originates from the interaction of two resonances of the illuminated nanostructure - just as the three preceding exemplary spectral profiles have - but similar to the singular peak profile shown in Fig. 3.6(a), the spectral locations of the resonances involved do not correspond to the maxima of the profile. In agreement to the first modification, the local minimum rather signifies one of the resonance frequencies, but deviating from the first modification, there is a significant spectral distance between the second resonance frequency and the closest spectral maximum. Differing from the first modification, two equally broad resonances with very little spectral separation cause this spectral profile that has been recorded in different experiments<sup>[252,262–267]</sup>.

Having identified different phenotypes of spectral profiles resulting from Fano resonances, more complicated scenarios in form of combination of Fig. 3.6(a) & (b)<sup>[268]</sup> or Fig. 3.5(a) and Fig. 3.6(b)<sup>[269]</sup> can be characterized as well. Additionally, the central distinctive feature between uncoupled Lorentzian lines and coupled Fano line becomes clear: symmetric individual spectral lines indicates uncoupled resonances, while asymmetric individual spectral lines indicate coupling between the resonances.

Finally, at this point it is important to mention that the alternative determination of the parameters, vital for the modeling of the quantum physical dynamics, so far only considered plasmonic cavities, while the cavity QED formalism is much more general. The dynamics of the quantum model describe the interaction of localized quantum systems with cavity modes without any further specification concerning the type of the cavity. But the assumption of a Lorentzian line profile for an individual cavity mode also holds beyond plasmonic cavities. Additional to experimental evidence of Lorentzian spectral profiles for semiconductor cavities with embedded quantum emitters featuring exciton-photon coupling<sup>[203]</sup>, there is also the theoretical deduction<sup>[270]</sup> of Lorentzian line shapes for morphology-dependent resonances, such as whispering gallery modes<sup>[271,272]</sup>. Consequently, both the cavity QED model as well as the corresponding parameter genesis via Lorentzian line fit can be expanded to treat semiconductor cavities as well as optical microcavities supporting morphology-dependent resonances.

## 4 Optical Nanoantenna Applications

With both a theoretical model available to describe the dynamics of plasmonic cavity modes coupled to quantum systems and the ability to determine model parameters corresponding to realistic quantum systems and optical nanoantennas, the next step is to explore the possible dynamical behavior that the combination of optical nanoantenna and quantum system can offer.

The following four exemplary setups of optical nanoantennas and quantum systems shall systematically highlight different aspects or properties of the combined system. To emphasize that only the fundamental field localization and enhancement, provided by optical nanoantennas, are required for the different applications, the basic geometry of the nanoantenna shall remain the same for all four applications: the nanorod or nanowire. A cuboid or cylinder, significantly and one-dimensionally elongated along the symmetry axis and made from metal. The most prominent response of such structures are the longitudinal resonances of transversal wire modes that occur due to the finite length of the nanorod<sup>[273]</sup>. The fundamental antenna mode thusly emerges when the extent of the nanorod matches half of the wavelength. Then the surface charge oscillation causes the ends of the nanorod to be oppositely charged, resulting in a dipolar charge distribution<sup>[274]</sup> with pronounced emission properties in both pattern<sup>[275]</sup> and strength<sup>[276]</sup>.

Hence, the fundamental plasmonic mode can be directly controlled through the length of the nanorod or -wire. This is done during the fabrication process, which can be both achieved by self-assembly<sup>[277]</sup> or growth<sup>[278]</sup> and lithography<sup>[279]</sup>. It is important to notice that the pertinent resonance wavelength is not the one in free space, but rather a shortened effective wavelength, due to the excitation electromagnetic field penetrating the metal domain at optical frequencies<sup>[280]</sup>, resulting in optical resonances of nanowire geometries at truly nanometric scales<sup>[281]</sup>. These properties render the nanorod or -wire a tractable and reliable nanoantenna geometry, both in theory and experiment, to realize multifarious applications from fluorescence enhancement<sup>[282]</sup> to single molecule sensing<sup>[283]</sup> and in vivo cancer therapy<sup>[284]</sup>.

---

The crucial building blocks for any of the outlined applications in this part are symbolically shown in Fig. 4.1 and shall be the following: nanorods, made either from gold or silver with a square cross section and a total length below any free space optical wavelength, different kinds of quantum systems, characterized by one or more dipole transitions with particular transition dipole moment magnitudes and orientations, and laser illumination from the far field, approximated as locally incident plane waves.

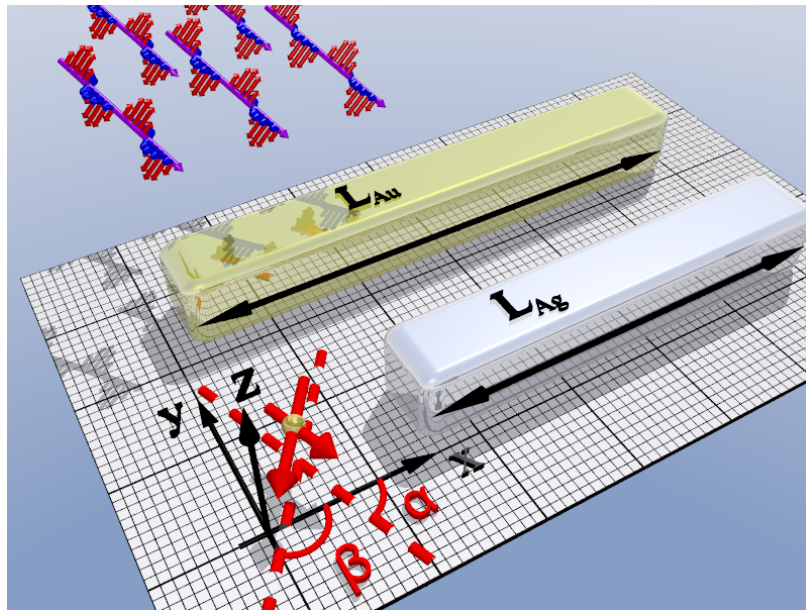


Figure 4.1: Symbolical depiction of building blocks, crucial for the presented applications, as they are listed: nanorods, characterized by their length, quantum systems, characterized by their position and transition dipole moments, and laser illumination, incident on the respective setup.

Consequently, the quantum systems located in close proximity to the nanorod antennas, or more precisely the dipole transitions of the quantum systems, can be influenced through the interaction with the nanoantenna, acting as a cavity featuring resonances at optical frequencies.

## 4.1 From Quenching to Emission Enhancement

Initiated by the landmark experimental demonstration of spontaneous emission enhancement of fluorescent molecules in the middle of the 20<sup>th</sup> century<sup>[285]</sup>, influencing of quantum systems, or more precisely their properties, through engineering of their environment<sup>[37]</sup> has remained in the focus of ongoing research activity.

The enhancement of fluorescence<sup>[286,287]</sup> as the performance bottleneck provides immediate benefits for plasmon-enhanced microscopy<sup>[28,288,289]</sup>, fluorescence imaging<sup>[81,290]</sup>, and light emitting devices<sup>[291,292]</sup> or light sources<sup>[293–295]</sup>. Consequently, the experimental demonstration of fluorescence enhancement through optical cavities in general<sup>[296–301]</sup> and plasmonic nanostructures in particular<sup>[302–306]</sup> has been the first step to establish different materials and geometries as viable for photonic applications involving the aforementioned phenomena.

Since photonic fluorescence enhancement only requires the fluorophores to emit at optical frequencies, various quantum systems have been used for experimental demonstration. One very promising group of candidates are molecular monolayer transition metal dichalcogenides. These quasi two-dimensional materials contain localized emitters with specific transition dipole moments and they feature excitons sensitive to doping<sup>[307,308]</sup> and exhibit the piezoelectric effect<sup>[309]</sup>. Additionally, they have been shown to perform as both sensitive photodetectors<sup>[310,311]</sup> and in low threshold lasing<sup>[312]</sup>.

The combined experimental and theoretical investigation of the fluorescence enhancement potential of monolayer molybdenum diselenide ( $\text{MoSe}_2$ ) due to the coupling to plasmonic nanoantennas, described in the following, was performed in collaboration with the research group of Prof. Yuri Kivshar from the Nonlinear Physics Centre of the Australian National University. The experimental realization was supervised by Prof. Dragomir N. Neshev and mainly executed by Haitao Chen. The results that are illustrated in the following have been published in H. Chen, *et al.*, *Scientific Reports* **6**, 22296 (2016)<sup>[313]</sup>.

### Quenching

After *prima facie* considerations, the mechanism behind the fluorescence enhancement due to the nanoantenna generally follows from the incoherent, weak coupling between the fluorescent transition in the  $\text{MoSe}_2$  monolayer and a resonant cavity mode of a nanoantenna in close proximity. As already outlined Eqn. (3.12) and Eqn. (3.13), the presence of an optical nanoantenna featuring a resonant cavity mode increases the relaxation rate of the quantum system by the rate  $R = \frac{4g^2}{\Gamma_{\text{tot}}}$ .

---

With the same rate, the quantum system couples to the cavity mode of the nanoantenna, which in turn emits into the far field at a rate of  $\Gamma^{\text{rad}}$ . Since the emission rates of nanoantennas usually exceed bare molecular rates of spontaneous emission, the overall emission rate from the fluorescent molecule is enhanced. This enables an accelerated traversing of the cycle of excitation and relaxation of the molecular transition involved in the fluorescence, which in turn can be measured systematically in a corresponding experiment.

The corresponding experiment, set up in Canberra, revolves around the following layout<sup>[313]</sup>: Initially, a  $\text{SiO}_2$  substrate is coated with a 10 nm layer of indium tin oxide (ITO). This allows for the preparation of arrays of gold nanorod antennas on top, through electron beam lithography. These arrays consist of individual rectangular antennas with a cross section of 40 nm by 40 nm and different lengths between 70 nm and 130 nm. The arrays are composed of identical antennas, aligned to maintain a separation distance of at least 400 nm in each direction. Additionally, the arrays do not cover the complete surface of the coated substrate to allow for a direct measurement of the fluorescence enhancement, as will be described in the following. Each sample, with an antenna array on top of the substrate, is characterized in transmittance regarding the fundamental resonance to identify the arrays resonant with the 785 nm photoluminescence peak of  $\text{MoSe}_2$ .

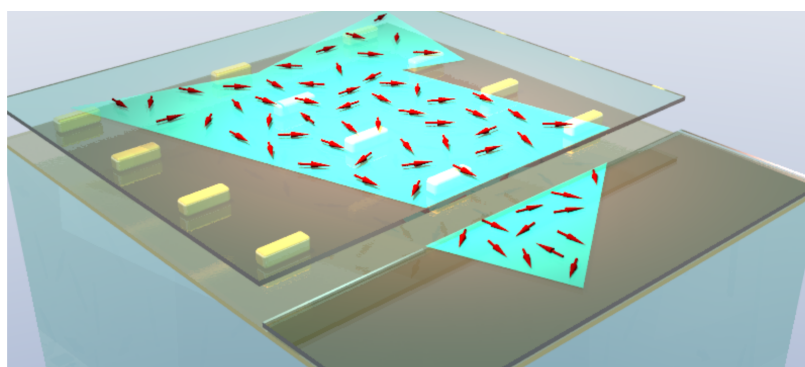


Figure 4.2: The considered experimental scenario: An array of gold nanorod antennas is fabricated on a glass substrate topped by an ITO layer. The array is covered by a glass spacer layer (optional) and a flake of monolayer  $\text{MoSe}_2$ . For reference purposes, an area without the nanorod array is measured as well.

In the next step, some selected the samples, featuring suitable arrays, are covered by silica layers of different thickness, through physical sputtering. These silica layers allows for a precise control of the distance between the nanoantenna array and the  $\text{MoSe}_2$  monolayer flake that is subsequently mechanically exfoliated from the bulk crystalline material and transferred to the sample. This means the suitable antenna arrays are covered by silica spacer layers, whose thickness ranges from

0 nm, i.e. no spacer, to a few nm. Since the antenna array intentionally does not cover the entire sample, if the monolayer flake is positioned accordingly, each individual sample contains areas with the monolayer on top of the antenna array, with a specific spacing, as well as areas with the monolayer on top of the bare coated substrate. This situation is symbolically depicted in Fig. 4.2.

The fluorescence measurements are performed by exciting the  $\text{MoSe}_2$  molecules with a supercontinuum laser at 532 nm with a spot size of about  $1 \mu\text{m}$ . The luminescence of the molecules at 785 nm is mapped with a scanning confocal microscope with additional spectral filtering. Recalling the theoretical model, the fluorescence enhancement is expected to be proportional to the cavity emission rate  $\Gamma^{\text{rad}}$  as well as the effective cavity coupling rate  $R \sim g^2$ . Here, the light-matter coupling rate  $g$  enters the considerations, with  $g \sim \mathbf{d}_{\text{ge}} \cdot \mathbf{E}_{\text{sca}}(\mathbf{r}_{\text{TLS}}, \omega)$ . As the transition dipole moment  $\mathbf{d}_{\text{ge}}$  is fixed for  $\text{MoSe}_2$ , the local field  $\mathbf{E}_{\text{sca}}(\mathbf{r}_{\text{TLS}}, \omega)$  is the parameter that can be influenced in the experiment. Due to the plasmonic nature of the cavity resonance of the nanoantenna, the local field closest to the surface is expected to feature the most pronounced hot spots. Consequently, the samples without spacer are expected to feature the strongest enhancement.

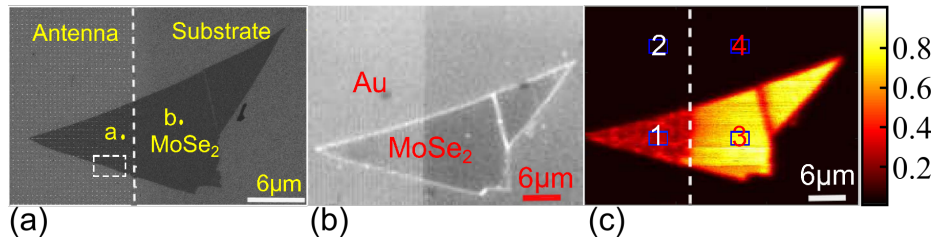


Figure 4.3: Experimental setup used for photoluminescence measurement:  $\text{MoSe}_2$  flake covering both nanoantenna array (left) and bare substrate (right). Scanning electron microscope (a)<sup>[313]</sup> and optical image (b)<sup>[313]</sup> of measurement sample. Corresponding spatial photoluminescence mapping of the same sample (c)<sup>[313]</sup>.

Electron microscopy and optical images of the sample setup without spacer are shown in Fig. 4.3(a) and (b) as well as qualitative photoluminescence measurements in Fig. 4.3(c). The fluorescence enhancement for the sample follows from combination of the photoluminescence measurements according to:  $(\text{1} - \text{2}) / (\text{3} - \text{4})$ . But closer inspection of the actual measurement image Fig. 4.3(c) without any further calculation already reveals prima facie counterintuitive behavior: The complete area of the  $\text{MoSe}_2$  flake covering the nanoantenna array is depicted darker, i.e. generating less photoluminescence, than the flake area positioned on the bare substrate.

The presence of the nanoantenna array has consequently quenched the fluorescence instead of enhancing it, as has been reported in literature<sup>[314]</sup>. Hence,

the experiment has revealed that the modeling of a single cavity mode coupled to the relaxation transition of the MoSe<sub>2</sub> is insufficient.

## Excitation Enhancement

To reveal the origin of the quenching, the investigation must begin with the excitation of the MoSe<sub>2</sub> flake by a laser illumination at 532 nm.

Numerically, the gold nanorod is modeled as a cuboid with the length of 127 nm, a square cross section of 40 nm by 40 nm, and radiused edges with a curvature radius of 10 nm. This results in a fundamental dipole resonance along the symmetry axis around the fluorescence wavelength of 785 nm of MoSe<sub>2</sub> with the dispersive material properties of gold modeled according to experimental data<sup>[45]</sup>. The modeling will be restricted to the dynamics surrounding single nanorods in the antenna array, since the individual nanoantennas are separated by at least 400 nm in any direction in the antenna array plane. Hence, any plasmonic enhancement effects due to neighboring antennas can be neglected. In agreement with the experimental situation (illumination spot size 1 μm for 40 nm by 40 nm by 127 nm cuboid) is modeled as an incident plane wave polarized perpendicular to the long axis of the nanorods in the antenna array plane.

Since the excitation enhancement relies on the same mechanism as the emission enhancement, the assistance through a cavity resonance, the corresponding rate is increased by  $R = \frac{4g^2}{\Gamma_{\text{tot}}}$ . Although the nanoantenna is not designed to explicitly support the excitation with a tailored resonance, the influence of the nanoantenna can still be quantified via the proportionality of the light-matter coupling rate:  $g \sim \mathbf{d}_{\text{ge}} \cdot \mathbf{E}_{\text{tot}}(\mathbf{r}_{\text{TLS}}, \omega)$ . Consequently, the excitation enhancement is given by

$$\frac{\Gamma_{\text{exc}}^{\text{na}}}{\Gamma_{\text{exc}}^{\text{fs}}} = \left| \frac{\mathbf{n}_{\text{TLS}} \cdot \mathbf{E}_{\text{tot}}^{\text{na}}(\mathbf{r}_{\text{TLS}}, \omega)}{\mathbf{n}_{\text{TLS}} \cdot \mathbf{E}_{\text{tot}}^{\text{fs}}(\mathbf{r}_{\text{TLS}}, \omega)} \right|^2. \quad (4.1)$$

Here,  $\mathbf{n}_{\text{TLS}}$  denotes the orientation of the transition dipole moment and  $\mathbf{r}_{\text{TLS}}$  the position of the two-level system, while  $\mathbf{E}_{\text{tot}}$  stands for the total electric field, with (superscript na) or without the nanoantenna (superscript fs).

As Eqn. (4.1) clearly reveals, both the position and the orientation of the transition dipole moment are crucial for the light-matter coupling and hence any plasmonic enhancement processes. Since neither its specific position nor its specific orientation can be easily controlled<sup>[315]</sup>, in case of a sizable MoSe<sub>2</sub> monolayer flake covering a myriad of individual nanoantennas, a qualitative description can be achieved by modeling a single nanoantenna and characteristic positions and orientations of the transition dipole moment.

Consequently, accounting for an arbitrary orientation in the monolayer plane, the amplitude of the total field is averaged according to  $\mathbf{n}_{\text{TLS}} \cdot \mathbf{E}_{\text{tot}}(\mathbf{r}_{\text{TLS}}, \omega) = \sqrt{|E_x(\mathbf{r}_{\text{TLS}}, \omega)|^2 + |E_y(\mathbf{r}_{\text{TLS}}, \omega)|^2}$ , with the sum over the field components parallel to the monolayer  $E_{x,y}$ . The resulting excitation rate enhancement mapping in a layer 7 nm above the top face of the actual nanoantenna is depicted in Fig. 4.4(a). Clearly visible are the distinct excitation enhancement along the outside and edge of the long sides of the nanorod geometry in contrast to the reduced excitation rate in the area above the central region of the top face of the nanoantenna. This leads to the selection of two characteristic points to further study the nanoantenna influence, while the distinguishability of the two points is included into the considerations: the first point above the geometrical center of the top face of the nanoantenna and the second point above one of the four rounded corners of the top face.

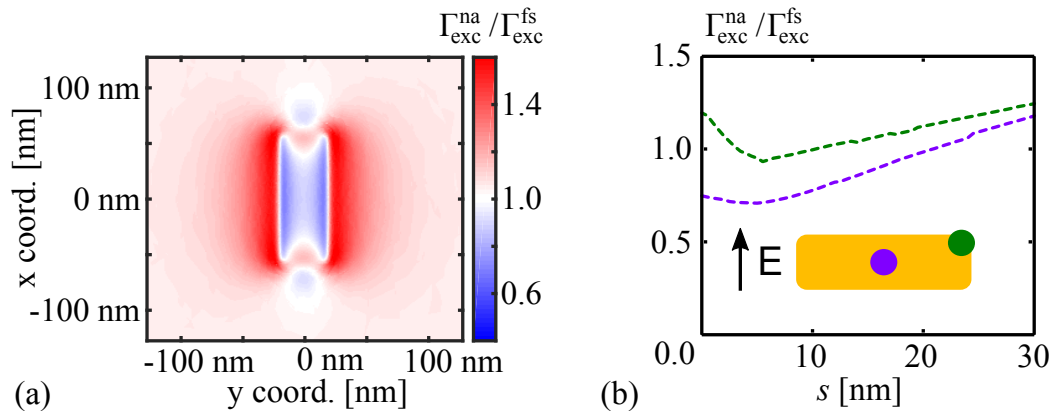


Figure 4.4: (a)<sup>[313]</sup> Excitation enhancement mapped in a layer 7 nm above the nanoantenna. (b)<sup>[313]</sup> Excitation enhancement shown over vertical distance to nanoantenna for characteristic points.

The influence of the vertical distance between the nanoantenna's top face and the excitation enhancement in the two selected points is shown in Fig. 4.4(b). Even though the excitation rate is mostly enhanced for the corner spot (green), except for a small region around 5 nm, and the excitation rate is mostly reduced for the central spot (purple), except for distances above 25 nm, the general behavior of the line graphs roughly coincides: For small distances the excitation rate reduces initially with increasing distance, up to around 5 nm. For greater distances the excitation rate generally increases with increasing distance to the nanoantenna. This behavior indicates a common mechanism for both points that is related to close proximity to the nanoantenna and detrimental to the desired enhancing effect of the nanoantenna.

## Emission Enhancement

In the next step, the emission from the  $\text{MoSe}_2$  monolayer shall be modeled to further illuminate any detrimental influences on the fluorescence. To this end, two specific transition dipole moment orientations, once parallel to the long axis of the nanorod and once perpendicular to it, but both times in plane with the monolayer flake, are simulated for two-level systems located at the previously determined characteristic locations: the central and the corner spot. Figure 4.5 portrays this conjuncture. These four individual scattering scenarios are realized with electric point dipoles corresponding to the transition dipole moments and positioned at different vertical distances  $s$  that account for different spacer thicknesses in the experiment.

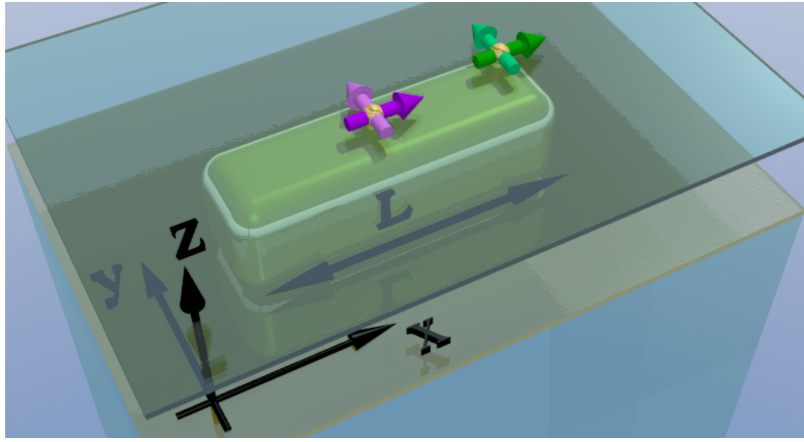


Figure 4.5: Symbolical depiction of the scenario: Transition dipole moments with specific orientations located at characteristic positions above the nanoantenna.

The fluorescence enhancement that the experiment is designed to investigate can be calculated according to<sup>[22]</sup>

$$\frac{\Gamma_{\text{flu}}^{\text{na}}}{\Gamma_{\text{flu}}^{\text{fs}}} = \frac{\Gamma_{\text{exc}}^{\text{na}} \eta_{\text{emi}}^{\text{na}}}{\Gamma_{\text{exc}}^{\text{fs}} \eta_{\text{emi}}^{\text{fs}}} . \quad (4.2)$$

Apparently, the excitation enhancement, as it is shown in Fig. 4.4(a) and (b), needs to be combined with the enhancement of the emission efficiency  $\eta_{\text{emi}}$  due to the presence of the nanoantenna. This emission efficiency enhancement in turn is composed of the radiative efficiency of the antenna itself  $\eta_{\text{rad}} = \Gamma_{\text{rad}}^{\text{na}} / (\Gamma_{\text{rad}}^{\text{na}} + \Gamma_{\text{non}}^{\text{na}})$  and the intrinsic quantum yield of the two-level system  $\eta_{\text{iqy}}$  according to<sup>[22,313]</sup>

$$\frac{\eta_{\text{emi}}^{\text{na}}}{\eta_{\text{emi}}^{\text{fs}}} = \frac{\Gamma_{\text{rad}}^{\text{na}}}{\Gamma_{\text{rad}}^{\text{na}} + \Gamma_{\text{non}}^{\text{na}} + \frac{1-\eta_{\text{iqy}}}{\eta_{\text{iqy}}}} \frac{\Gamma_{\text{rad}}^{\text{fs}} + \Gamma_{\text{non}}^{\text{fs}} + \frac{1-\eta_{\text{iqy}}}{\eta_{\text{iqy}}}}{\Gamma_{\text{rad}}^{\text{fs}}} . \quad (4.3)$$

From the individual scattering calculations for the different positions, orientations,

and spacer thicknesses, the required parameters in Eqn. (4.3) can be determined through Eqns. (3.5) and (3.6) and the result is shown in Fig. 4.6(a).

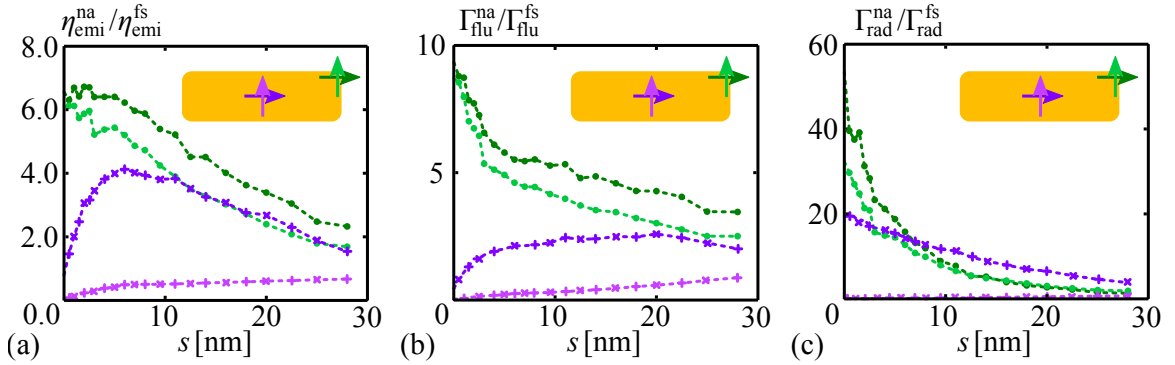


Figure 4.6: (a)<sup>[313]</sup> Emission efficiency enhancement plotted over different spacer thicknesses  $s$  above the nanoantenna. (b)<sup>[313]</sup> Corresponding fluorescence enhancement shown over spacer thickness  $s$ . (c)<sup>[313]</sup> Radiative Enhancement plotted over spacer layer thickness  $s$ . The differently colored line graphs correspond to different positions and orientations above the top face of the nanoantenna, as indicated by the insets showing a symbolical top view in each plot.

For these calculations, the intrinsic quantum yield of  $\text{MoSe}_2$  is assumed to be around  $\eta_{\text{iqy}} = 0.05$ <sup>[313,316]</sup>. The systematic behavior depicted in Fig. 4.6(a) shows a continuously decreasing emission efficiency enhancement for any orientation at the corner point for increasing distance to the nanoantenna. For the central point on the contrary, the orientation parallel to the nanorod symmetry axis increases from initial efficiency reduction up to a spacer distance of about 5 nm to roughly match the behavior at the corner point and decrease for bigger spacer distances. The other orientation in the central point starts at a significant emission efficiency reduction and only slightly increases farther from the nanoantenna top face.

Summarizing, this means that the emission efficiency enhancement in the central spot shows the same general behavior as the excitation enhancement: the plasmonic enhancement is spoiled in close proximity to the nanoantenna itself. For one orientation in the central spot, there is a form of recuperation of the enhancement visible as the distance increases. The corner spot on the other hand behaves as expected from coupling to a single highly radiative plasmonic mode: smaller plasmonic enhancement farther from the nanoantenna.

This general behavior also manifests for the fluorescence enhancement according to Eqn. (4.2), as depicted in Fig. 4.6(b): Enhancement in the corner spot and reduction in the central spot. The fact that this leads to a fluorescence quenching for the entire antenna array and the monolayer flake for low spacer thicknesses, as shown in Fig. 4.3(c), can be explained by geometrical arguments: Firstly, only a

---

fraction of the fluorescent two-level systems within the flake are located in the vicinity of the nanoantenna due to the vast spacing between the nanoantennas. This means the overall enhancement will not profoundly enlarge the averaged emission measurement from a certain area. Secondly, only the regions around the edges of the nanoantenna top face contribute to the enhancement for thin spacers, while the geometrically bigger central region of the antenna top face rather diminishes the emission of two-level systems. Hence, without further statistical analysis it is evident that too few of the two-level systems benefit from the enhancement at the nanoantenna edge.

With the experimental quenching measurement qualitatively reproduced, the question of its origin obtrudes. Since the corner spot shows exactly the expected behavior for the model of a single plasmonic cavity mode supporting the emission process, this model applies at least partially. It rather requires expansion to cover the behavior in the other positions as well. This assumption is verified by investigation the radiative enhancement due to the nanoantenna for the different spots and orientations, as it is shown in Fig. 4.6(c). Here, all spots and orientations generally behave in the same manner: The radiative enhancement is reduced with increasing spacer thickness, since the enhancement relies on the enhancement of the local field, which in turn becomes less pronounced with increasing distance to the nanoantenna surface.

Combined with the emission efficiency behavior from Fig. 4.6(a), this means that the quantum systems located at the corner spots or around the edge indeed only couples to a single highly radiative plasmonic mode supported by the nanoantenna. But for the central spot the non-radiative losses must disproportionately increase, in comparison to the coupling to a single mode, to cause the drop in efficiency for thin spacer layers. This is the result of the excitation of an additional, higher order plasmonic mode that only contributes in form of non-radiative losses. The dark mode may or may not exhibit significant radiative losses, the observed behavior that shall be modeled only allows the conclusion that the non-radiative losses have to be taken into account. The interplay between such bright<sup>[265,317]</sup> and dark<sup>[318,319]</sup> plasmonic modes has been observed before<sup>[261,320]</sup> and is in no way prohibited in the experimental setup with the near field coupling<sup>[321,322]</sup> between the quantum system and the nanoantenna, even though it was not intended by design of the experiment. This means that the quenching results from the simultaneous excitation of a bright and at least one dark mode. The coupling to the dark mode results in an enhancement of non-radiative losses which lowers the fluorescence enhancement through the drastically lowered emission efficiency.

But a solution to restore an overall enhancement due to the presence of the nanoantenna is also at hand: the emission efficiency enhancement exhibits a maximum for a spacer of about 7 nm and the enhancement catches up to the corner spot for one orientation. This means that the dark mode excitation is a true near field effect and hence it is reduced with increasing distance. Combined with the reduced plasmonic enhancement with increasing distance, this trade-off ensures an optimal spacer thickness with both biggest enhancement through the bright mode and lowest reduction through the dark mode.

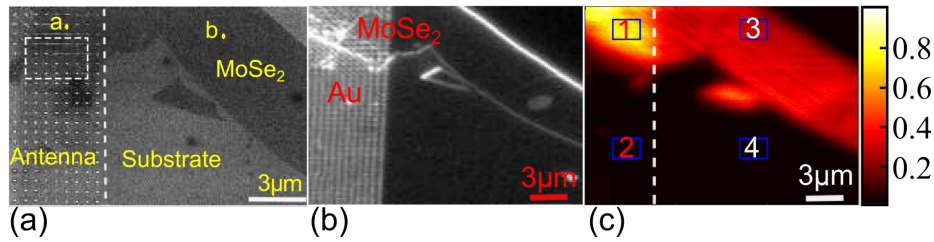


Figure 4.7: Experimental setup used for photoluminescence measurement with thicker spacer layer:  $\text{MoSe}_2$  flake covering both nanoantenna array (left) and bare substrate (right). Scanning electron microscope (a)<sup>[313]</sup> and optical image (b)<sup>[313]</sup> of measurement sample. Corresponding spatial photoluminescence mapping of the same second sample (c)<sup>[313]</sup>.

Ultimately, this conjecture regarding an overall restored fluorescence enhancement due to the nanoantenna can be experimentally proven for a spacer thickness of 7 nm, as shown in Fig. 4.7(a) to (c). Including a spacer layer of 7 nm thickness drastically alters the measurement outcome: The desired enhancement of the emission and fluorescence due to the presence of a specifically tailored nanoantenna is shown in Fig. 4.7(c) in region **1** in comparison to region **3**.

### Concluding Remarks

Even though the experimental measurements revealed a more complex behavior than initially expected, ultimately, the adjusted model could qualitatively reproduce the observed phenomena of both fluorescence quenching and enhancement, solely determined through the thickness of the spacer layer between the antenna array and the monolayer flake under realistic experimental conditions. Based on this fundamental agreement between theoretical description and experimental measurement, more elaborate processes can be outlined and theoretically described to motivate further experimental efforts in such a direction. It seems natural to initially further investigate the near-field interaction that played a crucial part in the previous interaction scenario.

---

## 4.2 Mode Conversion within Bimodal Nanoantennas

With the fundamental manipulation of emission properties in form of quenching and enhancement of a fluorescence rate demonstrated in an experimental context, the next logical step is to aim for higher functionalities in the form of the influencing.

The obvious ansatz is to investigate photonic devices, aiming for the unmatched plasmonic confinement<sup>[323]</sup> to either reduce their size or enhance their performance. Especially miniaturization mechanisms and integration techniques are still lacking for optical signal-processing schemes to compete with modern electronics<sup>[324]</sup>. At this point, plasmonics can provide a controllable means to elude the seemingly omnipresent diffraction limit, hence presenting itself as the stepping stone towards high-performance integrated photonic chip technology<sup>[325]</sup>. Consequently, active and passive devices combining high speed performance with compact geometrical dimensions, such as photodetectors<sup>[138,326–329]</sup>, electrooptic modulators<sup>[330–333]</sup>, plasmonic de-<sup>[334,335]</sup> and multiplexer<sup>[336–338]</sup>, antennas for energy harvesting<sup>[339–341]</sup>, waveguides<sup>[342–347]</sup>, and waveguide couplers<sup>[348–354]</sup> have been investigated.

### Bimodal Nanoantenna

The following three application examples shall extend the variety of photonic devices by a further, crucial mechanisms, beginning with the conversion between different modes<sup>[355]</sup> supported by the nanoantenna. The work presented in the following has been published in three devoted publications<sup>[356–358]</sup>. The benefit from such an interplay between cavity modes is to utilize or even exploit specific or even unique properties of nanoantenna modes in a controlled manner<sup>[359]</sup>.

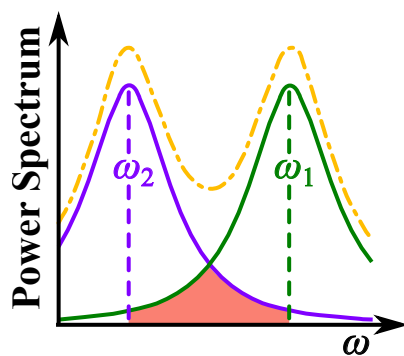


Figure 4.8: The spectrum of a bimodal nanoantenna shows two resonant modes at  $\omega_1$  and  $\omega_2$ ; here in green resp. purple<sup>[358]</sup>.

The most obvious conversion scenario involves an optical nanoantenna supporting two plasmonic modes as shown in Fig. 4.8. These modes may either appear as single Lorentzian peaks, as depicted in green and purple, or as a collective response in form of the sum of the two Lorentzians, as depicted in the dash-dotted yellow line graph. Such a spectral response constitutes what shall be called a bimodal nanoantenna throughout the following. But for two of the three following applications - the first and the last - most importantly, the modes must exhibit a sizable spectral mode overlap.

Returning to the conversion scenario, if one of the two modes is excitable via far-field illumination while the other one is not, the benefit of the mode conversion, in form of access to a prior inaccessible mode, is at hand. At this point, it is important to point out that the nomenclature used here, regarding bright and dark modes, follows concepts introduced in context with the Fano effect<sup>[237]</sup>: namely that the excitability determines the brightness resp. darkness of a mode. This is relevant since the literature is not consistent in this point. Hence, in case of laser illumination a responsive mode is considered bright, while a mode without measurable response is considered dark. This does not stipulate any other property of the modes involved per se, especially not the magnitude of the loss rates or the ratio of radiative and non-radiative loss rate. The results and dynamics presented in the following have been published in J. Straubel, *et al.*, *Optics Letters* **41** (10), 2294 (2016)<sup>[356]</sup>.

The implementation of the bimodal nanoantenna in this specific case takes the form of two aligned golden nanorods, each with a square cross section of 20 nm by 20 nm. The two nanorods have lengths of 130 nm resp. 140 nm and enclose a gap of 10 nm. This gap in turn houses a two-level system in a central position whose transition dipole moment must be aligned with the nanoantenna symmetry axis to ensure the functionality of the conversion scheme. Finally, this assembly is engulfed in a glass matrix with the relative permittivity of  $\epsilon_{\text{env}} = 2.25$  as it is shown in Fig. 4.9.

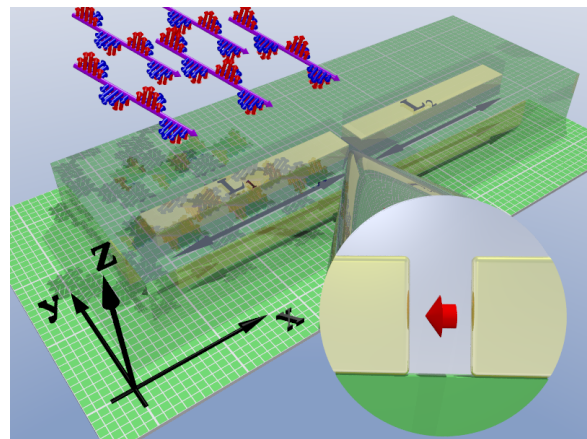


Figure 4.9: Symbolical: The double nanorod antenna contains a two-level system whose transition dipole moment is aligned with the symmetry axis of the nanoantenna. The entire configuration is embedded in a glass matrix and illuminated by a plane wave.

The ansatz of a bimodal nanoantenna in form of an aligned nanorod dimer originates on the one hand from the deliberation to rely on a well-investigated<sup>[261,360–363]</sup> and experimentally available<sup>[364–368]</sup> nanoantenna geometry to achieve a proof of principle of this photonic functionality. On the other hand, with two structures involved, each featuring its own resonances, and utilizing dipolar modes, potentially of higher order, a great deal of control through fundamental geometrical features over the spectral positions and further modal properties seems achievable, even though mode hybridization<sup>[369–373]</sup> is to be expected.

Performing scattering calculations for two different excitation scenarios reveals the behavior desired for the envisioned mode conversion scheme: While illuminated by a plane wave polarized parallel to the nanoantenna's symmetry axis and propagating parallel to the nanoantenna's top face normal, only mode 1 shows a visible scattering response, hence is identified as the bright mode for the conversion.

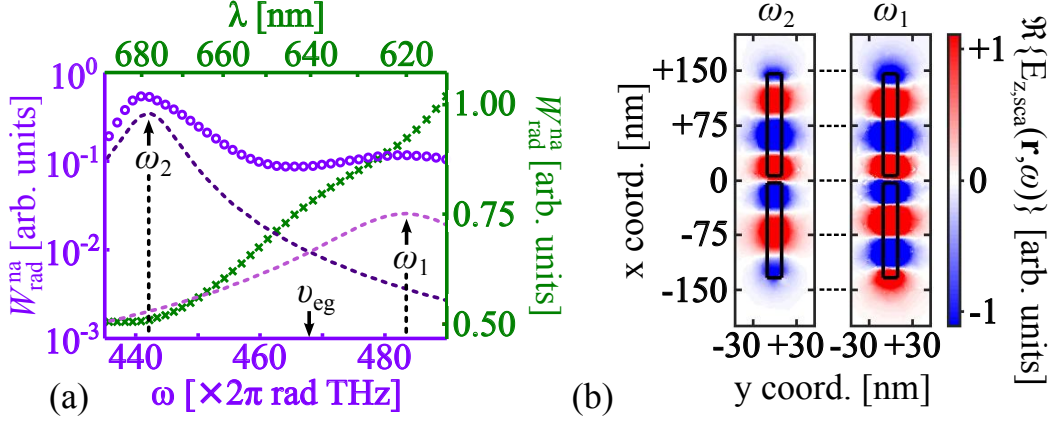


Figure 4.10: (a)<sup>[356]</sup> Scattering spectra of the bimodal nanoantenna: Purple circles represent scattering due to dipole excitation at the two-level system position, with the two dashed lines in purple shades showing the modal contributions of assumed Lorentzian shape. The green crosses show the scattering following plane wave illumination. (b)<sup>[356]</sup> Distribution of the characteristic field component mapped 10 nm above the nanoantenna's top face on resonance for  $\omega_1$  &  $\omega_2$ .

Following the illumination of an electric dipole located in the geometrical center of the nanoantenna gap and oriented according to the corresponding transition dipole moment of the two-level system - parallel to the nanoantenna's symmetry axis, the scattering spectrum shown in Fig. 4.10(a) features two distinct peaks. The spectrally local fit with Lorentzian lines according to Eqn. (3.16) determines the associated mode parameters<sup>[356]</sup>: Mode 1 is centered at  $\frac{\omega_1}{2\pi} = 484$  THz with a width in scattering of  $\frac{\Gamma_1^{\text{rad}}}{2\pi} = 28$  THz and a width in absorption of  $\frac{\Gamma_1^{\text{non}}}{2\pi} = 42$  THz. Mode 2 is centered at  $\frac{\omega_2}{2\pi} = 442$  THz with a width in scattering of  $\frac{\Gamma_2^{\text{rad}}}{2\pi} = 10$  THz and a width in absorption of  $\frac{\Gamma_2^{\text{non}}}{2\pi} = 8$  THz. The emergence of mode 2 for the near-field excitation<sup>[321,322]</sup> with the localized electric point dipole identifies mode 2 as the dark mode for the conversion. The dipole moment for these scattering calculations has been chosen to represent a nitrogen-vacancy center in diamond with a value of  $d_{\text{eg}} = 3.7 \times 10^{-29}$  Cm<sup>[374]</sup>. Equating the classical Purcell enhancement for the dipole excitation with the emission enhancement of the cavity QED model according to Eqn. (3.15) results in coupling rates of  $\frac{g_1}{2\pi} = 51$  GHz and  $\frac{g_2}{2\pi} = 40$  GHz for a spontaneous emission rate of  $\frac{\gamma_{\text{ge}}^{\text{spo}}}{2\pi} = 35$  MHz in the glass matrix.

Inspection of the field distribution characteristic for each mode as depicted in Fig. 4.10(b) confirms the identification of bright mode 1 and dark mode 2: Employing the resonance behavior of a nanowire<sup>[273]</sup> to describe the hybridized modes of the nanorod dimer, the mode number 6 can be assigned to the bright mode that exhibits a  $\pi$  phase difference between both ends of the dimer, which highlights the excitability through a local plane wave field. Whereas the mode number 5 can be assigned to the dark mode<sup>[254,375,376]</sup> with the field at both ends of the dimer in phase, resulting in the lack of response to the plane wave. However, the field distribution in the gap is similar for both modes and can be provided by a localized dipole. Consequently both modes are bright with respect to the dipole excitation.

Even though the dimer nanorod antenna with two nanorods of different lengths meets the requirement of symmetry breaking to generally provide far-field access to both longitudinal modes of even and odd nodal numbers<sup>[242,320,377,378]</sup> or couple the two<sup>[379]</sup>, the scattering due to the plane wave illumination demonstrates that the two-level system is required to enable access to the dark mode.

### Mode Conversion

Since any process involving a two-level system essentially operates on the single excitation and single photon level, the usage of the cavity QED light-matter interaction model is at hand. Incorporating the two plasmonic modes supported by the bimodal nanoantenna, the two-level system transition at  $\frac{\nu_{eg}}{2\pi} = 470$  THz representing the nitrogen-vacancy center in diamond<sup>[374]</sup>, and the external laser drive at  $\omega_{dri}$  and the strength expressed in terms of the Rabi frequency  $\Omega$ , the corresponding Hamiltonian, in a frame rotating with the drive frequency, reads<sup>[356]</sup>:

$$\begin{aligned} \mathcal{H}_{con}/\hbar = & \sum_{\xi=1,2} (\omega_{\xi} - \omega_{dri}) a_{\xi}^{\dagger} a_{\xi} + (\nu_{eg} - \omega_{dri}) \sigma_{eg} \sigma_{ge} \\ & + \sum_{\xi=1,2} g_{\xi} \left( \sigma_{eg} a_{\xi} + a_{\xi}^{\dagger} \sigma_{ge} \right) + \Omega \left( a_1^{\dagger} + a_1 \right) . \end{aligned} \quad (4.4)$$

Pivotal for the conversion scheme, the Hamiltonian (4.4) contains the direct driving of the bright nanoantenna mode 1 by an incident laser field at strength  $\Omega$ . Mode 1 in turn is coupled to the two-level system transition via coupling rate  $g_1$  and mode 2 couples to the two-level system transition at rate  $g_2$ . This Hamiltonian immediately reveals the working of the two-level system as a bridge to connect the two modes and hence grant access to the dark mode. To properly model any emission of the system back into the far field, the system needs to be opened up to radiation fields and other decay processes via a master equation formulation in appropriate

---

Lindblad form<sup>[356]</sup>:

$$\begin{aligned} \partial_t \rho_{\text{con}}(t) = & -\frac{i}{\hbar} [\mathcal{H}_{\text{con}}, \rho_{\text{con}}(t)] + \sum_{\xi=1,2} \Gamma_{\xi}^{\text{tot}} \mathcal{L}_{\xi}^{\text{cav}}(\rho_{\text{con}}(t), a_{\xi}) \\ & + \gamma_{\text{ge}}^{\text{spo}} \mathcal{L}_{\text{ge}}^{\text{spo}}(\rho_{\text{con}}(t), \sigma_{\text{ge}}) + \gamma^{\text{dep}} \mathcal{L}^{\text{dep}}(\rho_{\text{con}}(t), \sigma_{\text{eg}} \sigma_{\text{ge}}) \quad . \quad (4.5) \end{aligned}$$

Here, the decay channels, rivaling with the reversible energy exchange between cavity modes and two-level system, are the cavity losses of both modes  $\xi = 1$  and  $\xi = 2$ , implemented with each a total loss rate  $\Gamma_{\xi}^{\text{tot}} = \Gamma_{\xi}^{\text{rad}} + \Gamma_{\xi}^{\text{non}}$ , the spontaneous emission of the two-level system into the far field, at the previously mentioned rate in glass of  $\frac{\gamma_{\text{eg}}^{\text{spo}}}{2\pi} = 35$  MHz, and the dephasing<sup>[380,381]</sup> of the two-level system, at a characteristic rate  $\frac{\gamma^{\text{dep}}}{2\pi}$  in the low MHz range for nitrogen-vacancy centers in diamond<sup>[382]</sup>.

The stationary solution of Eqn. (4.5), acquired numerically<sup>[128]</sup>, provides the desired dynamics regarding the emission from the dark mode 2 into the far field, as a consequence of an external laser driving of the bright mode 1 and bridging via near-field coupling to the two-level system.

The cavity QED modeling of the mode conversion and its evaluation has been implemented by Dr. Karolina Słowik from the quantum mechanics division of the Nicolaus Copernicus University Torún in cooperation with Dr. Robert Filter from the Abbe Center of Photonics of the Friedrich Schiller University Jena. At this point it is important to highlight that the ratios of the obtained quantum model parameters, namely all cavity loss rates well in the THz range combined with coupling rates limited to the GHz range, locate the performance window of the proposed mode conversion scheme well within the incoherent weak coupling regime. Consequently, the semi-classical cavity QED interaction model, as it has been previously outlined, is perfectly well-suited to describe the desired mode conversion dynamics.

To properly analyze the mode conversion performance, the definition of specific figures of merit emerges naturally. An emission rate into the far field can benchmark the measurable result of the conversion. Based on Eqn. (4.5), the stationary modal emission rates into the far field can be established according to<sup>[356]</sup>

$$r_{\xi} = \Gamma_{\xi}^{\text{rad}} \langle a_{\xi}^{\dagger} a_{\xi} \rangle \quad , \quad (4.6)$$

with the modal population  $\langle a_{\xi}^{\dagger} a_{\xi} \rangle$  and the modal radiative loss rate  $\Gamma_{\xi}^{\text{rad}}$ . Figure 4.11(a) shows the dark mode emission rate  $r_2$ , pertinent to the conversion performance, over two parameters that are available for in situ modifications in an experimental realization: the strength  $\Omega$  and the detuning  $\delta\omega_{\text{dri}} = \omega_{\text{dri}} - \nu_{\text{eg}}$  of the

external driving of the bright mode 1. This plot primarily shows the combination of two mechanisms: The dark mode emission rate  $r_2$  increases proportional to the strength of the driving  $\Omega$  up to a saturation at  $r_2 \approx 70$  MHz. Additionally, the desired rate  $r_2$  is reduced with increasing detuning of the driving from the two-level transition frequency. This behavior is both intelligible and expected, as the conversion is fed by the driving and mediated by the two-level transition.

The second figure of merit shall be the conversion efficiency according to<sup>[356]</sup>

$$\eta_{\text{con}} = \frac{r_2}{r_1 + r_2} . \quad (4.7)$$

Determining the ratio of photons emitted in the desired dark mode compared to the total emitted photons in both modes, the conversion efficiency roughly benchmarks the return on invest in pumping. The conversion efficiency is plotted over both driving strength  $\Omega$  and detuning  $\delta\omega_{\text{dri}}$  in Fig. 4.11(b). While  $\eta_{\text{con}}$  reacts similarly to an increased detuning as the emission rate  $r_2$ , with an immediate decrease, the reduction of  $\eta_{\text{con}}$  with increasing pump strength reveals the most efficient conversion regime, with  $\eta_{\text{con}} \approx 0.5$ , for low pumping strength. Using the far-field driving strength the trade-off between conversion emission rate and efficiency can be scanned.

The asymmetry of both the optimal dark mode emission rate and the optimal dark mode conversion efficiency with respect to the detuning  $\delta\omega_{\text{dri}}$  visible in Fig. 4.11(a) and (b) is a consequence of the coupling of the two-level system to detuned nanoantenna modes<sup>[356]</sup> analogous to the vacuum Lamb shift<sup>[383]</sup> and with a magnitude of approximately 0.3 GHz<sup>[383]</sup>.

Even though this investigation shall only serve as a proof of principle of the mode conversion scheme via plasmonic light-matter interaction, it is possible to outline the potential performance on this general setup. Since the central point of the mode conversion relies on the mode coupling via the two-level system, the coupling rates  $g_1$  and  $g_2$  crucially determine the quality of the bridging role the two-level transition plays for the overall mode conversion. Hence, the two figures of merit, dark mode emission rate  $r_2$  and conversion efficiency  $\eta_{\text{con}}$  are shown in Fig. 4.11(a) and (b) over the two light-matter coupling rates.

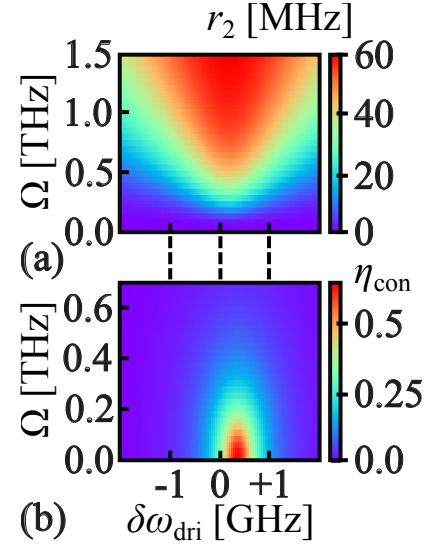


Figure 4.11: Dark mode emission rate  $r_2$  in (a)<sup>[356]</sup> and mode conversion efficiency  $\eta_{\text{con}}$  in (b)<sup>[356]</sup> plotted over the strength  $\Omega$  and detuning  $\delta\omega_{\text{dri}}$  of the external driving.

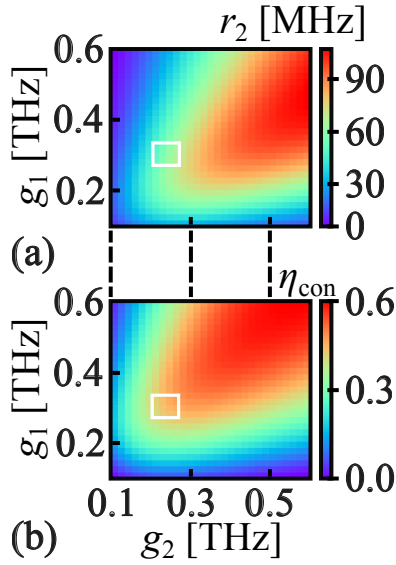


Figure 4.12: Dark mode emission rate  $r_2$  in (a)<sup>[356]</sup> and mode conversion efficiency  $\eta_{\text{con}}$  in (b)<sup>[356]</sup> plotted over the coupling rates  $g_1$  and  $g_2$  between the two cavity modes and the transition of the two-level system. The white squares highlight the parameter regime achievable with this very nanoantenna.

izable with an optimized nanoantenna design.

### Concluding Remarks

Through the proof of principle of cavity mode conversion mediated by light-matter coupling to a two-level system, a higher level of photonic functionality is realized in the incoherent weak coupling regime for the hybrid system of bimodal nanoantenna coupled to a quantum system characterized by an electric dipolar transition. At the core the mode conversion scheme relies on the near-field excitability of plasmonic cavity modes that already emerged in the theoretical modeling of the first application. But this time the near-field excitability has been deliberately employed to gain access to a cavity modes that remains dark for far-field excitation.

But to truly render itself a technology suitable for the next generation of information processing applications, the light-matter interaction utilizing plasmonic cavities must also demonstrate its aptitude in scenarios involving quantum information applications. This is what the following two examples shall illuminate.

Both the emission rate and the efficiency exhibit the same general behavior for an increase in the coupling rates: both show an initial increase as well, since the mode coupling directly depends on high coupling rates via the two-level system. But there is also an overall limit for the benefit of the mode conversion through increased coupling rates: The coupling rates directly compete with the cavity loss rates. This competition does not just classify weak or strong coupling regimes, it also determines whether the excited cavity mode emits into the far field or couples back to the two-level system. In case of the excited mode 1 the coupling is desired, while an excited mode 2 shall rather emit into the far field to ensure optimal mode conversion and efficiency.

The performance window achievable with the described bimodal nanoantenna and variation of the position of the two-level system along the symmetry axis within the nanorod dimer gap is shown as white squares in Fig. 4.11(a) and (b). Coupling parameters beyond the white squares may be real-

### 4.3 Bimodal Nanoantenna as Single Photon Source

In light of the ambitious aspiration of purely photonic transfer<sup>[384]</sup> and processing<sup>[385,386]</sup> of information that promises to surpass any classical limitations or benchmarks<sup>[387]</sup>, the importance of the availability of single photons, both in dependable supply and on demand, to accomplish light-matter interaction on the atom-photon level<sup>[19]</sup>, is indisputable.

Consequently, single photon sources, allocating a fundamental utensil, such as the elementary portions of electromagnetic energy for quantum physical experiments or applications of any fashion in a controlled manner, have been the subject of long-standing research activities. Resulting in no shortage of different incarnations: from spontaneous parametric down-conversion in nonlinear crystals either supplemented by spectral filtering<sup>[388–390]</sup> or a surrounding cavity<sup>[391–397]</sup>, to four-wave mixing in magneto-optical traps<sup>[398–400]</sup>, electroluminescent quantum dots<sup>[401–403]</sup>, and localized two-level systems driven by ns- to ps-pulses<sup>[404–406]</sup>.

But considering photonic devices utilizing plasmonic resonances, a plasmonic implementation augurs unique advantages, mainly with respect to a compact form and integrability<sup>[407]</sup>. But actually, any plasmon-mediated light-matter interaction with a single quantum system coupled to a radiative cavity mode meets the condition of single photon emission, given proper driving, may it be optically<sup>[408–411]</sup> or electronically<sup>[412–415]</sup>, due to the inherent single photon nature of the quantized interaction.

#### Bimodal Nanoantenna

However, the following example shall incorporate higher functionality on the side of the plasmonic cavity: The outlined plasmonic single photon source shall not just operate solely upon excitation with a plane wave laser drive, without any further requirements than a fixed frequency, it shall in addition allow for the implementation of a triggered *modus operandi*, realizing single photon generation on demand. Not to mention that the aforementioned triggered functioning does not require any change in fabrication or preparation. It can be controlled entirely by the laser illumination.

The implementation of such a plasmon-enhanced single photon source, including an optional trigger mechanism, relies once again on the interaction dynamics between plasmonic cavity modes and electric dipole transition between higher and lower energy states of a quantum system. The single photon generation also involves a bimodal nanoantenna composed of a nanorod dimer, but the pivotal

difference to the previous examples provides the quantum system in form of a level scheme more complicated than a mere two-level system. Incorporating a three-level system instead, more specifically a  $\Lambda$ -type quantum system, naturally enables more sophisticated dynamical behavior. The results and dynamics presented in the following have been published in J. Straubel, *et al.*, *Physical Review B* **93** (19), 195412 (2016)<sup>[357]</sup>.

While the basic process that grants the single photon nature, including the trigger mechanism, has been already discussed in form of a  $\Lambda$ -type system coupled to a single mode of a high finesse optical cavity<sup>[416]</sup>, this application example shall not just demonstrate the realization with a realistic plasmonic cavity, but also increase the performance by including two cavity modes. With the  $\Lambda$ -system at the core of the single photon generation, naturally the bimodal nanoantenna is geometrically tailored to accommodate its properties, mainly the two dipolar transitions involved in the single photon generation.

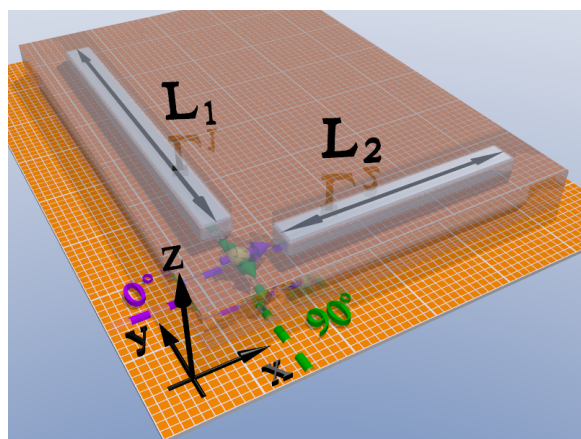


Figure 4.13: Symbolical: L-shaped nanorod dimer houses the  $\Lambda$ -type quantum dot in its vertex. The dipole transitions are shown through transition dipole moment orientations in green and purple and each nanorod is tailored to couple to one transition. The whole configuration is embedded in a glass matrix.

Self-assembled semiconductor InAs quantum dots have been investigated and shown to feature the desired  $\Lambda$ -type level scheme with two lower energy states and a shared higher energy state<sup>[417–419]</sup>. While the transitions between each lower and the mutual higher energy state are electric dipolar in nature, the transition between the lower energy states themselves is dipole forbidden. This behavior is rooted in the different polarizations of the two dipole transitions to the higher energy state, i.e. the  $90^\circ$  angle between the transition dipole moment orientations of the two transitions. Consequently, employing a nanorod dimer as the bimodal nanoantenna, it now takes an L-shaped form to couple to both dipolar transitions.

The single photon generation configuration involving a  $\Lambda$ -type quantum system is shown in Fig. 4.13. The nanorods each have a square cross section of 20 nm by 20 nm, lengths of 160 nm resp. 250 nm and are made from silver. Both nanorods have been positioned in such a way that they form an L-shape, enclosing a gap around the vertex of the L-shape by symmetrically displacing each nanorod 13.5 nm

from it. The  $\Lambda$ -type quantum dot is positioned in the vertex of the L-shape in a way that each transition dipole moment is parallel to one of the two nanorods. Finally, the entire setup is engulfed in a glass matrix with  $\varepsilon_{\text{env}} = 2.25$ .

At this point it is important to note that the change of the nanoantenna geometry from aligned nanorod dimer to L-shape with two nanorod arms does in no way constitute a constraint regarding the availability of such nanoantennas for experimental use or controllability of their geometrical features, as these nanoantennas are just as well investigated<sup>[363,420]</sup> and experimentally tested<sup>[364–366,368,421]</sup>. In general, also other nanoantennas could have been considered.

Incipiently, scattering simulation are performed with an electric dipole located in the vertex of the L-shape. The associated dipole moment, whose orientation is scanned in the plane of the nanorod dimer, is chosen with  $\mathbf{d}_{\text{eg}} = 6 \times 10^{-29}$  Cm so that experimentally measured spontaneous emission rates for quantum dots<sup>[419,422]</sup> can be reproduced according to Eqn. (2.40) from Weisskopf-Wigner theory.

Resulting scattering spectra for four characteristic dipole orientations are shown in Fig. 4.14(a). The corresponding angles of  $0^\circ$ ,  $30^\circ$ ,  $60^\circ$ , and  $90^\circ$  are measured with respect to the symmetry axis of the shorter nanorod. The scattering spectra, especially for  $0^\circ$  and  $90^\circ$ , shown in Fig. 4.14(a) reveal the behavior the nanoantenna is designed for: two nanoantenna modes at  $\frac{\omega_1}{2\pi} = 270$  THz (dark green line) and  $\frac{\omega_2}{2\pi} = 250$  THz (dark purple line) for two perpendicular orientations of the dipole moment in the nanoantenna plane. These two modes are the essential contribution of the nanoantenna and will couple to the transitions of the  $\Lambda$ -type quantum system. The central frequencies of these two modes are chosen according to typical values for quantum dots, hence can be easily shifted to another spectral range while still maintaining the single photon generation scheme, as long as the nanoantenna modes resonantly match the transitions of the  $\Lambda$ -type quantum system.

The modes are again fitted with Lorentzian lines according to Eqn. (3.16). This yields decay rates of  $\frac{\Gamma_1^{\text{rad}}}{2\pi} = 11$  THz,  $\frac{\Gamma_1^{\text{non}}}{2\pi} = 11$  THz,  $\frac{\Gamma_2^{\text{rad}}}{2\pi} = 16$  THz, and  $\frac{\Gamma_2^{\text{non}}}{2\pi} = 35$  THz. In the next step, the classical emission enhancement is again equated to the enhanced emission rate in the cavity QED model to determine the light-matter coupling rates for both cavity modes:  $\frac{g_1}{2\pi} = 91$  GHz and  $\frac{g_2}{2\pi} = 92$  GHz. Considering the values of  $\Gamma_\xi^{\text{tot}}$  and  $g_\xi$ , the incoherent weak coupling regime is ensured.

With the crucial light-matter interaction model parameters determined from two characteristic scattering and absorption spectra, the spectra for dipole moment orientations in between the characteristic values of  $0^\circ$  and  $90^\circ$  displayed in Fig. 4.14(a) expose a smooth transition from exclusively exciting one mode to exciting both modes with different strengths to exclusively exciting the other mode.

This behavior also shows in the field distributions in a plane 5 nm above the nanoantenna on resonance for each mode. These mappings display each mode mainly causing a response from the nanorod arm that the dipole moment is aligned with. Consequently, a rotation in the nanoantenna plane results in a corresponding projection of the dipolar field distribution on the two nanorod arm. This agrees with a continuous excitation of each mode according to the dipole orientation. Since the transition dipole moments of the suitable quantum dots intrinsically maintain the  $90^\circ$  angle, only the overall orientation of the quantum dot transition moments - each aligned with a nanorod - needs to be realized in an experiment. Ensuring this specific orientation is elementary for the single photon generation scheme, since each cavity mode should predominantly couple to only one of the two transitions.

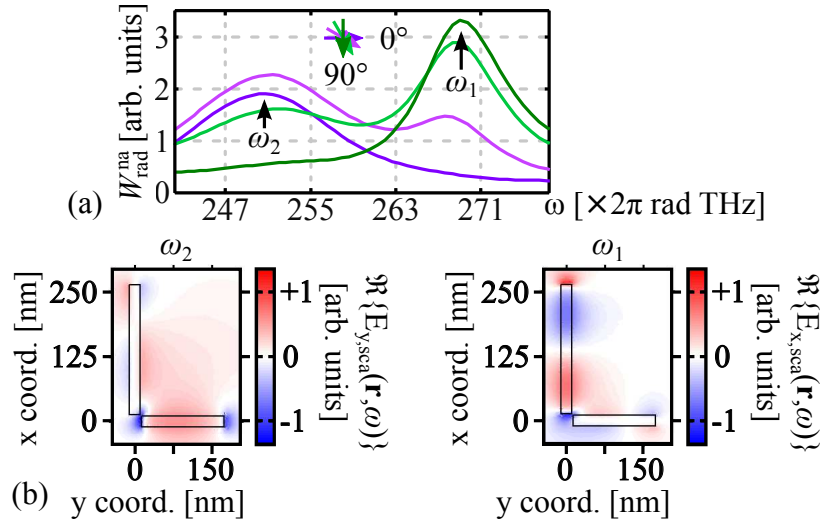


Figure 4.14: (a)<sup>[357]</sup> Scattering spectra of the bimodal nanoantenna shown for different dipole orientations: dark purple for  $0^\circ$ , bright purple for  $30^\circ$ , bright green for  $60^\circ$ , and dark green for  $90^\circ$ . (b)<sup>[357]</sup> Distribution of the characteristic field component mapped 5 nm above the nanoantenna's top face on resonance for  $\omega_1$  &  $\omega_2$ .

Furthermore, the distributions of the characteristic field components on resonance depicted in Fig. 4.14(b) display not just the expected mode hybridization<sup>[369–373]</sup>, but also another important difference between the two nanoantenna modes: The dominant field distribution of mode 1 at  $\omega_1$  along the longer nanorod exhibits a  $\pi$  phase difference between the two ends of the nanorod. Just like in case of the mode conversion example, this means that this mode is excitable via far-field plane wave excitation. In contrast, the dominant field distribution of mode 2 at  $\omega_2$  along the shorter nanorod shows both ends of the nanorod in phase. Regarding far-field excitation, mode 1 is bright and mode 2 dark. But both modes scatter into the far field upon point dipole excitation as shown in Fig. 4.14(a).

## Single Photon Generation Scheme

To model the actual single photon emission dynamics the cavity QED light-matter interaction model is once again called into action and once again the quantum modeling is performed by Dr. Karolina Słowik and Dr. Robert Filter. As already mentioned, to implement the single photon emission the  $\Lambda$ -type quantum system, consisting of the lower energy states  $|\Psi_1\rangle$  with the energy  $\hbar\nu_{|\Psi_1\rangle}$  and  $|\Psi_2\rangle$  with the energy  $\hbar\nu_{|\Psi_2\rangle}$  and the shared higher energy state  $|\Psi_e\rangle$  with the energy  $\hbar\nu_{|\Psi_e\rangle}$ , is coupled to two cavity modes - each transition to one mode. Additionally, with mode 1 being bright, i.e. receptive to far-field plane wave illumination, a direct far-field drive with  $\omega_{\text{dri}}$  through mode 1 can be carried out. The corresponding Hamiltonian, in the frame rotating with  $\omega_{\text{dri}}$ , reads<sup>[357]</sup>

$$\begin{aligned} \mathcal{H}_{\text{sin}}/\hbar = & \sum_{\xi=1,2} (\omega_{\xi} - \omega_{\text{dri}}) a_{\xi}^{\dagger} a_{\xi} + \sum_{\xi=1,2} v_{|\Psi_{\xi}\rangle} \sigma_{\xi\xi} + (v_{|\Psi_e\rangle} - \omega_{\text{dri}}) \sigma_{ee} \\ & + \sum_{\xi=1,2} \left( g_{\xi} a_{\xi}^{\dagger} \sigma_{\xi e} + g_{\xi}^* \sigma_{e\xi} a_{\xi} \right) + \left( \Omega a_1^{\dagger} + \Omega^* a_1 \right) . \end{aligned} \quad (4.8)$$

Here,  $\sigma_{\alpha\beta}$  denote the state transition operators of the quantum system according to  $\sigma_{\alpha\beta} = |\Psi_{\alpha}\rangle \langle\Psi_{\beta}|$ . Besides the free evolution of both the cavity modes and the quantum system in the first line of Eqn. (4.8), the second line contains the previously mentioned coupling between each transition and one cavity mode as well as the direct drive of mode 1 with the strength  $\Omega$ . The drive acting on the quantum system itself can be safely neglected due to the large polarization of the nanoantenna<sup>[357,423]</sup>.

With the intention to emit single photons into the far field, the cavity mediated light-matter interaction from Eqn. (4.8) naturally has to be transformed to an open quantum system by the usual means of master equation in Lindblad form<sup>[357]</sup>:

$$\begin{aligned} \partial_t \rho_{\text{sin}}(t) = & -\frac{i}{\hbar} [\mathcal{H}_{\text{sin}}, \rho_{\text{sin}}(t)] + \sum_{\xi=1,2} \Gamma_{\xi}^{\text{tot}} \mathcal{L}_{\xi}^{\text{cav}}(\rho_{\text{sin}}(t), a_{\xi}) \\ & + \sum_{\xi=1,2} \gamma_{\xi e}^{\text{dep}} \mathcal{L}_{\xi e}^{\text{dep}}(\rho_{\text{sin}}(t), \sigma_{ee} - \sigma_{\xi\xi}) + \gamma_{12}^{\text{dep}} \mathcal{L}_{12}^{\text{dep}}(\rho_{\text{sin}}(t), \sigma_{22} - \sigma_{11}) \\ & + \sum_{\xi=1,2} \gamma_{\xi e}^{\text{spo}} \mathcal{L}_{\xi e}^{\text{spo}}(\rho_{\text{sin}}(t), \sigma_{\xi e}) + \gamma_{12}^{\text{non}} \mathcal{L}^{\text{non}}(\rho_{\text{sin}}(t), \sigma_{12}) . \end{aligned} \quad (4.9)$$

This includes again the cavity losses of both cavity modes with the corresponding rates  $\Gamma_{\xi}^{\text{tot}} = \Gamma_{\xi}^{\text{rad}} + \Gamma_{\xi}^{\text{non}}$ . Additionally, the spontaneous emission of the quantum system is included that transitions the excited state  $|\Psi_e\rangle$  to either lower energy state,  $|\Psi_1\rangle$  resp.  $|\Psi_2\rangle$ . The spontaneous emission rate for suitable quantum systems

can be estimated to remain within the MHz range, i.e.  $\gamma_{\xi e}^{\text{spo}} \approx \text{MHz}^{[419,422]}$ . Furthermore, with the dipole-forbidden radiative transition between the lower energy states, a non-radiative population transfer, accessible for external pumping, should be incorporated. A typical value for quantum dots amounts to about an order of magnitude smaller than the spontaneous emission rate  $\gamma_{12}^{\text{non}} \approx \gamma_{\xi e}^{\text{spo}}/10^{[419]}$ . The dephasing of each transition is also taken into consideration: the radiative transitions from  $|\Psi_e\rangle$  to one of the lower energy states at a rate  $\gamma_{\xi e}^{\text{dep}}$  in the GHz range<sup>[418,424–427]</sup> and the non-radiative transition from  $|\Psi_2\rangle$  to  $|\Psi_1\rangle$  at a rate  $\gamma_{12}^{\text{dep}} \approx 10 \text{ MHz}^{[418]}$ .

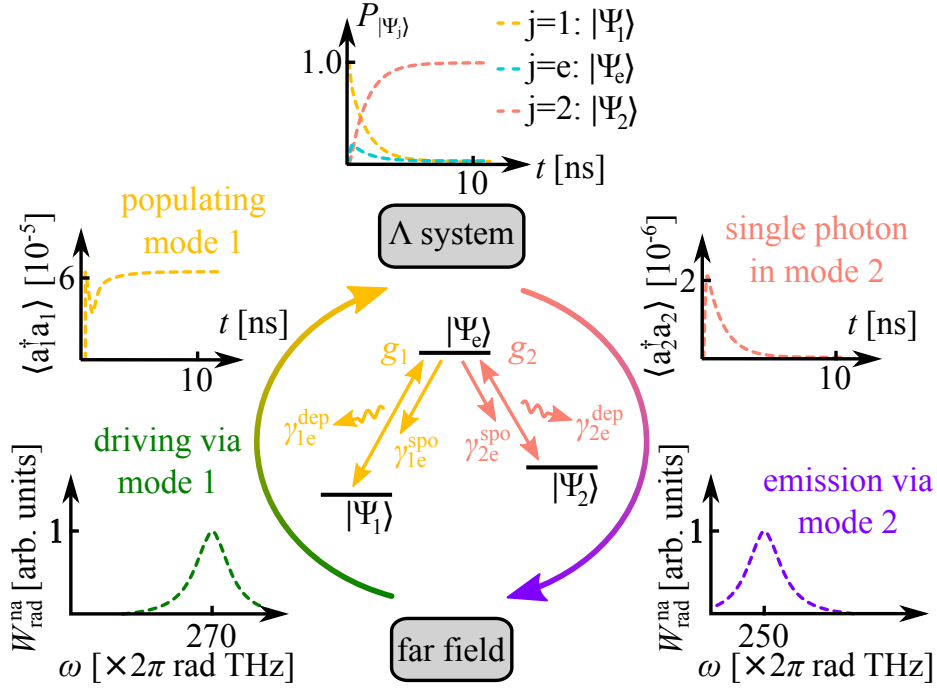


Figure 4.15: Single photon generation scheme<sup>[357]</sup>: Starting from the bottom left, clockwise, mode 1 is driven from the far-field (green dashed line). The population in mode 1 (yellow dashed line<sup>[357]</sup>) couples to the quantum system, which transitions to  $|\Psi_e\rangle$ . From  $|\Psi_e\rangle$  (turquoise dashed line<sup>[357]</sup>) the quantum system eventually transitions to the other lower energy state (bright orange dashed line<sup>[357]</sup>). This transition couples to mode 2 (purple dashed line), emitting into the far field.

Finally, the stationary solution to Eqn. (4.9) is determined numerically with open source software<sup>[128]</sup>. To investigate the dynamical behavior, the hybrid system consisting of the quantum system coupled to the nanoantenna was designed for, it is convenient to introduce the probabilities to find the  $\Lambda$ -type quantum system in any of the different states according to

$$P_{|\Psi_j\rangle} = \text{Tr}(\rho_{\Lambda\text{qs}} |\Psi_j\rangle \langle \Psi_j|) \quad , \quad (4.10)$$

with  $\rho_{\Lambda\text{qs}} = \text{Tr}_{\text{cav}}(\rho_{\text{sin}})$ , the corresponding partial density operator  $\rho_{\Lambda\text{qs}}$  and  $j =$

$\{1, 2, e\}$ . Monitoring these quantum system state probabilities together with the cavity mode populations  $\langle a_\xi^\dagger a_\xi \rangle$  with  $\xi = \{1, 2\}$ , the single photon generation and emission mechanism can be outlined as is depicted in Fig. 4.15.

Initially, the  $\Lambda$ -type quantum system shall be in state  $|\Psi_1\rangle$ , the lowest energy state out of the three. Since mode 1 is bright to external laser illumination, it can and shall be driven with a continuous laser field. This external drive fuels both radiative and nonradiative losses, characteristic to mode 1 (mode 1 symbolically shown in Fig. 4.15, bottom left, green dashed line). Given an appropriate strength  $\Omega$  of the external drive, the cavity mode losses  $\Gamma_1^{\text{tot}}$  can be surmounted, resulting in a built-up of a critical population in mode 1. But, through populating mode 1 with polaritons of suitable energy, the transition from  $|\Psi_1\rangle$  to  $|\Psi_e\rangle$  of the quantum system via light-matter coupling at rate  $g_1$  is impelled, as the nanoantenna is designed for mode 1 to be resonant with this transition at  $\frac{\omega_1}{2\pi} = \frac{v|\Psi_e\rangle - v|\Psi_1\rangle}{2\pi} = 270$  THz. Eventually, the quantum system will transition to the mutual excited state, dropping the population in mode 1 momentarily. But given the continuous external drive, the population in mode 1 will increase again up to the eventual steady state value according to the equipoise of losses in mode 1 and driving strength (population in mode 1 shown in Fig. 4.15, middle left, yellow dashed line).

Once in the highest energy state  $|\Psi_e\rangle$ , there are multiple relaxation paths for the quantum system to take: On the one hand, the transition back to  $|\Psi_1\rangle$ , either via spontaneous emission with  $\gamma_{1e}^{\text{spo}}$ , concatenated with the omni-directional emission of a photon into the far-field, or via excitation of the cavity mode 1 due to the light-matter coupling with  $g_1$ . In any case, the transition back to  $|\Psi_1\rangle$  simply resets the single photon generation scheme back to the beginning, since the driving is still applied and the excitation of the quantum system is continuously impelled. On the other hand, the quantum system can transition to  $|\Psi_2\rangle$ . This is done either via spontaneous emission with  $\gamma_{2e}^{\text{spo}}$ , concatenated with the omni-directional, or at least not specifically directed emission of a photon into the far-field, or via excitation of the cavity mode 2 due to the light-matter coupling with  $g_2$ , as mode 2 is resonant with this transition at  $\frac{\omega_2}{2\pi} = \frac{v|\Psi_e\rangle - v|\Psi_2\rangle}{2\pi} = 250$  THz by design.

Formally, both relaxation processes, each with two possible paths, are equal: there is a spontaneous emission path and a cavity mode excitation path. The spontaneous decay does result in the emission of a single photon into the far-field, but this emission is uncontrolled, i.e. omni-directional, hence undesired, if the single photon shall be used for subsequent quantum information purposes. However, the excitation of a cavity mode enables the coupling back to the quantum system, resulting in the transition back to  $|\Psi_e\rangle$ . This would also only set the single

---

photon generation back a step. But the excitation of the cavity mode is not just the most likely scenarios with the highest rate, it also the desired process.

While the excitation of mode 1 causes the emission of a photon into the far field with the efficiency  $\eta_1 = \frac{\Gamma_1^{\text{rad}}}{\Gamma_1^{\text{tot}}}$ , mode 2, when excited, emits a photon with the efficiency  $\eta_2 = \frac{\Gamma_2^{\text{rad}}}{\Gamma_2^{\text{tot}}}$ . But the crucial difference is that mode 1 constantly emits photons due to the continuous driving. However, mode 2 only emits a photon after the whole procedure involving the transition to and from the excited state  $|\Psi_e\rangle$  of the quantum system is traversed and most importantly, once in state  $|\Psi_2\rangle$  the quantum system remains in this meta-stable state (evolution of quantum system states shown in Fig. 4.15, top). Even though there is a decay mechanism back to  $|\Psi_1\rangle$ , it can be neglected on time scales of these single photon generation dynamics as the transition in general is dipole forbidden. This in turn guarantees no further population of mode 2 and no more emission from mode 2 (mode 2 population depicted in Fig. 4.15, middle right, bright orange dashed line), as the external drive, while still populating mode 1, causing emission here, can neither impel the transition from  $|\Psi_2\rangle$  to  $|\Psi_e\rangle$  nor from  $|\Psi_2\rangle$  to  $|\Psi_1\rangle$ .

Consequently, the cavity photon emitted by mode 2 into the far field (mode 2 symbolically shown in Fig. 4.15, bottom right, purple dashed line) remains a singular event providing the single photon nature. Further emission rate enhancement or a specific radiative pattern can be achieved through optimizing the geometry, which is omitted here.

## Implementing Trigger Mechanism

To advance the functionality of the hybrid system composed of bimodal nanoantenna and  $\Lambda$ -type quantum system to generate single photons on demand, no actual change in the setup is necessary. As already mentioned in the previous description of the single photon generation scheme, the transition from  $|\Psi_2\rangle$  to  $|\Psi_1\rangle$  can be impelled by external illumination. Consequently, applying appropriate pumping in form of a series of Gaussian pulses<sup>[357]</sup>:  $\Pi(t) = \Pi_0 \sum_{\kappa} e^{-\frac{(t-t_{\kappa})^2}{2\tau^2}}$  with the amplitude  $\Pi_0 = 2$  THz and width  $\tau = 1$  ns. With the reset transition enhanced enough to significantly contribute to the dynamic behavior, it has to be taken into consideration with an extended Jabłoński diagram, as shown in Fig. 4.16(a), and an additional term in Eqn. (4.9) in form of<sup>[357]</sup>:  $\Pi(t) \mathcal{L}^{\text{pump}}(\rho_{\Lambda\text{qs}}(t), \sigma_{12})$ . If the external driving subsequently also takes the form of a series of Gaussian pulses<sup>[357]</sup>:  $\Omega(t) = \Omega_0 \sum_{\kappa} e^{-\frac{(t-t_{\kappa}^*)^2}{2\tau^2}}$  with the amplitude  $\Omega_0 = 2$  THz, the performance of the hybrid system for single photon generation on demand can be investigated.

To that end an exemplary series of driving and pumping pulses centered at the times  $t_1^* = 4$  ns,  $t_2^* = 28$  ns,  $t_3^* = 64$  ns,  $t_1 = 16$  ns, and  $t_2 = 40$  ns, as depicted in Fig. 4.16(b) shall be incident on the hybrid system. Following a driving pulse, the quantum system ultimately transitions to state  $|\Psi_2\rangle$  as described for the single photon generation scheme, since the incidence of a driving field does not affect the desired single photon emission once state  $|\Psi_2\rangle$  is reached. This determines the appropriate driving pulse width and strength. After the photon emission from mode 2, the quantum system remains in state  $|\Psi_2\rangle$  until the whole procedure is reset by pumping  $|\Psi_2\rangle$  back to  $|\Psi_1\rangle$  with a pulse and the quantum system remains in  $|\Psi_1\rangle$  until a drive pulse sets the eventual photon emission from mode 2 in motion. The evolution of the  $|\Psi_j\rangle$  in (c)<sup>[357]</sup> shown over time.  $\Omega(t)$  and  $\Pi(t)$  from Fig. 4.16(b) are shown in Fig. 4.16(c) and follow the described causal chain of events.

Finally, to determine the single photon nature of the emission from mode 2, it is reasonable to resort to  $g^{(2)}(\tau)$  as it has been introduced in Eqn. (2.35). For mode 2 at zero time-delay this reads<sup>[357]</sup>:

$$g^{(2)}(0) = \frac{\langle a_2^\dagger a_2^\dagger a_2 a_2 \rangle}{\langle a_2^\dagger a_2 \rangle^2} . \quad (4.11)$$

Recalling, a  $g^{(2)}(0)$  value of 0 signifies the number state  $|1\rangle$ , the optimum for any single photon emission scenario.

Mapping  $g^{(2)}(0)$  over different driving  $\Omega_0$  and pumping  $\Pi_0$  strengths reveals an outstandingly high single photon quality in the emission, rendering the triggered single photon emission scheme successfully implemented. The reset through pumping is not detrimental for the single photon nature, because the emission

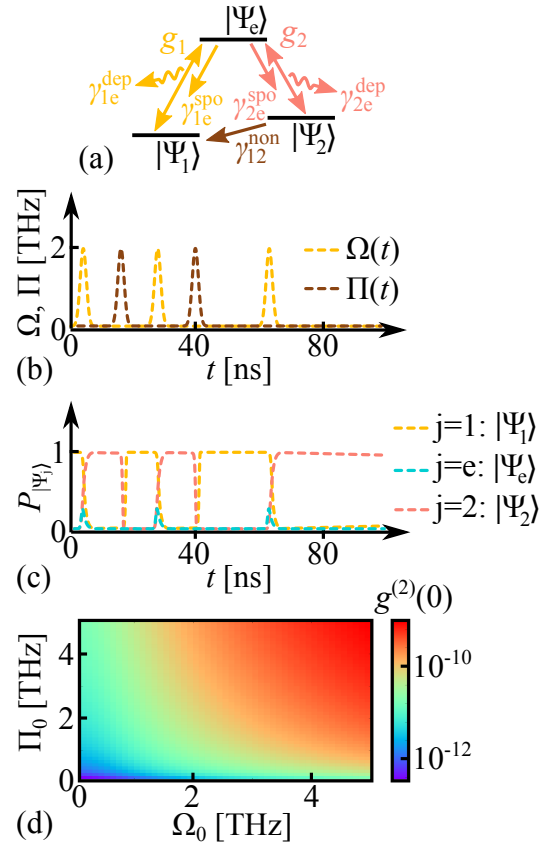


Figure 4.16: (a)<sup>[357]</sup> Jabłoński diagram includes reset transition.  $\Omega$  and  $\Pi$  pulses in (b)<sup>[357]</sup> and corresponding  $|\Psi_j\rangle$  in (c)<sup>[357]</sup> shown over time. (d)<sup>[357]</sup>  $g^{(2)}(0)$  plotted over drive  $\Omega_0$  and pump  $\Pi_0$  strengths.

---

rate  $\Gamma_2^{\text{rad}}$  exceeds driving and any light matter-coupling rate  $g_\xi$ , i.e. mode 2 decays before any additional population can be transferred to it.

### **Concluding Remarks**

For the implementation of the triggered single photon generation, the nanoantenna facilitates direct access to the radiative transitions of the quantum system. By deliberately feeding and extracting far-field photons to and from these transitions, the plasmonic cavity enables both control over and increase of emission of single photons in time without degrading the single photon nature.

The optical nanoantenna can provide even more functionality by originating the desired quantum optical phenomenon instead of only influencing it, as the final application shall demonstrate.

## 4.4 Bimodal Nanoantenna Emitting in Entangled Modes

Entanglement<sup>[428]</sup> is not just the most prominent phenomenon exclusive to quantum physical systems, it is also the central prerequisite for quantum computation schemes to elevate information processing performance to nonpareil heights<sup>[103,429]</sup>.

Consequently, entanglement has been the subject of numerous general conceptual investigations<sup>[430–434]</sup> as well as examinations of both different application scenarios<sup>[435–440]</sup> and aspects related to quantum information processing, directly<sup>[11,441–444]</sup> or indirectly<sup>[445–449]</sup>. Considering the possibilities and functionalities provided by cavity QED and its plasmonic implementation, corresponding research activity regarding entanglement follows naturally. This includes entanglement generally in context of quantum systems and photons<sup>[450–452]</sup> and especially involving cavities explicitly<sup>[453–455]</sup>.

To systematically make use of entanglement for any purpose, reliable sources of entangled photons<sup>[456–458]</sup> or means of entangling quantum systems<sup>[459–461]</sup> are in demand. Focusing on the realization of entanglement involving photons, the enhancement of the emission rate of any source of entangled photons through an optical nanoantenna<sup>[462]</sup> is evident. But as already mentioned, the optical nanoantenna can provide much more than just enhancement, as the following example shall outline. The results and dynamics presented in the following have been published in J. Straubel, *et al.*, *Physical Review B* **95** (8), 085421 (2017)<sup>[358]</sup>.

### Bimodal Nanoantenna

The fundamental process involved in the entangled emission is the coupling of the electric dipolar transition of a quantum system to two cavity modes, hence entangling the photon number in these modes. The generation of entanglement in this manner has already been conceptually described<sup>[463]</sup> and the involvement of a generally bimodal cavity follows naturally. The following shall illustrate the realization of this entanglement generation scheme using a plasmonic nanoantenna.

In fact, the very nanoantenna design from the previous example shall be the starting point to discuss the basic principle. Consequently, there are two nanorods, made from silver, whose symmetry axes are perpendicularly oriented, arranged in an L-shape by moving each nanorod 13.5 nm away from the vertex of the L-shape along each's symmetry axis. Both nanorods have square cross-sections of 20 nm by 20 nm and different lengths. The lengths of each nanorod shall be the one parameter of the nanodimer geometry whose influence on the desired entangled emission shall be investigated throughout the following. Initially, the

lengths are 160 nm and 250 nm respectively. Also similar to the previous example, the vertex of the L-shape, as the gap in the nanodimer, contains the quantum system. Furthermore, the entire hybrid system is once again embedded in a glass matrix with  $\epsilon_{\text{env}} = 2.25$ , as Fig. 4.17 shows.

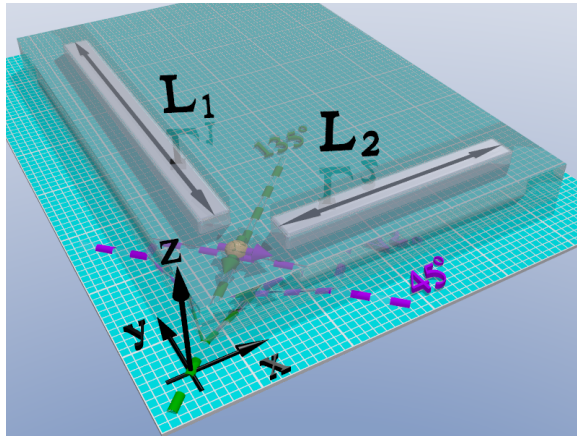


Figure 4.17: Symbolical: L-shaped bimodal nanorod dimer houses two-level system in its vertex. The single mode excitation dipole moment orientations corresponding to the new, higher frequency range are shown through the dashed lines in green and purple. The entire configuration is embedded in glass.

The nature of the quantum system constitutes the essential difference to the previous setup for triggered single photon generation. Instead of a  $\Lambda$ -type quantum system with two radiative transitions, in this scenario a two-level system featuring a single radiative transition suffices for the purpose of entangled emission. Consequently, the bimodal nanoantenna is not designed for any of the modes to resonantly couple to the dipolar transition of the two-level system. The one elementary condition for the entangled emission to be successful is that both nanoantenna modes share a spectral overlap and

for the two-level transition frequency to be spectrally located within this spectral overlap. Thusly, the transition is generally coupled to both modes. But the relaxation of the excited state involves the emission of only one photon by orders of magnitude of probability. Hence, the emitted photon can either be directly emitted into the farfield, being lost for the entanglement, or it can couple to a cavity mode. Since it can not be deterministically inferred which mode will be populated by the quantized energy from the relaxation, the generation of entanglement is generally possible and can be controlled by engineering the coupling of the transition to the two cavity modes as the following will show. The resulting emission from the cavity is a photon in one of the two modes. But in case of ideal calibration of the coupling, the photon can be detected in each mode with identical probability, hence entangling the cavity mode emission in the photon number.

Even though the result is not the textbook example of bipartite entanglement, such as a photon pair entangled in eachs polarization state, but rather two optical modes containing only one photon, quantum computing has been prominently discussed involving these very state<sup>[464]</sup>.

With the entanglement mechanism outlined, the implementation with a bimodal plasmonic cavity shall be discussed. From the previous example, one can already infer that the nanoantenna will resonantly respond to the excitation of an electric point dipole located in the vertex of the L-shape, depending on the specific orientation of the dipole moment. This behavior has already been observed before, as seen in Fig. 4.14(a), and de novo numerical scattering simulations with a dipole moment of  $d_{\text{eg}} = 6 \times 10^{-29} \text{ Cm}$  reaffirm this behavior, as can be seen in Fig. 4.18. In the frequency range between 300 THz and 400 THz the appearance and disappearance of two modal resonances, each for different dipole moment orientations  $\vartheta$ , can be witnessed. The dipole moment orientation  $\vartheta$  is again measured in  $[\circ]$  with respect to the symmetry axis of the shorter nanorod.

Due to the expected mode hybridization, the dipole moment orientations, associated with the individual resonances, rather correspond to the entire L-shaped nanoantenna geometry, instead of just one single nanorod arm. The two orientations that result in the exclusive excitation of one of the two modes can be identified as  $45^\circ$  and  $135^\circ$ . At this point it is important to note that the angle of exclusive excitation does not necessarily correspond to the brightest, i.e. strongest, signal in scattered or absorbed power. The two-dimensional mapping of scattered power over dipole moment orientation angle and frequency, as seen in Fig. 4.18, shall rather illustrate the smooth transition from solely exciting one mode to exciting both and finally exciting the other mode. Regarding the signal strength: Figure 4.14(a) already shows a stronger scattering response for a dipole moment  $30^\circ$  rotated away from the optimal, i.e. exclusively exciting one mode, orientation (bright purple line above dark purple line). This potentially misleading behavior originates from scattering contributions of modes that are off-resonantly excited.

The mechanism associated with the nanoantenna, relevant for the entangled emission, can be identified and observed as the ability to control the excitation strength of two modes through the orientation of the transition dipole moment, if the transition frequency is contained within the spectral overlap of the two modes. But even more importantly, scanning the scattered power of the nanoantenna for the two characteristic dipole moment orientations  $\vartheta = 45^\circ$  and  $\vartheta = 135^\circ$  over the length difference between the two arms of the nanoantenna  $\Delta L$  and the frequency reveals

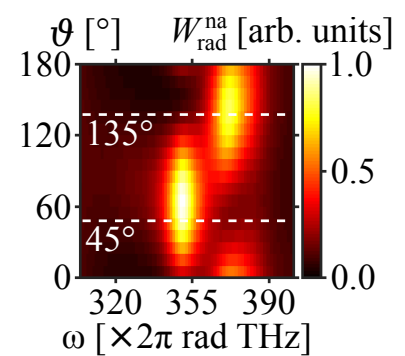


Figure 4.18: Scattered power mapped over dipole moment orientation  $\vartheta$  and frequency  $\omega$  shows two modes emerging alternately<sup>[358]</sup>.

multiple suitable pairs of modes, with each mode resonant for one characteristic  $\vartheta$ , for different  $\Delta L$  as Fig. 4.19 depicts. For the length difference scan, the longer

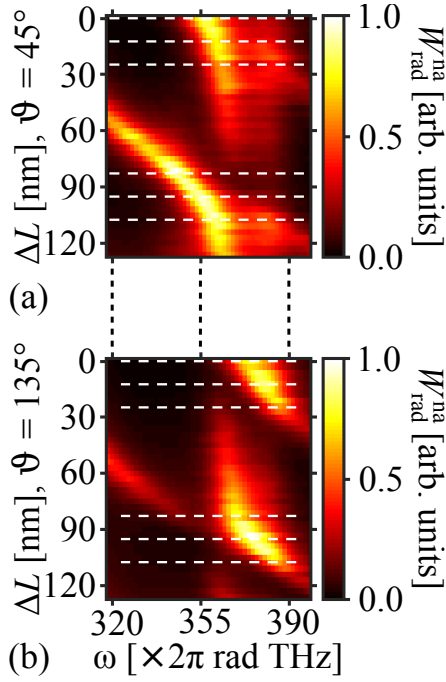


Figure 4.19: Scattered power mapped over nanorod length difference  $\Delta L$  and frequency  $\omega$  for the fixed orientation  $\vartheta = 45^\circ$  in (a)<sup>[358]</sup> and  $\vartheta = 135^\circ$  in (b)<sup>[358]</sup>. The dashed white lines indicate the selected mode pairs suitable for entangled emission with the corresponding parameters in Tab. 4.1.

nanoantenna arm remains unchanged while the shorter arm changes its length from half to equal length of the longer one. The emerging resonant mode pairs for  $\Delta L$  in the range  $\{0 \text{ nm}, 30 \text{ nm}\}$  and  $\{80 \text{ nm}, 110 \text{ nm}\}$  show that the entanglement emission scheme can be realized with many different nanoantenna geometries for the nanoantenna modes with similar resonance frequencies, lifting fabrication constraints regarding the precision of the lengths of the arms.

Selecting six nanoantenna geometries with specific length differences  $\Delta L$  and performing the previously outlined spectral fitting by Lorentzian lines yields the quantum model parameters as displayed in Tab. 4.1. Purely out of symmetry reasons, the following explicit calculations of the quantum physical dynamics are exemplarily performed and analyzed for a nanorod dimer consisting of a set of arms with equal length, i.e.  $\Delta L = 0 \text{ nm}$ . Consequently, the parameters for the corresponding cavity QED calculation are taken from the first line of the parameter Tab. 4.1.

$\Delta L$ [nm]	$\frac{\omega_1}{2\pi}$ [THz]	$\frac{\Gamma_1^{\text{rad}}}{2\pi}$ [THz]	$\frac{\Gamma_1^{\text{non}}}{2\pi}$ [THz]	$\frac{g_1}{2\pi}$ [GHz]	$\frac{\omega_2}{2\pi}$ [THz]	$\frac{\Gamma_2^{\text{rad}}}{2\pi}$ [THz]	$\frac{\Gamma_2^{\text{non}}}{2\pi}$ [THz]	$\frac{g_2}{2\pi}$ [GHz]
0	374	16	19	130	358	15	18	180
12	379	14	19	100	361	15	17	170
24	387	15	22	70	364	17	17	150
81	369	16	17	150	345	15	17	120
93	376	18	18	140	355	16	16	150
105	384	15	19	80	361	16	16	210

Table 4.1: Quantum model parameters<sup>[358]</sup> determined through fitting for 6 selected pairs of suitable modes. The ratio of the values of  $\Gamma_\xi^j$  and  $g_\xi$  locates the dynamics involving any of these mode pairs in the incoherent weak coupling regime.

The distribution of the characteristic out-of-plane mode field component is shown in Fig. 4.20 for a nanorod dimer with length difference  $\Delta L = 0 \text{ nm}$ . This field dis-

tribution identifies not just the fields as higher order dipolar resonances for each individual nanorod, as is expected, it also shows the mode field expanding over the whole L-shaped geometry of the nanoantenna.

Additionally, considering the field distribution around the whole nanoantenna geometry as it is shown in Fig. 4.20, it is apparent that both modes will radiate into the far field, since both are composed of highly radiative dipolar field distributions for each nanorod. In case of  $\omega_1$ , with  $\vartheta = 135^\circ$ , the exciting dipole moment is oriented along the bisector of the right angle between the two arms. Consequently, the mode fields of both nanorod ends close to the vertex are in phase, same holds for the far ends. This results in the overall dipole moment of the complete field distribution being naturally parallel to the exciting dipole moment located in the vertex. In case of  $\omega_2$ , with  $\vartheta = 45^\circ$ , the mode fields at the close nanorod ends are out of phase, as are the fields at the far ends. Hence, the overall dipole moment of the mode is again parallel to the exciting dipole moment, which is oriented along the line connecting the geometrical center points of the nanorod faces closest to the vertex.

This difference in orientation along with the corresponding difference in radiation pattern allows for unambiguity in identifying the modal origin of photons detected in the far field. Please note that this unambiguity does not hold for any photon emitted by the nanoantenna into the far field, since there are overlaps in the radiation patterns. But this identification aspect shall rather be seen as a proof of principle, since the nanoantenna has not been optimized in any way regarding disjoint radiation pattern of the emitting modes involved.

### Emission In Entangled Modes

With not just one nanoantenna geometry at hand to implement the entangled emission, but with one specific nanorod dimer selected, the one with  $\Delta L = 0$  nm, to exemplarily perform the corresponding cavity QED calculations, the quantum modeling shall commence. Just as in the previous cases, Dr. Karolina Słowik set up the cavity QED model, executed the numerical calculations and analyzed the steady state solutions.

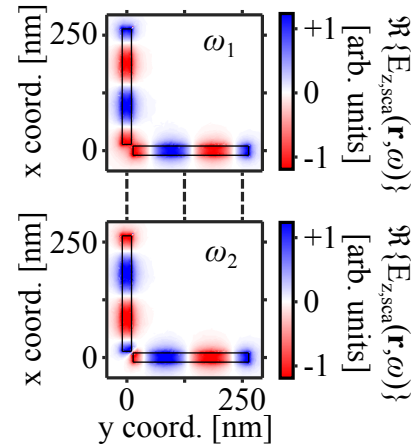


Figure 4.20: Modal fields<sup>[358]</sup> mapped in a plane 5 nm above the nanoantenna for a nanorod length difference of  $\Delta L = 0$  nm,  $\frac{\omega_1}{2\pi} = 374$  THz &  $\vartheta = 135^\circ$  (top) and  $\frac{\omega_2}{2\pi} = 358$  THz &  $\vartheta = 45^\circ$  (bottom).

---

Modeling the light-matter interaction between a two-level system and two cavity modes, the Hamiltonian reads<sup>[358]</sup>

$$\mathcal{H}_{\text{ent}}/\hbar = \sum_{\xi=1,2} \omega_{\xi} a_{\xi}^{\dagger} a_{\xi} + v_{\text{eg}} \sigma_{\text{eg}} \sigma_{\text{ge}} + \sum_{\xi=1,2} g_{\xi} \left( \sigma_{\text{eg}} a_{\xi} + a_{\xi}^{\dagger} \sigma_{\text{ge}} \right) . \quad (4.12)$$

This Hamiltonian only contains the free evolution of the two-level system, with a transition frequency chosen to be in the spectral overlap of the cavity modes  $v_{\text{eg}} \in \{\omega_2, \omega_1\}$ , the free evolution of the two cavity modes 1 and 2, and the coupling of the transition to each cavity mode according to  $g_1$  resp.  $g_2$ .

The reversible dynamics from Eqn. (4.12) are enriched by open cavity processes incorporated through a master equation formalism in Lindblad form<sup>[358]</sup>:

$$\begin{aligned} \partial_t \rho_{\text{ent}}(t) = & -\frac{i}{\hbar} [\mathcal{H}_{\text{ent}}, \rho_{\text{ent}}(t)] + \sum_{\xi=1,2} \Gamma_{\xi}^{\text{tot}} \mathcal{L}_{\xi}^{\text{cav}}(\rho_{\text{ent}}(t), a_{\xi}) + \Pi \mathcal{L}^{\text{pump}}(\rho_{\text{ent}}(t), \sigma_{\text{eg}}) \\ & + \gamma_{\text{ge}}^{\text{spo}} \mathcal{L}_{\text{ge}}^{\text{spo}}(\rho_{\text{ent}}(t), \sigma_{\text{ge}}) + \gamma^{\text{dep}} \mathcal{L}^{\text{dep}}(\rho_{\text{ent}}(t), \sigma_{\text{eg}} \sigma_{\text{ge}}) . \end{aligned} \quad (4.13)$$

These processes include the obvious cavity losses at a rate of  $\Gamma_{\xi}^{\text{tot}}$ , but also an incoherent pumping of the two-level system with  $\Pi$  that propels the emission in the entangled cavity modes. This pumping can be achieved by optical means<sup>[465]</sup>, strongly detuned from the transition, without affecting the desired emission properties. Additionally, the two-level system can decay via spontaneous emission at a rate  $\gamma_{\text{ge}}^{\text{spo}}$  according to Eqn. (2.40) in glass, and dephasing is incorporated at a rate  $\gamma^{\text{dep}} = 100 \text{ GHz}$ <sup>[358]</sup> typical for quantum dots (in agreement with the choice for the transition dipole moment). Subsequently, the stationary solution to Eqn. (4.13) is determined numerically with open source software<sup>[128]</sup>.

To analyze the entangled emission, appropriate figures of merit are in need. It is again reasonable to resort to a far-field emission rate to account for the emission performance. But unlike in Eqn. (4.6), for the emission in two cavity modes that are entangled in their photon number, every photon in any of the two modes counts, since the indeterminacy regarding which mode contains the emitted photon is at the core of the entanglement. Hence the rate of entangled emission reads<sup>[358]</sup>

$$r_{\text{ent}} = \sum_{\xi=1,2} r_{\xi} = \sum_{\xi=1,2} \Gamma_{\xi}^{\text{rad}} \langle a_{\xi}^{\dagger} a_{\xi} \rangle . \quad (4.14)$$

However, quantifying the degree of entanglement is not as obvious. It has been subject of general investigations<sup>[466]</sup>, but in light of the quantum harmonic oscillator involved, the logarithmic negativity<sup>[467,468]</sup> appears compelling, because it is a measure of entanglement not restricted to two-level systems.

From the stationary solution to Eqn. (4.13) follow photonic mode population numbers in the order of about  $10^{-5}$  for typical pumping strengths  $\Pi$  in the GHz range, as shown in Fig. 4.21(a). These values originate from the equipoise between photonic mode population  $\langle n_\xi \rangle$  and the plasmonic losses  $\Gamma_\xi^{\text{tot}}$  of the modes. To determine properties of photons emitted from the cavity modes, the partial photonic density  $\rho_{\text{pho}}$  is convenient. Furthermore, as illustrated by Fig. 4.21(b), although the vacuum state without any photonic population  $|n_1 n_2\rangle = |00\rangle$  is 5 orders more likely than a single emitted photon, the emission of two photons is 5 additional orders more unlikely. Consequently, eliminating the vacuum state from the considerations regarding the entanglement measure, will give a good indicator for the properties in case of a single emitted photon, the desired scenario.

The density matrix  $\rho_{\text{one}}^\angle$ , normalized and projected in the non-vacuum subspace follows from<sup>[358]</sup>:

$$\begin{aligned} \rho_{\text{one}}^\angle &= \mathcal{N}(\Upsilon_{\text{vac}}^\angle \rho_{\text{pho}} \Upsilon_{\text{vac}}^\angle) \quad , \quad \text{with} \quad \mathcal{N}(\rho) = \frac{\rho}{\text{Tr}\rho} \quad , \\ \Upsilon_{\text{vac}}^\angle &= \mathbf{I} - |00\rangle\langle 00| \quad , \quad \text{and} \quad \rho_{\text{pho}} = \text{Tr}_{\text{tls}}(\rho_{\text{ent}}) \quad . \end{aligned} \quad (4.15)$$

Here,  $\mathcal{N}$  ensures proper normalization, while  $\Upsilon_{\text{vac}}^\angle$  projects on the non-vacuum subspace. A further transformation is required since the density for both modes populated with one photon does still differ from the state emitted into the far field. The associated far-field density reads<sup>[358]</sup>

$$\rho_{\text{far}}^\angle = \mathcal{N}(\Upsilon_{\text{eff}}^\angle \rho_{\text{one}}^\angle \Upsilon_{\text{eff}}^\angle) \quad , \quad \text{with} \quad \Upsilon_{\text{eff}}^\angle = \sqrt{\eta_1} |10\rangle\langle 10| + \sqrt{\eta_2} |01\rangle\langle 01| \quad , \quad (4.16)$$

the projection onto the imperfect emission through the plasmonic cavity modes with the corresponding cavity mode efficiencies  $\eta_\xi$ . With the far-field density at hand the required entanglement measure in form of logarithmic negativity takes the form<sup>[428]</sup>

$$E_{\mathcal{N}}(\rho_{\text{far}}^\angle) = \log \left( \left\| \left( \rho_{\text{far}}^\angle \right)^{\text{T}_2} \right\| \right) \quad , \quad (4.17)$$

with the trace norm  $\|\cdot\|$  and the partial transpose in mode 2  $(\cdot)^{\text{T}_2}$ . The logarithmic negativity can be applied to systems of arbitrary dimensions and the value ranges from 0, the lowest, to 1, the highest.

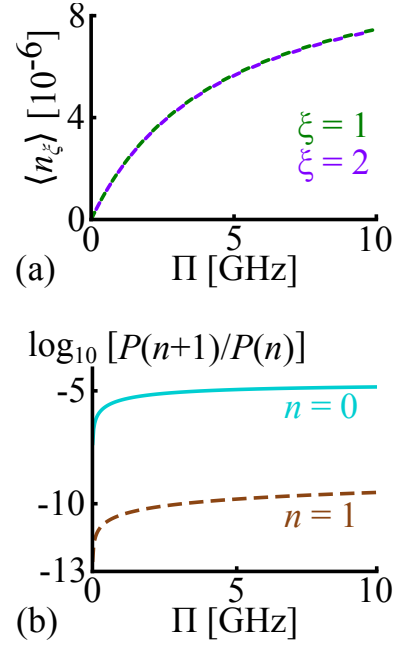


Figure 4.21: (a)<sup>[358]</sup> Mode populations  $\langle n_\xi \rangle$  and (b)<sup>[358]</sup> photon number probability ratios plotted over pumping strength  $\Pi$ .

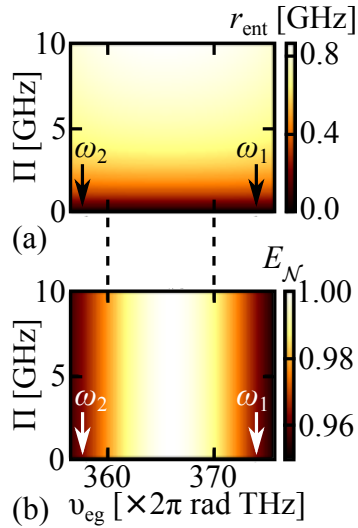


Figure 4.22: (a)<sup>[358]</sup> Entangled emission rate & (b)<sup>[358]</sup> logarithmic negativity plotted over transition frequency & pumping strength.

While the entangled emission rate does not depend on the value of  $\nu_{eg}$ , as Fig. 4.22(a) shows, a high degree of entanglement does require  $\nu_{eg}$  to be contained in the spectral mode overlap, i.e. between  $\omega_1$  and  $\omega_2$ . This behavior is expected, since the transition must be able to couple to both cavity modes for the entanglement to be generated and detuning hinders the coupling. Furthermore, Fig. 4.22(b) reveals that there is an optimal  $\nu_{eg}$  for a fixed transition dipole moment orientation. But since the colorbar for the frequency range of about 20 THz covers only 5% of  $E_N$  values, the need for an exact match of the optimal frequency cannot be deemed as crucial. Hence, the entanglement generation is somewhat robust against minor detunings, an additional benefit in light of experimental realization.

The next parameter is the transition frequency. While the entangled emission rate does not depend on the value of  $\nu_{eg}$ , as Fig. 4.22(a) shows, a high degree of entanglement does require  $\nu_{eg}$  to be contained in the spectral mode overlap, i.e. between  $\omega_1$  and  $\omega_2$ . This behavior is expected, since the transition must be able to couple to both cavity modes for the entanglement to be generated and detuning hinders the coupling. Furthermore, Fig. 4.22(b) reveals that there is an optimal  $\nu_{eg}$  for a fixed transition dipole moment orientation. But since the colorbar for the frequency range of about 20 THz covers only 5% of  $E_N$  values, the need for an exact match of the optimal frequency cannot be deemed as crucial. Hence, the entanglement generation is somewhat robust against minor detunings, an additional benefit in light of experimental realization.

Because the coupling to both cavity modes is the elementary aspect of the entanglement generation, the next parameters are the transition dipole moment magnitude  $d_{eg}$  and orientation  $\vartheta$ , quantum system parameters that influence the coupling. At first glance at Fig. 4.23 a similar behavior to the previous parameters

Analyzing the performance of the nanorod dimer cavity with  $\Delta L = 0$  nm with respect to the emission in entangled cavity modes, different system parameters demand investigation regarding their influence on the figures of merit  $r_{ent}$  and  $E_N$ .

Starting with parameters that can still be altered after the actual fabrication of the nanoantenna is finished. The obvious experimental system parameter is the strength of the external pump  $\Pi$ . Naturally, the rate of entangled emission grows with increasing pump strength and reaches the low GHz range for usual pumping strengths in the GHz range, as seen in Fig. 4.22(a). However, a GHz change of the pumping strength hardly influences the entanglement at all, as Fig. 4.22(b) depicts. Even though, extremely low pumping strengths naturally alter the entanglement, as a photon must be supplied to be emitted in entangled cavity modes, once the pumping supplies photons, especially with the desired one photon character, see Fig. 4.21(b), the degree of entanglement is independent of the pumping. Consequently, the entangled emission is available at a wide range of rates - a trait not to be underestimated and purely externally controlled by pumping.

is visible: While an altered dipole moment magnitude only influences the entangled emission rate rather than the degree of entanglement, the dipole moment orientation affects the figures of merit vice versa. An increased magnitude causes the emission rate to rise, since it increases the light-matter coupling rate. The eventual saturation in  $r_{\text{ent}}$ , seen in Fig. 4.23(a), follows from a fixed pumping strength  $\Pi$ , supplying the photons.

The orientation shows the expected behavior in Fig. 4.23(b): While a transition dipole moment orientation of either  $0^\circ$  or  $90^\circ$  is connected with the simultaneous excitation of both nanoantenna modes, as seen in Fig. 4.18, resulting in the coupling of the transition to both modes, an orientation of  $45^\circ$  exclusively excites mode 2, as seen in Fig. 4.19(a), prohibiting the vital coupling to both cavity modes. Consequently, the degree of entanglement drops to zero. The rate is not affected, because the photon is emitted into the far field, just not in two entangled cavity modes, but deterministically in mode 2.

This mechanism that the transition dipole moment orientation directly controls the state of the emission is further illuminated in Fig. 4.24(a). In terms of number states in each cavity mode  $|n_1 n_2\rangle$ , the states for both cavity modes entangled in their photon number, for one photon overall:  $|\Psi_\Phi\rangle$  and  $|\Psi_{\Phi+\frac{\pi}{2}}\rangle$ , take the form:

$$|\Psi_\Phi\rangle = \frac{1}{\sqrt{2}} (|10\rangle + e^{i\Phi} |01\rangle) \quad , \quad (4.18)$$

with the separable emission states  $|10\rangle$  and  $|01\rangle$ , for one photon in each mode. Beginning the orientation  $\vartheta$  scan at  $0^\circ$ , the dipole moment is parallel to the formerly shorter nanorod, both modes of the nanoantenna are excited (see Fig. 4.18),  $|\Psi_\Phi\rangle$  is emitted with the probability  $P(|\Psi_\Phi\rangle) = 1$  and consequently  $E_{\mathcal{N}}$  is maximal. Rotating the dipole moment,  $E_{\mathcal{N}}$  drops until it reaches the minimal value 0 at  $45^\circ$ , when the dipole moment is parallel to the line connecting the geometrical centers of the nanorod faces closest to the dipole. In this orientation only mode 2 is excited (see Fig. 4.18), the emission state is  $|n_1 n_2\rangle = |01\rangle$ , the probability for the photon to be in the other cavity mode is zero:  $P(|10\rangle) = 0$  and consequently the emission is not entangled.

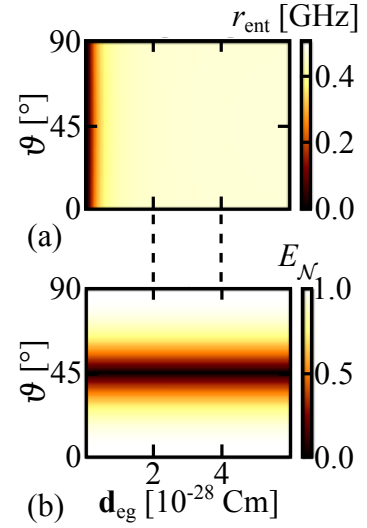


Figure 4.23: (a)<sup>[358]</sup> Entangled emission rate & (b)<sup>[358]</sup> logarithmic negativity plotted over magnitude & orientation of  $d_{\text{eg}}$ .

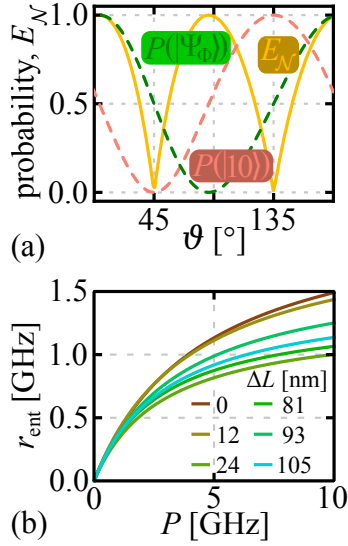


Figure 4.24: (a)<sup>[358]</sup> Emission state probability & logarithmic negativity plotted over dipole moment orientation. (b)<sup>[358]</sup> Emission rate plotted over pumping strength for the nanoantennas with different  $\Delta L$ .

With the workings of the emission in two entangled cavity modes illuminated, the final part of this investigation shall return to the six different nanoantenna geometry sets, differing in the length difference  $\Delta L$  between the two arms, that have been selected as suitable for entangled emission. Plotting the rate of entangled emission for each of these six over the pumping  $\Pi$ , as seen in Fig. 4.24(b), each shows behavior similar to the original geometry with  $\Delta L = 0$ : a continuous increase of  $r_{\text{ent}}$  with  $\Pi$ . At the highest pumping of  $\Pi = 10$  THz, the different geometries are shown to emit at rates between  $r_{\text{ent}} = 1.0$  GHz and  $r_{\text{ent}} = 1.5$  GHz. Consequently, with all geometries providing comparable performance, other reasons, beside the emission rate, can enter considerations regarding fabrication giving much desired experimental leeway.

## Concluding Remarks

The emission of a single photon in two photon-number entangled cavity modes of a plasmonic nanorod dimer cavity is implemented. The discussion of the underlying mechanism reveals the nanoantenna, when being adequately supplied with photons, to contribute the entanglement generation itself. Hence, this final example shows the nanoantenna to provide photonic functionality way beyond emission enhancement.

Additionally, spectrally overlapping cavity modes and controlled dipole moment orientation are worked out as conditions for the entangled emission. Consequently, a set of different nanoantennas is shown to generate entanglement, elevating the functionality to a general principle beyond a specific nanoantenna geometry.

## 5 Summary & Outlook

Summarizing, to realize the next generation of light-matter interaction applications, aiming to ultimately approach the implementation of quantum information processing, some possibilities of the localized plasmon-polariton platform are outlined.

To this end, the phenomenon of localized plasmon polaritons has been rooted in the optical field equations of electrodynamics and the linear metallic material response in form of the free electron gas model. Considering an interface between metallic media and an insulator, a surface state of the charge density emerged naturally, providing the unrivaled field localization associated with surface plasmon polaritons. Incorporating geometrical constraints on the surface propagation, in form of closed surfaces, yields localized surface plasmon polaritons, directly coupling to photons and with properties responsive to geometrical shaping.

The photonic input and output of the light-matter interaction is described by using fundamental elements of quantum optics, such as photonic number states and both entanglement and non-classical correlations involving photons. The interaction itself is modeled utilizing a cavity QED formalism in form of an expanded Jaynes-Cummings model. The model is opened up to far-field radiation and environmental dissipation through a master equation formalism in Lindblad form.

The first novel contribution outlined in this document is the merger of both the classical and quantum physical modeling. Consequently, it is possible to benefit from the fully classical model of plasmonic resonances to determine the parameters required for the cavity QED model from scattering calculations. Especially with the normalization of three dimensional scattering modes not available, the plasmonic loss rates follow from Lorentzian spectral line fits that in turn are shown to emerge directly from quantized surface waves. Additionally, the coupling is determined through matching of classical and cavity QED emission enhancement.

With the semi-classical light-matter interaction model in place, a plethora of applications can be implemented and their quantum dynamics simulated. Consequently, in this thesis the description of the modeling is accompanied by four different exemplary application calculations. At first, concomitant with experimen-

---

tal measurements, the fundamental molecular fluorescence influencing through cavity mode coupling is proven to beget qualitatively proper predictions. Furthermore, the hybrid system of a bimodal nanorod dimer cavity coupled to different two- and three-level systems is shown to facilitate different quantum optical functions. These numerical-calculation based investigations deal with the efficient conversion between bright and dark cavity modes, the triggered emission of single photons in a specific cavity mode, and the emission in two photon-number entangled cavity modes.

### **Subsumption In Research**

Countless experimental efforts are currently directed towards the realization of localized plasmon polariton mediated light-matter interaction, especially in the strong coupling regime. The lack of reliable, simple, and efficient means of theoretical modeling has hindered the description of higher functionality involving a plasmonic cavity, beyond selected geometries. In the weak coupling regime, the outlined model provides this very description for arbitrary cavity geometries and multiple cavity modes involved.

The outlined model provides easier means to model arbitrary cavity geometries, compared to Green's function based formalisms, and benefits from the efficient classical treatment of localized surface plasmon polaritons, compared to formalisms entirely based on density functional theory. Consequently, it is well-suited to accompany, support and expand the diverse experimental efforts.

Additionally, the three exemplary applications involving a bimodal nanoantenna demonstrate the potential the weak light-matter coupling regime still holds regarding a more elaborate functionality on the side of the optical nanoantenna. The realization of both fundamentally non-classical emission statistics and non-classical emission properties in the weak coupling regime lift the presumed requirement of strong coupling to implement any quantum physical dynamics.

### **Perspective**

Ultimately aiming to process, store, and transmit information using atoms and photons, the more elements and mechanisms that can be implemented in the weak light-matter coupling regime, the fewer demanding design requirements need to be met by the fabrication procedure to ensure strong coupling. But eventually, the strong coupling regime, necessary to conserve the quantum coherence, needs to be reached attempting to realize quantum information applications.

However, in ongoing work by Jens Oppermann, the light-matter interaction in

terms of cavity QED is coherently reformulated. Establishing a normalization procedure of free-space scattering modes<sup>[469]</sup>, the direct calculation of the light-matter coupling rate via spatial modal energy integration is enabled. Assuming Lorentzian cavity modes, Jaynes-Cummings model dynamics are retrieved and combined with input and output in form of far-field radiation modes<sup>[470]</sup>. Hence, setting up a self-contained cavity QED light-matter interaction formalism as open and connected to the far field, no requirement contradicts the outlined weak-coupling model and consequently the outlined applications can be directly incorporated to aid the development towards the realization of quantum information processing involving strong coupling.



# Bibliography

- [1] M. Humbert, 'Technology and workforce: Comparison between the information revolution and the industrial revolution', Tech. rep., University of California (Berkeley), School of Information, 2007.
- [2] J. Rifkin, *End of Work: The Decline of the Global Labor Force and the Dawn of the Post-Market Era*, Putnam Publishing Group, New York City, New York, USA, 1995.
- [3] M. Hilbert & P. López, 'The world's technological capacity to store, communicate, and compute information', *Science* **332(6025)**:60, 2011.
- [4] S. E. Thompson & S. Parthasarathy, 'Moore's law: the future of Si microelectronics', *Materials Today* **9(6)**:20, 2006.
- [5] L. B. Kish, 'End of Moore's law: thermal (noise) death of integration in micro and nano electronics', *Physics Letters A* **305(3)**:144, 2002.
- [6] L. Brillouin, 'Science and Information Theory', 2004.
- [7] S. Kumar, 'Fundamental Limits to Moore's Law', *arXiv preprint arXiv:1511.05956* 2015.
- [8] C. H. Bennett, 'Quantum Information', *Physics Today* **48(10)**:24, 1995.
- [9] S. L. Braunstein & A. K. Pati, *Quantum Information with Continuous Variables*, 1st ed., Springer Science+Business Media, Berlin, Germany, 2003.
- [10] C. Weedbrook, S. Pirandola, R. García-Patrón, N. J. Cerf, T. C. Ralph, J. H. Shapiro, & S. Lloyd, 'Gaussian quantum information', *Reviews of Modern Physics* **84(2)**:621, 2012.
- [11] C. H. Bennett & D. P. DiVincenzo, 'Quantum information and computation', *Nature* **404(6775)**:247, 2000.
- [12] M. A. Nielsen & I. L. Chuang, *Quantum Computation and Quantum Information*, 2nd ed., Cambridge University Press, Cambridge, England, UK, 2011.
- [13] H. Barnum, M. A. Nielsen, & B. Schumacher, 'Information transmission through a noisy quantum channel', *Physical Review A* **57(6)**:4153, 1998.
- [14] C. Macchiavello & G. M. Palma, 'Entanglement-enhanced information transmission over a quantum channel with correlated noise', *Physical Review A* **65(5)**:050301, 2002.
- [15] M. Harlander, R. Lechner, M. Brownnutt, R. Blatt, & W. Hänsel, 'Trapped-ion antennae for the transmission of quantum information', *Nature* **471(7337)**:200, 2011.
- [16] J. Maddox, 'Quantum information storage', *Nature* **327(6118)**:97, 1987.
- [17] C. Liu, Z. Dutton, C. H. Behroozi, & L. V. Hau, 'Observation of coherent optical information storage in an atomic medium using halted light pulses', *Nature* **409(6819)**:490, 2001.
- [18] P. C. Maurer, G. Kucsko, C. Latta, L. Jiang, N. Y. Yao, S. D. Bennett, F. Pastawski, D. Hunger, N. Chisholm, M. Markham, D. J. Twitchen, J. I. Cirac, & M. D. Lukin, 'Room-temperature quantum bit memory exceeding one second', *Science* **336(6086)**:1283, 2012.
- [19] C. Monroe, 'Quantum information processing with atoms and photons', *Nature* **416(6877)**:238, 2002.

- 
- [20] J. I. Cirac & P. Zoller, 'Quantum computations with cold trapped ions', *Physical Review Letters* **74(20)**:4091, 1995.
- [21] A. Steane, 'The ion trap quantum information processor', *Applied Physics B: Lasers and Optics* **64(6)**:623, 1997.
- [22] P. Bharadwaj, B. Deutsch, & L. Novotny, 'Optical antennas', *Advances in Optics and photonics* **1(3)**:438, 2009.
- [23] A. E. Krasnok, I. S. Maksymov, A. I. Denisyuk, P. A. Belov, A. E. Miroshnichenko, C. R. Simovski, & Y. S. Kivshar, 'Optical nanoantennas', *Physics-Uspekhi* **56(6)**:539, 2013.
- [24] K. B. Crozier, A. Sundaramurthy, G. S. Kino, & C. F. Quate, 'Optical antennas: Resonators for local field enhancement', *Journal of Applied Physics* **94(7)**:4632, 2003.
- [25] L. Novotny & N. Van Hulst, 'Antennas for light', *Nature Photonics* **5(2)**:83, 2011.
- [26] H. Fischer & O. J. F. Martin, 'Engineering the optical response of plasmonic nanoantennas', *Optics Express* **16(12)**:9144, 2008.
- [27] D. Weber, J. Katzmann, F. Neubrech, T. Härtling, & A. Pucci, 'Spectral tuning of IR-resonant nanoantennas by nanogap engineering', *Optical Materials Express* **1(7)**:1301, 2011.
- [28] T. Kalkbrenner, U. Håkanson, A. Schädle, S. Burger, C. Henkel, & V. Sandoghdar, 'Optical microscopy via spectral modifications of a nanoantenna', *Physical Review Letters* **95(20)**:200801, 2005.
- [29] W. Zhao & J. M. Karp, 'Tumour targeting: Nanoantennas heat up', *Nature Materials* **8(6)**:453, 2009.
- [30] T. Schumacher, K. Kratzer, D. Molnar, M. Hentschel, H. Giessen, & M. Lippitz, 'Nanoantenna-enhanced ultrafast nonlinear spectroscopy of a single gold nanoparticle', *Nature Communications* **2**:333, 2011.
- [31] S. Stapfner, L. Ost, D. Hunger, J. Reichel, I. Favero, & E. M. Weig, 'Cavity-enhanced optical detection of carbon nanotube Brownian motion', *Applied Physics Letters* **102(15)**:151910, 2013.
- [32] K. C. Toussaint Jr., B. J. Roxworthy, S. Michaud, H. Chen, A. M. Bhuiya, & Q. Ding, 'Plasmonic nanoantennas: from nanotweezers to plasmonic photography', *Optics and Photonics News* **26(6)**:24, 2015.
- [33] F. B. Zarrabi, M. Naser-Moghadasi, S. Heydari, M. Maleki, & A. S. Arezomand, 'Cross-slot nano-antenna with graphene coat for bio-sensing application', *Optics Communications* **371**:34, 2016.
- [34] J. B. Khurgin, 'How to deal with the loss in plasmonics and metamaterials', *Nature Nanotechnology* **10(1)**:2, 2015.
- [35] D. Pissuwan, S. M. Valenzuela, & M. B. Cortie, 'Therapeutic possibilities of plasmonically heated gold nanoparticles', *TRENDS in Biotechnology* **24(2)**:62, 2006.
- [36] H. Duan, A. I. Fernández-Domínguez, M. Bosman, S. A. Maier, & J. K. W. Yang, 'Nanoplasmonics: classical down to the nanometer scale', *Nano Letters* **12(3)**:1683, 2012.
- [37] M. Wubs, L. G. Suttorp, & A. Lagendijk, 'Multipole interaction between atoms and their photonic environment', *Physical Review A* **68(1)**:013822, 2003.
- [38] J. D. Jackson, *Classical Electrodynamics*, 3rd ed., John Wiley & Sons, Hoboken, New Jersey, USA, 1998.
- [39] A. Zangwill, *Modern Electrodynamics*, 1st ed., Cambridge University Press, Cambridge, England, UK, 2012.
- [40] L. D. Landau, E. M. Lifshitz, & L. P. Pitaevskii, *Electrodynamics of Continuous Media*, vol. 8 of *Course of Theoretical Physics*, 2nd ed., Butterworth-Heinemann, Oxford, England, UK, 1984.
- [41] P. Drude, 'Zur Elektronentheorie der Metalle', *Annalen der Physik* **306(3)**:566, 1900.
- [42] E. Hecht, *Optics*, 4th ed., Addison-Wesley, Boston, Massachusetts, USA, 2001.
-

- 
- [43] J. H. Van Vleck, *The Theory of Electric and Magnetic Susceptibilities*, Oxford University Press, Oxford, England, UK, 1932.
- [44] P. B. Johnson & R. W. Christy, 'Optical constants of the noble metals', *Physical Review* **B 6(12)**:4370, 1972.
- [45] E. D. Palik, *Handbook of Optical Constants of Solids*, vol. 3, Academic Press, Cambridge, Massachusetts, USA, 1998.
- [46] E. M. Purcell & D. J. Morin, *Electricity and Magnetism*, 3rd ed., Cambridge University Press, Cambridge, England, UK, 2013.
- [47] J. L. Volakis, A. Chatterjee, & L. C. Kempel, *Finite Element Method Electromagnetics: Antennas, Microwave Circuits, and Scattering Applications*, vol. 6 of *Electromagnetic Wave Theory*, 1st ed., John Wiley & Sons, Hoboken, New Jersey, USA, 1998.
- [48] COMSOL, Burlington, Massachusetts, USA, *COMSOL Multiphysics Reference Manual*, comsol 5.2a ed., 2016.
- [49] C. Kittel, *Introduction to Solid State Physics*, 8th ed., John Wiley & Sons, Hoboken, New Jersey, USA, 2004.
- [50] H. Raether, *Excitation of Plasmons and Interband Transitions by Electrons*, 1st ed., Springer Science+Business Media, Berlin, Germany, 1980.
- [51] G. Ruthemann, 'Diskrete Energieverluste mittelschneller Elektronen beim Durchgang durch dünne Folien', *Annalen der Physik* **437(3-4)**:113, 1948.
- [52] G. Priftis, A. Theodossiou, & K. Alexopoulos, 'Plasmon observation in X-ray scattering', *Physics Letters* **A 27(8)**:577, 1968.
- [53] R. H. Ritchie, 'Plasma losses by fast electrons in thin films', *Physical Review* **106(5)**:874, 1957.
- [54] A. Zangwill, *Physics at Surfaces*, 1st ed., Cambridge University Press, Cambridge, England, UK, 1988.
- [55] F. Seitz, *The Modern Theory of Solids*, McGraw-Hill Education, New York City, New York, USA, 1940.
- [56] M. Schlüter & L. Jau Sham, 'Density functional theory', *Physics Today* **35**:36, 1982.
- [57] D. D. Koelling, 'Self-consistent energy band calculations', *Reports on Progress in Physics* **44(2)**:139, 1981.
- [58] D. M. Ceperley & B. J. Alder, 'Ground state of the electron gas by a stochastic method', *Physical Review Letters* **45(7)**:566, 1980.
- [59] N. D. Lang & W. Kohn, 'Theory of metal surfaces: charge density and surface energy', *Physical Review* **B 1(12)**:4555, 1970.
- [60] F. Forstmann, 'On the theory of surface states in nearly free electron systems', *Zeitschrift für Physik A Hadrons and Nuclei* **235(1)**:69, 1970.
- [61] W. Shockley, 'On the surface states associated with a periodic potential', *Physical Review* **56(4)**:317, 1939.
- [62] S. A. Maier, *Plasmonics: Fundamentals and Applications*, 1st ed., Springer Science+Business Media, Berlin, Germany, 2007.
- [63] H. Raether, *Surface Plasmons on Smooth and Rough Surfaces and on Gratings*, vol. 111 of *Springer Tracts in Modern Physics*, 1st ed., Springer Science+Business Media, Berlin, Germany, 1988.
- [64] G. Goubau, 'Surface waves and their application to transmission lines', *Journal of Applied Physics* **21(11)**:1119, 1950.
- [65] E. Kretschmann & H. Raether, 'Radiative decay of non radiative surface plasmons excited by light', *Zeitschrift für Naturforschung* **A 23(12)**:2135, 1968.
-

- 
- [66] A. Otto, 'Excitation of nonradiative surface plasma waves in silver by the method of frustrated total reflection', *Zeitschrift für Physik* **216(4)**:398, 1968.
- [67] E. J. Zeman & G. C. Schatz, 'An accurate electromagnetic theory study of surface enhancement factors for silver, gold, copper, lithium, sodium, aluminum, gallium, indium, zinc, and cadmium', *Journal of Physical Chemistry* **91(3)**:634, 1987.
- [68] D. L. Feldheim & C. A. Foss, *Metal Nanoparticles: Synthesis, Characterization, and Applications*, 1st ed., CRC Press, Boca Raton, Florida, USA, 2001.
- [69] C. F. Bohren, & D. R. Huffman, *Absorption and Scattering of Light by Small Particles*, 1st ed., Wiley-VCH, Weinheim, Baden-Württemberg, Germany, 1983.
- [70] U. Kreibig & M. Vollmer, *Optical Properties of Metal Clusters*, vol. 25 of *Springer Series in Materials Science*, 1st ed., Springer Science+Business Media, Berlin, Germany, 1995.
- [71] G. Mie, 'Beiträge zur Optik trüber Medien, speziell kolloidaler Metallösungen', *Annalen der Physik* **330(3)**:377, 1908.
- [72] D. J. Griffiths, *Introduction to Electrodynamics*, 3rd ed., Prentice Hall, Upper Saddle River, New Jersey, USA, 1999.
- [73] F. De Lange, A. Cambi, R. Huijbens, B. de Bakker, W. Rensen, M. Garcia-Parajo, N. van Hulst, & C. G. Figdor, 'Cell biology beyond the diffraction limit: near-field scanning optical microscopy', *Journal of Cell Science* **114(23)**:4153, 2001.
- [74] A. Ianoul, D. D. Grant, Y. Rouleau, M. Bani-Yaghoub, L. J. Johnston, & J. P. Pezacki, 'Imaging nanometer domains of  $\beta$ -adrenergic receptor complexes on the surface of cardiac myocytes', *Nature Chemical Biology* **1(4)**:196, 2005.
- [75] B. I. de Bakker, F. de Lange, A. Cambi, J. P. Korterik, E. M. H. P. van Dijk, N. F. van Hulst, C. G. Figdor, & M. F. Garcia-Parajo, 'Nanoscale Organization of the Pathogen Receptor DC-SIGN Mapped by Single-Molecule High-Resolution Fluorescence Microscopy', *ChemPhysChem* **8(10)**:1473, 2007.
- [76] N. Liu, M. L. Tang, M. Hentschel, H. Giessen, & A. P. Alivisatos, 'Nanoantenna-enhanced gas sensing in a single tailored nanofocus', *Nature Materials* **10(8)**:631, 2011.
- [77] M. Mesch, C. Zhang, P. V. Braun, & H. Giessen, 'Functionalized hydrogel on plasmonic nanoantennas for noninvasive glucose sensing', *Acs Photonics* **2(4)**:475, 2015.
- [78] H. Shiigi, T. Kinoshita, M. Fukuda, D. Q. Le, T. Nishino, & T. Nagaoka, 'Nanoantennas as biomarkers for bacterial detection', *Analytical Chemistry* **87(7)**:4042, 2015.
- [79] T. H. Taminiau, R. J. Moerland, F. B. Segerink, L. Kuipers, & N. F. van Hulst, ' $\lambda/4$  resonance of an optical monopole antenna probed by single molecule fluorescence', *Nano Letters* **7(1)**:28, 2007.
- [80] S. S. Acimovic, M. P. Kreuzer, M. U. González, & R. Quidant, 'Plasmon near-field coupling in metal dimers as a step toward single-molecule sensing', *ACS Nano* **3(5)**:1231, 2009.
- [81] M. F. Garcia-Parajo, 'Optical antennas focus in on biology', *Nature Photonics* **2(4)**:201, 2008.
- [82] G. Von Maltzahn, J.-H. Park, A. Agrawal, N. K. Bandaru, S. K. Das, M. J. Sailor, & S. N. Bhatia, 'Computationally guided photothermal tumor therapy using long-circulating gold nanorod antennas', *Cancer Research* **69(9)**:3892, 2009.
- [83] W. Lu, A. K. Singh, S. A. Khan, D. Senapati, H. Yu, & P. C. Ray, 'Gold nano-popcorn-based targeted diagnosis, nanotherapy treatment, and in situ monitoring of photothermal therapy response of prostate cancer cells using surface-enhanced Raman spectroscopy', *Journal of the American Chemical Society* **132(51)**:18103, 2010.
- [84] Y.-C. Ou, J. A. Webb, S. Faley, D. Shae, E. M. Talbert, S. Lin, C. C. Cutright, J. T. Wilson, L. M. Bellan, & R. Bardhan, 'Gold nanoantenna-mediated photothermal drug delivery from thermosensitive liposomes in breast cancer', *ACS Omega* **1(2)**:234, 2016.

- 
- [85] S. H. Zainud-Deen, N. A. Eltresy, H. A. Malhat, & K. H. Awadalla, 'Single/dual-polarized infrared rectenna for solar energy harvesting', *Advanced Electromagnetics* **5(2)**:1, 2016.
- [86] Y. M. El-Toukhy, M. Hussein, M. F. O. Hameed, A. M. Heikal, M. M. Abd-Elrazzak, & S. S. A. Obayya, 'Optimized tapered dipole nanoantenna as efficient energy harvester', *Optics Express* **24(14)**:A1107, 2016.
- [87] A. Bonakdar, J. Kohoutek, D. Dey, & H. Mohseni, 'Optomechanical nanoantenna', *Optics Letters* **37(15)**:3258, 2012.
- [88] K. Chen, G. Razinskas, T. Feichtner, S. Grossmann, S. Christiansen, & B. Hecht, 'Electromechanically tunable suspended optical nanoantenna', *Nano Letters* **16(4)**:2680, 2016.
- [89] F. Della Picca, R. Berte, M. Rahmani, P. Albella, J. M. Bujjamer, M. Poblet, E. Cortés, S. A. Maier, & A. V. Bragas, 'Tailored hypersound generation in single plasmonic nanoantennas', *Nano Letters* **16(2)**:1428, 2016.
- [90] G. Lozano, D. J. Louwers, S. R. K. Rodríguez, S. Murai, O. T. A. Jansen, M. A. Verschuuren, & J. G. Rivas, 'Plasmonics for solid-state lighting: enhanced excitation and directional emission of highly efficient light sources', *Light: Science & Applications* **2(5)**:e66, 2013.
- [91] K. L. Tsakmakidis, R. W. Boyd, E. Yablonovitch, & X. Zhang, 'Large spontaneous-emission enhancements in metallic nanostructures: towards LEDs faster than lasers', *Optics Express* **24(16)**:17916, 2016.
- [92] R. Guo, M. Decker, F. Setzpfandt, I. Staude, D. N. Neshev, & Y. S. Kivshar, 'Plasmonic Fano nanoantennas for on-chip separation of wavelength-encoded optical signals', *Nano Letters* **15(5)**:3324, 2015.
- [93] K. Nakayama, Y. Tonooka, M. Ota, Y. Ishii, & M. Fukuda, 'Passive Plasmonic Demultiplexers Using Multimode Interference', *Journal of Lightwave Technology* **36(10)**:1979, 2018.
- [94] M. W. Knight, H. Sobhani, P. Nordlander, & N. J. Halas, 'Photodetection with active optical antennas', *Science* **332(6030)**:702, 2011.
- [95] H. Chalabi, D. Schoen, & M. L. Brongersma, 'Hot-electron photodetection with a plasmonic nanostripe antenna', *Nano Letters* **14(3)**:1374, 2014.
- [96] A. Alù & N. Engheta, 'Wireless at the nanoscale: optical interconnects using matched nanoantennas', *Physical Review Letters* **104(21)**:213902, 2010.
- [97] Y. Yang, Q. Li, & M. Qiu, 'Broadband nanophotonic wireless links and networks using on-chip integrated plasmonic antennas', *Scientific Reports* **6**:19490, 2016.
- [98] A. V. Krasavin & A. V. Zayats, 'Photonic signal processing on electronic scales: electro-optical field-effect nanoplasmonic modulator', *Physical Review Letters* **109(5)**:053901, 2012.
- [99] P. Markov, K. Appavoo, R. F. Haglund, & S. M. Weiss, 'Hybrid Si-VO<sub>2</sub>-Au optical modulator based on near-field plasmonic coupling', *Optics Express* **23(5)**:6878, 2015.
- [100] Y. Liu, S. Palomba, Y. Park, T. Zentgraf, X. Yin, & X. Zhang, 'Compact magnetic antennas for directional excitation of surface plasmons', *Nano Letters* **12(9)**:4853, 2012.
- [101] J. Lin, J. P. B. Mueller, Q. Wang, G. Yuan, N. Antoniou, X.-C. Yuan, & F. Capasso, 'Polarization-controlled tunable directional coupling of surface plasmon polaritons', *Science* **340(6130)**:331, 2013.
- [102] L. D. Landau & E. M. Lifshitz, *Mechanics*, vol. 1 of *Course of Theoretical Physics*, 3rd ed., Butterworth-Heinemann, Oxford, England, UK, 1976.
- [103] G. Grynberg, A. Aspect, & C. Fabre, *Introduction to Quantum Optics: from the Semi-Classical Approach to Quantized Light*, 1st ed., Cambridge University Press, Cambridge, England, UK, 2010.
- [104] J.-L. Basdevant & J. Dalibard, *The Quantum Mechanics Solver: How to Apply Quantum Theory to Modern Physics*, 2nd ed., Springer Science+Business Media, Berlin, Germany, 2006.
- [105] E. Schrödinger, 'Die gegenwärtige Situation in der Quantenmechanik', *Naturwissenschaften* **23(48)**:807, 1935.
-

- 
- [106] S. Haroche & J.-M. Raimond, *Exploring the Quantum: Atoms, Cavities, and Photons*, 1st ed., Oxford University Press, Oxford, England, UK, 2006.
- [107] R. Hafenbrak, S. M. Ulrich, P. Michler, L. Wang, A. Rastelli, & O. G. Schmidt, 'Triggered polarization-entangled photon pairs from a single quantum dot up to 30 K', *New Journal of Physics* **9(9)**:315, 2007.
- [108] E. Poem, Y. Kodriano, C. Tradonsky, B. D. Gerardot, P. M. Petroff, & D. Gershoni, 'Radiative cascades from charged semiconductor quantum dots', *Physical Review B* **81(8)**:085306, 2010.
- [109] M. Müller, S. Bounouar, K. D. Jöns, M. Glässl, & P. Michler, 'On-demand generation of indistinguishable polarization-entangled photon pairs', *Nature Photonics* **8(3)**:224, 2014.
- [110] L. Mandel & E. Wolf, *Optical Coherence and Quantum Optics*, 1st ed., Cambridge University Press, Cambridge, England, UK, 1995.
- [111] R. J. Glauber, 'The quantum theory of optical coherence', *Physical Review* **130(6)**:2529, 1963.
- [112] R. Loudon, *The Quantum Theory of Light*, 3rd ed., Oxford University Press, Oxford, England, UK, 2000.
- [113] D. F. Walls & G. J. Milburn, *Quantum Optics*, 2nd ed., Springer Science+Business Media, Berlin, Germany, 2008.
- [114] P. Meystre & M. Sargent, *Elements of Quantum Optics*, 4th ed., Springer Science+Business Media, Berlin, Germany, 2007.
- [115] M. O. Scully & M. S. Zubairy, *Quantum Optics*, 1st ed., Cambridge University Press, Cambridge, England, UK, 1997.
- [116] C. Cohen-Tannoudji, J. Dupont-Roc, & G. Grynberg, *Atom-Photon Interactions: Basic Processes and Applications*, 1st ed., Wiley-VCH, Weinheim, Baden-Württemberg, Germany, 1992.
- [117] E. T. Jaynes & F. W. Cummings, 'Comparison of quantum and semiclassical radiation theories with application to the beam maser', *Proceedings of the IEEE* **51(1)**:89, 1963.
- [118] S. Haroche & D. Kleppner, 'Cavity quantum electrodynamics', *Physics Today* **42(1)**:24, 1989.
- [119] B. W. Shore & P. L. Knight, 'The Jaynes-Cummings model', *Journal of Modern Optics* **40(7)**:1195, 1993.
- [120] W. Vogel & R. L. de Matos Filho, 'Nonlinear Jaynes-Cummings dynamics of a trapped ion', *Physical Review A* **52(5)**:4214, 1995.
- [121] J. M. Fink, M. Göppl, M. Baur, R. Bianchetti, P. J. Leek, A. Blais, & A. Wallraff, 'Climbing the Jaynes-Cummings ladder and observing its nonlinearity in a cavity QED system', *Nature* **454(7202)**:315, 2008.
- [122] J. Kasprzak, S. Reitzenstein, E. A. Muljarov, C. Kistner, C. Schneider, M. Strauss, S. Höfling, A. Forchel, & W. Langbein, 'Up on the Jaynes-Cummings ladder of a quantum-dot/microcavity system', *Nature Materials* **9(4)**:304, 2010.
- [123] T. Hümmer, G. M. Reuther, P. Hänggi, & D. Zueco, 'Nonequilibrium phases in hybrid arrays with flux qubits and nitrogen-vacancy centers', *Physical Review A* **85(5)**:052320, 2012.
- [124] R. Albrecht, A. Bommer, C. Deutsch, J. Reichel, & C. Becher, 'Coupling of a single nitrogen-vacancy center in diamond to a fiber-based microcavity', *Physical Review Letters* **110(24)**:243602, 2013.
- [125] E. F. Schubert, Y.-H. Wang, A. Y. Cho, L.-W. Tu, & G. J. Zydzik, 'Resonant cavity light-emitting diode', *Applied Physics Letters* **60(8)**:921, 1992.
- [126] H.-P. Breuer & F. Petruccione, *The Theory of Open Quantum Systems*, 1st ed., Oxford University Press, Oxford, England, UK, 2002.
- [127] J. R. Johansson, P. D. Nation, & F. Nori, 'QuTiP: An open-source Python framework for the dynamics of open quantum systems', *Computer Physics Communications* **183(8)**:1760, 2012.
- [128] P. D. Nation & J. R. Johansson, 'QuTiP: Quantum Toolbox in Python', online at <http://qutip.org/>, 2011.

- [129] Y. Yamamoto & A. Imamoglu, *Mesoscopic Quantum Optics*, chap. Mesoscopic quantum optics, John Wiley & Sons, Hoboken, New Jersey, USA, 1999.
- [130] A. F. Koenderink, 'On the use of Purcell factors for plasmon antennas', *Optics Letters* **35(24)**:4208, 2010.
- [131] V. V. Temnov & U. Woggon, 'Superradiance and subradiance in an inhomogeneously broadened ensemble of two-level systems coupled to a low-Q cavity', *Physical Review Letters* **95(24)**:243602, 2005.
- [132] Q.-X. Mu, Y.-H. Ma, & L. Zhou, 'Output squeezing and entanglement generation from a single atom with respect to a low-Q cavity', *Physical Review A* **81(2)**:024301, 2010.
- [133] C. Gao, C. Wang, L.-y. He, & R. Zhang, 'Atomic entanglement purification and concentration using coherent state input-output process in low-Q cavity QED regime', *Optics Express* **21(4)**:4093, 2013.
- [134] Y. Gong & J. Vučković, 'Design of plasmon cavities for solid-state cavity quantum electrodynamics applications', *Applied Physics Letters* **90(3)**:033113, 2007.
- [135] A. E. Krasnok, A. E. Miroshnichenko, P. A. Belov, & Y. S. Kivshar, 'All-dielectric optical nanoantennas', *Optics Express* **20(18)**:20599, 2012.
- [136] M. Decker & I. Staude, 'Resonant dielectric nanostructures: a low-loss platform for functional nanophotonics', *Journal of Optics* **18(10)**:103001, 2016.
- [137] Y. Wu, C. Zhang, N. M. Estakhri, Y. Zhao, J. Kim, M. Zhang, X.-X. Liu, G. K. Pribil, A. Alù, C.-K. Shih, & X. Li, 'Intrinsic optical properties and enhanced plasmonic response of epitaxial silver', *Advanced Materials* **26(35)**:6106, 2014.
- [138] I. Goykhman, B. Desiatov, J. Khurgin, J. Shappir, & U. Levy, 'Locally oxidized silicon surface-plasmon Schottky detector for telecom regime', *Nano Letters* **11(6)**:2219, 2011.
- [139] S. Linic, P. Christopher, & D. B. Ingram, 'Plasmonic-metal nanostructures for efficient conversion of solar to chemical energy', *Nature Materials* **10(12)**:911, 2011.
- [140] J. Verdú, H. Zoubi, C. Koller, J. Majer, H. Ritsch, & J. Schmiedmayer, 'Strong magnetic coupling of an ultracold gas to a superconducting waveguide cavity', *Physical Review Letters* **103(4)**:043603, 2009.
- [141] A. Imamoglu, 'Cavity QED based on collective magnetic dipole coupling: spin ensembles as hybrid two-level systems', *Physical Review Letters* **102(8)**:083602, 2009.
- [142] S. M. Hein & H. Giessen, 'Tailoring magnetic dipole emission with plasmonic split-ring resonators', *Physical Review Letters* **111(2)**:026803, 2013.
- [143] J. R. Zurita-Sánchez & L. Novotny, 'Multipolar interband absorption in a semiconductor quantum dot. I. Electric quadrupole enhancement', *Journal of the Optical Society of America B* **19(6)**:1355, 2002.
- [144] R. Filter, S. Mühligh, T. Eichelkraut, C. Rockstuhl, & F. Lederer, 'Controlling the dynamics of quantum mechanical systems sustaining dipole-forbidden transitions via optical nanoantennas', *Physical Review B* **86(3)**:035404, 2012.
- [145] S. J. D. Phoenix, 'Counter-rotating contributions in the Jaynes-Cummings model', *Journal of Modern Optics* **36(9)**:1163, 1989.
- [146] M. Tavis & F. W. Cummings, 'Exact solution for an N-molecule-radiation-field Hamiltonian', *Physical Review* **170(2)**:379, 1968.
- [147] R. H. Dicke, 'Coherence in spontaneous radiation processes', *Physical Review* **93(1)**:99, 1954.
- [148] S. M. Barnett & P. L. Knight, 'Collective and quantum effects in models of Rydberg atom maser evolution', *Journal of Modern Optics* **31(4)**:435, 1984.
- [149] S. Haroche & J. M. Raimond, 'Radiative properties of Rydberg states in resonant cavities', in 'Advances in Atomic and Molecular Physics', vol. 20, 347, Elsevier, Amsterdam, Netherlands, 1985.

- 
- [150] X.-s. Li & N.-y. Bei, 'A generalized three-level Jaynes-Cummings model', *Physics Letters A* **101(3)**:169, 1984.
- [151] N. N. Bogolubov, F. Le Kien, & A. S. Shumovsky, 'Exact results for a model of a three-level atom', *Physics Letters A* **107(4)**:173, 1985.
- [152] N. N. Bogolubov, F. Le Kien, & A. S. Shumovski, 'Two-phonon process in a three-level system', *Physics Letters A* **101(4)**:201, 1984.
- [153] M. S. Zubairy & J. J. Yeh, 'Photon statistics in multiphoton absorption and emission processes', *Physical Review A* **21(5)**:1624, 1980.
- [154] E. A. Kochetov, 'Exactly solvable non-linear generalisations of the Jaynes-Cummings model', *Journal of Physics A: Mathematical and General* **20(9)**:2433, 1987.
- [155] E. I. Aliskenderov, K. A. Rustamov, A. S. Shumovsky, & T. Quang, 'On the Jaynes-Cummings model with multiphoton transitions in a cavity', *Journal of Physics A: Mathematical and General* **20(18)**:6265, 1987.
- [156] I. Ashraf, J. Gea-Banacloche, & M. S. Zubairy, 'Theory of the two-photon micromaser: photon statistics', *Physical Review A* **42(11)**:6704, 1990.
- [157] P. Alsing & M. S. Zubairy, 'Collapse and revivals in a two-photon absorption process', *Journal of the Optical Society of America B* **4(2)**:177, 1987.
- [158] J. Seke, 'Extended Jaynes-Cummings model', *Journal of the Optical Society of America B* **2(6)**:968, 1985.
- [159] S. Swain, 'An exact solution of the multiatom, multimode model Hamiltonian of quantum optics', *Journal of Physics A: General Physics* **5(1)**:L3, 1972.
- [160] S.-C. Gou, 'Quantum behavior of a two-level atom interacting with two modes of light in a cavity', *Physical Review A* **40(9)**:5116, 1989.
- [161] A. S. Parkins, 'Resonance fluorescence of a two-level atom in a two-mode squeezed vacuum', *Physical Review A* **42(11)**:6873, 1990.
- [162] P. M. Alsing, D. A. Cardimona, & H. J. Carmichael, 'Suppression of fluorescence in a lossless cavity', *Physical Review A* **45(3)**:1793, 1992.
- [163] W. K. Lai, V. Bužek, & P. L. Knight, 'Dynamics of a three-level atom in a two-mode squeezed vacuum', *Physical Review A* **44(9)**:6043, 1991.
- [164] C. M. Savage, 'Quantum optics with one atom in an optical cavity', *Journal of Modern Optics* **37(11)**:1711, 1990.
- [165] T. Quang, P. L. Knight, & V. Bužek, 'Quantum collapses and revivals in an optical cavity', *Physical Review A* **44(9)**:6092, 1991.
- [166] J. E. Bernard, A. A. Madej, L. Marmet, B. G. Whitford, K. J. Siemsen, & S. Cundy, 'Cs-based frequency measurement of a single, trapped ion transition in the visible region of the spectrum', *Physical Review Letters* **82(16)**:3228, 1999.
- [167] M. Mack, F. Karlewski, H. Hattermann, S. Hockh, F. Jessen, D. Cano, & J. Fortágh, 'Measurement of absolute transition frequencies of Rb 87 to nS and nD Rydberg states by means of electromagnetically induced transparency', *Physical Review A* **83(5)**:052515, 2011.
- [168] M. G. U. J. Petersilka, U. J. Gossmann, & E. K. U. Gross, 'Excitation energies from time-dependent density-functional theory', *Physical Review Letters* **76(8)**:1212, 1996.
- [169] V. I. Korobov, 'Calculation of transitions between metastable states of antiprotonic helium including relativistic and radiative corrections of order  $R_\infty \alpha^4$ ', *Physical Review A* **77(4)**:042506, 2008.

- [170] P. G. Eliseev, H. Li, A. Stintz, G. T. Liu, T. C. Newell, K. J. Malloy, & L. F. Lester, 'Transition dipole moment of InAs/InGaAs quantum dots from experiments on ultralow-threshold laser diodes', *Applied Physics Letters* **77(2)**:262, 2000.
- [171] J. Qi, F. C. Spano, T. Kirova, A. Lazoudis, J. Magnes, L. Li, L. M. Narducci, R. W. Field, & A. M. Lyyra, 'Measurement of transition dipole moments in lithium dimers using electromagnetically induced transparency', *Physical Review Letters* **88(17)**:173003, 2002.
- [172] H. Kuhn, 'Classical aspects of energy transfer in molecular systems', *The Journal of Chemical Physics* **53(1)**:101, 1970.
- [173] R. R. Chance, A. Prock, & R. Silbey, 'Lifetime of an emitting molecule near a partially reflecting surface', *The Journal of Chemical Physics* **60(7)**:2744, 1974.
- [174] R. K. Chang & A. J. Campillo, *Optical Processes in Microcavities*, vol. 3 of *Advanced Series in Applied Physics*, 1st ed., World Scientific, Singapore, Republic of Singapore, 1996.
- [175] K. Srinivasan, M. Borselli, O. Painter, A. Stintz, & S. Krishna, 'Cavity Q, mode volume, and lasing threshold in small diameter AlGaAs microdisks with embedded quantum dots', *Optics Express* **14(3)**:1094, 2006.
- [176] D. Hunger, T. Steinmetz, Y. Colombe, C. Deutsch, T. W. Hänsch, & J. Reichel, 'A fiber Fabry-Perot cavity with high finesse', *New Journal of Physics* **12(6)**:065038, 2010.
- [177] M. S. Tame, K. R. McEnery, Ş. K. Özdemir, J. Lee, S. A. Maier, & M. S. Kim, 'Quantum plasmonics', *Nature Physics* **9(6)**:329, 2013.
- [178] E. Waks & D. Sridharan, 'Cavity QED treatment of interactions between a metal nanoparticle and a dipole emitter', *Physical Review A* **82(4)**:043845, 2010.
- [179] A. Archambault, T. V. Teperik, F. Marquier, & J.-J. Greffet, 'Surface plasmon Fourier optics', *Physical Review B* **79(19)**:195414, 2009.
- [180] A. Archambault, F. Marquier, J.-J. Greffet, & C. Arnold, 'Supplement to Quantum theory of spontaneous and stimulated emission of surface plasmons', *Physical Review B* **82(3)**:035411, 2010.
- [181] A. Archambault, F. Marquier, J.-J. Greffet, & C. Arnold, 'Quantum theory of spontaneous and stimulated emission of surface plasmons', *Physical Review B* **82(3)**:035411, 2010.
- [182] W. H. Louisell & W. H. Louisell, *Quantum Statistical Properties of Radiation*, vol. 7, 1st ed., John Wiley & Sons, Hoboken, New Jersey, USA, 1973.
- [183] E. M. Lifshitz & L. P. Pitaevskii, *Statistical Physics, Part 2: Theory of the Condensed State*, vol. 9 of *Course of Theoretical Physics*, 1st ed., Butterworth-Heinemann, Oxford, England, UK, 1980.
- [184] P. W. Anderson, *Concepts in Solids: Lectures on the Theory of Solids*, vol. 58 of *World Scientific Lecture Notes In Physics*, World Scientific, Singapore, Republic of Singapore, 1997.
- [185] R. A. Ferrell, 'Predicted radiation of plasma oscillations in metal films', *Physical Review* **111(5)**:1214, 1958.
- [186] E. A. Stern & R. A. Ferrell, 'Surface plasma oscillations of a degenerate electron gas', *Physical Review* **120(1)**:130, 1960.
- [187] O. Schubert, J. Becker, L. Carbone, Y. Khalavka, T. Provalska, I. Zins, & C. Sönnichsen, 'Mapping the polarization pattern of plasmon modes reveals nanoparticle symmetry', *Nano Letters* **8(8)**:2345, 2008.
- [188] S. Viarbitskaya, A. Teulle, R. Marty, J. Sharma, C. Girard, A. Arbouet, & E. Dujardin, 'Tailoring and imaging the plasmonic local density of states in crystalline nanoprisms', *Nature Materials* **12(5)**:426, 2013.
- [189] E. M. Purcell & C. R. Pennypacker, 'Scattering and absorption of light by nonspherical dielectric grains', *The Astrophysical Journal* **186**:705, 1973.

- 
- [190] S. G. Rodrigo, F. J. García-Vidal, & L. Martín-Moreno, 'Influence of material properties on extraordinary optical transmission through hole arrays', *Physical Review B* **77(7)**:075401, 2008.
- [191] A. Teulle, R. Marty, S. Viarbitskaya, A. Arbouet, E. Dujardin, C. Girard, & G. C. Des Francs, 'Scanning optical microscopy modeling in nanoplasmonics', *Journal of the Optical Society of America B* **29(9)**:2431, 2012.
- [192] D. Pines & D. Bohm, 'A collective description of electron interactions: II. Collective vs individual particle aspects of the interactions', *Physical Review* **85(2)**:338, 1952.
- [193] D. Pines, 'Classical and quantum plasmas', *Journal of Nuclear Energy. Part C: Plasma Physics, Accelerators, Thermonuclear Research* **2(1)**:5, 1961.
- [194] H. J. Lipkin, 'Collective description of electron interactions without subsidiary conditions', *Physical Review Letters* **2(4)**:159, 1959.
- [195] A. Auffèves, J.-M. Gérard, & J.-P. Poizat, 'Pure emitter dephasing: A resource for advanced solid-state single-photon sources', *Physical Review A* **79(5)**:053838, 2009.
- [196] P. Törmä & W. L. Barnes, 'Strong coupling between surface plasmon polaritons and emitters: a review', *Reports on Progress in Physics* **78(1)**:013901, 2014.
- [197] K. J. Vahala, 'Optical microcavities', *Nature* **424(6950)**:839, 2003.
- [198] H. Mabuchi & A. C. Doherty, 'Cavity quantum electrodynamics: coherence in context', *Science* **298(5597)**:1372, 2002.
- [199] J. R. Buck & H. J. Kimble, 'Optimal sizes of dielectric microspheres for cavity QED with strong coupling', *Physical Review A* **67(3)**:033806, 2003.
- [200] K. Słowik, R. Filter, J. Straubel, F. Lederer, & C. Rockstuhl, 'Strong coupling of optical nanoantennas and atomic systems', *Physical Review B* **88(19)**:195414, 2013.
- [201] R. Esteban, J. Aizpurua, & G. W. Bryant, 'Strong coupling of single emitters interacting with phononic infrared antennae', *New Journal of Physics* **16(1)**:013052, 2014.
- [202] J. Galego, F. J. Garcia-Vidal, & J. Feist, 'Cavity-induced modifications of molecular structure in the strong-coupling regime', *Physical Review X* **5(4)**:041022, 2015.
- [203] J. P. Reithmaier, G. Şek, A. Löffler, C. Hofmann, S. Kuhn, S. Reitzenstein, L. V. Keldysh, V. D. Kulakovskii, T. L. Reinecke, & A. Forchel, 'Strong coupling in a single quantum dot-semiconductor microcavity system', *Nature* **432(7014)**:197, 2004.
- [204] Y. Colombe, T. Steinmetz, G. Dubois, F. Linke, D. Hunger, & J. Reichel, 'Strong atom-field coupling for Bose–Einstein condensates in an optical cavity on a chip', *Nature* **450(7167)**:272, 2007.
- [205] G. Zengin, M. Wersäll, S. Nilsson, T. J. Antosiewicz, M. Käll, & T. Shegai, 'Realizing strong light-matter interactions between single-nanoparticle plasmons and molecular excitons at ambient conditions', *Physical Review Letters* **114(15)**:157401, 2015.
- [206] R. Chikkaraddy, B. de Nijs, F. Benz, S. J. Barrow, O. A. Scherman, E. Rosta, A. Demetriadou, P. Fox, O. Hess, & J. J. Baumberg, 'Single-molecule strong coupling at room temperature in plasmonic nanocavities', *Nature* **535(7610)**:127, 2016.
- [207] A. Auffèves, D. Gerace, J.-M. Gérard, M. F. Santos, L. C. Andreani, & J.-P. Poizat, 'Controlling the dynamics of a coupled atom-cavity system by pure dephasing', *Physical Review B* **81(24)**:245419, 2010.
- [208] R. Filter, K. Słowik, J. Straubel, F. Lederer, & C. Rockstuhl, 'Nanoantennas for ultrabright single photon sources', *Optics Letters* **39(5)**:1246, 2014.
- [209] W. Lukosz & R. E. Kunz, 'Light emission by magnetic and electric dipoles close to a plane interface. I. Total radiated power', *Journal of the Optical Society of America* **67(12)**:1607, 1977.

- [210] R. R. Chance, A. Prock, & R. Silbey, 'Molecular fluorescence and energy transfer near interfaces', *Advances in Chemical Physics* **37(1)**:65, 1978.
- [211] W. L. Barnes, 'Fluorescence near interfaces: the role of photonic mode density', *Journal of Modern Optics* **45(4)**:661, 1998.
- [212] T. Klar, M. Perner, S. Grosse, G. Von Plessen, W. Spirkl, & J. Feldmann, 'Surface-plasmon resonances in single metallic nanoparticles', *Physical Review Letters* **80(19)**:4249, 1998.
- [213] A. M. Michaels, M. Nirmal, & L. E. Brus, 'Surface enhanced Raman spectroscopy of individual Rhodamine 6G molecules on large Ag nanocrystals', *Journal of the American Chemical Society* **121(43)**:9932, 1999.
- [214] J. R. Krenn, G. Schider, W. Rechberger, B. Lamprecht, A. Leitner, F. R. Aussenegg, & J. C. Weeber, 'Design of multipolar plasmon excitations in silver nanoparticles', *Applied Physics Letters* **77(21)**:3379, 2000.
- [215] J. J. Mock, M. Barbic, D. R. Smith, D. A. Schultz, & S. Schultz, 'Shape effects in plasmon resonance of individual colloidal silver nanoparticles', *The Journal of Chemical Physics* **116(15)**:6755, 2002.
- [216] K. G. Thomas, S. Barazzouk, B. I. Ipe, S. T. S. Joseph, & P. V. Kamat, 'Uniaxial plasmon coupling through longitudinal self-assembly of gold nanorods', *The Journal of Physical Chemistry B* **108(35)**:13066, 2004.
- [217] A. M. Funston, C. Novo, T. J. Davis, & P. Mulvaney, 'Plasmon coupling of gold nanorods at short distances and in different geometries', *Nano Letters* **9(4)**:1651, 2009.
- [218] T. K. Sau, A. L. Rogach, F. Jäckel, T. A. Klar, & J. Feldmann, 'Properties and applications of colloidal nonspherical noble metal nanoparticles', *Advanced Materials* **22(16)**:1805, 2010.
- [219] Y. Hu, S. J. Noelck, & R. A. Drezek, 'Symmetry breaking in gold-silica-gold multilayer nanoshells', *ACS Nano* **4(3)**:1521, 2010.
- [220] M. Bosman, E. Ye, S. F. Tan, C. A. Nijhuis, J. K. W. Yang, R. Marty, A. Mlayah, A. Arbouet, C. Girard, & M.-Y. Han, 'Surface plasmon damping quantified with an electron nanoprobe', *Scientific Reports* **3**:1312, 2013.
- [221] C. J. Orendorff, A. Gole, T. K. Sau, & C. J. Murphy, 'Surface-enhanced Raman spectroscopy of self-assembled monolayers: sandwich architecture and nanoparticle shape dependence', *Analytical Chemistry* **77(10)**:3261, 2005.
- [222] F. Le, N. Z. Lwin, J. M. Steele, M. Käll, N. J. Halas, & P. Nordlander, 'Plasmons in the metallic nanoparticle-film system as a tunable impurity problem', *Nano Letters* **5(10)**:2009, 2005.
- [223] C. L. Nehl, H. Liao, & J. H. Hafner, 'Optical properties of star-shaped gold nanoparticles', *Nano Letters* **6(4)**:683, 2006.
- [224] N. Liu, H. Guo, L. Fu, S. Kaiser, H. Schweizer, & H. Giessen, 'Plasmon hybridization in stacked cut-wire metamaterials', *Advanced Materials* **19(21)**:3628, 2007.
- [225] J. Alegret, T. Rindzevicius, T. Pakizeh, Y. Alaverdyan, L. Gunnarsson, & M. Kall, 'Plasmonic properties of silver trimers with trigonal symmetry fabricated by electron-beam lithography', *The Journal of Physical Chemistry C* **112(37)**:14313, 2008.
- [226] J. B. Lassiter, J. Aizpurua, L. I. Hernandez, D. W. Brandl, I. Romero, S. Lal, J. H. Hafner, P. Nordlander, & N. J. Halas, 'Close encounters between two nanoshells', *Nano Letters* **8(4)**:1212, 2008.
- [227] M. W. Knight, Y. Wu, J. B. Lassiter, P. Nordlander, & N. J. Halas, 'Substrates matter: influence of an adjacent dielectric on an individual plasmonic nanoparticle', *Nano Letters* **9(5)**:2188, 2009.
- [228] N. Liu, H. Liu, S. Zhu, & H. Giessen, 'Stereometamaterials', *Nature Photonics* **3(3)**:157, 2009.
- [229] B. Yan, A. Thubagere, W. R. Premasiri, L. D. Ziegler, L. Dal Negro, & B. M. Reinhard, 'Engineered SERS substrates with multiscale signal enhancement: nanoparticle cluster arrays', *ACS Nano* **3(5)**:1190, 2009.

- 
- [230] M. Hu, A. Ghoshal, M. Marquez, & P. G. Kik, 'Single particle spectroscopy study of metal-film-induced tuning of silver nanoparticle plasmon resonances', *The Journal of Physical Chemistry C* **114(16)**:7509, 2010.
- [231] U. Fano, 'Effects of configuration interaction on intensities and phase shifts', *Physical Review* **124(6)**:1866, 1961.
- [232] A. Bianconi, 'Ugo Fano and shape resonances', in 'AIP Conference Proceedings', vol. 652, 13, AIP, 2003.
- [233] B. Luk'yanchuk, N. I. Zheludev, S. A. Maier, N. J. Halas, P. Nordlander, H. Giessen, & C. T. Chong, 'The Fano resonance in plasmonic nanostructures and metamaterials', *Nature Materials* **9(9)**:707, 2010.
- [234] A. E. Miroshnichenko, S. Flach, & Y. S. Kivshar, 'Fano resonances in nanoscale structures', *Reviews of Modern Physics* **82(3)**:2257, 2010.
- [235] N. J. Halas, S. Lal, W.-S. Chang, S. Link, & P. Nordlander, 'Plasmons in strongly coupled metallic nanostructures', *Chemical Reviews* **111(6)**:3913, 2011.
- [236] S. Bandopadhyay, B. Dutta-Roy, & H. S. Mani, 'Understanding the Fano resonance through toy models', *American Journal of Physics* **72(12)**:1501, 2004.
- [237] B. Gallinet & O. J. F. Martin, 'Ab initio theory of Fano resonances in plasmonic nanostructures and metamaterials', *Physical Review B* **83(23)**:235427, 2011.
- [238] Y. S. Joe, A. M. Satanin, & C. S. Kim, 'Classical analogy of Fano resonances', *Physica Scripta* **74(2)**:259, 2006.
- [239] B. Gallinet & O. J. F. Martin, 'Influence of electromagnetic interactions on the line shape of plasmonic Fano resonances', *ACS Nano* **5(11)**:8999, 2011.
- [240] A. Christ, S. G. Tikhodeev, N. A. Gippius, J. Kuhl, & H. Giessen, 'Waveguide-plasmon polaritons: strong coupling of photonic and electronic resonances in a metallic photonic crystal slab', *Physical Review Letters* **91(18)**:183901, 2003.
- [241] E. M. Hicks, S. Zou, G. C. Schatz, K. G. Spears, R. P. Van Duyne, L. Gunnarsson, T. Rindzevicius, B. Kasemo, & M. Käll, 'Controlling plasmon line shapes through diffractive coupling in linear arrays of cylindrical nanoparticles fabricated by electron beam lithography', *Nano Letters* **5(6)**:1065, 2005.
- [242] V. A. Fedotov, M. Rose, S. L. Prosvirnin, N. Papasimakis, & N. I. Zheludev, 'Sharp trapped-mode resonances in planar metamaterials with a broken structural symmetry', *Physical Review Letters* **99(14)**:147401, 2007.
- [243] S. N. Sheikholeslami, A. García-Etxarri, & J. A. Dionne, 'Controlling the interplay of electric and magnetic modes via Fano-like plasmon resonances', *Nano Letters* **11(9)**:3927, 2011.
- [244] Y. Xu, Y. Li, R. K. Lee, & A. Yariv, 'Scattering-theory analysis of waveguide-resonator coupling', *Physical Review E* **62(5)**:7389, 2000.
- [245] A. Naweed, G. Farca, S. I. Shopova, & A. T. Rosenberger, 'Induced transparency and absorption in coupled whispering-gallery microresonators', *Physical Review A* **71(4)**:043804, 2005.
- [246] N. A. Mirin, K. Bao, & P. Nordlander, 'Fano resonances in plasmonic nanoparticle aggregates', *The Journal of Physical Chemistry A* **113(16)**:4028, 2009.
- [247] M. Tomita, K. Totsuka, R. Hanamura, & T. Matsumoto, 'Tunable Fano interference effect in coupled-microsphere resonator-induced transparency', *Journal of the Optical Society of America B* **26(4)**:813, 2009.
- [248] J. A. Fan, C. Wu, K. Bao, J. Bao, R. Bardhan, N. J. Halas, V. N. Manoharan, P. Nordlander, G. Shvets, & F. Capasso, 'Self-assembled plasmonic nanoparticle clusters', *Science* **328(5982)**:1135, 2010.
- [249] J. A. Fan, K. Bao, C. Wu, J. Bao, R. Bardhan, N. J. Halas, V. N. Manoharan, G. Shvets, P. Nordlander, & F. Capasso, 'Fano-like interference in self-assembled plasmonic quadrumer clusters', *Nano Letters* **10(11)**:4680, 2010.

- [250] I. M. Pryce, K. Aydin, Y. A. Kelaita, R. M. Briggs, & H. A. Atwater, 'Highly strained compliant optical metamaterials with large frequency tunability', *Nano Letters* **10(10)**:4222, 2010.
- [251] T. Shegai, S. Chen, V. D. Miljković, G. Zengin, P. Johansson, & M. Käll, 'A bimetallic nanoantenna for directional colour routing', *Nature Communications* **2**:481, 2011.
- [252] N. Verellen, Y. Sonnefraud, H. Sobhani, F. Hao, V. V. Moshchalkov, P. V. Dorpe, P. Nordlander, & S. A. Maier, 'Fano resonances in individual coherent plasmonic nanocavities', *Nano Letters* **9(4)**:1663, 2009.
- [253] L. V. Brown, H. Sobhani, J. B. Lassiter, P. Nordlander, & N. J. Halas, 'Heterodimers: plasmonic properties of mismatched nanoparticle pairs', *ACS Nano* **4(2)**:819, 2010.
- [254] M. Hentschel, M. Saliba, R. Vogelgesang, H. Giessen, A. P. Alivisatos, & N. Liu, 'Transition from isolated to collective modes in plasmonic oligomers', *Nano Letters* **10(7)**:2721, 2010.
- [255] F. López-Tejeira, R. Paniagua-Domínguez, R. Rodríguez-Oliveros, & J. A. Sánchez-Gil, 'Fano-like interference of plasmon resonances at a single rod-shaped nanoantenna', *New Journal of Physics* **14(2)**:023035, 2012.
- [256] A. Christ, T. Zentgraf, J. Kuhl, S. G. Tikhodeev, N. A. Gippius, & H. Giessen, 'Optical properties of planar metallic photonic crystal structures: experiment and theory', *Physical Review* **B 70(12)**:125113, 2004.
- [257] T. Pakizeh, C. Langhammer, I. Zoric, P. Apell, & M. Käll, 'Intrinsic Fano interference of localized plasmons in Pd nanoparticles', *Nano Letters* **9(2)**:882, 2009.
- [258] R. Adato, A. A. Yanik, J. J. Amsden, D. L. Kaplan, F. G. Omenetto, M. K. Hong, S. Erramilli, & H. Altug, 'Ultra-sensitive vibrational spectroscopy of protein monolayers with plasmonic nanoantenna arrays', *Proceedings of the National Academy of Sciences* **106(46)**:19227, 2009.
- [259] N. Verellen, F. López-Tejeira, R. Paniagua-Domínguez, D. Vercruysse, D. Denkova, L. Lagae, P. Van Dorpe, V. V. Moshchalkov, & J. A. Sánchez-Gil, 'Mode parity-controlled Fano- and Lorentz-like line shapes arising in plasmonic nanorods', *Nano Letters* **14(5)**:2322, 2014.
- [260] F. Hao, P. Nordlander, Y. Sonnefraud, P. V. Dorpe, & S. A. Maier, 'Tunability of subradiant dipolar and Fano-type plasmon resonances in metallic ring/disk cavities: implications for nanoscale optical sensing', *ACS Nano* **3(3)**:643, 2009.
- [261] Z.-J. Yang, Z.-S. Zhang, L.-H. Zhang, Q.-Q. Li, Z.-H. Hao, & Q.-Q. Wang, 'Fano resonances in dipole-quadrupole plasmon coupling nanorod dimers', *Optics Letters* **36(9)**:1542, 2011.
- [262] M. W. Klein, T. Tritschler, M. Wegener, & S. Linden, 'Lineshape of harmonic generation by metallic nanoparticles and metallic photonic crystal slabs', *Physical Review* **B 72(11)**:115113, 2005.
- [263] N. Liu, L. Langguth, T. Weiss, J. Kästel, M. Fleischhauer, T. Pfau, & H. Giessen, 'Plasmonic analogue of electromagnetically induced transparency at the Drude damping limit', *Nature Materials* **8(9)**:758, 2009.
- [264] Y. Sonnefraud, N. Verellen, H. Sobhani, G. A. E. Vandenbosch, V. V. Moshchalkov, P. Van Dorpe, P. Nordlander, & S. A. Maier, 'Experimental realization of subradiant, superradiant, and Fano resonances in ring/disk plasmonic nanocavities', *ACS Nano* **4(3)**:1664, 2010.
- [265] J. B. Lassiter, H. Sobhani, J. A. Fan, J. Kundu, F. Capasso, P. Nordlander, & N. J. Halas, 'Fano resonances in plasmonic nanoclusters: geometrical and chemical tunability', *Nano Letters* **10(8)**:3184, 2010.
- [266] N. Verellen, P. Van Dorpe, C. Huang, K. Lodewijks, G. A. E. Vandenbosch, L. Lagae, & V. V. Moshchalkov, 'Plasmon line shaping using nanocrosses for high sensitivity localized surface plasmon resonance sensing', *Nano Letters* **11(2)**:391, 2011.
- [267] A. Nazir, S. Panaro, R. Proietti Zaccaria, C. Liberale, F. De Angelis, & A. Toma, 'Fano coil-type resonance for magnetic hot-spot generation', *Nano Letters* **14(6)**:3166, 2014.
- [268] F. Hao, Y. Sonnefraud, P. V. Dorpe, S. A. Maier, N. J. Halas, & P. Nordlander, 'Symmetry breaking in plasmonic nanocavities: subradiant LSPR sensing and a tunable Fano resonance', *Nano Letters* **8(11)**:3983, 2008.

- 
- [269] A. Lovera, B. Gallinet, P. Nordlander, & O. J. F. Martin, 'Mechanisms of Fano resonances in coupled plasmonic systems', *ACS Nano* **7(5)**:4527, 2013.
- [270] P. W. Barber & R. K. Chang, *Optical Effects Associated with Small Particles*, vol. 1 of *Advanced Series in Applied Physics*, World Scientific, Singapore, Republic of Singapore, 1988.
- [271] B. R. Johnson, 'Theory of morphology-dependent resonances: shape resonances and width formulas', *Journal of the Optical Society of America A* **10(2)**:343, 1993.
- [272] J. Zeng, F. Zhao, J. Qi, Y. Li, C.-H. Li, Y. Yao, T. R. Lee, & W.-C. Shih, 'Internal and external morphology-dependent plasmonic resonance in monolithic nanoporous gold nanoparticles', *RSC Advances* **4(69)**:36682, 2014.
- [273] J. Dorfmueller, R. Vogelgesang, W. Khunsin, C. Rockstuhl, C. Etrich, & K. Kern, 'Plasmonic nanowire antennas: experiment, simulation, and theory', *Nano Letters* **10(9)**:3596, 2010.
- [274] J. Aizpurua, G. W. Bryant, L. J. Richter, F. J. G. De Abajo, B. K. Kelley, & T. Mallouk, 'Optical properties of coupled metallic nanorods for field-enhanced spectroscopy', *Physical Review B* **71(23)**:235420, 2005.
- [275] A. G. Curto, T. H. Taminiau, G. Volpe, M. P. Kreuzer, R. Quidant, & N. F. Van Hulst, 'Multipolar radiation of quantum emitters with nanowire optical antennas', *Nature Communications* **4**:1750, 2013.
- [276] T. Søndergaard & S. I. Bozhevolnyi, 'Metal nano-strip optical resonators', *Optics Express* **15(7)**:4198, 2007.
- [277] B. Pietrobon, M. McEachran, & V. Kitaev, 'Synthesis of size-controlled faceted pentagonal silver nanorods with tunable plasmonic properties and self-assembly of these nanorods', *ACS Nano* **3(1)**:21, 2008.
- [278] H. Wang, T. B. Huff, D. A. Zweifel, W. He, P. S. Low, A. Wei, & J.-X. Cheng, 'In vitro and in vivo two-photon luminescence imaging of single gold nanorods', *Proceedings of the National Academy of Sciences of the United States of America* **102(44)**:15752, 2005.
- [279] P. Ghenuche, S. Cherukulappurath, T. H. Taminiau, N. F. van Hulst, & R. Quidant, 'Spectroscopic mode mapping of resonant plasmon nanoantennas', *Physical Review Letters* **101(11)**:116805, 2008.
- [280] L. Novotny, 'Effective wavelength scaling for optical antennas', *Physical Review Letters* **98(26)**:266802, 2007.
- [281] G. W. Bryant, F. J. Garcia de Abajo, & J. Aizpurua, 'Mapping the plasmon resonances of metallic nanoantennas', *Nano Letters* **8(2)**:631, 2008.
- [282] H. Yuan, S. Khatua, P. Zijlstra, M. Yorulmaz, & M. Orrit, 'Thousand-fold enhancement of single-molecule fluorescence near a single gold nanorod', *Angewandte Chemie International Edition* **52(4)**:1217, 2013.
- [283] P. Zijlstra, P. M. R. Paulo, & M. Orrit, 'Optical detection of single non-absorbing molecules using the surface plasmon resonance of a gold nanorod', *Nature Nanotechnology* **7(6)**:379, 2012.
- [284] E. B. Dickerson, E. C. Dreaden, X. Huang, I. H. El-Sayed, H. Chu, S. Pushpanketh, J. F. McDonald, & M. A. El-Sayed, 'Gold nanorod assisted near-infrared plasmonic photothermal therapy (PPTT) of squamous cell carcinoma in mice', *Cancer Letters* **269(1)**:57, 2008.
- [285] E. M. Purcell, 'Spontaneous emission probabilities at radio frequencies', *Physical Review* **69(11 & 12)**:681, 1946.
- [286] E. Fort & S. Grésillon, 'Surface enhanced fluorescence', *Journal of Physics D: Applied Physics* **41(1)**:013001, 2007.
- [287] H. Kaupp, C. Deutsch, H.-C. Chang, J. Reichel, T. W. Hänsch, & D. Hunger, 'Scaling laws of the cavity enhancement for nitrogen-vacancy centers in diamond', *Physical Review A* **88(5)**:053812, 2013.
- [288] R. Vogelgesang, J. Dorfmueller, R. Esteban, R. T. Weitz, A. Dmitriev, & K. Kern, 'Plasmonic nanostructures in aperture-less scanning near-field optical microscopy (aSNOM)', *Physica Status Solidi (b) - Basic Solid State Physics* **245(10)**:2255, 2008.

- [289] M. T. Wenzel, T. Härtling, P. Olk, S. C. Kehr, S. Grafstrøm, S. Winnerl, M. Helm, & L. M. Eng, 'Gold nanoparticle tips for optical field confinement in infrared scattering near-field optical microscopy', *Optics Express* **16(16)**:12302, 2008.
- [290] C. Höppener & L. Novotny, 'Antenna-based optical imaging of single Ca<sup>2+</sup> transmembrane proteins in liquids', *Nano Letters* **8(2)**:642, 2008.
- [291] S. Pillai, K. R. Catchpole, T. Trupke, G. Zhang, J. Zhao, & M. A. Green, 'Enhanced emission from Si-based light-emitting diodes using surface plasmons', *Applied Physics Letters* **88(16)**:161102, 2006.
- [292] G. Sun, J. B. Khurgin, & R. A. Soref, 'Plasmonic light-emission enhancement with isolated metal nanoparticles and their coupled arrays', *Journal of the Optical Society of America B* **25(10)**:1748, 2008.
- [293] K. Ziemelis, 'Display technology: glowing developments', *Nature* **399(6735)**:408, 1999.
- [294] E. F. Schubert & J. K. Kim, 'Solid-state light sources getting smart', *Science* **308(5726)**:1274, 2005.
- [295] A. J. Shields, 'Semiconductor quantum light sources', *Nature Photonics* **1(4)**:215, 2007.
- [296] Y. Yamamoto, S. Machida, & G. Björk, 'Microcavity semiconductor laser with enhanced spontaneous emission', *Physical Review A* **44(1)**:657, 1991.
- [297] T. D. Happ, I. I. Tartakovskii, V. D. Kulakovskii, J.-P. Reithmaier, M. Kamp, & A. Forchel, 'Enhanced light emission of In<sub>x</sub>Ga<sub>1-x</sub>As quantum dots in a two-dimensional photonic-crystal defect microcavity', *Physical Review B* **66(4)**:041303, 2002.
- [298] A. Badolato, K. Hennessy, M. Atatüre, J. Dreiser, E. Hu, P. M. Petroff, & A. Imamoglu, 'Deterministic coupling of single quantum dots to single nanocavity modes', *Science* **308(5725)**:1158, 2005.
- [299] S. Noda, M. Fujita, & T. Asano, 'Spontaneous-emission control by photonic crystals and nanocavities', *Nature Photonics* **1(8)**:449, 2007.
- [300] H. Sumikura, E. Kuramochi, H. Taniyama, & M. Notomi, 'Ultrafast spontaneous emission of copper-doped silicon enhanced by an optical nanocavity', *Scientific Reports* **4**:5040, 2014.
- [301] N. Somaschi, V. Giesz, L. De Santis, J. C. Loredó, M. P. Almeida, G. Hornecker, S. L. Portalupi, T. Grange, C. Antón, J. Demory, C. Gómez, I. Sagnes, N. D. Lanzillotti-Kimura, A. Lemaitre, A. Auffeves, A. G. White, L. Lanco, & P. Senellart, 'Near-optimal single-photon sources in the solid state', *Nature Photonics* **10(5)**:340, 2016.
- [302] Y. C. Jun, R. Pala, & M. L. Brongersma, 'Strong modification of quantum dot spontaneous emission via gap plasmon coupling in metal nanoslits', *The Journal of Physical Chemistry C* **114(16)**:7269, 2009.
- [303] R. Esteban, T. V. Teperik, & J.-J. Greffet, 'Optical patch antennas for single photon emission using surface plasmon resonances', *Physical Review Letters* **104(2)**:026802, 2010.
- [304] E. J. R. Vesseur, F. J. G. de Abajo, & A. Polman, 'Broadband Purcell enhancement in plasmonic ring cavities', *Physical Review B* **82(16)**:165419, 2010.
- [305] K. J. Russell, T.-L. Liu, S. Cui, & E. L. Hu, 'Large spontaneous emission enhancement in plasmonic nanocavities', *Nature Photonics* **6(7)**:459, 2012.
- [306] T. B. Hoang, G. M. Akselrod, C. Argyropoulos, J. Huang, D. R. Smith, & M. H. Mikkelsen, 'Ultrafast spontaneous emission source using plasmonic nanoantennas', *Nature Communications* **6**:7788, 2015.
- [307] K. F. Mak, K. He, C. Lee, G. H. Lee, J. Hone, T. F. Heinz, & J. Shan, 'Tightly bound trions in monolayer MoS<sub>2</sub>', *Nature Materials* **12(3)**:207, 2013.
- [308] S. Mouri, Y. Miyauchi, & K. Matsuda, 'Tunable photoluminescence of monolayer MoS<sub>2</sub> via chemical doping', *Nano Letters* **13(12)**:5944, 2013.
- [309] H. Zhu, Y. Wang, J. Xiao, M. Liu, S. Xiong, Z. J. Wong, Z. Ye, Y. Ye, X. Yin, & X. Zhang, 'Observation of piezoelectricity in free-standing monolayer MoS<sub>2</sub>', *Nature Nanotechnology* **10(2)**:151, 2015.

- 
- [310] O. Lopez-Sanchez, D. Lembke, M. Kayci, A. Radenovic, & A. Kis, 'Ultrasensitive photodetectors based on monolayer MoS<sub>2</sub>', *Nature Nanotechnology* **8(7)**:497, 2013.
- [311] S. Lei, F. Wen, L. Ge, S. Najmaei, A. George, Y. Gong, W. Gao, Z. Jin, B. Li, J. Lou, J. Kono, R. Vajta, P. Ajayan, & N. J. Halas, 'An atomically layered InSe avalanche photodetector', *Nano Letters* **15(5)**:3048, 2015.
- [312] S. Wu, S. Buckley, J. R. Schaibley, L. Feng, J. Yan, D. G. Mandrus, F. Hatami, W. Yao, J. Vučković, A. Majumdar, & X. Xu, 'Monolayer semiconductor nanocavity lasers with ultralow thresholds', *Nature* **520(7545)**:69, 2015.
- [313] H. Chen, J. Yang, E. Rusak, J. Straubel, R. Guo, Y. W. Myint, J. Pei, M. Decker, I. Staude, C. Rockstuhl, Y. Lu, Y. S. Kivshar, & D. Neshev, 'Manipulation of photoluminescence of two-dimensional MoSe<sub>2</sub> by gold nanoantennas', *Scientific Reports* **6**:22296, 2016.
- [314] D. Englund, D. Fattal, E. Waks, G. Solomon, B. Zhang, T. Nakaoka, Y. Arakawa, Y. Yamamoto, & J. Vučković, 'Controlling the spontaneous emission rate of single quantum dots in a two-dimensional photonic crystal', *Physical Review Letters* **95(1)**:013904, 2005.
- [315] J. A. Schuller, S. Karaveli, T. Schiros, K. He, S. Yang, I. Kyriassis, J. Shan, & R. Zia, 'Orientation of luminescent excitons in layered nanomaterials', *Nature Nanotechnology* **8(4)**:271, 2013.
- [316] K. F. Mak, C. Lee, J. Hone, J. Shan, & T. F. Heinz, 'Atomically thin MoS<sub>2</sub>: a new direct-gap semiconductor', *Physical Review Letters* **105(13)**:136805, 2010.
- [317] R. Singh, C. Rockstuhl, F. Lederer, & W. Zhang, 'Coupling between a dark and a bright eigenmode in a terahertz metamaterial', *Physical Review B* **79(8)**:085111, 2009.
- [318] Z.-G. Dong, H. Liu, M.-X. Xu, T. Li, S.-M. Wang, J.-X. Cao, S.-N. Zhu, & X. Zhang, 'Role of asymmetric environment on the dark mode excitation in metamaterial analogue of electromagnetically-induced transparency', *Optics Express* **18(21)**:22412, 2010.
- [319] T. G. Habteyes, S. Dhuey, S. Cabrini, P. J. Schuck, & S. R. Leone, 'Theta-shaped plasmonic nanostructures: bringing "dark" multipole plasmon resonances into action via conductive coupling', *Nano Letters* **11(4)**:1819, 2011.
- [320] S. Panaro, A. Nazir, C. Liberale, G. Das, H. Wang, F. De Angelis, R. Proietti Zaccaria, E. Di Fabrizio, & A. Toma, 'Dark to bright mode conversion on dipolar nanoantennas: a symmetry-breaking approach', *ACS Photonics* **1(4)**:310, 2014.
- [321] R. M. Bakker, A. Boltasseva, Z. Liu, R. H. Pedersen, S. Gresillon, A. V. Kildishev, V. P. Drachev, & V. M. Shalaev, 'Near-field excitation of nanoantenna resonance', *Optics Express* **15(21)**:13682, 2007.
- [322] M. Schnell, A. Garcia-Etxarri, A. J. Huber, K. Crozier, J. Aizpurua, & R. Hillenbrand, 'Controlling the near-field oscillations of loaded plasmonic nanoantennas', *Nature Photonics* **3(5)**:287, 2009.
- [323] J. A. Schuller, E. S. Barnard, W. Cai, Y. C. Jun, J. S. White, & M. L. Brongersma, 'Plasmonics for extreme light concentration and manipulation', *Nature Materials* **9(3)**:193, 2010.
- [324] D. K. Gramotnev & S. I. Bozhevolnyi, 'Plasmonics beyond the diffraction limit', *Nature Photonics* **4(2)**:83, 2010.
- [325] R. Zia, J. A. Schuller, A. Chandran, & M. L. Brongersma, 'Plasmonics: the next chip-scale technology', *Materials Today* **9(7-8)**:20, 2006.
- [326] T. Ishi, J. Fujikata, K. Makita, T. Baba, & K. Ohashi, 'Si nano-photodiode with a surface plasmon antenna', *Japanese Journal of Applied Physics* **44(3L)**:L364, 2005.
- [327] G. Konstantatos & E. H. Sargent, 'Nanostructured materials for photon detection', *Nature Nanotechnology* **5(6)**:391, 2010.
- [328] A. Sobhani, M. W. Knight, Y. Wang, B. Zheng, N. S. King, L. V. Brown, Z. Fang, P. Nordlander, & N. J. Halas, 'Narrowband photodetection in the near-infrared with a plasmon-induced hot electron device', *Nature Communications* **4**:1643, 2013.

- [329] J. Miao, W. Hu, Y. Jing, W. Luo, L. Liao, A. Pan, S. Wu, J. Cheng, X. Chen, & W. Lu, 'Surface plasmon-enhanced photodetection in few layer MoS<sub>2</sub> phototransistors with Au nanostructure arrays', *Small* **11(20)**:2392, 2015.
- [330] W. Cai, J. S. White, & M. L. Brongersma, 'Compact, high-speed and power-efficient electrooptic plasmonic modulators', *Nano Letters* **9(12)**:4403, 2009.
- [331] A. Melikyan, L. Alloatti, A. Muslija, D. Hillerkuss, P. C. Schindler, J. Li, R. Palmer, D. Korn, S. Muehlbrandt, D. Van Thourhout, B. Chen, R. Dinu, M. Sommer, C. Koos, M. Kohl, W. Freude, & J. Leuthold, 'High-speed plasmonic phase modulators', *Nature Photonics* **8(3)**:229, 2014.
- [332] J. T. Kim, 'CMOS-compatible hybrid plasmonic modulator based on vanadium dioxide insulator-metal phase transition', *Optics Letters* **39(13)**:3997, 2014.
- [333] W. Heni, C. Hoessbacher, C. Haffner, Y. Fedoryshyn, B. Baeuerle, A. Josten, D. Hillerkuss, Y. Salamin, R. Bonjour, A. Melikyan, M. Kohl, D. L. Elder, L. R. Dalton, C. Hafner, & J. Leuthold, 'High speed plasmonic modulator array enabling dense optical interconnect solutions', *Optics Express* **23(23)**:29746, 2015.
- [334] J. Tao, X. G. Huang, & J. H. Zhu, 'A wavelength demultiplexing structure based on metal-dielectric-metal plasmonic nano-capillary resonators', *Optics Express* **18(11)**:11111, 2010.
- [335] H. Liu, Y. Gao, B. Zhu, G. Ren, & S. Jian, 'A T-shaped high resolution plasmonic demultiplexer based on perturbations of two nanoresonators', *Optics Communications* **334**:164, 2015.
- [336] L. Dobrzynski, A. Akjouj, B. Djafari-Rouhani, J. O. Vasseur, M. Bouazaoui, J. P. Vilcot, H. Al Wahsh, P. Zielinski, & J. P. Vigneron, 'Simple nanometric plasmon multiplexer', *Physical Review E* **69(3)**:035601, 2004.
- [337] Y. Fang, Z. Li, Y. Huang, S. Zhang, P. Nordlander, N. J. Halas, & H. Xu, 'Branched silver nanowires as controllable plasmon routers', *Nano Letters* **10(5)**:1950, 2010.
- [338] R.-M. Ma, X. Yin, R. F. Oulton, V. J. Sorger, & X. Zhang, 'Multiplexed and electrically modulated plasmon laser circuit', *Nano Letters* **12(10)**:5396, 2012.
- [339] A. J. Morfa, K. L. Rowlen, T. H. Reilly III, M. J. Romero, & J. van de Lagemaat, 'Plasmon-enhanced solar energy conversion in organic bulk heterojunction photovoltaics', *Applied Physics Letters* **92(1)**:013504, 2008.
- [340] H. A. Atwater & A. Polman, 'Plasmonics for improved photovoltaic devices', *Nature Materials* **9(3)**:205, 2010.
- [341] A. Aubry, D. Y. Lei, A. I. Fernández-Domínguez, Y. Sonnefraud, S. A. Maier, & J. B. Pendry, 'Plasmonic light-harvesting devices over the whole visible spectrum', *Nano Letters* **10(7)**:2574, 2010.
- [342] S. I. Bozhevolnyi, V. S. Volkov, E. Devaux, J.-Y. Laluet, & T. W. Ebbesen, 'Channel plasmon subwavelength waveguide components including interferometers and ring resonators', *Nature* **440(7083)**:508, 2006.
- [343] S. Lal, S. Link, & N. J. Halas, 'Nano-optics from sensing to waveguiding', *Nature Photonics* **1(11)**:641, 2007.
- [344] G. Veronis & S. Fan, 'Modes of subwavelength plasmonic slot waveguides', *Journal of Lightwave Technology* **25(9)**:2511, 2007.
- [345] A. V. Krasavin & A. V. Zayats, 'Passive photonic elements based on dielectric-loaded surface plasmon polariton waveguides', *Applied Physics Letters* **90(21)**:211101, 2007.
- [346] C. Min & G. Veronis, 'Absorption switches in metal-dielectric-metal plasmonic waveguides', *Optics Express* **17(13)**:10757, 2009.
- [347] D. Dai & S. He, 'A silicon-based hybrid plasmonic waveguide with a metal cap for a nano-scale light confinement', *Optics Express* **17(19)**:16646, 2009.

- 
- [348] F. López-Tejiera, S. G. Rodrigo, L. Martín-Moreno, F. J. García-Vidal, E. Devaux, T. W. Ebbesen, J. R. Krenn, I. P. Radko, S. I. Bozhevolnyi, M. U. González, J. C. Weeber, & A. Dereux, 'Efficient unidirectional nanoslit couplers for surface plasmons', *Nature Physics* **3(5)**:324, 2007.
- [349] J. S. Q. Liu, R. A. Pala, F. Afshinmanesh, W. Cai, & M. L. Brongersma, 'A submicron plasmonic dichroic splitter', *Nature Communications* **2**:525, 2011.
- [350] A. Baron, E. Devaux, J.-C. Rodier, J.-P. Hugonin, E. Rousseau, C. Genet, T. W. Ebbesen, & P. Lalanne, 'Compact antenna for efficient and unidirectional launching and decoupling of surface plasmons', *Nano Letters* **11(10)**:4207, 2011.
- [351] F. J. Rodríguez-Fortuño, G. Marino, P. Ginzburg, D. O'Connor, A. Martínez, G. A. Wurtz, & A. V. Zayats, 'Near-field interference for the unidirectional excitation of electromagnetic guided modes', *Science* **340(6130)**:328, 2013.
- [352] J. Petersen, J. Volz, & A. Rauschenbeutel, 'Chiral nanophotonic waveguide interface based on spin-orbit interaction of light', *Science* 1257671, 2014.
- [353] T. P. H. Sidiropoulos, M. P. Nielsen, T. R. Roschuk, A. V. Zayats, S. A. Maier, & R. F. Oulton, 'Compact optical antenna coupler for silicon photonics characterized by third-harmonic generation', *ACS Photonics* **1(10)**:912, 2014.
- [354] A. Y. Piggott, J. Lu, T. M. Babinec, K. G. Lagoudakis, J. Petykiewicz, & J. Vučković, 'Inverse design and implementation of a wavelength demultiplexing grating coupler', *Scientific Reports* **4**:7210, 2014.
- [355] J. Giergiel, C. E. Reed, J. C. Hemminger, & S. Ushioda, 'Surface-plasmon-polariton mode conversion on rough interfaces', *Physical Review B* **36(6)**:3052, 1987.
- [356] J. Straubel, R. Filter, C. Rockstuhl, & K. Słowik, 'Efficient mode conversion in an optical nanoantenna mediated by quantum emitters', *Optics Letters* **41(10)**:2294, 2016.
- [357] J. Straubel, R. Filter, C. Rockstuhl, & K. Słowik, 'Plasmonic nanoantenna based triggered single-photon source', *Physical Review B* **93(19)**:195412, 2016.
- [358] J. Straubel, R. Sarniak, C. Rockstuhl, & K. Słowik, 'Entangled light from bimodal optical nanoantennas', *Physical Review B* **95(8)**:085421, 2017.
- [359] E. Verhagen, M. Spasenović, A. Polman, & L. K. Kuipers, 'Nanowire plasmon excitation by adiabatic mode transformation', *Physical Review Letters* **102(20)**:203904, 2009.
- [360] Z.-J. Yang, Z.-S. Zhang, Z.-H. Hao, & Q.-Q. Wang, 'Fano resonances in active plasmonic resonators consisting of a nanorod dimer and a nano-emitter', *Applied Physics Letters* **99(8)**:081107, 2011.
- [361] J. Fontana & B. R. Ratna, 'Highly tunable gold nanorod dimer resonances mediated through conductive junctions', *Applied Physics Letters* **105(1)**:011107, 2014.
- [362] R.-C. Ge & S. Hughes, 'Design of an efficient single photon source from a metallic nanorod dimer: a quasi-normal mode finite-difference time-domain approach', *Optics Letters* **39(14)**:4235, 2014.
- [363] W. An, T. Zhu, & Q. Z. Zhu, 'Numerical investigation of radiative properties and surface plasmon resonance of silver nanorod dimers on a substrate', *Journal of Quantitative Spectroscopy and Radiative Transfer* **132**:28, 2014.
- [364] P. Pramod & K. G. Thomas, 'Plasmon coupling in dimers of Au nanorods', *Advanced Materials* **20(22)**:4300, 2008.
- [365] L. Shao, K. C. Woo, H. Chen, Z. Jin, J. Wang, & H.-Q. Lin, 'Angle-and energy-resolved plasmon coupling in gold nanorod dimers', *ACS Nano* **4(6)**:3053, 2010.
- [366] J. Kumar, X. Wei, S. Barrow, A. M. Funston, K. G. Thomas, & P. Mulvaney, 'Surface plasmon coupling in end-to-end linked gold nanorod dimers and trimers', *Physical Chemistry Chemical Physics* **15(12)**:4258, 2013.

- [367] H. Aouani, M. Rahmani, M. Navarro-Cía, & S. A. Maier, 'Third-harmonic-upconversion enhancement from a single semiconductor nanoparticle coupled to a plasmonic antenna', *Nature Nanotechnology* **9(4)**:290, 2014.
- [368] J. Wu, X. Lu, Q. Zhu, J. Zhao, Q. Shen, L. Zhan, & W. Ni, 'Angle-resolved plasmonic properties of single gold nanorod dimers', *Nano-Micro Letters* **6(4)**:372, 2014.
- [369] B. Willingham, D. W. Brandl, & P. Nordlander, 'Plasmon hybridization in nanorod dimers', *Applied Physics B* **93(1)**:209, 2008.
- [370] S.-C. Yang, H. Kobori, C.-L. He, M.-H. Lin, H.-Y. Chen, C. Li, M. Kanehara, T. Teranishi, & S. Gwo, 'Plasmon hybridization in individual gold nanocrystal dimers: direct observation of bright and dark modes', *Nano Letters* **10(2)**:632, 2010.
- [371] B. Lahiri, S. G. McMeekin, R. M. De La Rue, & N. P. Johnson, 'Resonance hybridization in nanoantenna arrays based on asymmetric split-ring resonators', *Applied Physics Letters* **98(15)**:153116, 2011.
- [372] M. Abb, Y. Wang, P. Albella, C. H. De Groot, J. Aizpurua, & O. L. Muskens, 'Interference, coupling, and nonlinear control of high-order modes in single asymmetric nanoantennas', *ACS Nano* **6(7)**:6462, 2012.
- [373] P. Alonso-González, P. Albella, F. Golmar, L. Arzubiaga, F. Casanova, L. E. Hueso, J. Aizpurua, & R. Hillenbrand, 'Visualizing the near-field coupling and interference of bonding and anti-bonding modes in infrared dimer nanoantennas', *Optics Express* **21(1)**:1270, 2013.
- [374] A. Lenef, S. W. Brown, D. A. Redman, S. C. Rand, J. Shigley, & E. Fritsch, 'Electronic structure of the N-V center in diamond: experiments', *Physical Review B* **53(20)**:13427, 1996.
- [375] M. Hentschel, D. Dregely, R. Vogelgesang, H. Giessen, & N. Liu, 'Plasmonic oligomers: the role of individual particles in collective behavior', *ACS Nano* **5(3)**:2042, 2011.
- [376] X. Liu, J. Gu, R. Singh, Y. Ma, J. Zhu, Z. Tian, M. He, J. Han, & W. Zhang, 'Electromagnetically induced transparency in terahertz plasmonic metamaterials via dual excitation pathways of the dark mode', *Applied Physics Letters* **100(13)**:131101, 2012.
- [377] L. S. Slaughter, Y. Wu, B. A. Willingham, P. Nordlander, & S. Link, 'Effects of symmetry breaking and conductive contact on the plasmon coupling in gold nanorod dimers', *ACS Nano* **4(8)**:4657, 2010.
- [378] J. Zhang, K. F. MacDonald, & N. I. Zheludev, 'Near-infrared trapped mode magnetic resonance in an all-dielectric metamaterial', *Optics Express* **21(22)**:26721, 2013.
- [379] S. Han, R. Singh, L. Cong, & H. Yang, 'Engineering the Fano resonance and electromagnetically induced transparency in near-field coupled bright and dark metamaterial', *Journal of Physics D: Applied Physics* **48(3)**:035104, 2014.
- [380] A. Shnirman, Y. Makhlin, & G. Schön, 'Noise and decoherence in quantum two-level systems', *Physica Scripta* **2002(T102)**:147, 2002.
- [381] F. Marquardt & A. Püttmann, 'Introduction to dissipation and decoherence in quantum systems', *arXiv preprint arXiv:0809.4403* 2008.
- [382] J. R. Maze, J. M. Taylor, & M. D. Lukin, 'Electron spin decoherence of single nitrogen-vacancy defects in diamond', *Physical Review B* **78(9)**:094303, 2008.
- [383] J. Hou, K. Słowik, F. Lederer, & C. Rockstuhl, 'Dissipation-driven entanglement between qubits mediated by plasmonic nanoantennas', *Physical Review B* **89(23)**:235413, 2014.
- [384] H. J. Kimble, 'The quantum internet', *Nature* **453(7198)**:1023, 2008.
- [385] A. Beveratos, R. Brouri, T. Gacoin, A. Villing, J.-P. Poizat, & P. Grangier, 'Single photon quantum cryptography', *Physical Review Letters* **89(18)**:187901, 2002.
- [386] A. Ourjoumteev, R. Tualle-Brouri, J. Laurat, & P. Grangier, 'Generating optical Schrödinger kittens for quantum information processing', *Science* **312(5770)**:83, 2006.
- [387] J. I. Cirac & H. J. Kimble, 'Quantum optics, what next?', *Nature Photonics* **11(1)**:18, 2017.

- 
- [388] A. Haase, N. Piro, J. Eschner, & M. W. Mitchell, 'Tunable narrowband entangled photon pair source for resonant single-photon single-atom interaction', *Optics Letters* **34(1)**:55, 2009.
- [389] C. Clausen, I. Usmani, F. Bussieres, N. Sangouard, M. Afzelius, H. de Riedmatten, & N. Gisin, 'Quantum storage of photonic entanglement in a crystal', *Nature* **469(7331)**:508, 2011.
- [390] K.-H. Luo, H. Herrmann, S. Krapick, B. Brecht, R. Ricken, V. Quiring, H. Suche, W. Sohler, & C. Silberhorn, 'Direct generation of genuine single-longitudinal-mode narrowband photon pairs', *New Journal of Physics* **17(7)**:073039, 2015.
- [391] Z. Y. Ou & Y. J. Lu, 'Cavity enhanced spontaneous parametric down-conversion for the prolongation of correlation time between conjugate photons', *Physical Review Letters* **83(13)**:2556, 1999.
- [392] M. Scholz, L. Koch, & O. Benson, 'Statistics of narrow-band single photons for quantum memories generated by ultrabright cavity-enhanced parametric down-conversion', *Physical Review Letters* **102(6)**:063603, 2009.
- [393] M. Förtsch, J. U. Fürst, C. Wittmann, D. Strekalov, A. Aiello, M. V. Chekhova, C. Silberhorn, G. Leuchs, & C. Marquardt, 'A versatile source of single photons for quantum information processing', *Nature Communications* **4**:1818, 2013.
- [394] T. Grange, G. Hornecker, D. Hunger, J.-P. Poizat, J.-M. Gérard, P. Senellart, & A. Auffèves, 'Cavity-funneled generation of indistinguishable single photons from strongly dissipative quantum emitters', *Physical Review Letters* **114(19)**:193601, 2015.
- [395] M. Rambach, A. Nikolova, T. J. Weinhold, & A. G. White, 'Sub-megahertz linewidth single photon source', *APL Photonics* **1(9)**:096101, 2016.
- [396] H. Kaupp, T. Hümmer, M. Mader, B. Schlederer, J. Benedikter, P. Haeusser, H.-C. Chang, H. Fedder, T. W. Hänsch, & D. Hunger, 'Purcell-enhanced single-photon emission from nitrogen-vacancy centers coupled to a tunable microcavity', *Physical Review Applied* **6(5)**:054010, 2016.
- [397] J. Benedikter, H. Kaupp, T. Hümmer, Y. Liang, A. Bommer, C. Becher, A. Krueger, J. M. Smith, T. W. Hänsch, & D. Hunger, 'Cavity-enhanced single-photon source based on the silicon-vacancy center in diamond', *Physical Review Applied* **7(2)**:024031, 2017.
- [398] S. Du, J. Wen, M. H. Rubin, & G. Y. Yin, 'Four-wave mixing and biphoton generation in a two-level system', *Physical Review Letters* **98(5)**:053601, 2007.
- [399] L. Zhao, X. Guo, C. Liu, Y. Sun, M. M. T. Loy, & S. Du, 'Photon pairs with coherence time exceeding 1  $\mu$ s', *Optica* **1(2)**:84, 2014.
- [400] K. Liao, H. Yan, J. He, S. Du, Z.-M. Zhang, & S.-L. Zhu, 'Subnatural-linewidth polarization-entangled photon pairs with controllable temporal length', *Physical Review Letters* **112(24)**:243602, 2014.
- [401] V. Zwiller, H. Blom, P. Jonsson, N. Panev, S. Jeppesen, T. Tsegaye, E. Goobar, M.-E. Pistol, L. Samuelson, & G. Björk, 'Single quantum dots emit single photons at a time: antibunching experiments', *Applied Physics Letters* **78(17)**:2476, 2001.
- [402] Z. Yuan, B. E. Kardynal, R. M. Stevenson, A. J. Shields, C. J. Lobo, K. Cooper, N. S. Beattie, D. A. Ritchie, & M. Pepper, 'Electrically driven single-photon source', *Science* **295(5552)**:102, 2002.
- [403] T. Heindel, C. Schneider, M. Lermer, S. H. Kwon, T. Braun, S. Reitzenstein, S. Höfling, M. Kamp, & A. Forchel, 'Electrically driven quantum dot-micropillar single photon source with 34% overall efficiency', *Applied Physics Letters* **96(1)**:011107, 2010.
- [404] B. Darquié, M. P. A. Jones, J. Dingjan, J. Beugnon, S. Bergamini, Y. Sortais, G. Messin, A. Browaeys, & P. Grangier, 'Controlled single-photon emission from a single trapped two-level atom', *Science* **309(5733)**:454, 2005.
- [405] P. Maunz, D. L. Moehring, S. Olmschenk, K. C. Younge, D. N. Matsukevich, & C. Monroe, 'Quantum interference of photon pairs from two remote trapped atomic ions', *Nature Physics* **3(8)**:538, 2007.
- [406] I. Aharonovich, S. Castelletto, D. A. Simpson, C. H. Su, A. D. Greentree, & S. Prawer, 'Diamond-based single-photon emitters', *Reports on Progress in Physics* **74(7)**:076501, 2011.

- [407] E. Ozbay, 'Plasmonics: merging photonics and electronics at nanoscale dimensions', *Science* **311(5758)**:189, 2006.
- [408] Y. Jin & X. Gao, 'Plasmonic fluorescent quantum dots', *Nature Nanotechnology* **4(9)**:571, 2009.
- [409] A. Kinkhabwala, Z. Yu, S. Fan, Y. Avlasevich, K. Müllen, & W. E. Moerner, 'Large single-molecule fluorescence enhancements produced by a bowtie nanoantenna', *Nature Photonics* **3(11)**:654, 2009.
- [410] A. G. Curto, G. Volpe, T. H. Taminiau, M. P. Kreuzer, R. Quidant, & N. F. van Hulst, 'Unidirectional emission of a quantum dot coupled to a nanoantenna', *Science* **329(5994)**:930, 2010.
- [411] K. Munechika, Y. Chen, A. F. Tillack, A. P. Kulkarni, I. J.-L. Plante, A. M. Munro, & D. S. Ginger, 'Spectral control of plasmonic emission enhancement from quantum dots near single silver nanoprisms', *Nano Letters* **10(7)**:2598, 2010.
- [412] Z. C. Dong, X. L. Zhang, H. Y. Gao, Y. Luo, C. Zhang, L. G. Chen, R. Zhang, X. Tao, Y. Zhang, J. L. Yang, & J. G. Hou, 'Generation of molecular hot electroluminescence by resonant nanocavity plasmons', *Nature Photonics* **4(1)**:50, 2010.
- [413] A. Fujiki, T. Uemura, N. Zettsu, M. Akai-Kasaya, A. Saito, & Y. Kuwahara, 'Enhanced fluorescence by surface plasmon coupling of Au nanoparticles in an organic electroluminescence diode', *Applied Physics Letters* **96(4)**:14, 2010.
- [414] S. G. Zhang, X. W. Zhang, Z. G. Yin, J. X. Wang, J. J. Dong, H. L. Gao, F. T. Si, S. S. Sun, & Y. Tao, 'Localized surface plasmon-enhanced electroluminescence from ZnO-based heterojunction light-emitting diodes', *Applied Physics Letters* **99(18)**:181116, 2011.
- [415] Y. Xiao, J. P. Yang, P. P. Cheng, J. J. Zhu, Z. Q. Xu, Y. H. Deng, S. T. Lee, Y. Q. Li, & J. X. Tang, 'Surface plasmon-enhanced electroluminescence in organic light-emitting diodes incorporating Au nanoparticles', *Applied Physics Letters* **100(1)**:8, 2012.
- [416] A. Kuhn, M. Hennrich, T. Bondo, & G. Rempe, 'Controlled generation of single photons from a strongly coupled atom-cavity system', *Applied Physics B* **69(5-6)**:373, 1999.
- [417] M. V. G. Dutt, J. Cheng, B. Li, X. Xu, X. Li, P. R. Berman, D. G. Steel, A. S. Bracker, D. Gammon, S. E. Economou, R.-B. Liu, & L. J. Sham, 'Stimulated and spontaneous optical generation of electron spin coherence in charged GaAs quantum dots', *Physical Review Letters* **94(22)**:227403, 2005.
- [418] X. Xu, B. Sun, P. R. Berman, D. G. Steel, A. S. Bracker, D. Gammon, & L. J. Sham, 'Coherent population trapping of an electron spin in a single negatively charged quantum dot', *Nature Physics* **4(9)**:692, 2008.
- [419] J. M. Elzerman, K. M. Weiss, J. Miguel-Sanchez, & A. Imamoglu, 'Optical amplification using Raman transitions between spin-singlet and spin-triplet states of a pair of coupled In-GaAs quantum dots', *Physical Review Letters* **107(1)**:017401, 2011.
- [420] Y. Binfeng, H. Guohua, C. Jiawei, & C. Yiping, 'Fano resonances induced by strong interactions between dipole and multipole plasmons in T-shaped nanorod dimer', *Plasmonics* **9(3)**:691, 2014.
- [421] X. Lu, J. Wu, Q. Zhu, J. Zhao, Q. Wang, L. Zhan, & W. Ni, 'Circular dichroism from single plasmonic nanostructures with extrinsic chirality', *Nanoscale* **6(23)**:14244, 2014.
- [422] U. Resch-Genger, M. Grabolle, S. Cavaliere-Jaricot, R. Nitschke, & T. Nann, 'Quantum dots versus organic dyes as fluorescent labels', *Nature Methods* **5(9)**:763, 2008.
- [423] K. Słowik, R. Filter, J. Straubel, F. Lederer, & C. Rockstuhl, 'Strong coupling of optical nanoantennas and atomic systems', *Physical Review B* **88(19)**:195414, 2013.
- [424] D. Gammon, E. S. Snow, B. V. Shanabrook, D. S. Katzer, & D. Park, 'Homogeneous linewidths in the optical spectrum of a single gallium arsenide quantum dot', *Science* **273(5271)**:87, 1996.
- [425] N. H. Bonadeo, G. Chen, D. Gammon, D. S. Katzer, D. Park, & D. G. Steel, 'Nonlinear nano-optics: Probing one exciton at a time', *Physical Review Letters* **81(13)**:2759, 1998.
- [426] P. Borri, W. Langbein, J. Mørk, J. M. Hvam, F. Heinrichsdorff, M.-H. Mao, & D. Bimberg, 'Dephasing in InAs/GaAs quantum dots', *Physical Review B* **60(11)**:7784, 1999.

- 
- [427] A. Zrenner, 'A close look on single quantum dots', *Journal of Chemical Physics* **112(18)**:7790, 2000.
- [428] R. Horodecki, P. Horodecki, M. Horodecki, & K. Horodecki, 'Quantum entanglement', *Reviews of Modern Physics* **81(2)**:865, 2009.
- [429] R. Jozsa & N. Linden, 'On the role of entanglement in quantum-computational speed-up', in 'Proceedings of the Royal Society of London **A**: Mathematical, Physical and Engineering Sciences', vol. 459, 2011, The Royal Society, 2003.
- [430] C. H. Bennett, H. J. Bernstein, S. Popescu, & B. Schumacher, 'Concentrating partial entanglement by local operations', *Physical Review A* **53(4)**:2046, 1996.
- [431] S. Hill & W. K. Wootters, 'Entanglement of a pair of quantum bits', *Physical Review Letters* **78(26)**:5022, 1997.
- [432] W. K. Wootters, 'Entanglement of formation of an arbitrary state of two qubits', *Physical Review Letters* **80(10)**:2245, 1998.
- [433] G. Vidal, J. I. Latorre, E. Rico, & A. Kitaev, 'Entanglement in quantum critical phenomena', *Physical Review Letters* **90(22)**:227902, 2003.
- [434] L. Amico, R. Fazio, A. Osterloh, & V. Vedral, 'Entanglement in many-body systems', *Reviews of Modern Physics* **80(2)**:517, 2008.
- [435] T. B. Pittman, Y. H. Shih, D. V. Strekalov, & A. V. Sergienko, 'Optical imaging by means of two-photon quantum entanglement', *Physical Review A* **52(5)**:R3429, 1995.
- [436] A. N. Boto, P. Kok, D. S. Abrams, S. L. Braunstein, C. P. Williams, & J. P. Dowling, 'Quantum interferometric optical lithography: exploiting entanglement to beat the diffraction limit', *Physical Review Letters* **85(13)**:2733, 2000.
- [437] K. Boström & T. Felbinger, 'Deterministic secure direct communication using entanglement', *Physical Review Letters* **89(18)**:187902, 2002.
- [438] Y. Li, K. Zhang, & K. Peng, 'Multiparty secret sharing of quantum information based on entanglement swapping', *Physics Letters A* **324(5-6)**:420, 2004.
- [439] J. Appel, P. J. Windpassinger, D. Oblak, U. B. Hoff, N. Kjærgaard, & E. S. Polzik, 'Mesoscopic atomic entanglement for precision measurements beyond the standard quantum limit', *Proceedings of the National Academy of Sciences* **106(27)**:10960, 2009.
- [440] M. Sarovar, A. Ishizaki, G. R. Fleming, & K. B. Whaley, 'Quantum entanglement in photosynthetic light-harvesting complexes', *Nature Physics* **6(6)**:462, 2010.
- [441] S.-B. Zheng & G.-C. Guo, 'Efficient scheme for two-atom entanglement and quantum information processing in cavity QED', *Physical Review Letters* **85(11)**:2392, 2000.
- [442] A. Sørensen & K. Mølmer, 'Entanglement and quantum computation with ions in thermal motion', *Physical Review A* **62(2)**:022311, 2000.
- [443] H. Jeong, M. S. Kim, & J. Lee, 'Quantum-information processing for a coherent superposition state via a mixed-entangled coherent channel', *Physical Review A* **64(5)**:052308, 2001.
- [444] S. Tanzilli, W. Tittel, M. Halder, O. Alibart, P. Baldi, N. Gisin, & H. Zbinden, 'A photonic quantum information interface', *Nature* **437(7055)**:116, 2005.
- [445] J. I. Cirac, P. Zoller, H. J. Kimble, & H. Mabuchi, 'Quantum state transfer and entanglement distribution among distant nodes in a quantum network', *Physical Review Letters* **78(16)**:3221, 1997.
- [446] W. Dür, H.-J. Briegel, J. I. Cirac, & P. Zoller, 'Quantum repeaters based on entanglement purification', *Physical Review A* **59(1)**:169, 1999.
- [447] M. Muraio, M. B. Plenio, & V. Vedral, 'Quantum-information distribution via entanglement', *Physical Review A* **61(3)**:032311, 2000.

- [448] C.-W. Chou, J. Laurat, H. Deng, K. S. Choi, H. De Riedmatten, D. Felinto, & H. J. Kimble, 'Functional quantum nodes for entanglement distribution over scalable quantum networks', *Science* **316(5829)**:1316, 2007.
- [449] K. S. Choi, H. Deng, J. Laurat, & H. J. Kimble, 'Mapping photonic entanglement into and out of a quantum memory', *Nature* **452(7183)**:67, 2008.
- [450] M. D. Lukin, S. F. Yelin, & M. Fleischhauer, 'Entanglement of atomic ensembles by trapping correlated photon states', *Physical Review Letters* **84(18)**:4232, 2000.
- [451] G. Chen, N. H. Bonadeo, D. G. Steel, D. Gammon, D. S. Katzer, D. Park, & L. J. Sham, 'Optically induced entanglement of excitons in a single quantum dot', *Science* **289(5486)**:1906, 2000.
- [452] J. Volz, M. Weber, D. Schlenk, W. Rosenfeld, J. Vrana, K. Saucke, C. Kurtsiefer, & H. Weinfurter, 'Observation of entanglement of a single photon with a trapped atom', *Physical Review Letters* **96(3)**:030404, 2006.
- [453] J.-M. Raimond, M. Brune, & S. Haroche, 'Manipulating quantum entanglement with atoms and photons in a cavity', *Reviews of Modern Physics* **73(3)**:565, 2001.
- [454] G.-P. Guo, C.-F. Li, J. Li, & G.-C. Guo, 'Scheme for the preparation of multiparticle entanglement in cavity QED', *Physical Review A* **65(4)**:042102, 2002.
- [455] E. Solano, G. S. Agarwal, & H. Walther, 'Strong-driving-assisted multipartite entanglement in cavity QED', *Physical Review Letters* **90(2)**:027903, 2003.
- [456] P. G. Kwiat, K. Mattle, H. Weinfurter, A. Zeilinger, A. V. Sergienko, & Y. Shih, 'New high-intensity source of polarization-entangled photon pairs', *Physical Review Letters* **75(24)**:4337, 1995.
- [457] J.-W. Pan, D. Bouwmeester, H. Weinfurter, & A. Zeilinger, 'Experimental entanglement swapping: entangling photons that never interacted', *Physical Review Letters* **80(18)**:3891, 1998.
- [458] C.-Y. Lu & J.-W. Pan, 'Quantum optics: push-button photon entanglement', *Nature Photonics* **8(3)**:174, 2014.
- [459] D. Jaksch, H.-J. Briegel, J. I. Cirac, C. W. Gardiner, & P. Zoller, 'Entanglement of atoms via cold controlled collisions', *Physical Review Letters* **82(9)**:1975, 1999.
- [460] C.-W. Chou, H. De Riedmatten, D. Felinto, S. V. Polyakov, S. J. Van Enk, & H. J. Kimble, 'Measurement-induced entanglement for excitation stored in remote atomic ensembles', *Nature* **438(7069)**:828, 2005.
- [461] T. Wilk, A. Gaëtan, C. Evellin, J. Wolters, Y. Miroshnychenko, P. Grangier, & A. Browaeys, 'Entanglement of two individual neutral atoms using Rydberg blockade', *Physical Review Letters* **104(1)**:010502, 2010.
- [462] I. S. Maksymov, A. E. Miroshnichenko, & Y. S. Kivshar, 'Plasmonic nanoantennas for efficient control of polarization-entangled photon pairs', *Physical Review A* **86(1)**:011801, 2012.
- [463] M. B. Plenio & S. F. Huelga, 'Entangled light from white noise', *Physical Review Letters* **88(19)**:197901, 2002.
- [464] E. Knill, R. Laflamme, & G. J. Milburn, 'A scheme for efficient quantum computation with linear optics', *Nature* **409(6816)**:46, 2001.
- [465] W. Demtröder, *Laser Spectroscopy: Basic Concepts and Instrumentation*, 3rd ed., Springer Science+Business Media, Berlin, Germany, 2002.
- [466] V. Vedral, M. B. Plenio, M. A. Rippin, & P. L. Knight, 'Quantifying entanglement', *Physical Review Letters* **78(12)**:2275, 1997.
- [467] G. Vidal & R. F. Werner, 'Computable measure of entanglement', *Physical Review A* **65(3)**:032314, 2002.
- [468] M. B. Plenio, 'Logarithmic negativity: a full entanglement monotone that is not convex', *Physical Review Letters* **95(9)**:090503, 2005.

- 
- [469] J. Oppermann, J. Straubel, I. Fernandez-Corbaton, & C. Rockstuhl, 'Normalization approach for scattering modes in classical and quantum electrodynamics', *Physical Review A* **97(5)**:052131, 2018.
- [470] J. Oppermann, J. Straubel, K. Słowik, & C. Rockstuhl, 'Quantum description of radiative decay in optical cavities', *Physical Review A* **97(1)**:013809, 2018.

## ACKNOWLEDGEMENT

I want to thank my doctorate supervisor Carsten Rockstuhl for bringing me to KIT and letting me experience in situ the establishment of his research group. I want to thank him for entrusting me with this PhD project, for all the good scientific advice he shared and for having a sympathetic ear for his entire group. I greatly enjoyed the constructive working environment he created as well as his scientific enthusiasm.

Furthermore, I am deeply indebted to Karolina Słowik, who has guided and accompanied me on my scientific endeavors and on whom I could always rely. I want to thank her for her patience, her knowledge, her time, her humor, and not least her compassion for an inexperienced PhD student.

I want to thank my diploma supervisor and colleague Robert Filter for his well-meaning recommendations for all possible situations and his passion both in science and daily life. I owe gratitude to our experimental collaborators in Canberra, especially Haitao Chen and Dragomir Neshev. Not just for the educational experience of bringing together theoretical and experimental means, but also for caringly hosting a short visit to Australia. I want to thank Evgenia Rusak, Mirko Göddel, and Jens Oppermann for suffering through my supervision of their master or bachelor projects and especially Jens for his interest in and continuing hard work on common topics. I am certain his entire PhD project will be just as remarkable as his work so far has been.

I want to thank the Karlsruhe School of Optics & Photonics for the financial support and our solid state optics group at KIT with all its previous and current members in general for being the magnificent, understanding and collegial bunch that they are. Inspired by the head of our group, with everyone contributing to the best of their ability, hands-on help, just as collective experience and practical advice, was always just a question away.

Schlussendlich, für mich persönlich jedoch zweifelsohne von größter Bedeutung, möchte ich meiner Familie danken. Ihre grenzenlose Geduld, ihr immerwährendes Verständnis und ihre unbedingte Unterstützung erachte ich keinesfalls als selbstverständlich.



## EIDESSTATTLICHE VERSICHERUNG

- Bei der eingereichten Dissertation zu dem Thema '**LIGHT-MATTER INTERACTION IN HYBRID QUANTUM PLASMONIC SYSTEMS**' handelt es sich um meine eigenständig erbrachte Leistung.
- Ich habe nur die angegebenen Quellen und Hilfsmittel benutzt und mich keiner unzulässigen Hilfe Dritter bedient. Insbesondere habe ich wörtlich oder sinngemäß aus anderen Werken übernommene Inhalte als solche kenntlich gemacht.
- Die Arbeit oder Teile davon habe ich bislang nicht an einer Hochschule des In- oder Auslands als Bestandteil einer Prüfungs- oder Qualifikationsleistung vorgelegt.
- Die Richtigkeit der vorstehenden Erklärungen bestätige ich.

Ich versichere an Eides statt, dass ich nach bestem Wissen die reine Wahrheit erkläre und nichts verschwiegen habe.

Karlsruhe, den 30. April 2018

